DISSERTATION

CHARACTERIZATION OF A DENSE MEDIUM PLASMA REACTOR FOR NAVAL WASTEWATER TREATMENT AND THE DEVELOPMENT OF A TUBULAR HIGH-DENSITY PLASMA REACTOR

Submitted by:

Derek C. Johnson

Department of Chemical & Biological Engineering

In partial fulfillment of the requirements

For the Degree of Doctor of Philosophy

Colorado State University

Fort Collins, CO

Spring 2006

Reproduced with permission of the copyright owner. Further reproduction prohibited without permission.

UMI Number: 3226135

INFORMATION TO USERS

The quality of this reproduction is dependent upon the quality of the copy submitted. Broken or indistinct print, colored or poor quality illustrations and photographs, print bleed-through, substandard margins, and improper alignment can adversely affect reproduction.

In the unlikely event that the author did not send a complete manuscript and there are missing pages, these will be noted. Also, if unauthorized copyright material had to be removed, a note will indicate the deletion.

UMI®

UMI Microform 3226135

Copyright 2006 by ProQuest Information and Learning Company.

All rights reserved. This microform edition is protected against unauthorized copying under Title 17, United States Code.

ProQuest Information and Learning Company
300 North Zeeb Road
P.O. Box 1346
Ann Arbor, MI 48106-1346

Reproduced with permission of the copyright owner. Further reproduction prohibited without permission.

COLORADO STATE UNIVERSITY

January 11, 2006

WE HEREBY RECOMMEND THAT THE DISSERTATION PREPARED UNDER OUR SUPERVISION BY DEREK C JOHNSON ENTITLED CHARACTERIZATION OF A DENSE MEDIUM PLASMA REACTOR FOR NAVAL WASTEWATER TREATMENT AND THE DEVELOPMENT OF A TUBULAR HIGH-DENSITY PLASMA REACTOR BE ACCEPTED AS FULFILLING IN PART REQUIREMENTS FOR THE DEGREE OF DOCTOR OF PHILOSOPY.

Committee on Graduate Work

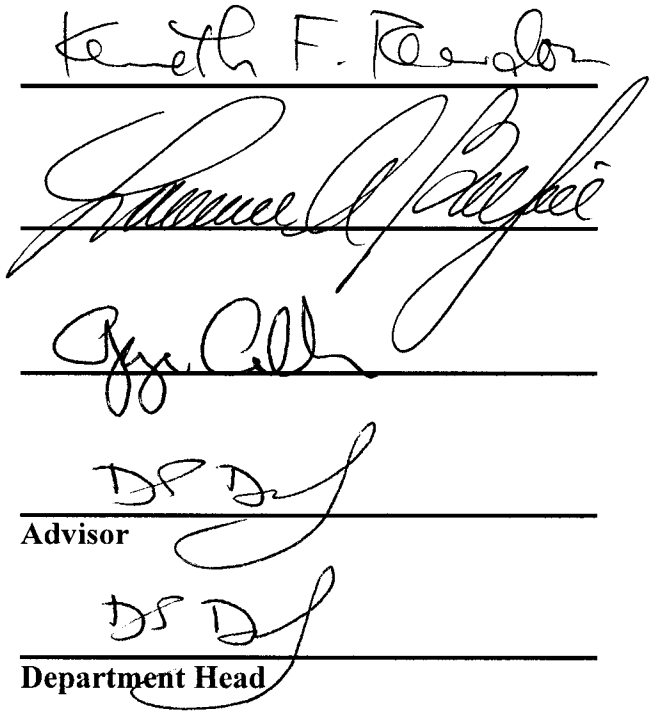

Advisor

Department Head

Reproduced with permission of the copyright owner. Further reproduction prohibited without permission.

ABSTRACT OF **DISSERTATION**

CHARACTERIZATION OF A DENSE MEDIUM PLASMA REACTOR FOR NAVAL WASTEWATER TREATMENT AND THE DEVELOPMENT OF A TUBULAR HIGH-DENSITY PLASMA REACTOR

Plasma treatment of contaminated water appears to be a promising alternative for the oxidation of aqueous organic pollutants. This study examines the kinetic and oxidation mechanisms of methyl *t*-butyl ether (MTBE) in a dense medium plasma reactor (DMPR) utilizing gas chromatography-mass spectrometry and gas chromatography-thermal conductivity techniques. A rate law is developed for the removal of MTBE from an aqueous solution in the DMPR. Rate constants are also derived for three reactor configurations and two pin array spin rates. The oxidation products from the treatment of MTBE contaminated water in the DMPR were found to be predominately carbon dioxide, with smaller amounts of acetone, *t*-butyl formate and formaldehyde. The lack of stable intermediate products suggests that the MTBE is, to some extent, oxidized directly to carbon dioxide, making the DMPR a promising tool in the future remediation of water. Chemical and physical mechanisms, together with carbon balances, are used to describe the formation of the oxidation products and the important aspects of the plasma discharge.

Computational fluid dynamics is applied to the study of 3D fluid flow in a DMPR under different operating conditions. Reaction mechanisms and rates for the removal of MTBE

Reproduced with permission of the copyright owner. Further reproduction prohibited without permission.

in a DMPR are developed from experimental data to determine the plasma volume, the rate of interphase mass transfer and the photolysis rate of MTBE via UV emission from the plasma. The simulations show that, in the DMPR, the volume of fluid in contact with the plasma only constitutes a maximum of approximately 10% of the fluid passing through the recirculation channels. The simulations also predict large pressure gradients on the pin electrode tips, resulting in a small discharge area located away from the region in which the radius of curvature is minimized. This result has been confirmed experimentally in the fact that it is observed that the pin electrodes sputter metal from an area of similar size and location to the low-pressure region predicted by the simulations. The chemical kinetics developed in this study are incorporated into the simulation to model the attenuation of MTBE in the DMPR. Fluid volumes are assigned the appropriate reaction mechanism and corresponding reaction rates. The simulation results accurately capture the experimental observations in that the MTBE concentration is reduced to approximately 5% of its original value in 11 min. Although only a small fraction of the fluid interacts with the plasma, oxidation due to the plasma is shown to be the major loss mechanism.

Experiments have yielded a number of important insights into the energy distribution, sparging and oxidation of MTBE, benzene, ethylbenzene, toluene, *m*- and *p*-xylene, and *o*-xylene (BTEX) in a DMPR. It has been found that the DMPR transferred a relatively small amount of electrical energy, approximately 4% in the form of sensible heat, to the surrounding bulk liquid. Rate constants associated with plasma initiated oxidation, interphase mass transfer and photolysis were determined using a combination of nonlinear

Reproduced with permission of the copyright owner. Further reproduction prohibited without permission.

least squares analysis and MATLAB® optimization techniques for each species. The rate constants developed for the DMPR, in conjunction with a species mass balance on a prototype tubular high-density plasma reactor, have been applied to determine the removal rates of MTBE and BTEX when operating in batch and continuous flow configurations. The dependence of contaminant concentration on parameters such as treatment time, the number of pin electrodes, electrode gap and volumetric flow rate has been determined. It was found that, under various design specifications and operating conditions, the tubular high-density plasma reactor may be an effective tool for the removal of volatile organic compounds from aqueous solutions

Derek C Johnson
Department of Chemical & Biological Engineering
Colorado State University
Fort Collins, CO 80523
Spring 2006

Reproduced with permission of the copyright owner. Further reproduction prohibited without permission.

ACKNOWLEDGMENTS

I would like to thank David S. Dandy and Vasgen A. Shamamian for their guidance. I would also like to acknowledge support for this work from the National Institutes of Health (grant number: EB00726), Office of Naval Research (grant number: N00014-00-WX2-1163) and the National Science Foundation's Fast Track to Work Scholarship Program.

Reproduced with permission of the copyright owner. Further reproduction prohibited without permission.

Table of Contents

Reproduced with permission of the copyright owner. Further reproduction prohibited without permission.

Reproduced with permission of the copyright owner. Further reproduction prohibited without permission.

List of Tables

Chapter 1

Chapter 2

Chapter 3

Reproduced with permission of the copyright owner. Further reproduction prohibited without permission.

Chapter 4

Chapter 5

Reproduced with permission of the copyright owner. Further reproduction prohibited without permission.

Reproduced with permission of the copyright owner. Further reproduction prohibited without permission.

List of Figures

Chapter 1

Chapter 2

Chapter 3

Reproduced with permission of the copyright owner. Further reproduction prohibited without permission.

Reproduced with permission of the copyright owner. Further reproduction prohibited without permission.

Chapter 4

Reproduced with permission of the copyright owner. Further reproduction prohibited without permission.

Reproduced with permission of the copyright owner. Further reproduction prohibited without permission.

Chapter 5

Reproduced with permission of the copyright owner. Further reproduction prohibited without permission.

Reproduced with permission of the copyright owner. Further reproduction prohibited without permission.

Chapter One

1.0 Introduction

Potable water treatment, in its simplest form, dates back over four thousand years. These simple treatment processes are recorded in Sanskrit medical lore and Egyptian wall inscriptions (Baker, 1949). Instructions for water purification by boiling it in copper vessels, exposing it to sunlight, filtering it through charcoal and cooling in an earthen vessel are also contained in Sanskrit writings (Viessman and Hammer, 1998). With an exponential growth in world population, currently exceeding 6.5 billion, the need to supply clean water has proven increasingly difficult. This complex problem was apparent as early as 98 A.D. Rome where the first engineering report on water supply and treatment was written (Baker, 1949). Approximately six hundred years later, an elaborate dissertation on the distillation of water and other liquids was written by an Arabian alchemist (Viessman and Hammer, 1998). The water treatment field was further advanced in the late 1600s by the efforts of Luc Antonio Porzio, an Italian physician, who published the first known book describing sedimentation basins and sand filters (Baker, 1949). In most of the United States, little attention was given to potable or wastewater treatment until after the civil war. Since turbidity was not a major problem, the first sand filters were slow. It was not until the end of the nineteenth century that rapid sand filters and coagulants were used to increase the efficiency of potable water treatment facilities (Viessman

Reproduced with permission of the copyright owner. Further reproduction prohibited without permission.

and Hammer, 1998).

Disposal of human waste was another problem that became apparent in the last half of the nineteenth century. The original solution was to dispose of the waste in the existing storm drains. This practice, however, overwhelmed many receiving water bodies, especially small lakes and slow moving streams with low throughput resulting in general health problems; especially during drought and summer months when bacteria and algae take advantage of the increased sunlight. This prompted the treatment of wastewater and development of separate storm drains and sewer systems. Throughout the twentieth century, increasing demands have taxed not only potable water treatment facilities, but wastewater treatment facilities as well. While water quality standards have become increasing stringent, the quality of the influent has deteriorated. This compounds that fact that as the adverse effects of long term exposure to industrial chemicals become apparent, more are being classified as toxic. As drinking water supplies and wastewater effluents begin to contain trace amounts of toxic chemicals due to accidental and intentional releases, the use of increasingly sophisticated water analysis and treatment technologies are required.

Due to the need to treat wastewater at large flow rates with highly varying compositions, most countries, including the Unites States, have turned to biological treatment. It is an effective, energy-efficient way to clean foul water. Conventional biological wastewater treatment usually consists of preliminary treatment, primary settling, biological aeration, secondary settling, sludge thickening and disposal, and disinfection. A diagram of a typi-

Reproduced with permission of the copyright owner. Further reproduction prohibited without permission.

cal wastewater treatment facility is presented in Figure 1.1. The effluent from some of the more advanced facilities, which include tertiary treatment processes, is cleaner than the receiving water body. However, conventional and advanced biological treatment plants are large, have a high capital expense and the biological organisms that treat the water are sensitive to changes in waste concentrations and toxic pollutants. Some countries do not have the required space or monetary resources to construct effective biological wastewater treatment facilities that could adequately treat the input generated by its population. In these cases, poorly or untreated wastewater is discharged into the receiving water body, which inevitably becomes over-taxed. Disease outbreaks and environmental problems soon follow. Unfortunately, an efficient chemical or electrical process to treat wastewater, which would require less space and a lower capital investment, has not been developed. If an efficient and effective electrical or chemical treatment process was developed, space-limited countries, as well as sea vessels, space shuttles and space stations, which have limited resources, could adequately treat wastewater for discharge to a nearby water body or reuse as potable water.

1.1 U.S. Navy's Need

Section 312 of the Federal Water Pollution Control Act was modified by the National Defense Authorization Act of 1996 requiring that the Secretary of Defense and the Administrator of the Environmental Protection Agency (EPA) generate uniform national discharge standards (UNDS) for vessels of the armed forces (U.S. EPA and U.S. DoD, 2001). These standards are being developed to augment the protection of harbors and coastal areas, encourage environmentally sound management practices, help standardize

Reproduced with permission of the copyright owner. Further reproduction prohibited without permission.

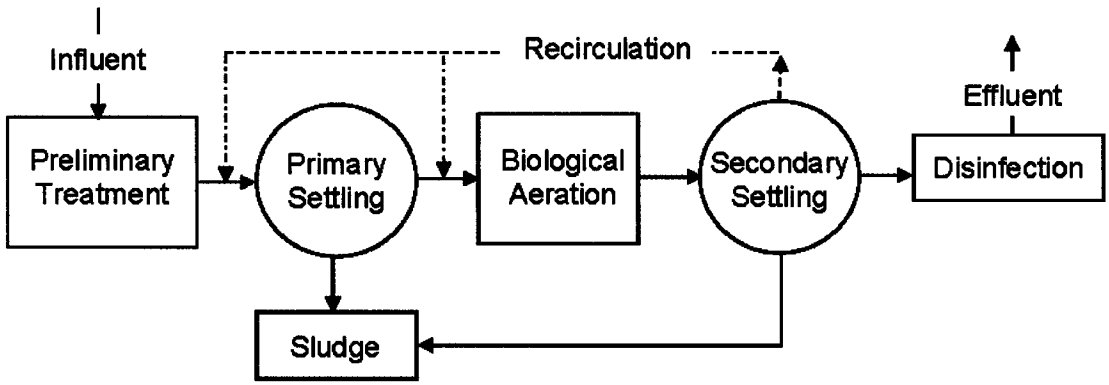

Figure 1.1: A diagram of a conventional wastewater treatment facility (Viessman and Hammer, 1998).

Reproduced with permission of the copyright owner. Further reproduction prohibited without permission.

crew training and determine how future ships will be built (U.S. EPA et al., 2001). The program is also intended to stimulate "innovative" vessel pollution and effluent control technologies. The UNDS requires the identification of all discharges associated with normal vessel operations and subsequently determines which of the discharges will be regulated. The criteria for determining the regulated discharges are based on the potential for adverse impacts on the marine environment (U.S. Government, 1999). The extent of the treatment mandated by the UNDS determines if the discharge can be controlled through changes in operation procedure, or if the discharge requires treatment by a marine pollution control device (MPCD) (U.S. Government, 1999). The UNDS regulations are enforced on armed forces vessels in all inland waters and ocean waters within 12 nautical miles of the U.S. coast (U.S. EPA et al., 2001).

A vessel of the armed forces is (a) any vessel owned or operated by the Department of Defense (DoD), other than a time of voyage chartered vessel; and (b) any vessel owned or operated by the Department of Transportation that is designated by the secretary of the department for use by the Coast Guard (U.S. Government, 1999). Vessels that are currently regulated are Army, Navy, Air Force, Marine Corps, Military Sealift Command (MSC) and Coast Guard ships (U.S. EPA et al., 2001). As of 1997, the Navy, of the six armed forces subdivisions, by far has the most vessels under its command that would fall under this new regulation with 4,760 of 7,170 total ships (U.S. Government, 1999). With such a large contingent of ships affected by the standards, MPCDs are being developed to allow the Navy to carryout mission requirements unencumbered by environmental regulations. The Navy also requires the treatment system to be efficient, reliable, have a low

Reproduced with permission of the copyright owner. Further reproduction prohibited without permission.

manpower requirement and meet the shipboard requirements for space and shock.

1.1.1 UNDS-Phase I

On August 25, 1998, UNDS Phase I was published requiring MPCDs on 25 of the 39 identified discharges from military vessels. The 25 regulated and 14 unregulated discharges are listed in Table 1.1 (U.S. EPA et al., 2001; U.S. Government, 1999). A detailed report has been prepared for each of the 39 identified discharges and is available from the DoD website. Each report contains a description of the discharge, the system and equipment involved in generating the discharge, the chemical composition of the discharge and the current pollution control device or procedure in use, if any, to mitigate the environmental impact. Of the 39 identified discharges, graywater is the biggest pollution problem facing the Navy.

Graywater is wastewater from showers, baths and galleys (U.S. Government, 1996). On most of the armed forces vessels, however, graywater is collected with drainage from laundry, interior deck drains, lavatory sinks, water fountains and miscellaneous shop sinks (U.S. EPA and U.S. DoD, 2001). Most naval ships discharge untreated graywater into the surrounding water body while not in port. The estimated discharge rate of graywater from naval ships within 12 nautical miles of the U.S. shore is calculated from the following equation (U.S. EPA and U.S. DoD, 2001):

$$\begin{pmatrix} \text{graywater} \\ \text{discharge} \\ \text{rate} \end{pmatrix} = \left(\frac{\#\,\text{transits}}{\text{year}}\right) \text{x} \left(\frac{\text{time}}{\text{transit}}\right) \text{x} \begin{pmatrix} \text{production} \\ \text{rate} \end{pmatrix} \text{x} \begin{pmatrix} \#\ \text{of} \\ \text{personnel} \end{pmatrix}. \qquad (1.1)$$

Reproduced with permission of the copyright owner. Further reproduction prohibited without permission.

Table 1.1: Thirty nine discharges from military vessels identified by the UNDS.

Discharges Requiring Pollution Control Devices		Discharges Not Requiring Pollution Control Devices
Surface Vessel Bilgewater/Oil-Water Separator Discharge	Catapult Water Brake Tank and Post-Launch Retraction Exhaust	Submarine Acoustic Countermeasures Launcher Discharge
Chain Locker Effluent	Clean Ballast	Cathodic Protection
Distillation and Reverse Osmosis Brine	Controllable Pitch Propeller Hydraulic Fluid	Catapult Wet Accumulator Discharge
Deck Runoff	Dirt Ballast	Freshwater Lay-Off
Compensated Fuel Ballast	Elevator Pit Effluent	Steam Condensate
Firemain Systems	Gas Turbine Water Wash	Portable Damage Control Drain Pump Discharge
Graywater	Hull Coating Leachate	Rudder Bearing Lubrication
Motor Gasoline Compensating Discharge	Non-Oily Machinery Wastewater	Portable Damage Control Drain Pump Wet Exhaust
Photographic Laboratory Drains	Seawater Cooling Overboard Discharge	Mine Countermeasures Equipment Lubrication
Seawater Piping Biofouling Prevention	Small Boat Engine Wet Exhaust	Stern Tube Seals and Underwater Bearing Lubrication
Sonar Dome Discharge	Submarine Bilgewater	Boiler Blowdown
Aqueous Film-Forming Foam	Underwater Ship Husbandry	Submarine Emergency Diesel Engine Wet Exhaust
Welldeck Discharges		Submarine Outboard Equipment Grease and External Hydraulics
		Refrigeration and Air Conditioning Condensate

Reproduced with permission of the copyright owner. Further reproduction prohibited without permission.

The Navy estimates that the average vessel makes approximately 20 transits per year with an average transit time of 4 hours, has a generation rate of 30 gal/(capita×day) and an average of 400 personnel on board (U.S. EPA and U.S. DoD, 2001). This yields an annual production of approximately 40,000 gallons of graywater per vessel.

The environmental impact of graywater is significant when factoring in the estimated concentrations of components that are known to harm the environment as well as estimated nutrient loadings and oxygen-demanding substances (U.S. EPA and U.S. DoD, 2001). Ranges of the various water quality parameters, which are important when determining the environmental impact, are listed in Table 1.2 along with its recommended discharge value set by the EPA. The data was obtained from six graywater components–wash basins, showers, food preparation, laundry, dishwasher effluent and deep sink effluent (U.S. EPA and U.S. DoD, 2001). The range of various metal concentrations from the following graywater components–potable water sink, galley drains, sink and scullery–are listed in Table 1.3 along with the most stringent state acute water quality criteria (SWQC). Due to the high total solids, oxygen demand, nutrient loading and metal concentrations, the nature of discharge report concluded that graywater must be treated by a MPCD before discharged within 12 nautical miles of the U.S. coast or in inland waters.

1.1.2 UNDS-Phase II & III

Phase II, which is in progress, will create discharge standards for the releases outlined in Phase I. Phase III will establish requirements for the design, installation and operation of MPCDs to meet the standards developed during Phase II. The DoD and EPA are

Reproduced with permission of the copyright owner. Further reproduction prohibited without permission.

Table 1.2: A list of water quality parameter values measured from graywater and their corresponding recommended value set by the EPA.

Water Quality Parameter	Graywater Value	EPA Recommended Value
pH	6.74 – 10.0	6.5 – 9.0
Total Suspended Solids (TSS)	94 – 4695 (mg/L)	30 (mg/L)
Total Dissolved Solids (TDS)	225 – 8064 (mg/L)	500 (mg/L)
Biochemical Oxygen Demand (BOD)	144 – 2618 (mg/L)	30 (mg/L)
Phosphate (PO_4^{3-}), Phosphorous	1.03 – 28.2 (mg/L)	1.0 (mg/L)

Reproduced with permission of the copyright owner. Further reproduction prohibited without permission.

Table 1.3: A list of heavy metal concentrations measured from graywater and the corresponding most stringent state water quality criteria (SWQC).

Metal	Graywater Concentration (mg/L)	SWQC (mg/L)
Silver	0.007 – 0.012	0.0012
Cadmium	0.004 – 0.017	0.005 *
Chromium	0.002 – 0.03	0.1 *
Copper	0.25 – 3.4	0.0024
Lead	0.042 – 1.56	0.0056
Mercury	0.0002 – 0.0095	0.000025
Nickel	0.025 – 0.113	0.0083
Zinc	0.19 – 2.36	0.0846

* Denotes maximum contaminant level goal (MCLG)–defined as the concentration of a compound present in drinking water with which no known risks to health are expected–in the absence of a SWQC.

Reproduced with permission of the copyright owner. Further reproduction prohibited without permission.

authorized to review discharge standards, taking into account any new information, and update the regulation accordingly (U.S. EPA et al., 2001). The final goal of this program is to increase the ability of the armed forces to better design and build environmentally sound vessels, train crews to operate vessels in a manner that is protective of the environment and maintain domestic and international operational flexibility (U.S. Government, 1999). To accomplish this task, a MPCD which allows the U.S. Navy to carry out its mission, while at the same time meeting stringent shipboard requirements for space, shock and manpower, needs to be developed. Treatment processes employing advanced oxidation technologies (AOT) appear to be a promising alternative to those currently utilized by the U.S. Navy.

Reproduced with permission of the copyright owner. Further reproduction prohibited without permission.

1.2 References

Baker, M.N., 1949. The Quest for Pure Water. American Water Works Association, New York, NY, USA, 1-11.

Viessman, W.J. and Hammer, M.J., 1998. Water Supply and Pollution Control, 6th ed. Addison Wesley, Menlo Park, CA, USA.

U.S. EPA and U.S. DoD, Jan. 30, 2001. Nature of Discharge Report: Graywater. http://unds.bah.com/phaseI.htm.

U.S. EPA, U.S. DoD, USCG, Jan. 30, 2001. Uniform National Discharge Standards. http://unds.bah.com/.

U.S. Government, 1999. 64 CFR 25126.

U.S. Government, 1996. Federal Water Pollution Control Act as amended, section 312a.

Reproduced with permission of the copyright owner. Further reproduction prohibited without permission.

Chapter Two

2.0 Plasma Induced Oxidation Technologies

Plasma induced oxidation technologies utilize plasma as the medium in which electrical energy is transferred into a fluid to degrade organic compounds. A plasma is an ionized gaseous complex containing electrons, ions and gaseous atoms or molecules in various energy states. Plasma may be well suited to decontaminate water due to its ability to produce reactive species that are more numerous and energetic than those produced in traditional chemical reactors. The active species produced make it possible to degrade organic compounds in a way that was previously economically impractical by other methods (Lieberman and Lichtenberg, 1994). A plasma can be generated by producing an electrical discharge in an insulating fluid, such as water or air, and may be classified as either a thermal (hot) or non-thermal (cold) plasma (Lieberman and Lichtenberg, 1994).

A thermal plasma is comprised of gas atoms, molecules, ions and electrons in local thermal equilibrium, and is generally produced by an atmospheric pressure, high-energy discharge (Lieberman and Lichtenberg, 1994). The electrons produced from a thermal discharge contain enough kinetic energy to completely atomize a volatile organic molecule upon collision. When the constitute atoms emerge from the plasma stream, thermodynamically favored species are formed. A non-thermal plasma is comprised of gas atoms,

Reproduced with permission of the copyright owner. Further reproduction prohibited without permission.

molecules and ions at room temperature with electrons at a much higher energy state. In this case, the electrons have enough kinetic energy to cause the cleavage of chemical bonds; however, the complete atomization of the molecule is not guaranteed (Lieberman and Lichtenberg, 1994). This is due to the fact that non-thermal discharges require a lower applied voltage, resulting in smaller amounts of energy transferred to the plasma stream when compared to thermal discharges. A non-thermal plasma that has been studied extensively and can be initiated by applying a voltage drop across two electrodes submerged in an aqueous solution to promote oxidation are glow discharges.

2.1 Glow Discharge

Glow discharge plasmas can be identified by the modest amount of visible light emanating from the discharge. The resulting glow varies in color as a function of the fluid in which the discharge is initiated. The glow occurs as a result of interactions between the electrons produced by the discharge with atoms and/or molecules causing excitation and the subsequent release of a photon to return to the ground energy state (Roth, 1995). These plasmas have generated research activity because of the unique chemical reactions that can be induced not only in low-pressure gases, but aqueous solutions as well. Degradation of organic compounds (Tezuka and Iwasaki, 1997; Tezuka and Iwasaki, 1998; Tezuka and Iwasaki, 2001; Tezuka and Iwasaki, 2002), creation of bioorganic carbon molecules from elemental carbon (Harada and Suzuki, 1977) and electrical discharge machining (Tezuka and Iwasaki, 2002) are just a few examples of practical applications employing an aqueous glow discharge. In addition to having low power densities ranging from below 10^{-4} to tens of W/cm^3 (Roth, 1995), aqueous glow discharge plasmas have an

Reproduced with permission of the copyright owner. Further reproduction prohibited without permission.

additional advantage over low-pressure glow discharges. The fact that they are initiated at atmospheric pressure allows the plasma to be incorporated into continuous flow reactors, whereas batch reactors are the only viable configuration for reduced pressure plasmas. This advantage can cut production time as well as reduce cost because expensive vacuum pump systems are not needed.

The transition to a glow discharge is well documented for low-pressure dc electrical discharges. The nonlinear current-voltage curve, shown in Figure 2.1 (Roth, 1995), relates the approximate current needed to produce discharges in different plasma regions. An electrical breakdown voltage and a corresponding discontinuous zone, points E through F, characterize the transition from the dark discharge region to the glow region. During this transition, the current and excitation of the gas is sufficient to produce a plasma glow (Roth, 1995). After the discontinuous segment of the curve, there exists another segment in which the voltage across the discharge is essentially independent of the discharge current, points F through G. The combination of the two previous segments is termed the normal glow region. The abnormal glow region of the current-voltage curve, points G through H, is characterized by an increase in current with voltage. This trend continues until the power inputted into the solution is such that the formation of filamentary streamer plasma discharges can be supported. Although the current-voltage curve and the specific regions presented previously correspond to low-pressure dc discharges, it nonetheless yields insight into the behavior of glow plasmas in aqueous solutions.

A general voltage-current curve for an applied dc potential across electrodes submersed

Reproduced with permission of the copyright owner. Further reproduction prohibited without permission.

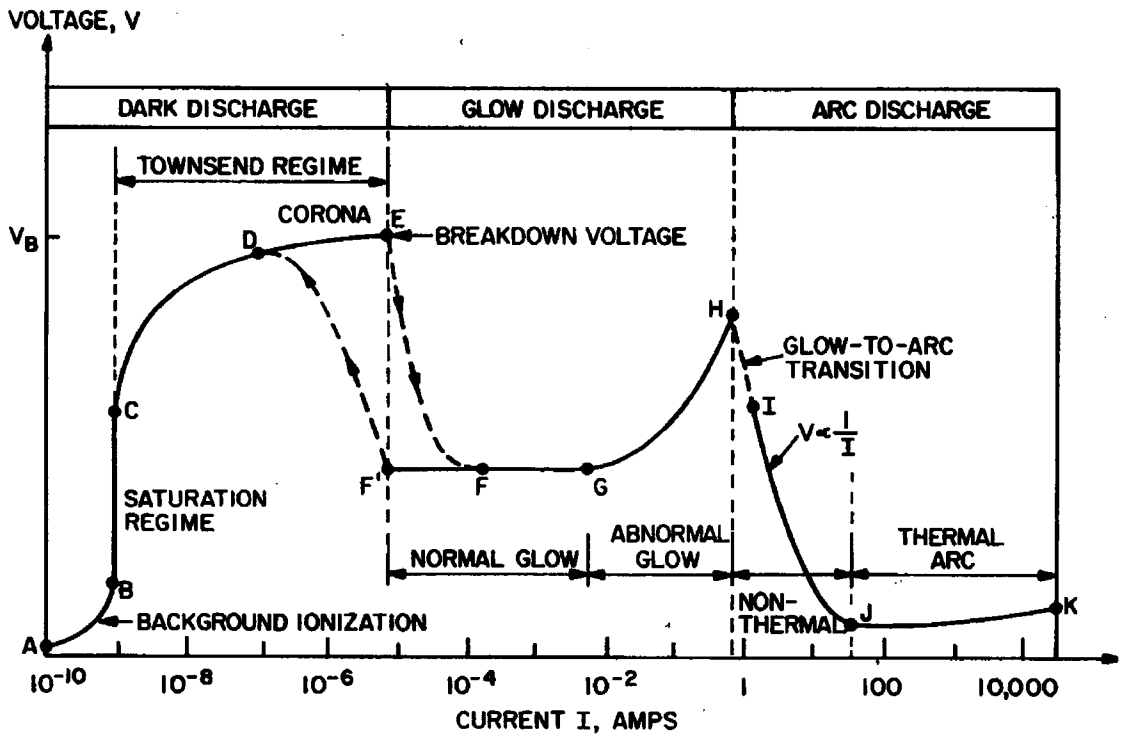

Figure 2.1: Current-voltage curve for a low-pressure dc electric discharge tube (Roth, 1995).

Reproduced with permission of the copyright owner. Further reproduction prohibited without permission.

in an aqueous solution is shown in Figure 2.2 (Hickling and Ingram, 1964). In an aqueous solution, the conditions are such that dark plasma discharges cannot be supported, thereby giving rise to electrolysis, i.e. the breakdown of water due to electrochemical mechanisms. In this region, the curve approximates Ohm's law, as seen by the linear increase in current with applied voltage (Hickling and Linacre, 1954). As the applied voltage is increased, the minimum potential required to transform the liquid into a plasma, defined as the breakdown voltage, may be reached. As the breakdown voltage is approached, electrolysis will continue or the transition to a glow discharge can proceed, depending on the internal resistance of the dc power supply (Roth, 1995). If the resistance is too high, the power supply cannot produce the current required to vaporize the surrounding fluid and electrolysis continues. However, if the internal resistance of the power supply is low enough to produce the required current to vaporize the surrounding liquid, the transition to a glow discharge occurs.

The breakdown voltage for which conventional electrolysis ceases to exist corresponds to the formation of a sheath of solvent vapor at the electrode surface due to ohmic heating. The sheath, which has a lower density than the surrounding fluid, separates the electrode from the liquid and creates conditions that allow current to flow as a glow discharge (Kellogg, 1950; Tezuka and Iwasaki, 2001). As in low-pressure dc discharges, a discontinuous region precedes the glow region where both the current and voltage fluctuate. In the glow region, shown in Figure 2.2, the current and current density are relatively independent of the applied voltage (Hickling and Ingram, 1964). During the onset of a glow discharge, the plasma is concentrated around a small portion of the electrode surface

Reproduced with permission of the copyright owner. Further reproduction prohibited without permission.

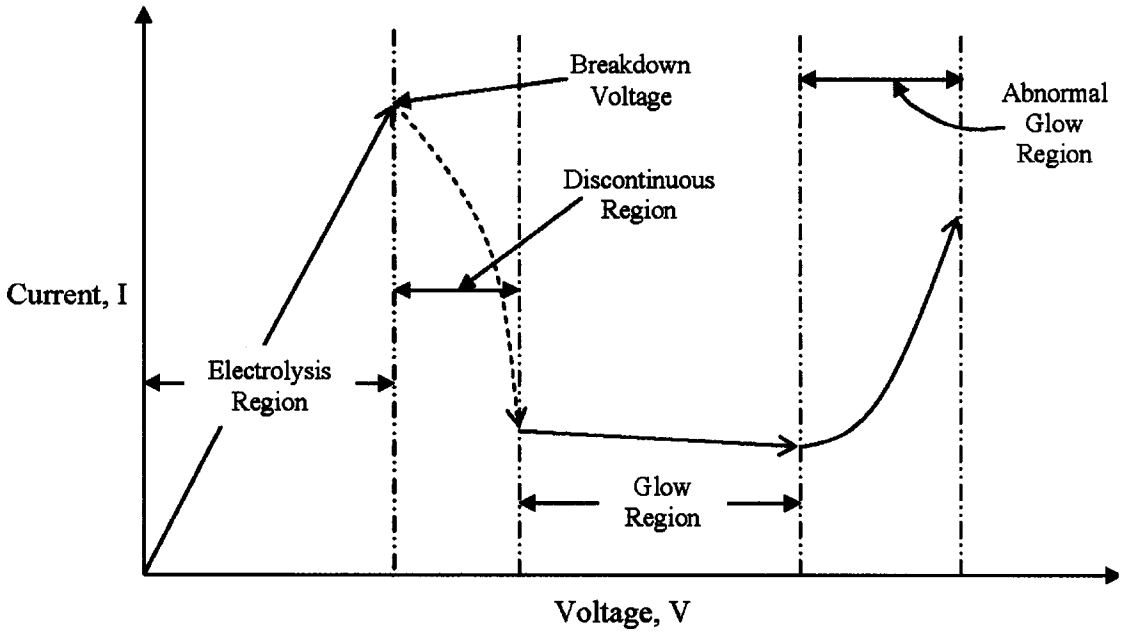

Figure 2.2: Current-voltage relationship for electrolysis and glow plasma regions in an aqueous solution powered by a dc potential (Hickling and Ingram, 1964).

Reproduced with permission of the copyright owner. Further reproduction prohibited without permission.

and is confined to this area until an increase in voltage results in an increase in current (Hickling and Ingram, 1964). This behavior indicates a transition to the abnormal glow region, also shown in Figure 2.2. The abnormal glow region is characterized by a response of the plasma volume to changes in the applied potential. As the voltage is increased, the plasma continues to occupy more of the electrode surface until the entire surface area is encompassed by the plasma. Although there is an increase in current in this region with an increase in voltage, the current density within the plasma remains relatively constant because of the increase in the plasma volume (Hickling and Ingram, 1964). The conditions created in the abnormal glow region, such as a large plasma volume, are such that chemistry initiated by the plasma and electrolysis mechanisms can be utilized to oxidize organic contaminants.

The degradation of organic compounds solvated in water utilizing contact glow discharge electrolysis has been previously explored (Mazzocchin et al., 1973; Harada and Terasawa, 1980; Harada et al., 1980; Kokufuta et al., 1980; Kokufuta et al., 1985; Tezuka and Iwasaki, 1997; Tezuka and Iwasaki, 1998; Gao et al., 2001; Tezuka and Iwasaki, 2001). This process is termed contact glow discharge electrolysis (CGDE) because the glow discharge is initiated in the liquid solution resulting in both plasma and electrolysis reaction pathways. Previous glow discharge oxidation experiments were conducted by initiating a glow discharge in the gas phase above the liquid solution requiring the reactive species to diffuse through the gas-liquid interface. A schematic of a typical experimental reactor employing CGDE to degrade organic compounds is shown in Figure 2.3. Contact glow discharge electrolysis generates a unique reaction zone in which highly

Reproduced with permission of the copyright owner. Further reproduction prohibited without permission.

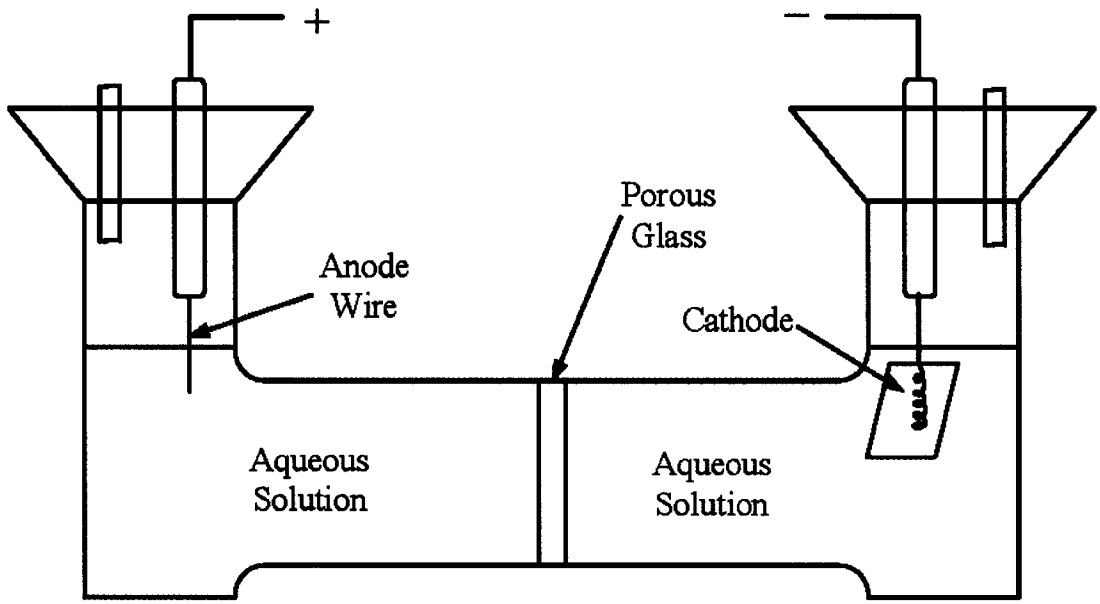

Figure 2.3: A schematic of a typical experimental apparatus used to perform contact glow discharge electrolysis (Hickling and Ingram, 1964; Gao et al., 2001).

Reproduced with permission of the copyright owner. Further reproduction prohibited without permission.

reactive species are created and sustained by a dc glow discharge between an electrode and the surface of an electrolytic solution (Gao et al., 2001; Tezuka and Iwasaki, 2002). The glow discharge and the liquid phase adjacent to the plasma-analyte interface are the primary reaction zones in CGDE reactors (Gao et al., 2001).

In the plasma sheath surrounding the anode, water vapor is ionized or promoted to a higher energy state due to collisions with electrons of various energies. Depending on the electron temperature and the collision cross section of the atom, molecule, or ion, the following reactions can occur (Joshi et al., 1995):

$$e^- + H_2O \rightarrow \cdot H + \cdot OH + e^- \quad (2.1)$$

$$e^- + H_2O \rightarrow H_2O^+ + 2e^- \quad (2.2)$$

$$e^- + H_2O \rightarrow H_2O^* + e^- \quad (2.3)$$

$$2H_2O^* \rightarrow H_2O_2 + H_2 \quad (2.4)$$

$$e^- + H_2O_2 \rightarrow \cdot OH + OH^- \quad (2.5)$$

$$e^- + H_2O_2 \rightarrow 2(\cdot OH) + e^- \quad (2.6)$$

$$H_2O_2 + h\nu \rightarrow 2(\cdot OH) \quad (2.7)$$

Hydroxyl radical (·OH) and hydrogen peroxide (H_2O_2), both powerful oxidants, then diffuse into the solution and can initiate oxidation reactions through hydrogen abstraction. Due to the potential gradient, the ions in the plasma sheath are accelerated into the interface between the plasma and the electrolytic solution with enough kinetic energy to initiate chemical reactions similar to those enumerated above (Tezuka and Iwasaki, 2002). Although CGDE produces powerful oxidizing species, the process is limited by the diffu-

Reproduced with permission of the copyright owner. Further reproduction prohibited without permission.

sion of the species into the bulk solution. A more efficient way to transfer the electrical energy into the solution is to generate an arc discharge.

2.2 Arc Discharge

An arc discharge is distinguished from a glow discharge by its luminosity, current density and cathode fall voltage (Roth, 1995). For example, arcs are extremely luminescent, whereas glow discharges, while producing visible light, are not as intense. Distinguishing between a thermal and non-thermal arc, however, is considerably more difficult. The fluid pressure, electron temperature, arc current, electric field/pressure (*E/p)* ratio, power dissipated per unit length of the arc and luminous intensity all affect arc properties, but none can be used to quantitatively distinguish between thermal and non-thermal behavior (Roth, 1995). With only a few exceptions, however, the electron density of thermal arcs are higher than non-thermal arcs. Unfortunately, the electron density cannot be measured as an absolute. Therefore, only the equilibrium state of the electrons with the surrounding atoms, molecules and ions can be used to determine the thermal state of the plasma. Non-thermal arcs are not in local thermal equilibrium, resulting in electron temperatures that are higher than the surrounding gas atoms, molecules and ions. In contrast, the electrons produced in thermal arcs are in local thermal equilibrium with the surrounding gas atoms, molecules and ions. Typical plasma parameters and their corresponding values for non-thermal and thermal gas discharges are tabulated in Table 2.1. Although the values presented in Table 2.1 are only applicable to gas discharges, it demonstrates the difficulty in ascertaining the thermal state of an arc discharge.

Reproduced with permission of the copyright owner. Further reproduction prohibited without permission.

Table 2.1: Plasma parameters and the corresponding values for both thermal and non-thermal arc discharges in a gas (Roth, 1995; Roth, 2001).

Plasma Parameter	Non-thermal Arc	Thermal Arc
Equilibrium State	Kinetic	Local Thermal Equilibrium
Electron Density, n_e (#/m^3)	$10^{20} < n_e < 10^{21}$	$10^{22} < n_e < 10^{25}$
Electron Temp., T_e (eV)	$0.2 < T_e < 2.0$	$1.0 < T_e < 10$
Arc Current, I (A)	$1 < I < 50$	$50 < I < 10^4$
$I E$ (kW/cm)	$I E < 1.0$	$I E > 1.0$
Typical Cathode Emission	Thermionic	Field
Luminous Intensity	Bright	Dazzling

Reproduced with permission of the copyright owner. Further reproduction prohibited without permission.

Arc discharges are utilized in industry to increase surface reaction rates, melt, sinter, or evaporate materials, and weld or cut refractory materials (Lieberman and Lichtenberg, 1994). Until the beginning of the twentieth century, however, most arc discharges were non-thermal and used as a source of light (Roth, 2001). Classical nomenclature was derived from the early industrial uses of arc discharges and lends itself readily to the discussion of arc discharges initiated in a liquid medium. A schematic, derived from this nomenclature, is shown in Figure 2.4. The regions of the arc discharge, which are important in aqueous arc discharges, are enumerated below (Roth, 1995):

1.) The *cathode* is the negatively biased electrode.

2.) The *cathode spots* are point(s) in which the plasma is in contact with the cathode. These points experience elevated temperatures, more so than the bulk of the cathode, in which material can be lost due to vaporization.

3.) The *positive column* encompasses most of the plasma volume. Only a small percent of the voltage drop occurs in this region.

4.) The *plasma core* is the bulk of the plasma where most, if not all, of the gas is dissociated. For thermal arcs, the plasma core is in local thermal equilibrium and will exhibit black body radiation.

5.) The *aureole* is a region of hot gas, not in thermal equilibrium, where plasma chemistry can take place. This is the region in which radicals and other highly reactive species are formed.

Application of an aqueous plasma discharge to degrade organic pollutants in wastewater is a relatively new process. It is characterized by the production of high oxidation

Reproduced with permission of the copyright owner. Further reproduction prohibited without permission.

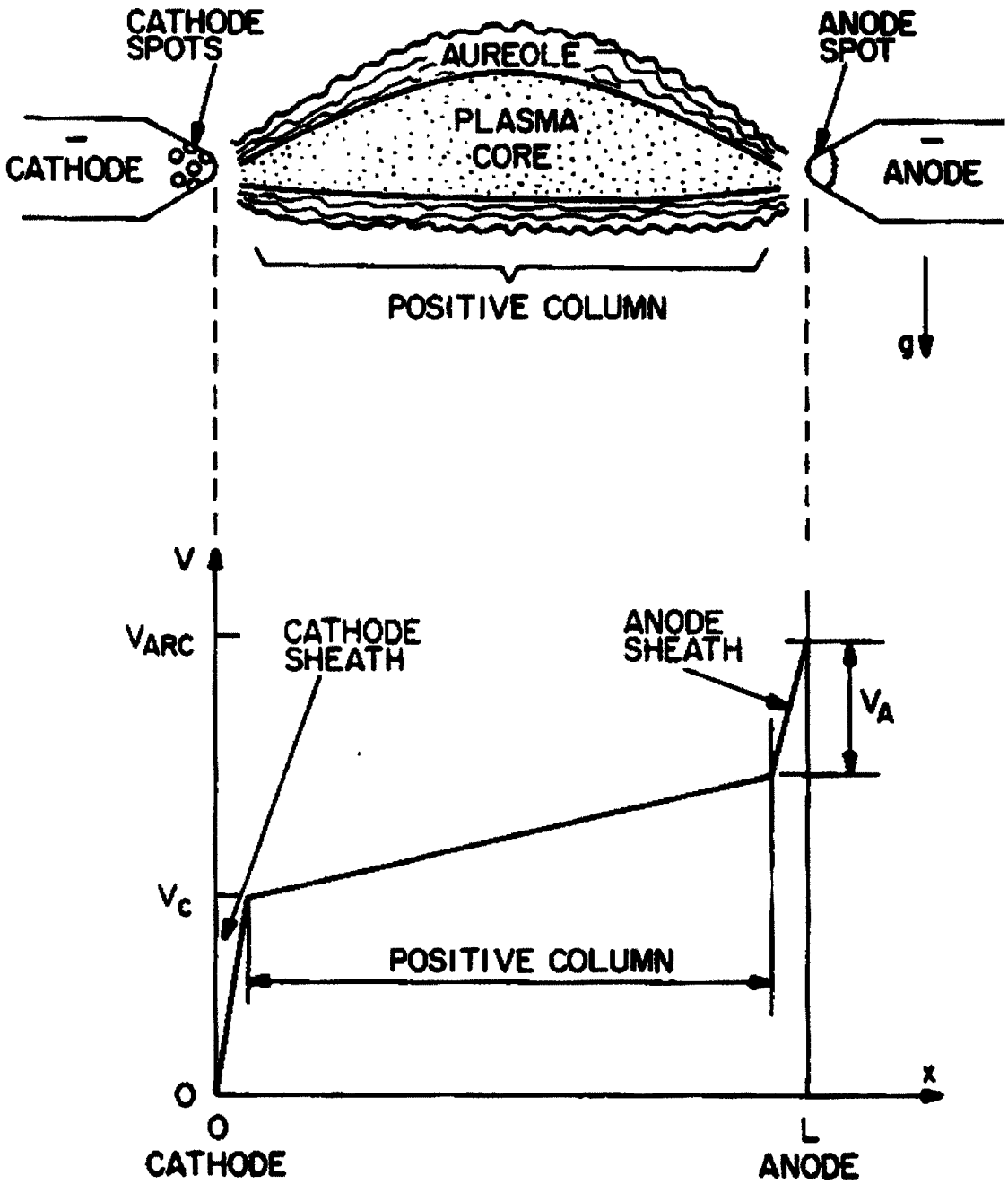

Figure 2.4: An illustration of an arc discharge based on classic nomenclature and the corresponding voltage distribution along the discharge axis (Roth, 1995).

Reproduced with permission of the copyright owner. Further reproduction prohibited without permission.

potential species in the aureole such as ·OH, H_2O_2 and ·O (Sun et al., 1997; Willberg et al.,1996a). Both non-thermal and thermal arc discharges are oxidation technologies in which energy is electrically introduced into an aqueous solution through a plasma channel. Under specific conditions, a plasma discharge can be created where many different reactive oxidizing species–·OH, ·H, ·O, O_2, ·HO_2, O_2^-, H_2O_2, O_3, and others–can exist (Sun et al., 1999). These oxidizing species react with contaminant molecules. In the event that complete oxidation cannot be achieved, the goal is to chemically transform the original pollutants into less hazardous hydrocarbons that are straightforward to remediate with a secondary treatment or dispose of completely. While both non-thermal and thermal arc discharges can be utilized to produce oxidizing species, the difference in the thermal equilibrium state of the plasmas leads to distinct differences in the removal mechanism and kinetics associated with the discharge.

2.2.1 Non-thermal Discharges

Non-thermal arcs have traditionally been utilized in gas treatment processes such as ozone removal, dust precipitation and the conversion of undesirable gaseous species such as nitrogen oxides (NO_x), sulfur oxides (SO_x) and some hydrocarbons (Cooper and Alley, 1994). Non-thermal arc discharges are more energetic than glow discharges and the electrons possess sufficient kinetic energy to break bonds in the plasma core as well as initiate oxidation by forming highly reactive species in the aureole. However, relatively little research has been done to determine the potential for this oxidation technology to completely degrade organic or biological molecules in an efficient and inexpensive way. Because of this, stable intermediates in the case of incomplete oxidation, and the reaction mechanism of organic degradation due to a non-thermal discharge are not well known.

Reproduced with permission of the copyright owner. Further reproduction prohibited without permission.

However, research on the breakdown of non-conducting fluids in a strong electric field and the physical characteristics of the arc tubules that make up both non-thermal and thermal discharges have been researched and can lead to insights on the chemical reaction mechanism and kinetics.

2.2.1.1 Breakdown Theory

The electrical breakdown of an insulating liquid is the sudden transition of that liquid to a conductor while under the influence of a strong electric field (Devins et al., 1977). Mechanisms for the electric breakdown of polarizable, non-conducting, i.e. dielectric, liquids between two electrodes have been previously investigated (Clements et al., 1987; Béroual, 1993; Gavrilov et al., 1994; Jones and Kunhardt, 1994; Jones and Kunhardt, 1995; Béroual et al., 1998; Lisitsyn et al., 1999; Akiyama et al., 2000). Two main theories, electronic and thermal, have been utilized to explain the ionization of non-conducting liquids, resulting in a conducting path between the electrodes. The electronic theory is analogous to the Townsend theory of gas breakdown in which electrons gain sufficient energy from the electric field and are accelerated into adjacent molecules initiating electron multiplication through collisional ionization (Clements et al., 1987). In the high electric field region, which is initially at the surface of the electrode to which the potential is applied, water is dissociated. The ions form a conducting region allowing the electric field to traverse the electrode gap along a path to the other electrode (Clements et al., 1987). The process is repeated until the energy is exhausted or until the electrode gap is propagated. This process is sometimes referred to as avalanche-streamers or ionization waves.

Reproduced with permission of the copyright owner. Further reproduction prohibited without permission.

With respect to the thermal, or bubble, breakdown theory, a "hole" conduction mechanism (Yanshin et al., 1974) involving hydronium ions (H_3O^+) results in the formation of bubbles in the fluid adjacent to the electrode surface due to local heating. After the creation of a vapor bubble, the potential drop across the electrodes is also applied to the bubbles, initiating the breakdown of the gas. The result is the formation of a highly conductive, spherical plasmoid. The plasmoid is separated from the surrounding water by a thin film of water vapor (Sunka et al., 1999). As the gas is ionized within each bubble, additional liquid between the electrodes is heated, promoting bubble growth and further ionization until the energy is exhausted or the gap is completely traversed (Yanshin et al., 1974; Sharbaugh et al., 1978). The potential advantage of such a discharge is that it can be generated using relatively slow rising voltage pulses, even in highly conductive aqueous solutions, and that the plasma is not necessarily in direct contact with the electrodes (Sunka et al., 1999). The separation of the plasma from the electrodes would reduce the electrode temperature and thus result in a reduction in the sputtering rate, and thus a longer electrode life. However, detailed studies of the discharge, in particular those focused on AOT, are lacking (Sunka et al., 1999).

While experimental data support both breakdown mechanisms, it is clear that the electrical breakdown of dielectric liquids is a complex process in which neither theory can fully explain all of the experimental results. Thus, it is believed that the true mechanism is a combination of both the electronic and thermal theories in which one may dominate depending on the breakdown conditions. It has been observed experimentally that if the voltage pulse duration is short and the electric field strength is high, the avalanche-

Reproduced with permission of the copyright owner. Further reproduction prohibited without permission.

streamer breakdown mechanism dictates the fluid ionization process. However, the bubble mechanism dominates for processes employing a longer pulse duration, such as in continuous discharges, and require a lower applied potential.

2.2.1.2 Plasma Characteristics

The length and propagation velocity of arc tubules produced by an electrical discharge in water is dependent on (1) the electrode geometry, (2) the properties of the applied voltage (polarity, magnitude and pulse width) and (3) the water conductivity and impurities (Clements et al., 1987). With respect to the electrode geometry, a plasma discharge emanating from a surface with a low radius of curvature requires the lowest voltage drop. This is due to the fact that the electric field strength is a function of the radius of curvature and is maximized when the radius is minimized. For this reason, most aqueous phase plasma discharge reactors employ a point-to-plane electrode configuration. Aqueous plasma discharges can also be manipulated by adjusting the properties of the applied voltage.

The bias of the applied voltage, positive or negative, affects the properties of the plasma arcs initiated in an aqueous solution. For a given voltage drop and pulse width, positive polarity arc tubules, i.e. arc discharges that originate from the positively charged electrode, can be sustained over a larger electrode gap when compared to arcs that originate from the negatively biased electrode (Joshi et al., 1995). Tubules with a negative polarity, however, form many short side branches that are not observed on positive arcs (Clements et al., 1987). This fact can be used to explain the difference in propagation length for the two polarities. While arcs with a positive bias utilize the energy inputted

Reproduced with permission of the copyright owner. Further reproduction prohibited without permission.

into the system predominately to propagate the electrode gap, a negatively biased arc expends a significant amount of energy to form side branches which terminate into the fluid instead of increasing its propagation length. This results in the longer positive arc tubule length when compared to the negatively biased plasma. While the polarity has been shown to affect the geometry of the arc tubules, it has not been determined, however, if the discharge polarity results in a measurable difference in the plasma volume. The magnitude of the applied potential and pulse width also affect the length of both positive and negative arc discharges.

The propagation length of an arc discharge increases with an increase in voltage and pulse width. An increase in the propagation length for a negative polarity arc has been shown to be a function of the square root of the applied potential (Clements et al., 1987). This would indicate that the propagation of a negative tubule asymptotes at a predefined critical distance, which is a function of the discharge conditions. With respect to a positive streamer, its velocity is constant while propagating across the electrode gap and is also a function of the applied voltage. This suggests that the electric field strength is constant at the arc tubules propagating tip (Devins et al., 1977). Negative arcs, on the other hand, are considerably slower when compared to positive arcs (Clements et al., 1987). This could be attributed to the fact that negatively biased arc tubules possess numerous propagating tips due to the additional branches that are formed as the tubule traverses the electrode gap. As additional branches are formed, each tip requires energy to promote the adjacent fluid to the plasma state. Thus, a significant amount of the energy inputted into the plasma is utilized to form the branching network, resulting in a reduction of the

Reproduced with permission of the copyright owner. Further reproduction prohibited without permission.

overall propagation velocity. While the electrode geometry, applied potential and pulse width dictate the plasma characteristics, the conductivity of the liquid in which the discharge is initiated affects the electrical requirements necessary to initiate and sustain the plasma.

2.2.1.3 Solution Conductivity

In liquids, conductivity is a measure of the solution's ability to conduct an electrical current due to the presence of ions. When a potential is applied across two electrodes submersed in an aqueous solution, the positive and negative ions will move toward oppositely charged electrodes resulting in current flow. The amount of current an electrolytic solution can conduct is a function of the ionization fraction and is thus dependent on the kind of solute, solute concentration and ion mobility. For example, strong acids solvated in water will, in most cases, completely dissociate and support current flow, while compounds that do not ionize, such as covalent organic molecules, will not conduct a current. The most common unit for measuring conductivity in apparatuses utilizing an aqueous plasma discharge is μS/cm.

Non-thermal discharges, both negatively and positively biased, begin to shorten and are less intense as the water conductivity decreases (Clements et al., 1987). Thus, as the free ion concentration approaches zero, the distance for which a stable thermal discharge can be maintained is reduced (Sunka et al., 1999). This is due to the fact that local heating of the fluid adjacent to the electrodes is reduced as the number of species with the ability to carry a charge decreases; therefore making it difficult to initiate the electrical breakdown of the solution by either of the above mention mechanisms. However, if the solution con-

Reproduced with permission of the copyright owner. Further reproduction prohibited without permission.

ductivity is too high, a discharge becomes difficult to initiate due to the fact that the solution inductance is such that significant currents are produced without transforming the fluid into a plasma (Clements et al., 1987). Thus, the electric field strength required to initiate the discharge is difficult not only to produce, but maintain as well. As in solutions with lower conductivities, thermal arcs become more difficult to sustain under highly conductive conditions. This would suggest that an optimal solution conductivity, or range of conductivities, exists which facilitate the formation of both non-thermal and thermal arcs. Sunka et al. (1999) observed a continued shortening of the arc propagation length as the solution conductivity increased above 200 μS/cm. Clements et al. (1987) also demonstrated a reduction in streamer formation and thus lower concentrations of oxidizing species when salt concentrations resulted in conductivities greater than 200 μS/cm. When using a pulse power supply, the production of oxidizing species has been shown to be more efficient when solution conductivities are in the range of 10-100 μS/cm (Sunka et al., 1999). However, solution conductivities on the order of 1 μS/cm results in unfavorable discharge conditions that continue to deteriorate as the conductivity decreases. Thus, conductivities in the range of 1-200 μS/cm are preferred when utilizing plasma to degrade aqueous contaminants.

As previously mentioned, the solution composition affects conductivity and thus the residence time required to treat a given amount of solution. If the solution contains radical scavengers such as carbonate or phosphate ions, not only is the conductivity effected, but the oxidizing radical concentration is also reduced; further diminishing the processes effectiveness. A large concentration of free radical scavengers has been shown to decrease

Reproduced with permission of the copyright owner. Further reproduction prohibited without permission.

the oxidation rate of organic compounds (Goheen et al., 1992). There is also evidence that some cations may have the ability to scavenge oxidizing anions as well. For example, Goheen et al. (1992) demonstrated that the sodium cation (Na^+) has the ability to scavenge superoxide anions (HO_2^-). The complexities associated with the solution conductivity, and the ion composition that makes the aqueous solution electrolytic, not only affects the plasma discharge, but the mechanism for which aqueous organics are attenuated as well.

2.2.1.4 Reaction Mechanism

An arc discharge in water, whether thermal or non-thermal, results in the formation of many potent oxidizing species capable of completely attenuating an organic pollutant. The reaction mechanism for the formation of reactive species by the plasma involves excitation, ionization and dissociation of water molecules; similar to what has been observed experimentally for radiolytic processes such as γ-radiation, electron beam radiation, pulsed radiolysis and photochemical processes (Spinks and Woods, 1990; Chatterjee, 1987; Hughes, 1973; Bednar, 1969; Swallow, 1960). These processes, which produce radical and molecular species through interactions with high-energy electrons, are initiated through the following reactions (Spinks and Woods, 1990; Hughes, 1973; Bednar, 1969; Joshi et al., 1995).

$$e_{aq}^- + H_2O \rightarrow \cdot H + \cdot OH + e_{aq}^- \quad (2.8)$$

$$E_{plasma} + 2H_2O \rightarrow H_2O_2 + H_2 \quad (2.9)$$

$$e_{aq}^- + H_2O \rightarrow H_2O^+ + 2e_{aq}^- \quad (2.10)$$

Reproduced with permission of the copyright owner. Further reproduction prohibited without permission.

The species produced by the discharge are at a higher energy state and undergo propagation reactions through collisions with other species, such as molecule oxygen, present in solution. The propagation reactions, some of which are listed below, perpetuate the formation of additional reactive species that can initiate the oxidation of organic species solvated in water.

$$\cdot H + O_2 \rightarrow HO_2\cdot \quad (2.11)$$

$$\cdot H + H_2O_2 \rightarrow H_2O + \cdot OH \quad (2.12)$$

$$\cdot OH + H_2O_2 \rightarrow H_2O + HO_2\cdot \quad (2.13)$$

$$H_2O^+ + H_2O \rightarrow \cdot OH + H_3O^+ \quad (2.14)$$

$$e_{aq}^- + \cdot OH \rightarrow OH^- \quad (2.15)$$

$$e_{aq}^- + \cdot H + H_2O \rightarrow OH^- + H_2 \quad (2.16)$$

$$e_{aq}^- + H_2O_2 \rightarrow \cdot OH + OH^- \quad (2.17)$$

$$e_{aq}^- + H_2O \rightarrow \cdot H + OH^- \quad (2.18)$$

While the species formed by the plasma discharge and through propagation reactions are effective in initiating oxidation reactions, they can also react with each other, Eqs. (2.19–2.26), thereby terminating the process. Thus, energy must be continuously inputted into the system to initiate the formation of the oxidizing species.

$$\cdot H + \cdot OH \rightarrow H_2O \quad (2.19)$$

$$2(\cdot OH) \rightarrow H_2O_2 \quad (2.20)$$

$$2(HO_2\cdot) \rightarrow H_2O_2 + O_2 \quad (2.21)$$

$$\cdot H + HO_2\cdot \rightarrow H_2O_2 \quad (2.22)$$

$$2(\cdot H) \rightarrow H_2 \quad (2.23)$$

Reproduced with permission of the copyright owner. Further reproduction prohibited without permission.

$$HO_2\cdot + \cdot OH \rightarrow H_2O + O_2 \quad (2.24)$$

$$H_3O^+ + \cdot OH \rightarrow 2H_2O \quad (2.25)$$

$$H_2O^+ + e^-_{aq} \rightarrow H_2O \quad (2.26)$$

Since the formation of reactive species is proportional to the amount of energy inputted into the system, increasing its magnitude, or utilizing the energy more efficiently, should result in an increase in the oxidizing species density as well as their spatial distribution (Joshi et al., 1995). An increase in the process efficiency will therefore result in an enhanced reaction rate.

2.2.1.5 Reaction Rate

The reaction rate, which correlates the residence time necessary to treat a given amount of pollutant, is dependent on many factors and proceeds by a complex set of chemical reactions. It has been observed that the reaction rate is a function of the applied potential, current, stirring rate, salinity, electrode spacing, solution composition, pH and gas bubbled into the system (Goheen et al., 1992). The dependence of the reaction rate is related to the electric field strength through relationships linking the applied potential to the electric field for specific electrode geometries (Sharma et al., 1993). Thus, the rate of pollutant degradation in a reactor configuration employing a point-to-plane electrode configuration is also a function of the applied electric field. This would indicate that reducing the radius of curvature reduces the breakdown voltage; thereby making the process more efficient. The reaction rate has also been shown to be directly proportional to the current and thus the number of electrons produced by the discharge, which in turn initiates the production of oxidizing radicals and molecular species (Goheen et al., 1992). Thus, the production of the species is dependent on the energy input and the efficiency for which

Reproduced with permission of the copyright owner. Further reproduction prohibited without permission.

the energy is utilized. Since the hydroxyl radical is the most powerful, nonselective oxidant produced by an aqueous plasma discharge (Sun et al., 2000), the highest reactor efficiency is achieved if the formation of hydroxyl radicals is maximized. This can be accomplished by creating production conditions that favor the formation of hydroxyl radicals directly, or by the decomposition of molecular species, and reducing mass transfer limitations thereby promoting interactions with contaminant species.

In general, reaction rates have been shown to be highly dependent on stirring rates. Goheen et al. (1992) observed that as the stirring rate increases, the residence time required to attenuate the original pollutant concentration below a set value decreases. The additional agitation from the mixing process increases the mass transfer rate of contaminate species from the bulk to the plasma channel. The transport rate of reactive species to the bulk solution is also enhanced, resulting in an appreciable quantity of oxidizing species such as hydroxyl radical to be transported into the bulk solution, which subsequently initiate oxidation reactions. However, the effects of an accelerated stirring rate on a thermal discharge have not been thoroughly investigated. Extremely high stirring rates could cause the plasma bubbles, which will be discussed in the subsequent section, to collapse, nullifying the effects of transient supercritical water conditions and thus reducing the oxidation potential. On the other hand, large spin rates could accelerate the transport of the plasma bubbles into the bulk solution, resulting in a more efficient process. When trying to enhance energy efficiency in both a thermal or non-thermal plasma treatment process, the solution pH should also be considered.

Reproduced with permission of the copyright owner. Further reproduction prohibited without permission.

The solution pH has the most significant effect on the oxidation rate when ozone is utilized in the treatment process. If molecular oxygen is introduced into the path of the plasma, significant quantities of ozone will be produced. If the solution pH is acidic, ozone does not readily decompose and will oxidize organic compounds directly. However, when the pH is neutral or basic, ozone will tend to decompose into many transient oxidizing species, most importantly hydroxyl radical. This is significant because the hydroxyl radical is a more efficient, less selective oxidizing agent. While non-thermal arcs have been successfully incorporated into AOT, they lack some of the physical features associated with thermal arcs that promote oxidation; making them less efficient when used to oxidize organic molecules.

2.2.2 *Thermal Discharges*

A thermal discharge occurs when a non-thermal arc completely propagates the length of the gap, contacting both electrodes. The result is the transformation of the non-thermal plasma into a conductive, high-current arc. When a thermal arc discharge is initiated in an aqueous solution, five individual effects simultaneously occur that contribute to organic oxidation: (1) a strong electric field; (2) production of various free radicals; (3) an over-pressure shock wave; (4) intense ultraviolet radiation; and (5) ozone production if oxygen is present (Sun et al., 1998; Chang et al, 1998). These effects are categorized as either localized or extended and are labeled based on the region over which the effect takes place (Willberg et al., 1996b). Local effects are defined as those that occur in the immediate vicinity of the plasma and are attributed to the strong electric field and formation of oxidizing species.

Reproduced with permission of the copyright owner. Further reproduction prohibited without permission.

The electric field strength dictates the extent to which the fluid in the plasma core ionizes due to electron-impact dissociation reactions. As the field strength is increased, the resistance associated with the fluid between the electrodes decreases as a result of an increase in the fractional ionization. Thus, as the resistance decreases, the magnitude of current conducted through the medium increases for a given applied dc voltage. This is advantageous due to the fact that the electron density, and corresponding electron temperature, increase with increasing current. The current magnitude produced by a thermal discharge is such that electrons generated in the plasma core have characteristic temperatures above ten thousand Kelvin, resulting in the emission of a wide radiation spectrum (Sun et al., 1998; Robinson et al., 1973a). The electron temperatures are high enough to cause the thermal decomposition of virtually any organic compound promoted to the plasma state. Electrons from the plasma core can also be accelerated out of the region by the electric field causing the dissociation of the surrounding water molecules. The dissociation of the water molecules, in conjunction with the radiation from the discharge, creates highly reactive species in a gaseous state surrounding the plasma core, resulting in conditions similar to those observed in supercritical water oxidation experiments (Chang et al., 1998; Sun et al., 2000). These processes, occurring in both the plasma core and aureole, complement one another to degrade a variety of organic contaminants and are also effective for sterilization (Gurol and Vatistas, 1987).

The extended effects of a thermal arc discharge are defined as those that occur outside the plasma channel, and are principally due to the shock wave and UV radiation that propagate into the bulk solution (Sun et al., 2000). The shock wave is intense, with character-

Reproduced with permission of the copyright owner. Further reproduction prohibited without permission.

istic pressures of several thousands to tens of thousands of atmospheres, and is caused by the expanding plasma region (Sun et al, 1998). The strong shock wave generated by the discharge has been used in various industrial applications for approximately thirty years (Wesley and Ayres, 1984), therefore stimulating numerous scientists to study the properties and characteristics of the waves (Skvortsov et al., 1961; Robinson et al., 1973a; Robinson et al., 1973b; Chang et al., 1998). The shock wave has been shown to produce cavitational effects similar to those created in sonochemical experiments and is the catalyst for sonolytic initiated oxidation of organic compounds (Hua et al., 1995). The oxidation, which proceeds almost exclusively by hydroxyl radical attack, has been shown to occur in the cavitation zone, where a high radical density is observed (Chang et al., 1998). With respect to the radiation emitted from the discharge, wavelengths less than 185 nm are absorbed by the fluid adjacent to the plasma channel, leading to the expansion of the plasma core (Sun et al., 2000). The remaining spectrum, energy with wavelengths longer than 185 nm, radiates through the bulk solution and can lead to the formation of hydroxyl radicals through the dissociation of water molecules. Oxidation initiated by extended effects therefore proceeds predominately by hydroxyl radical attack, unless ozone in also generated by the discharge due to the presence of molecule oxygen.

When compared to non-thermal discharges, the additional oxidation effects created by a thermal plasma results in conditions that are more effective in degrading organic molecules. Localized effects are enhanced as a result of a larger plasma core (Clements et al., 1987). Thermal discharges also produce oxidizing radicals in the bulk solution, in addition to the aureole, due to the intense radiation produced by the discharge (Sunka et al,

Reproduced with permission of the copyright owner. Further reproduction prohibited without permission.

1999). Oxidizing species are therefore produced in greater number and the spatial distribution of these species is wider (Sun et al., 1998). With respect to a non-thermal arc discharge, the UV radiation is weaker and the shock wave is almost nonexistent. It has been shown experimentally that radiation emitted from a thermal discharge has a more active role in initiating oxidation than in non-thermal discharges (Sun et al., 2000). The result is an insignificant production rate of hydroxyl radicals outside the immediate vicinity of the non-thermal plasma channel. Due to the weak shock wave and relatively low radiation intensity, the extended effects of a non-thermal discharge are negligible relative to the effects produced by a thermal discharge. Another advantage of thermal discharges is that, for the same applied voltage, more current can be passed through the liquid medium. This is advantageous because the attenuation rate of organic molecules solvated in water increases with an increase in current. Not surprisingly, Sun et al. (2000) clearly showed that the additional oxidation pathways associated with a thermal discharge increased the overall efficiency of the process.

In addition to the thermal equilibrium state of the plasma, it has also been shown that the removal efficiency of organic compounds in an aqueous solution can be greatly influenced by specific additives that utilize the energy released by the discharge (Sun et al., 2000). This suggests that the overall energy efficiency of a reactor employing an arc discharge can be improved. While both non-thermal and thermal arcs can both achieve complete attenuation of the original contaminant molecule, thermal discharges tend to require less energy and time to complete the process. The dense medium plasma reactor incorporated a novel reactor design which utilizes thermal plasma discharges to degrade

Reproduced with permission of the copyright owner. Further reproduction prohibited without permission.

organic compounds and also has the ability to incorporate additional advance oxidation technologies to improve the overall removal efficiency.

2.3 Dense Medium Plasma Reactor (DMPR)

The dense medium plasma reactor (DMPR), shown in Figure 2.5, was developed by Denes and coworkers (Denes and Young, 1996; Denes et al., 2002) to react liquid/vapor phase chemicals in an induced plasma state using low temperature plasma chemistry. The DMPR produces sustained discharges in a vapor/liquid medium which may by significantly more efficient in the processing of liquid phase material then current technologies (Denes and Young, 1996; Denes et al., 2002). The reactor is composed of a cylindrical glass chamber (7) with two stainless steel upper and bottom caps (9, 17) and a cooling jacket (4). The rotating upper electrode (19) is equipped with a quartz jacket to avoid the penetration of the reaction media to the electrode-sustaining central shaft and bearings. The upper electrode is a rotating shaft which terminates into an interchangeable ceramic pin array (8) and holder (23). The stationary hollow electrode is equipped with an interchangeable conical cross section end-piece with channels (25) for solution recirculation and gas flow. Both the spirally located pin array and the interchangeable metallic disk of the lower electrode can be made of different metals as required by the specific plasma treatment. In this case, for the decontamination of water both the spirally located pin array and the interchangeable metallic part of the lower electrode are made of titanium. The distance between the pin array and the lower electrode can be varied by a micrometric (thimble) screw system. The reactor is vacuum tight (copper gasket sealing) and the rotation of the upper electrode is assured through a magnetic coupling system

Reproduced with permission of the copyright owner. Further reproduction prohibited without permission.

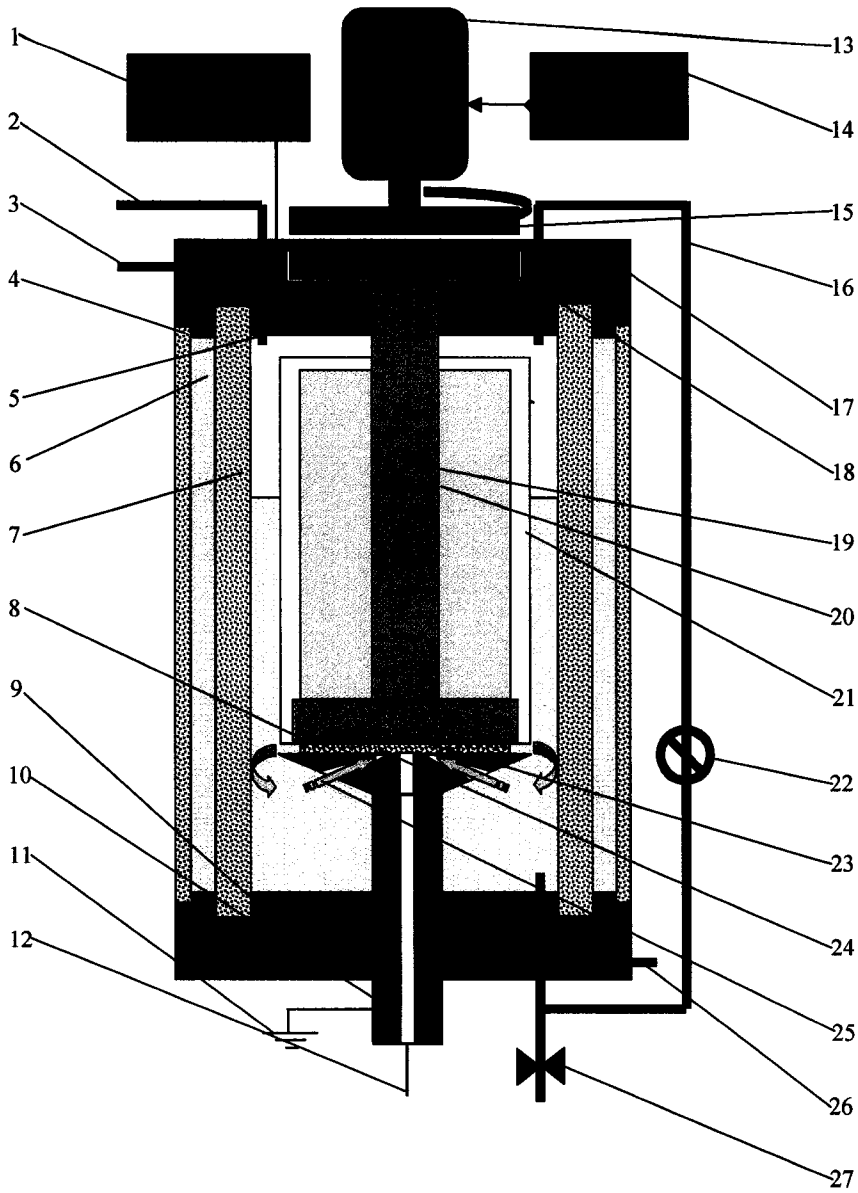

Figure 2.5: Schematic of the dense medium plasma reactor. *1* – dc power supply; *2* – gases evacuation; *3, 26* – coolant exit and inlet; *4, 7* – glass cylinders; *5* – electrical contact; *6* – coolant; *8* – ceramic pin-array; *9, 17* – caps; *10* – non-rotating electrode; *11* – ground; *12* – gas inlet; *13* – motor; *14* – digital controller; *15, 18* – magnetic coupling system; *16* – liquid inlet; *19* – rotating electrode; *20* – sealed volume; *21* – quartz isolator; *22* – recirculation pump; *23* – pins; *24* – electrical discharges; *25* – recirculated flux; *27* – valve (Denes and Young, 1996; Denes et al., 2002).

Reproduced with permission of the copyright owner. Further reproduction prohibited without permission.

(15, 18). This allows the processing of liquid and gas-phase toxic media.

The rotation of the upper pin array is digitally controlled with a spin rate range of 0-2500 rpm. Rotating the array serves several important purposes. The action spatially homogenizes the multiple micro-arcs and activates a larger effective volume of fluid. Spinning the pin array also simultaneously pumps fresh liquid and vapors into the discharge zone, thus thinning the boundary layer between the emission tips and the bulk fluid. The plasma can be initiated and sustained using adjustable and commercially available dc or ac power supplies. Although the actual mechanism for electron emission and energy transport through the liquid is not well characterized at this time, the rotation of the electrode, and the spirally arranged pin array system (which acts as a high current density field emission arc source), generates numerous micro discharges which produces a larger plasma volume than previous point-to-plane configurations. Reactive or inert gases can also be introduced into the reaction media during the plasma process through the stationary electrode. The simultaneous presence of a gas also contributes to the homogenization of the reaction system and enhances the micro-arc formation process as a result of the lower fluid density between the electrodes.

The DMPR is an attractive plasma processing tool for the efficient decontamination of water. The rapid spinning of the pin array and the resulting micro-arc system essentially converts the plasma processing, which has traditionally been controlled by the surface-analyte interface, to a volumetric process. The individual arc tubules, under spin, sweep out a cylindrical shell volume of plasma while simultaneously pumping fresh fluid into

Reproduced with permission of the copyright owner. Further reproduction prohibited without permission.

the wake of the filament reaction zone; thereby thinning the diffusive boundary layer and enhancing mobility of free radicals into the bulk solution. As a result, the oxidation processes initiated by the plasma discharge will be more efficient and the subsequent oxidation kinetics will take on volumetric character.

2.3.1 Microbial Disinfection

The DMPR has been investigated as a tool for the disinfection of microbial contaminated water. Experiments conducted by Manolache et al. (2001) focused on quantifying the inactivation of specific bacteria and the specific deactivation mechanisms produced by the DMPR responsible for the disinfection. Water was artificially contaminated with sixteen gram positive and gram negative bacterial species from the following generas: *Bacillus, Corynebacterium, Enterobacter, Klebsiella, Micrococcus, Proteus, Pseudomonas, Shigella,* and *Staphylococcus*. Each disinfection experiment treated approximately 200 mL of microbial contaminated water in the DMPR chamber. The results are tabulated in Table 2.2.

To reduce the voltage required to initiate a plasma discharge, oxygen or argon was bubbled through the plasma zone. With 20 s of Ar plasma treatment, 91% of the colony forming units (cfu) per mL of solution were either inactivated or destroyed. This increased to greater than 98% when the solution was treated for 60 s. The results were slightly better with an oxygen plasma treatment. After 20 s, 98.8% of the cfu/mL were disinfected, with only a slight increase of 0.13% and 0.53% for an additional 40 s and 100 s of treatment, respectively. The destruction of the cfu in the DMPR was impressive; however, the exact mechanism of the bactericidal effect in the reactor was not

Reproduced with permission of the copyright owner. Further reproduction prohibited without permission.

Table 2.2: Results for the disinfection experiments performed by Manolache et al. (2001) utilizing a DMPR.

Treatment Time (s)	Sample Time (day)	Argon Plasma		Oxygen Plasma	
		$Log_{10}C_m$ (cfu/mL)	Change (%)	$Log_{10}C_m$ (cfu/mL)	Change (%)
No Treatment	initial	4.75		4.89	
	1	4.82	17.62		
	3			5.05	44.5
	7	4.70	-11.0	4.72	-32.4
20	initial	3.70	-91.1	2.96	-98.8
	1	BDL	-99.9		
	3			BDL	-99.9
60	initial	2.98	-98.3	2.91	-98.85
	1	BDL	-99.9		
	3			BDL	-99.9
120	initial			2.70	-99.4
	3			BDL	-99.9

Reproduced with permission of the copyright owner. Further reproduction prohibited without permission.

determined. Thus, the specific aspects of the reactor and disinfection procedure responsible for the bacterial inactivation are unknown.

2.3.2 *Oxidation of Aqueous Aromatic Organics*

The DMPR has also been used to oxidize aqueous aromatic organic pollutants (Manolache et al., 2004). Distilled water was contaminated with benzene, toluene, ethylbenzene, *m*- and *p*-xylene, and *o*-xylene at concentrations ranging from 173-194, 150-219, 131-271, 482-860, and 197-377 pg/μL, respectively. Each decontamination experiment treated approximately 200 mL of contaminated water while oxygen was bubbled into the reactor chamber through the middle of the stationary electrode. Due to the relative volatility of the aromatics used in the experiments, sparge tests, for which data is presented in Table 2.3, were performed to determine the mass of organics sparged from the solution by interphase mass transfer versus the mass of organics oxidized by the plasma. The oxygen flow rates used in the experiments were sufficiently high to sparge most of the organics out of the solution. At longer treatment times, however, Manolache et al. (2004) demonstrated that the mass transfer rate of the organics from the liquid to the gas was minuscule, therefore allowing the oxidation effect of the plasma to be studied.

Five experiments were performed to quantify the effects of varying the oxygen flow rate and current on the removal of the organic species from solution. A tabulation of experiment conditions and results are contained in Table 2.4. Of the compounds tested, benzene was the most difficult aromatic to remove from the solution. The removal efficiency, however, only differed by a few percent for all six aromatic compounds. While the destruction of the aromatics by the plasma was shown to exist, the formation of stable

Reproduced with permission of the copyright owner. Further reproduction prohibited without permission.

Table 2.3: Loss of benzene, toluene, ethylbenzene, *m*- and *p*-xylene, and *o*-xylene due to interphase mass transfer in the DMPR as a function of time for five oxygen flow rates (Manolache et al., 2004).

Time (s)	O_2 Flow Rate (slm)	Concentration (ppm)				
		Benzene	Toluene	Ethyl-benzene	*m*- and *p*-Xylene	*o*-Xylene
0	0	194	220	271	860	377
5	0.255	173	150	131	483	197
60	0.255	23	14	11	50	24
115	0.255	23	18	18	75	34
0	0	194	220	271	860	377
21	0.356	31	22	21	89	44
99	0.356	22	13	13	56	27
0	0	194	220	271	860	377
21	0.153	50	35	35	145	66
99	0.153	18	11	12	56	27
0	0	194	220	271	860	377
60	0.1	30	22	29	119	54
0	0	194	220	271	860	377
60	0.41	28	23	24	118	41

Reproduced with permission of the copyright owner. Further reproduction prohibited without permission.

Table 2.4: The removal of benzene, toluene, ethylbenzene, *m*- and *p*-xylene, and *o*-xylene from an aqueous solution due to treatment in a DMPR as a function of oxygen flow rate and current (Manolache et al., 2004).

Time (s)	O_2 Flow Rate (slm)	Current (A)	Concentration (ppm)				
			Benzene	Toluene	Ethyl-benzene	*m*- and *p*-Xylene	*o*-Xylene
0	0	0	194	220	271	860	377
5	0.25	1.5	58	30	35	150	67
60	0.25	1.5	3.81	1.9	0.5	2.2	0.8
115	0.25	1.5	0.1	0.04	0.01	0.03	0.02
0	0	0	194	220	271	860	377
60	0.25	0.5	6.1	3.3	1.1	5.2	2.1
0	0	0	194	220	271	860	377
60	0.25	2.5	0.1	0.04	0.002	0.03	0.02
0	0	0	194	220	271	860	377
28	0.34	0.9	8	4.3	1.5	6.6	2.8
92	0.34	0.9	3	1.2	0.3	1	0.4
0	0	0	194	220	271	860	377
28	0.34	2.1	6	2.8	0.6	2.9	1.3
92	0.34	2.1	0.001	0.001	0.0004	0.004	0.002
0	0	0	194	220	271	860	377
28	0.17	0.9	7.4	3.8	1.3	5.6	2.4
92	0.17	0.9	0.3	0.1	0.02	0.04	0.02
0	0	0	194	220	271	860	377
28	0.17	2.1	1.8	0.6	0.1	0.3	0.2
92	0.17	2.1	0.03	0.01	0.002	0.01	0.005
0	0	0	194	220	271	860	377
60	0.1	1.5	3	1.2	0.2	0.9	0.4
0	0	0	194	220	271	860	377
60	0.41	1.5	3.6	1.4	0.3	1.3	0.5

Reproduced with permission of the copyright owner. Further reproduction prohibited without permission.

intermediate oxidation products was not investigated. Thus, the oxidation pathway and the physical mechanism responsible for the oxidation of the aromatic compounds were not determined.

The need for an energy efficient method to treat organically polluted water with highly reactive transient species has motivated research and the incorporation of non-thermal and thermal plasmas generated by various types of electrical discharges into treatment processes (Sunka et al., 1999). It is essential to develop an understanding of the reaction mechanism and kinetics involved in the process in order to design, scale-up and operate an electrical discharge reactor on a large scale. Once a better understanding of the reaction mechanism and the operating conditions that control the discharge is realized, other compounds and AOT can be incorporated into the reactor design; thereby enhancing the energy efficiency of the treatment process. For example, the use of H_2O_2 and a semiconductor, such as titanium dioxide, in conjunction with the plasma discharge, could enhance the oxidizing power of the reactor. Energy not used to expand the plasma channel, wavelengths greater then 185 nm, could be utilized to either degrade hydrogen peroxide into hydroxyl radicals or to create oxidizing species through photocatalysis. There are certainly other compounds, groups of compounds and/or adaptive processes which can be explored to promote the oxidation reactions and increase energy efficiency. It is also important to understand these aspects in order to assess the feasibility and efficiency of aqueous phase plasma discharge reactors in degrading organic compounds. To help ascertain the removal mechanisms associated with the DMPR, and thus improve the process efficiency, the oxidation of methyl *tert*-butyl ether is explored.

Reproduced with permission of the copyright owner. Further reproduction prohibited without permission.

2.4 References

Akiyama, H., 2000. Streamer discharges in liquids and their applications. IEEE Trans. Dielectr. Electr. Insul. 7, 646-653.

Bednar, J., 1969. Theoretical Foundations of Radiation Chemistry. Kluwer Academic Publishers, Dordrecht.

Béroual, A., 1993. Electronic and Gaseous Processes in the Prebreakdown Phenomena of Dielectric Liquids.

Béroual, A. Zahn, M., Badent, A., Kisi, K., Schwabe, A.J., Yamashita, H., Yamazawa, K., Danikas, M., Chadband, W.G., Torshin, Y., 1998. Propagation and Structure of Streamer in Liquid Dielectrics. IEEE Electr. Insul. Magazine, 14, 6-17.

Chang, J.S., Looy, P.C., Urashima, K., Bryden, A.D., Yoshimura, K., 1998. Proceedings of the Asia-Pacific Workshop on Water & Air Treatment by Advanced Oxidation Technology. Tsukuba, Japan, 148.

Chatterjee, A., 1987. Interaction of ionizing radiation with matter, in Farhatziz, Rodgers, M.A.J. (eds) Radiation Chemistry: Principles and Applications, VCH Publishers, New York, NY, USA, 321-348.

Reproduced with permission of the copyright owner. Further reproduction prohibited without permission.

Clements, J.S., Sato, M., Davis, R.H., 1987. Preliminary Investigation of Prebreakdown Phenomena and Chemical-Reactions Using A Pulsed High-Voltage Discharge in Water. IEEE Trans. Ind. Appl. 23, 224-235.

Cooper, D.C. and Alley, F.C., 1994. Air Pollution Control, A Design Approach, 2nd ed. Waveland Press, Inc., Prospect Heights, IL, USA.

Denes, F.S., Young, R.A., 1996. Apparatus for reactions in dense-medium plasmas. U.S. Patent #5,534,232.

Denes, F.S., Manolache, S.O., Hershkowitz, N., 2002. Method and apparatus for producing colloidal nanoparticles in a dense medium plasma. U.S. Patent Application # 20020037320.

Devins, J. C., Rzad, S. J., Schwabe, R. J., 1977. Role of Electronic Processes in Electrical Breakdown of Insulating Liquids. Can. J. Chem.-Rev. Can. Chim. 55, 1899-1905.

Gao, J., Hu, Z., Wang, X., Hou, J., Lu, X., Kang, J., 2001. Oxidative degradation of acridine orange induced by plasma with contact glow discharge electrolysis. Thin Solid Films 390, 154-158.

Gavrilov, I.M., Kukhta, V.R., Lopatin, V.V., Petrov, P.G., 1994. Dynamics of Prebreakdown Phenomena in a Uniform Field in Water. IEEE Trans. Dielectr. Electr. Insul. 1, 496-502.

Reproduced with permission of the copyright owner. Further reproduction prohibited without permission.

Goheen, S.C., Durhlam, D.E., McCulloh, M., Heat, W.O., 1992. The Degradation of Organic Dyes by Corona Discharge. Proc. Second Int. Symp. Chem. Oxidation. Nashville, TN., 356-367.

Gurol, M. D., Vatistas, R., 1987. Oxidation of phenolic compounds by ozone and ozone + u.v. radiation: A comparative study. Water Res. 21, 895-900.

Harada, K., Suzuki, S., 1977. Formation of Amino-Acids from Elemental Carbon by Contact Glow-Discharge Electrolysis. Nature 266, 275-276.

Harada, K., Terasawa, J., 1980. Oxidative-Degradation of Beta-Amino and Gamma-Amino Acids by Contact Glow-Discharge Electrolysis. Chem. Lett. 4, 441-444.

Harada, K.,Terasawa, J.I.,Gunji, H., 1980. Oxidative-Degradation of Hydroxy Amino-Acids by Contact Glow- Discharge Electrolysis. Chem. Lett. 12, 1545-1548.

Hickling, A., Linacre, J.K., 1954. Glow-Discharge Electrolysis .2. The Anodic Oxidation of Ferrous Sulphate. J. Chem. Soc., FEB, 711-720.

Hickling, A., Ingram, M.D., 1964. Contact Glow-Discharge Electrolysis. Trans. Faraday Soc. 60, 783-793.

Hua, I., Hochemer, R.H., Hoffmann, M.R., 1995. Sonochemical degradation of p-nitrophenol in a parallel-plate near-field acoustical processor. Environ. Sci. Technol. 29, 2790-2796.

Hughes, G., 1973. Radiation Chemistry. Clarendon Press, Oxford.

Reproduced with permission of the copyright owner. Further reproduction prohibited without permission.

Jones, H.M., Kunhardt, E.E., 1994. The Influence of Pressure and Conductivity on the Pulsed Breakdown of Water. IEEE Trans. Dielectr. Electr. Insul. 1, 1016-1025.

Jones, H.M., Kunhardt, E.E., 1995. Prebreakdown Currents in Water and Aqueous Solutions and Their Influence on Pulsed Dielectric breakdown. J. Appl. Phys. 78, 3308-3314.

Joshi, A.A., Locke, B.R., Arce, P., Finney, W.C., 1995. Formation of Hydroxyl Radicals, Hydrogen-Peroxide and Aqueous Electrons by Pulsed Streamer Corona Discharge in Aqueous-Solution. J. Hazard. Mater. 41, 3-30.

Kellogg, J., 1950. Anode Effect in Aqueous Electrolysis. J. Electrochem. Soc. 97, 133-142.

Kokufuta, E.,Fujii, S.,Ishibashi, H.,Yokoi, H.,Harada, K.,Nakamura, I., 1980. Degradation of Poly(Acrylamide) in Aqueous-Solution by Glow- Discharge Electrolysis. Polym. Bull. 3, 173-178.

Kokufuta, E.,Shibasaki, T.,Nakamura, I.,Harada, K.,Sodeyama, T., 1985. Degradation of Polyethylene-Glycol in a Localized Reaction Zone During Glow-Discharge Electrolysis. J. Chem. Soc.-Chem. Commun. 2, 100-102.

Lieberman, M.A., Lichtenberg, A.J., 1994. Principles of plasma discharges and materials processing. John Wiley & Sons, New York, NY, USA.

Lisitsyn, I.V., Nomiyama, H., Katsuki, S., Akiyama, H., 1999. Thermal Processes in a Streamer Discharge. IEEE Trans. Dielectr. Electr. Insul. 6, 351-356.

Reproduced with permission of the copyright owner. Further reproduction prohibited without permission.

Manolache, S., Somers, E.B., Wong, A.C.L., Shamamian, V., Denes, F., 2001. Dense medium plasma environments: A new approach for the disinfection of water. Environ. Sci. Technol. 35, 3780-3785.

Manolache, S.O., Shamamian, V.A., Denes, F., 2004. Dense medium plasma-plasma-enhanced decontamination of water of aromatic compounds. J. Environ. Engin. 130, 17-25.

Mazzocchin, G.A., Bontempelli, G., Magno, F., 1973. Glow-Discharge Electrolysis on Methanol. J. Electroanal. Chem. 42, 243-252.

Robinson, J.W., Ham, M., Balaster, A.N., 1973a. Ultraviolet Radiation from Electrical Discharges in Water. J. Appl. Phys. 44. 72-75.

Robinson, J.W., Ham, M., Balaster, A.N., 1973b. Finite-Difference Simulation of an Electrical Discharge in Water. J. Appl. Phys. 44. 76-81.

Roth, J.R., 1995. Industrial Plasma Engineering Vol. 1: Principles. Institute of Physics Publishing, Philadelphia, PA, USA.

Roth, J.R., 2001. Industrial plasma engineering vol. 2. Applications to nonthermal plasma processing. Institute of Physics Publishing, Philadelphia, PA, USA.

Sharbaugh, A.H., Devins, J.C., Rzad, S.J., 1978. Progress In Field Of Electric Breakdown In Dielectric Liquids. IEEE Trans. Electr. Insul. 13, 249-276.

Reproduced with permission of the copyright owner. Further reproduction prohibited without permission.

Sharma, A.K., Locke, B.R., Arce, P., Finney, W.C., 1993. A Preliminary-Study of Pulsed Streamer Corona Discharge for the Degradation of Phenol in Aqueous-Solutions. Hazard. Waste Hazard. Mater. 10, 209-219.

Skvortsov, Y.V., Komelkov, V.S., Kuznetsov, N.M., 1961. Expansion of a Spark Channel in a Liquid. Sov. Phys.-Tech. Phys. 18, 1303-1306.

Spinks, J.W.T., Woods, R.J., 1990. An Introduction to Radiation Chemistry. Wiley, New York, NY, USA.

Sun, B., Sato, M., and Clements, J.S., 1997. Optical study of active species produced by a pulsed streamer corona discharge in water. J. Electros. 39, 189-202.

Sun, B., Sato, M., Harano, A., Clements, J.S., 1998. Non-uniform pulse discharge-induced radical production in distilled water. J. Electros. 43, 115-126.

Sun, B., Sato, M., Clements, J.S., 1999. Use of a pulsed high-voltage discharge for removal of organic compounds in aqueous solution. J. Phy. D: Appl. Phy. 32, 1908-1915.

Sun, B., Sato, M., Clements, J.S., 2000. Oxidative processes occurring when pulsed high voltage discharges degrade phenol in aqueous solution. Environ. Sci. Technol. 34, 509-513.

Sunka, P., Babicky, V., Clupek, M., Lukes, P., Simek, M., Schmidt, J., Cernak, M., 1999. Generation of chemically active species by electrical discharges in water. Plasma Sources Sci. Techno. 8, 258-265.

Reproduced with permission of the copyright owner. Further reproduction prohibited without permission.

Swallow, A.J., 1960. Radiation Chemistry of Organic Compounds. Pergamon Press, Oxford.

Tezuka, M., Iwasaki, M., 1997. Oxidative degradation of phenols by contact glow discharge electrolysis. Denki Kagaku 65, 1057-1060.

Tezuka, M., Iwasaki, M., 1998. Plasma induced degradation of chlorophenols in an aqueous solution. Thin Solid Films 316, 123-127.

Tezuka, M., Iwasaki, M., 2001. Plasma-induced degradation of aniline in aqueous solution. Thin Solid Films 386, 204-207.

Tezuka, M., Iwasaki, M., 2002. Aromatic cyanation in contact glow discharge electrolysis of acetonitrile. Thin Solid Films 407, 169-173.

Wesley, R.H., Ayres, R.A., 1984. Method and apparatus for electrohydraulic fracturing of rock and the like. U.S. Patent 4,479,680.

Willberg, D.M., Lang, P.S., Hochemer, R.H., Kratel, A., Hoffmann, M.R., 1996a. Degradation of 4-chlorophenol, 3,4-dichloroaniline, and 2,4,6-trinitrotoluene in an electrohydraulic discharge reactor. Environ. Sci. Technol. 30, 2526-2534.

Willberg, D.M., Lang, P.S., Hochemer, R.H., Kratel, A.W., Hoffmann, M.R., 1996b. Electrohydraulic destruction of hazardous wastes. CHEMTECH. 26, 52-57.

Yanshin, E.V., Ovchinnikov, I.T., Vershinin, Yu.N., 1974. Optical Study of Nanosecond Prebreakdown Phenomena in Water. Sov. Phys.-Tech. Phys. 18, 1303-1306.

Reproduced with permission of the copyright owner. Further reproduction prohibited without permission.

The text of Chapter 3 consists of an article that appears in Environmental Science & Technology 37 (20), 4804-4810 (2003).

Reproduced with permission of the copyright owner. Further reproduction prohibited without permission.

Chapter Three

3.0 Oxidation of Methyl *tert*-Butyl Ether in a DMPR

Plasma treatment of contaminated water appears to be a promising alternative for the oxidation of aqueous organic pollutants. This study examines the kinetic and oxidation mechanisms of methyl *t*-butyl ether (MTBE) in a DMPR utilizing gas chromatography-mass spectrometry and gas chromatography-thermal conductivity techniques. A rate law is developed for the removal of MTBE from an aqueous solution in the DMPR. Rate constants are also derived for three reactor configurations and two pin array spin rates. The oxidation products from the treatment of MTBE contaminated water in the DMPR were found to be predominately carbon dioxide, with smaller amounts of acetone, *t*-butyl formate and formaldehyde. The lack of stable intermediate products suggests that the MTBE is, to some extent, oxidized directly to carbon dioxide, making the DMPR a promising tool in the future remediation of water. Chemical and physical mechanisms, together with carbon balances, are used to describe the formation of the oxidation products and the important aspects of the plasma discharge.

3.1 Introduction

Increasingly stringent regulations on wastewater discharge of organic compounds require that new, innovative ways of treatment be sought. Direct oxidation of organics using

Reproduced with permission of the copyright owner. Further reproduction prohibited without permission.

oxygen at normal/ambient conditions is too slow, and creating temperature and pressure conditions that increase the reaction rate, such as those used in supercritical water oxidation, are currently too costly (Sunka et al., 1999). The oxidation of organic compounds to water and carbon dioxide is an appealing treatment method if complete oxidation can be achieved, or at the very least, the pollutants can be converted into substances that do not require additional treatment. Thus, if the original compound is transformed into a more toxic material or a substance that is more difficult to remediate, the treatment process is deemed ineffective.

Ethers are volatile, explosive, odorous compounds used as solvents, refrigerants, artificial flavors, drugs and softeners for plastics. An industrially significant ether and the focus of this study is methyl *tert*-butyl ether (Riddick et al., 1986; Sterner, 1999). MTBE's principal use was as an anti-knock agent in gasoline, replacing tetraethyl lead, to ensure that catalytic converters used to reduce vehicle emissions are not deactivated by the deposition of lead from the exhaust. Ethers can be thought of as derivatives of water in which alkyl groups have replaced both hydrogen atoms. In fact, the carbon-oxygen-carbon bond angle is only slightly larger than the hydrogen-oxygen-hydrogen angle in water (Solomons, 1996). Due to these similarities short-chained ethers are highly soluble and hence difficult to separate from water; thereby allowing this class of compounds to propagate through groundwater facilely. Sufficient quantities of MTBE have been concentrated in groundwater through leaks in underground storage tanks and gasoline spills, causing nationwide concern. Advanced oxidation technologies (AOT) are techniques that involve an input of energy—chemical, electrical and/or radiative—into a fluid matrix

Reproduced with permission of the copyright owner. Further reproduction prohibited without permission.

to produce highly reactive oxidizing species, particularly hydroxyl radical, which in turn oxidize the organics, ideally to carbon dioxide and water. It is anticipated that AOT will be able to chemically treat organic pollutants such as MTBE that have physical properties similar to the solvent, thereby alleviating the difficulties of treating this class of organic compounds present in water.

The most effective means of oxidizing organics and avoiding unwanted intermediate compounds is to use highly reactive species such as hydroxyl radical (·OH), singlet oxygen radical (·O), ozone (O_3) and hydrogen peroxide (H_2O_2) (Sun et al., 1999). The treatment of organically polluted water by radicals is extremely important not only in the purification of water but for industrial processes as well. Saturated organic material of high molecular weight present in trace amounts can be degraded rather quickly to low molecular weight carboxylic and dicarboxylic acids using various AOT (Schuchmann et al., 1995; Legrini et al., 1993). In these processes, hydroxyl radical is considered one of the most important oxidizing agents in the purification of water and in degrading organics (Schuchmann et al., 1995; Legrini et al., 1993). It is a short-lived, extremely potent oxidizing agent that will indiscriminately oxidize organic compounds, mainly by hydrogen abstraction (Legrini et al., 1993). The hydrogen abstraction reaction generates an organic radical, which subsequently reacts with molecular oxygen to yield a peroxy radical, see Eqs. (3.1) and (3.2). The intermediates then initiate thermal chain oxidative reactions, which result in the formation of CO_2, water and inorganic salts (Legrini et al., 1993).

$$RH + \cdot OH \rightarrow \cdot R + H_2O \qquad (3.1)$$

Reproduced with permission of the copyright owner. Further reproduction prohibited without permission.

$$\cdot R + O_2 \rightarrow \cdot OOR \quad (3.2)$$

A number of processes, such as direct ozonation (Gurol and Vatistas, 1987; Hoigne and Bader, 1976; Hoigne and Bader, 1979), ultraviolet radiation photolysis (Glaze et al., 1987), high-energy electron irradiation (Nickelsen et al., 1992), supercritical water oxidation (Thornton and Savage, 1990), wet air oxidation (Joglekar et al., 1991), UV-H_2O_2 oxidation (Legrini et al., 1993), sonochemistry (Petrier et al., 1998), photocatalysis (Davis and Huang, 1990) and several other AOT have been explored or are currently used to remove hazardous chemicals from contaminated water. Most of these methods focus on the *in-situ* production of hydroxyl radical. Commercial processes for the treatment of municipal wastewater and potable water have developed from research conducted on direct ozonation. Trace aqueous organic compounds have been degraded in the laboratory by processes, such as electrochemistry (DeSucre and Watkinson, 1981) and aqueous plasma (Sun et al., 1997; Sato et al., 1996; Joshi et al., 1995; Robinson et al., 1973; Sun et al., 1998), in which an electrical potential was applied across the fluid. Most of these processes have fallen short of their potential, whether due to energy inefficiency, low throughput or an inability to scale up the process for industrial use. However, some AOT such as plasma treatment are considered to be promising alternatives for the treatment of water pollutants.

Application of an aqueous plasma discharge to degrade organic pollutants in wastewater is a relatively new process. The process is characterized by the production of high oxidation potential species such as ·OH, H_2O_2 and ·O (Sun et al., 1997; Willberg et al., 1996).

Reproduced with permission of the copyright owner. Further reproduction prohibited without permission.

Both non-thermal and thermal discharges, created by large voltage drops across an insulating fluid such as water, are oxidation technologies in which energy is electrically introduced into an aqueous solution through a plasma channel. Under specific conditions a strong electric field is produced which in turn produces a plasma discharge where many different reactive oxidizing species— ·OH, ·H, ·O, $\cdot HO_2$, O_2^-, H_2O_2, O_3 and others—can subsist (Sun et al., 1999). These oxidizing species react with contaminant molecules, ideally degrading them completely to carbon dioxide and water. If complete oxidation is not achieved, it is desirable that pollutants are at least degraded into less hazardous hydrocarbons that are easier to remediate with a secondary treatment or disposed of completely.

The need for an energy-efficient method to treat organically polluted wastewater utilizing potent oxidizing species has motivated research into the application of plasma generation by various types of electrical discharges, mainly non-thermal discharges, thermal discharges and contact glow discharge electrolysis. It is essential to develop an understanding of the chemical reaction mechanism and the chemical kinetics involved in these processes to be able to design, scale and operate an electrical discharge reactor. It is also important to understand the reaction mechanism and kinetics to assess the feasibility and efficiency of degrading organic compounds in plasma reactors.

3.2 Experimental Methods

Water contaminated with MTBE was treated using a DMPR developed by Denes and coworkers (Denes and Young, 1996; Manolache et al., 2001). The reactor was developed

Reproduced with permission of the copyright owner. Further reproduction prohibited without permission.

to react liquid/vapor phase chemicals in an induced plasma state, using low temperature plasma chemistry in which the liquid temperature remains relatively close to ambient temperatures. The advantages associated with this reactor over typical plasma processing reactors are that these reactions are conducted at atmospheric pressure and approximately room temperature, and the discharge is controlled by electron flux instead of by thermionic emission. The DMPR was designed to (1) emit a higher current, continuous discharge at lower voltages than previous point-to-plate aqueous plasma discharge reactors, (2) reduce mass transfer limitations inherent to high-voltage point-to-plane plasma reactors, and (3) influence aspects of the chemistry occurring in and on the surface of the arcs (Manolache et al., 2001).

The DMPR utilized in this study includes a reaction vessel containing a rotating upper electrode, a stationary lower electrode, cooling system, gas introduction and discharge ports. The upper electrode is a pin array that can rotate at speeds up to 2500 rpm. Rotating the upper electrode distributes the sputtered metal from the pin electrodes evenly on the stationary electrode, preventing pitting and unwanted changes in the relative distance between the electrodes. Spinning the pin array also induces convective mass transfer, thereby reducing mass transfer limitations that are apparent in high voltage point-to-plane plasma reactors. Rotating the upper electrode has an additional benefit of reducing the inception voltage by abating the effective distance between the pin electrodes and the stationary electrode.

Oxygen was injected into the system through the middle of the stationary electrode. A

Reproduced with permission of the copyright owner. Further reproduction prohibited without permission.

nebulizer was added to the original reactor configuration, allowing the liquid and oxygen to be transported coaxially through the middle of the stationary electrode to the reaction zone. This arrangement ensured that the solution in the reaction zone would be saturated with oxygen and that the oxygen bubble surface area would be maximized. This reactor configuration is referred to as the coaxial configuration, while an aqueous discharge without a nebulizer or coaxial flow is termed the original configuration. The oxygen bubbles in the reaction zone reduce the apparent density of the medium between the pin and stationary electrodes, thereby lowering the inception voltage of the arcs as well as influencing the chemistry that is performed in and on the surface of the arc tubules. A third reactor configuration was developed to force the plasma discharge to occur only through oxygen; this third configuration prevented the aqueous solution from coming into contact with the plasma and is referred to as the gas discharge configuration. A schematic of the DMPR and the modified reactor configurations can be found in Figure 3.1.

Gas transported through the system was vented through a valve at the top of the reaction vessel to keep the reactor at atmospheric pressure. A gas collection system was constructed with the capability to collect the gas samples and recirculate gas through the reaction zone, i.e., the plasma. Opaque tedlar® bags were used to collect and house the gas used in all DMPR experiments, preventing unwanted photolysis of the organics and loss to the walls.

The reactor was equipped with a cooling jacket to ensure the glass-to-metal seals in the reactor did not fail, but at the same time allowing a controlled increase of the reaction

Reproduced with permission of the copyright owner. Further reproduction prohibited without permission.

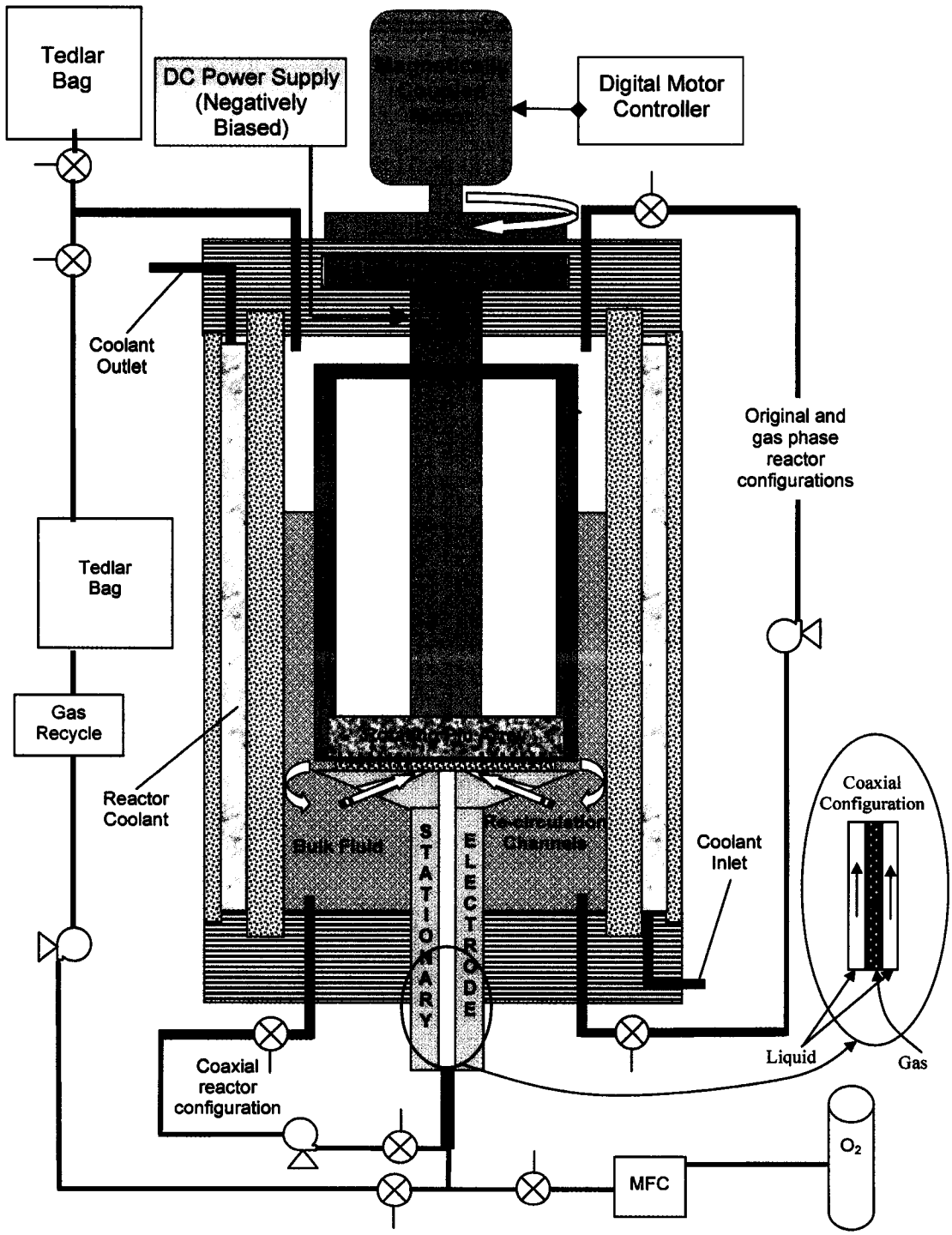

Figure 3.1: A schematic of the original DMPR and a modified reactor configuration implemented by Johnson and coworkers. A more detailed description of the original reactor can be found in Denes et al. (1996) and Manolache et al. (2001).

Reproduced with permission of the copyright owner. Further reproduction prohibited without permission.

medium temperature with time. Tap water, with a temperature of approximately 295 K, was flushed through the jacket at 1.17 ± 0.04 L/min. The initial temperature of the reaction media was 295 ± 1 K and reached steady state at 309 ± 1 K for all experiments.

The DMPR experiments were performed with an applied voltage of 200 ± 25 V and a resulting current of 1.00 ± 0.15 A. Because of the fluctuations in the plasma, neither the applied potential nor the current displayed steady state behavior. Thus, the voltage and current readings represent time-averaged values while the error represents the fluctuation in each parameter. The pin array spin rate was 1000 rpm unless noted otherwise. Oxygen was bubbled through the middle of the stationary electrode at a flow rate of 400 mL/min and was not recirculated through the system. The electrode gap was 500 μm. A 250 mL, 50 ppm MTBE solution was recirculated through the middle of the stationary electrode coaxially with the oxygen at approximately 100 mL/min. In the first product study experiment, the contaminated solution was treated with plasma for 10 min. In the second product study experiment, the contaminated solution was treated with plasma for 11 min. All other operating conditions remained the same.

Methyl *t*-butyl ether (≥99.8% purity), and the anticipated intermediate products of plasma treatment–*t*-butyl formate (≥99.0% purity), acetone (≥99.8% purity), anhydrous *t*-butyl alcohol (> 99.5% purity) and formaldehyde (HPLC Grade)–were obtained from Aldrich Chemical Co. Carbon dioxide calibrations were carried out by dilution of a Scott Gases standard. Millipore water was generated by a Milli-Q ultrapure water system and was used as the solvent.

Reproduced with permission of the copyright owner. Further reproduction prohibited without permission.

The aqueous samples were analyzed using a Varian Saturn GC-MS system. The liquid samples collected from the DMPR, each 5.00 ± 0.02 mL, were diluted with 15.00 ± 0.04 mL of millipore water in a Supelco 22-mL amber screw-top sampling vial. The samples were adsorbed onto a 100-μm polydimethylsiloxane solid phase micro-extraction (SPME) fiber. To adsorb the organics onto the fiber, a small stir bar was inserted into the sample vial. The vial was then placed in a 50 °C isothermal bath and the stir bar was rotated at 300 rpm, while the fiber was inserted into the vial through a septum for 13 min. The fiber was then immediately inserted into the injection port of the Varian GC. The samples were allowed to desorb in the GC injection port for approximately 10 min, conditioning the fiber for the subsequent sample. The injection port of the gas chromatographic instrument had a splitless flow into the column for one minute to ensure the desorbed species were trapped at the beginning of the column. After that, the gas flow rate became split with a 25:1 flow ratio for the remaining run time. The reactant and products were separated with a 30 m by 0.25 mm Phenomenex ZB-624 column, designed to separate volatile organic compounds. Two GC oven temperature control methods were used to analyze the compounds. The first method used an initial oven temperature of 0 °C, which was held at this temperature for 5 min, and then ramped at a rate of 10 °C/min to 100 °C. The oven temperature was then ramped at 50 °C/min to a final temperature of 225 °C. Liquid nitrogen was used to cool the column below ambient temperatures. The second method had an initial oven temperature of 45 °C that was held for one minute and then ramped at a rate of 10 °C/min to 120 °C. The oven temperature was ramped again at 30 °C/min to a final temperature of 200 °C. Ultra-high-purity-grade helium was used as the carrier gas for both methods. The mass spectral analyses were per-

Reproduced with permission of the copyright owner. Further reproduction prohibited without permission.

formed in electron ionization mode with a scan range of 35 to 200 *m/z* and a background mass of 34 *m/z*.

Gas samples collected in tedlar® bags were analyzed using a Varian GC with a thermal conductivity detector (TCD). Carbon dioxide was separated in a 15 ft by 1/8 inch 60/80 Carboxen 1000 packed column (Supelco). A 25-mL sample loop was purged using a pressurized analytical sample. After the loop was sufficiently purged, it was switched into the column flow, which was He at a rate of 30 mL/min. The column was maintained at 60 °C and the thermal conductivity detector at 220 °C.

3.3 Results

The principle products of the oxidation of MTBE in the DMPR are carbon dioxide (CO_2), acetone ($C(CH_3)_2O$), *t*-butyl formate ($(CH_3)_3OCHO$) and formaldehyde (CH_2O). The mechanistic pathways used to predict the formation of oxidation products and to carry out the carbon balances are illustrated in Figures 3.2 and 3.3. Chromatographs of the DMPR product study at various times are presented in Figures 3.4 and 3.5. The figures illustrate primary oxidation products formed when aqueous MTBE is oxidized in a DMPR. In Figures 3.4 and 3.5, "TOT" is the total ion count for mass-to-charge ratios of 35 to 200. MTBE was quantified using the sum of the signals for 73, 57 and 41 *m/z*; deuterated benzene, the internal standard, by the signal sums for 84, 56 and 52 *m/z*; acetone by the signal for 43 *m/z*; and *t*-butyl formate was quantified using the signal sums for 57, 59 and 41 *m/z*.

Reproduced with permission of the copyright owner. Further reproduction prohibited without permission.

Reproduced with permission of the copyright owner. Further reproduction prohibited without permission.

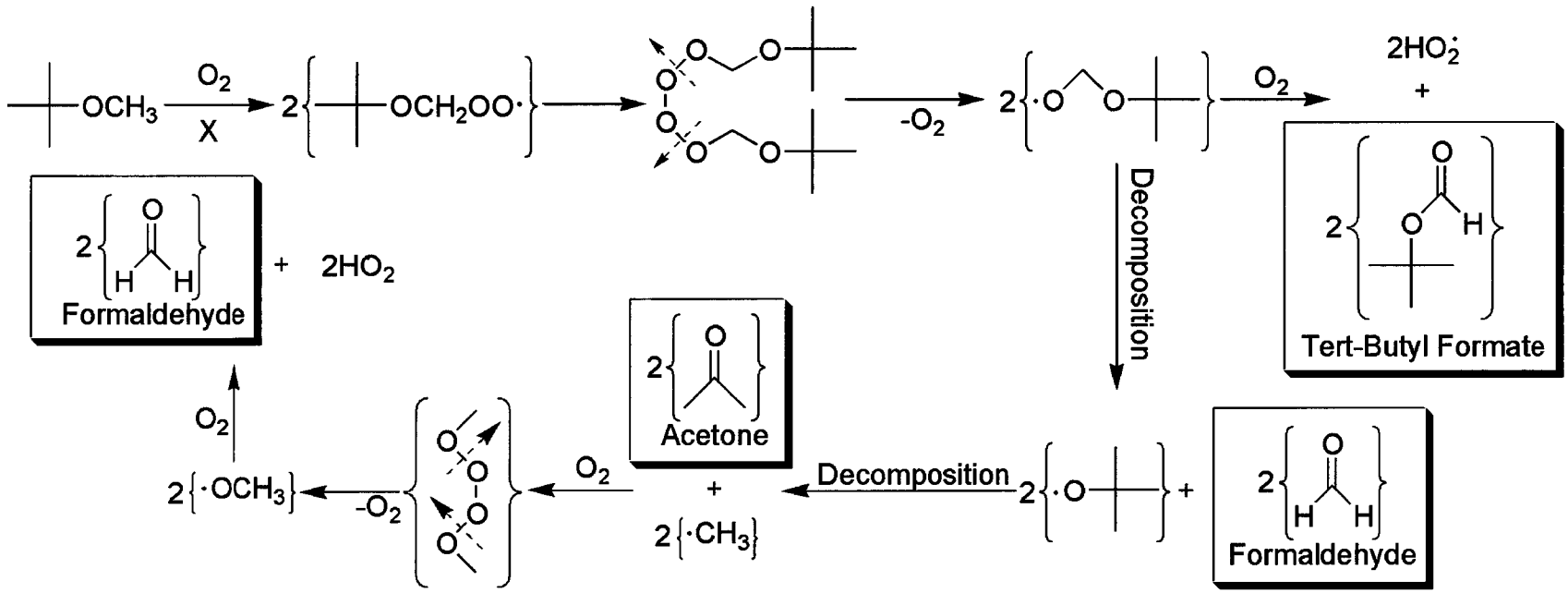

Figure 3.2: Reaction mechanism for the oxidation of MTBE in a DMPR by reactive oxidizing species (X) produced by the plasma discharge, site 1. The boxed compounds were identified in this study.

Reproduced with permission of the copyright owner. Further reproduction prohibited without permission.

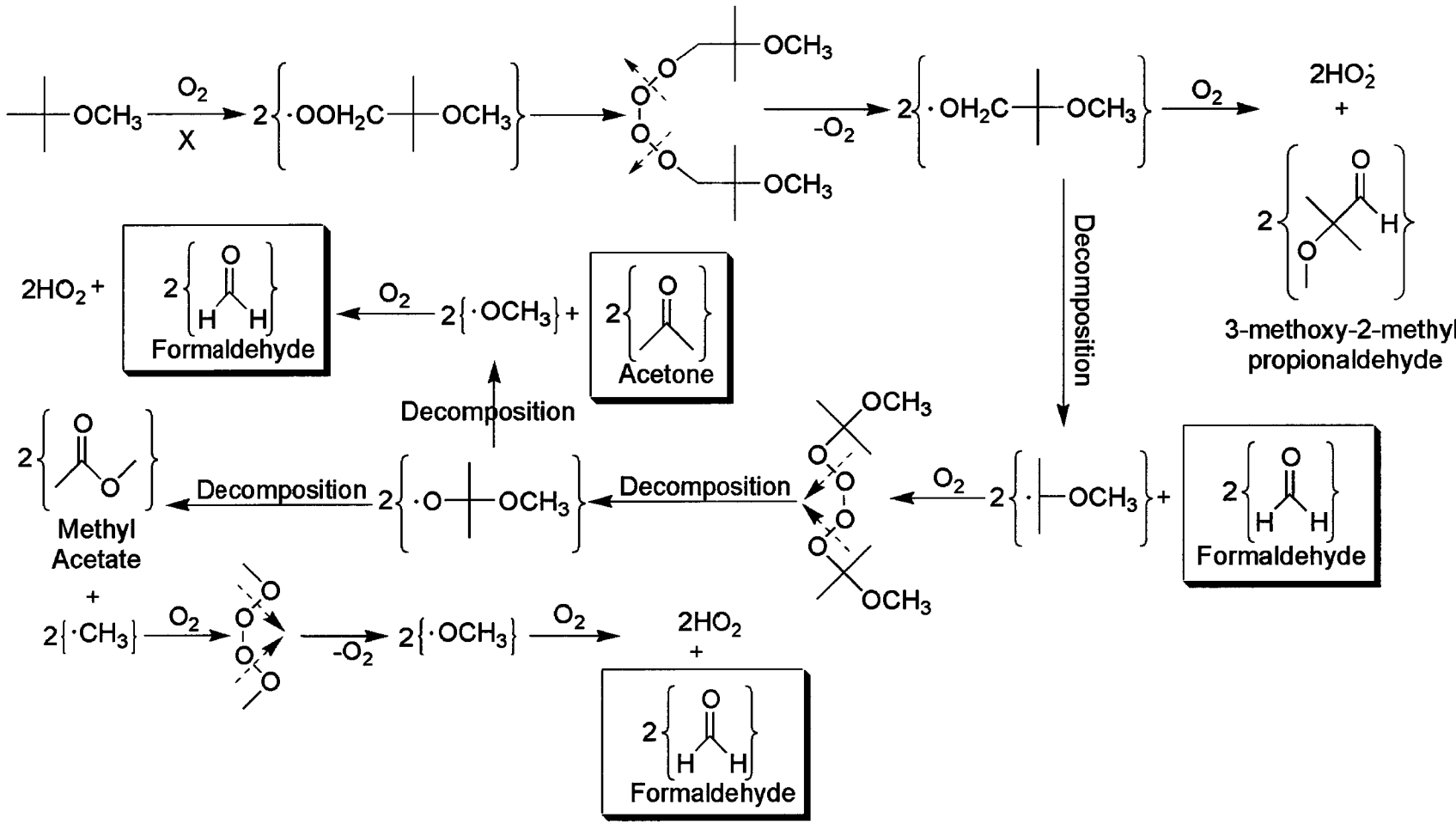

Figure 3.3: Reaction mechanism for the oxidation of MTBE in a DMPR by reactive oxidizing species (X) produced by the plasma discharge, site 2. The boxed compounds were identified in this study.

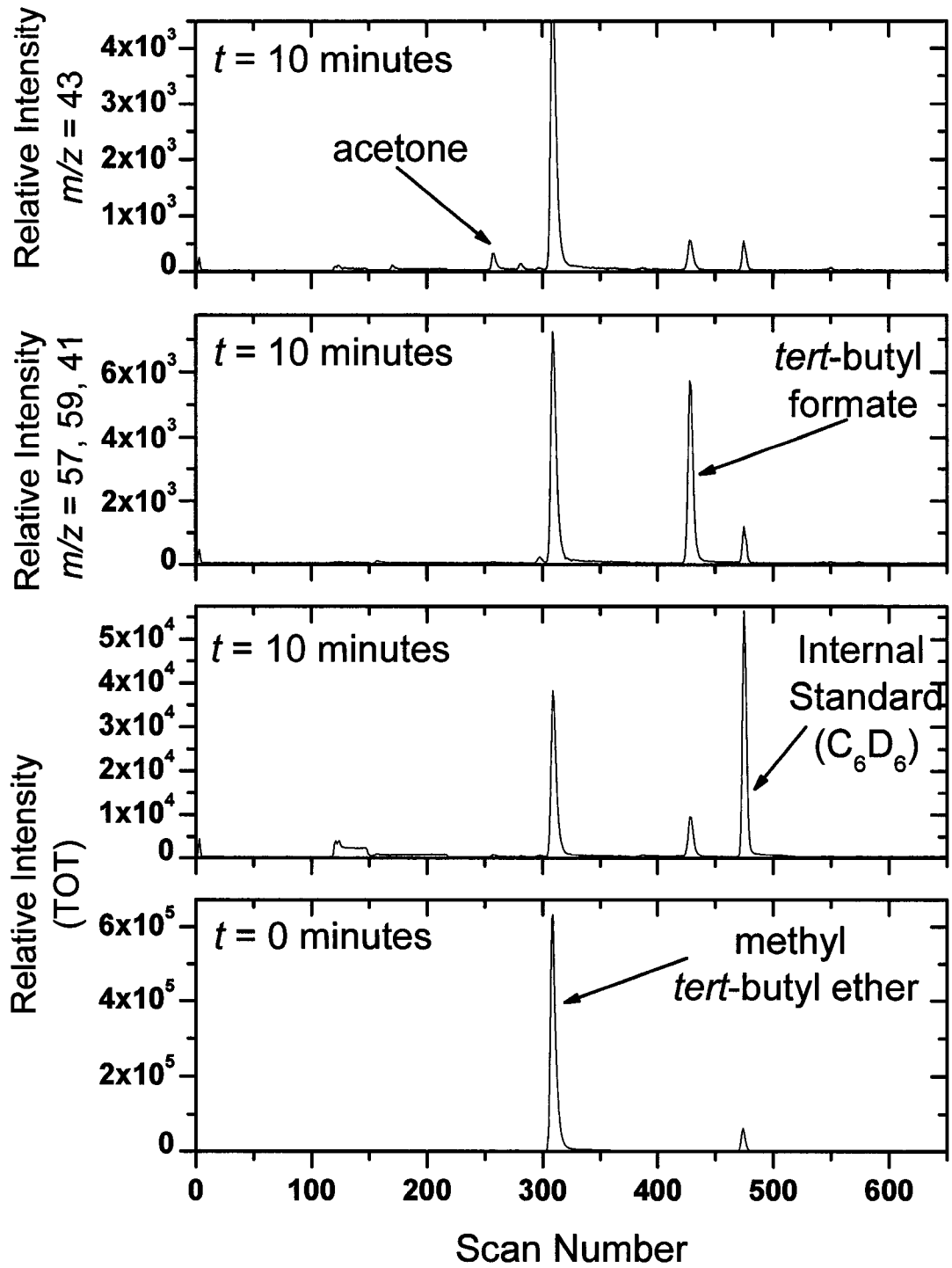

Figure 3.4: Chromatographs from the 10-min product study. The bottom total ion chromatograph (TOT) was taken at t = 0 min, while the other three chromatographs show MTBE and oxidation products at t = 10 min. Compounds detected by the GC-MS were MTBE, deuterated benzene, *t*-butyl formate and acetone.

Reproduced with permission of the copyright owner. Further reproduction prohibited without permission.

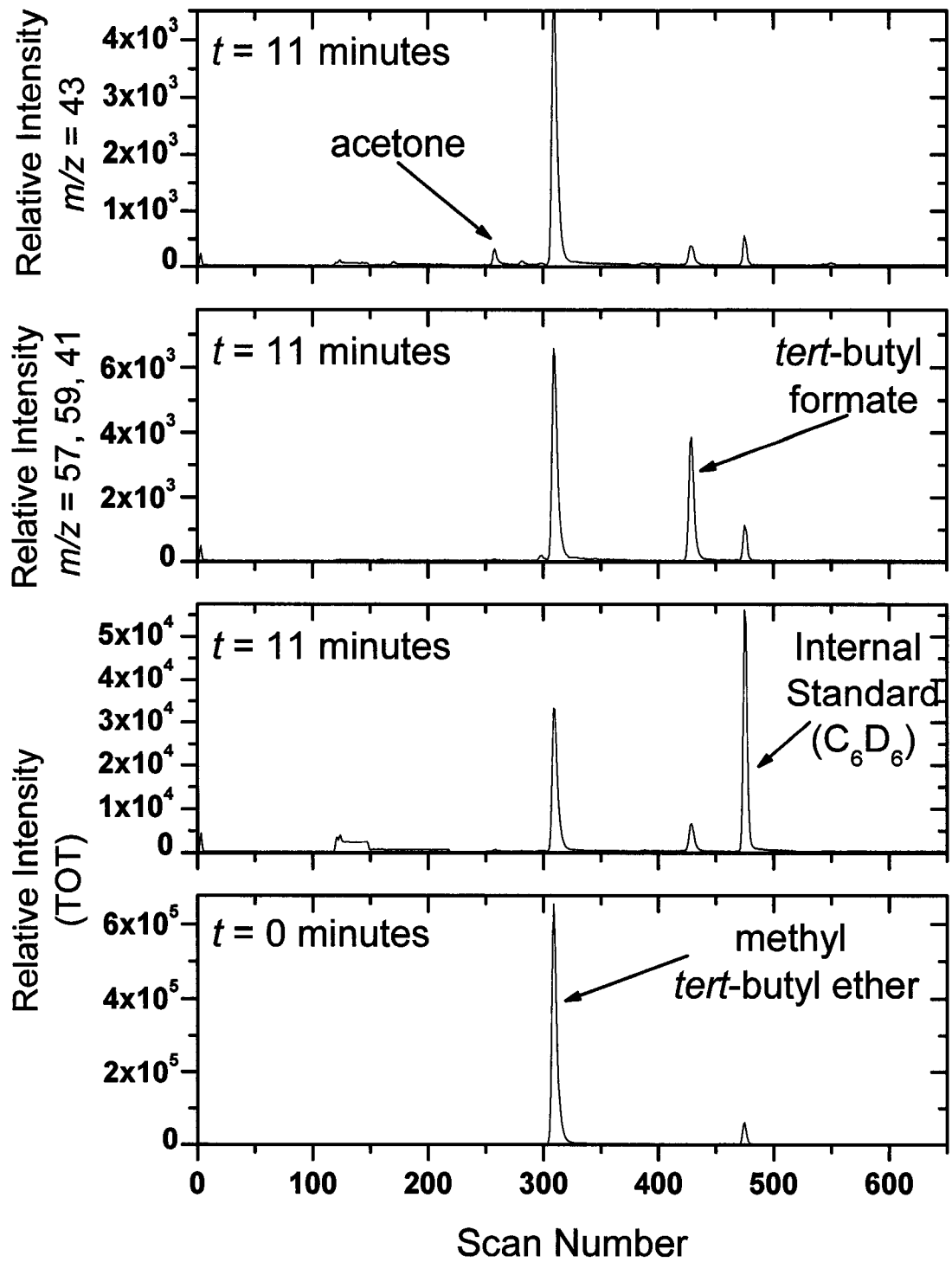

Figure 3.5: Chromatographs from the 11-min product study. The bottom total ion chromatograph (TOT) was taken at t = 0 min, while the other three chromatographs show MTBE and oxidation products at t = 11 min. Compounds detected by the GC-MS were MTBE, deuterated benzene, t-butyl formate and acetone.

Reproduced with permission of the copyright owner. Further reproduction prohibited without permission.

Quantitative analysis of the total carbon in the DMPR at different times during treatment is presented in Figures 3.6 and 3.7. In these figures, the total amount of carbon (μmol) for the different species is plotted against treatment time. Real time sampling of carbon dioxide was not possible, so a cumulative CO_2 concentration was determined for each experiment. The total amount of carbon dioxide produced, in terms of carbon, is plotted for t = 10 and 11 min in Figures 3.6 and 3.7, respectively. The observed product concentrations for acetone and *t*-butyl formate were corrected to account for secondary reactions with hydroxyl radical using a correction factor, F (Atkinson et al., 1982).

$$F = \left(\frac{k_m + k_p}{k_m} \right) \frac{1 - N_t}{N_t^k - N_t} \tag{3.3}$$

k_M and k_p are rate constants for the hydroxyl radical reaction with MTBE and a product compound, respectively, N_t is the normalized MTBE concentration at time t, and k is the ratio of k_p and k_M. The measured primary product concentrations from the experiments have been multiplied by F to obtain the corrected product yields plotted in Figures 3.6 and 3.7. The rate constants associated with the reactions between MTBE, the observed oxidation products and hydroxyl radical may be found in Table 3.1. The calculated correction factor ranges for these products are given in Table 3.2. A large correction factor magnitude indicates that a product reacts relatively quickly with hydroxyl radical; thereby interfering with primary product quantification. However, over the time scale of the experiments, the amount of *tert*-butyl formate formed due to the oxidation of MTBE is negligible. Furthermore, the oxidation of acetone does not produce compounds that are also products of the MTBE oxidation. Therefore, only corrections for the loss of primary products due to the reaction with hydroxyl radical were taken into account. While the loss of primary oxidation products due to reaction with hydroxyl radical is accounted for,

Reproduced with permission of the copyright owner. Further reproduction prohibited without permission.

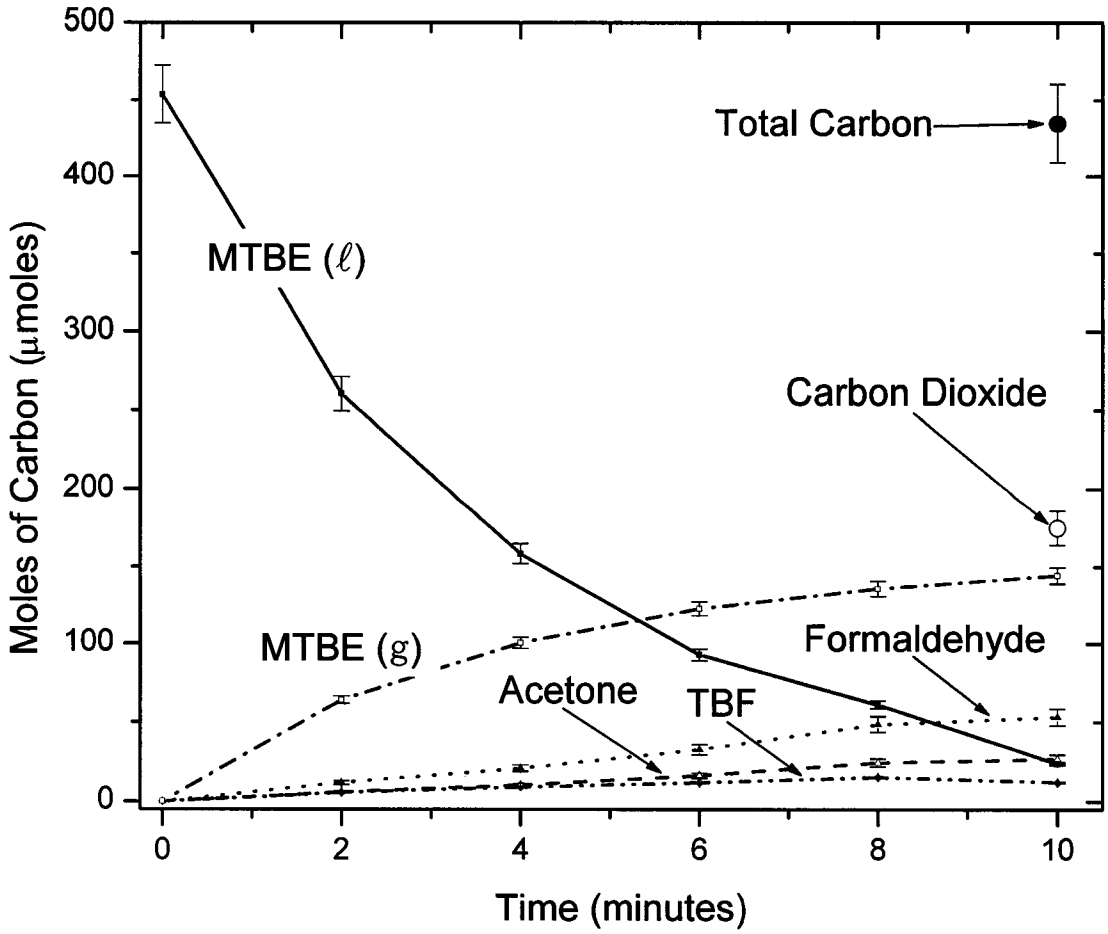

Figure 3.6: Carbon balance as a function of time for the oxidation of MTBE in a DMPR; 100% of the inputted carbon was recovered, within error, after the allotted treatment time of 10 min. The decrease of aqueous MTBE and the production of carbon dioxide, gaseous MTBE, *t*-butyl formate, acetone and formaldehyde are shown.

Reproduced with permission of the copyright owner. Further reproduction prohibited without permission.

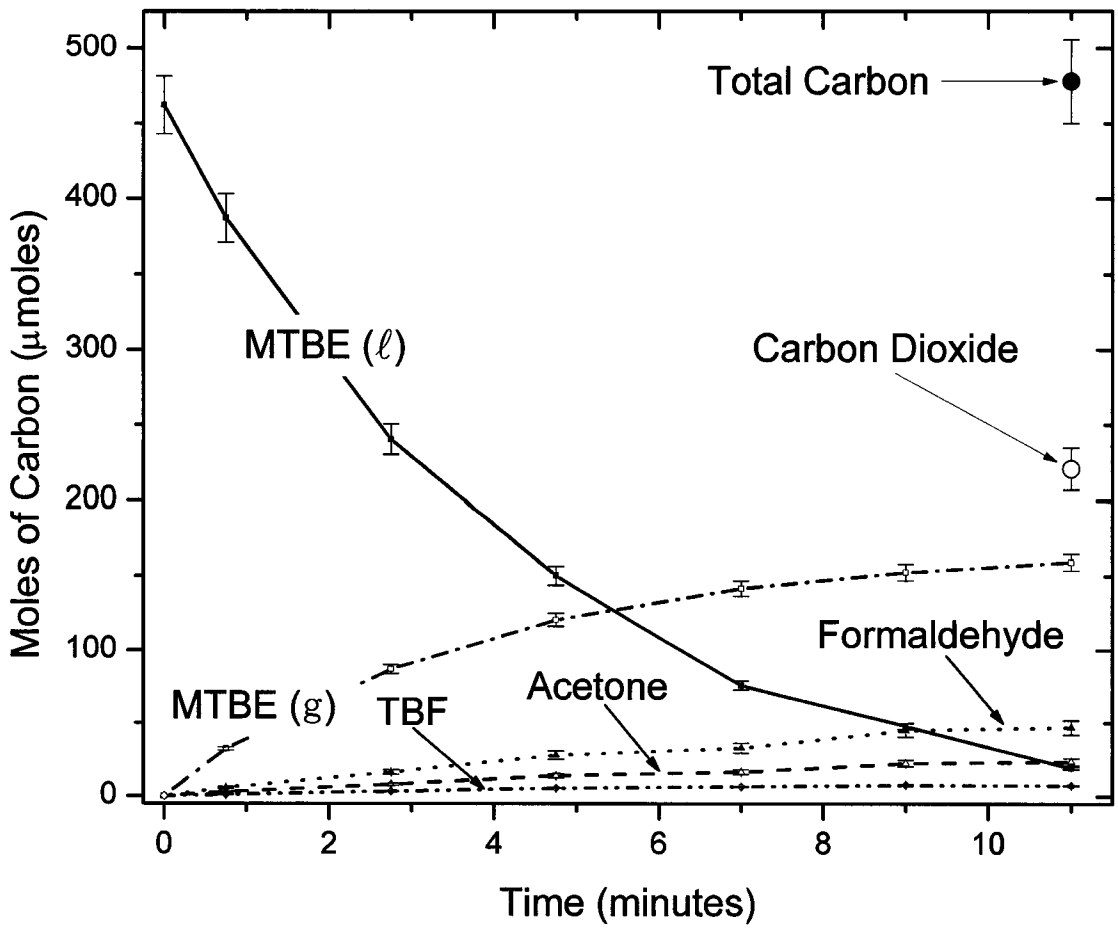

Figure 3.7: Carbon balance as a function of time for the oxidation of MTBE in a DMPR; 100% of the inputted carbon was recovered, within error, after the allotted treatment time of 11 min. The decrease of aqueous MTBE and the production of carbon dioxide, gaseous MTBE, *t*-butyl formate, acetone and formaldehyde are shown.

Reproduced with permission of the copyright owner. Further reproduction prohibited without permission.

Table 3.1: Rate constants for the hydroxyl radical reaction with MTBE and primary reaction products.

Molecule	Rate Constant ($mM^{-1}s^{-1}$)	Reference
MTBE	1.71×10^9	(Mezyk et al., 2004)
t-butyl formate	5.23×10^8	(Hardison et al., 2002)
acetone	1.1×10^8	(Buxton et al., 1988)

Reproduced with permission of the copyright owner. Further reproduction prohibited without permission.

Table 3.2: Ranges of the correction factor, F, used to correct measured primary product concentrations for secondary losses due to reaction with hydroxyl radical.

Product	F-Factor Range
acetone	1.01 – 1.15
t-butyl formate	1.00 – 1.89

Reproduced with permission of the copyright owner. Further reproduction prohibited without permission.

the concentration of these products are sufficiently low that the correction does not have an appreciable affect, approximately 2%, on the overall carbon balances.

In the first experiment 94.2 ± 5.8% of the carbon, in the form of MTBE, was accounted for after the 10-min reaction period. Of the total recovered carbon, 41.0 ± 2.6% was carbon dioxide, 33.8 ± 1.2% was gaseous MTBE (due to sparging of the aqueous organic), 12.4 ± 1.3% was formaldehyde, 4.46 ± 0.45% was acetone, 5.62 ± 0.23% was aqueous MTBE and 2.75 ± 0.10% was *t*-butyl formate. In the second experiment, 101.8 ± 5.7% of the carbon, in the form of MTBE, was accounted for after the 11-min reaction period. Of the total recovered carbon, 47.0 ± 2.9% was carbon dioxide, 33.9 ± 1.2% was gaseous MTBE (due to sparging of the aqueous organic), 10.0 ± 1.0% was formaldehyde, 3.45 ± 0.35% was acetone, 4.11 ± 0.17% was aqueous MTBE and 1.55 ± 0.05% was *t*-butyl formate. Least-squares analysis was used to determine the error in the observed reactant and products mass. The reported errors represent a 96% confidence level.

The rate equation describing MTBE removal in the DMPR was found to be pseudo-first order with respect to the MTBE concentration. The removal rate constants for MTBE in the gas phase discharge configuration, coaxial configuration (1000 rpm), coaxial configuration (500 rpm) and original configuration were 0.47 s^{-1}, 0.27 s^{-1}, 0.22 s^{-1} and 0.18 s^{-1}, respectively. The experimental conditions and results for all three configurations are contained in Table 3.3.

Reproduced with permission of the copyright owner. Further reproduction prohibited without permission.

3.4 Discussion & Conclusion

The experiments conducted on the DMPR focused on identifying the oxidation mechanism(s) of MTBE and the kinetics associated with the removal of this compound for three reactor configurations and two upper electrode spin rates. The DMPR utilizes plasma as the medium in which electric energy is transferred into a fluid media to degrade organic compounds. Plasma is a highly ionized gaseous phase consisting of electrons, ions, gas phase atoms, molecules and molecular fragments in various energy states. A plasma is generated by producing an electrical discharge in an insulating fluid such as water, and may be classified as either a thermal (hot) or non-thermal (cold) plasma (Lieberman and Lichtenberg, 1994). A thermal plasma is comprised of gas atoms and electrons in local thermal equilibrium and is generally produced by high pressure (atmospheric) spark/arc discharges (Lieberman and Lichtenberg, 1994). Thermal plasma channels also emit a broad spectrum of radiation, including ultraviolet (UV) radiation, and generate a powerful shock wave due to expansion against the surrounding fluid (Sunka et al., 1999). The electrons produced from a thermal discharge have sufficient kinetic energy to completely dissociate any organic compound into its constituent atoms.

As discussed above, the plasma channel formed by a spark discharge is a high temperature radiation source with a wide emission spectrum. The temperature of the plasma stream can exceed 10,000 K (Sun et al., 1998), which is sufficient to decompose virtually any organic compound. As atoms leave the plasma, they combine to form thermodynamically favored species; carbon from the organic molecule will react with oxygen initially present in the aqueous solution or in the bubbled gas to form carbon dioxide. Based

Reproduced with permission of the copyright owner. Further reproduction prohibited without permission.

Table 3.3: Experimental conditions and results for the aqueous oxidation of MTBE in various DMPR configurations.

Experimental Conditions		**Experimental Results**	
Voltage	200 ± 25 V	**Original Configuration**	
Current	1.0 ± 0.15 A	Treatment Time	11 min
Sample Volume	250 mL	MTBE Reduction	86.6 ± 3.3%
Initial MTBE Concentration	50 ppm	**Coaxial Configuration**	
Liquid Recirculation Rate	100 mL/min	Treatment Time	10 min
Electrode Gap	500 μm	MTBE Reduction	94.2 ± 5.8%
Gas Flow Rate	400 sccm	**Gas Phase Configuration**	
Pin Array Spin Rate	1000 rpm	Treatment Time	10 min
		MTBE Reduction	100 ± 7.0%

Reproduced with permission of the copyright owner. Further reproduction prohibited without permission.

on the observation that a significant amount of carbon dioxide was produced and there was a concomitant absence of stable intermediate oxidation products, including carbon monoxide, it must be concluded that the bulk of the oxidation of MTBE occurs within the plasma channel of the DMPR. The above statement is also substantiated by the fact that MTBE attenuated by other AOT relying on active species such as hydroxyl radical are characterized by the formation of large quantities of *tert*-butyl formate, *tert*-butyl alcohol, acetone, and methyl acetate, resulting in low MTBE mineralization (Burbano et al., 2005; Xu et al., 2004; Graham et al., 2004; Burbano et al., 2002). This result is advantageous in that MTBE is directly oxidized to carbon dioxide through a less complicated, faster chemical mechanism. However, the mass of MTBE that can be oxidized is directly proportional to the volume of the plasma produced, making this route unfeasible in a single discharge reactor. However, the DMPR used in this study has 25 concurrent discharges, greatly increasing its potential to directly oxidize organic compounds within the plasma stream.

While direct oxidation within the plasma is an important degradation route, it has also been observed that MTBE undergoes oxidation within the liquid phase in the DMPR through reaction with reactive species. Hydroxyl radical and other unstable species form at the plasma/fluid interface (Roth, 1995). The plasma discharges are roughly cylindrical in shape and do not possess sufficient surface area to produce an appreciable amount of oxidizing radicals that can significantly reduce the concentration of an organic pollutant in a reasonable time. Diffusion and convective mass transfer can govern the rate for which an oxidizing radical produced on the surface of the arc and an organic molecule

Reproduced with permission of the copyright owner. Further reproduction prohibited without permission.

can interact outside the plasma stream. Since the radicals and the organics are constrained by the solvent molecules and remain trapped for approximately 10^{-11} s undergoing numerous collisions, and the activation energy for radical-radical and radical-molecule reactions is low, the chemical reactions are facile (Steinfeld et al., 1999). In a dilute organic solution, it is more probable for a radical to be trapped in the same solvent cage with another radical near the discharge site, initiating a quenching reaction. Thus, the quenching reaction rate is orders of magnitude higher than the transport rate of an organic from the solution bulk to the reaction zone or of a radical from the reaction zone to the solution bulk. Therefore, it is unlikely that an appreciable amount of radical-organic solvent cage interactions will occur. Oxidation resulting from the transport of organics to the radicals is possible, however, it would proceed slowly and the efficiency would decrease as the driving force decreased. However, due to the numerous discharges produced in the DMPR, the plasma/fluid interfacial area is greatly increased. Spinning the pin array also increases the rate of mass transport in the DMPR when compared to single point-to-plane discharge reactors by inducing convective mass transfer.

To determine whether direct oxidation of MTBE to CO_2, without appreciable formation of stable intermediate products, occurred only when MTBE was cycled through the reaction zone, the reactor was modified to the gas discharge configuration. In this configuration, the plasma discharge traveled only through the oxygen introduced into the reactor through the middle of the stationary electrode. This mode of operation eliminated any possible MTBE electron-impact dissociation reactions that may have been responsible for a significant portion of the degradation of MTBE and the subsequent formation of carbon

Reproduced with permission of the copyright owner. Further reproduction prohibited without permission.

dioxide. In this case, the MTBE oxidation process could only occur by reaction with active species. It was observed that, in this configuration, carbon dioxide was not produced and the only oxidation products detected during the 10-min treatment experiment were the result of the primary and secondary oxidation pathways. Because of this, it is concluded that the oxidation of MTBE to carbon dioxide only occurs, on the time scale of these experiments, as a result of cycling the contaminated liquid through the reaction zone.

3.4.1 Reaction Mechanism

Reactive oxidizing species formed by the electrical discharge, particularly hydroxyl radical, are responsible for the initiation of the aqueous oxidation of MTBE in the coaxial and original DMPR configurations. While this oxidation pathway has been shown to be of secondary importance in the coaxial configuration, small quantities of stable products form that, depending on the precursor, could potentially be toxic. The importance of such products led to a more detailed study of this oxidation pathway. After the abstraction of a hydrogen atom from MTBE by a reactive oxidizing species, it is oxidized by O_2 to form a peroxy radical. Two peroxy radicals may then combine, but due to instabilities, decompose into alkoxy radicals. Figure 3.2 and Figure 3.3 provide details concerning the widely accepted oxidation mechanism of aqueous MTBE (Vollhardt and Schore, 1994). It is the alkoxy radical that can undergo further decomposition, react with O_2 or isomerize. Isomerization in this system, however, is not likely due to the chemical structure of MTBE. Isomerization occurs predominantly by a 1-5 hydrogen abstraction mechanism, forming a six-member ring. However, MTBE only has the ability to form a five-member ring. The bond angle of the five-member ring invokes stress on the intermediate making

Reproduced with permission of the copyright owner. Further reproduction prohibited without permission.

the rearrangement unlikely. Thus, isomerization is not considered. During decomposition, the carbon adjacent to the radical oxygen atom breaks its bond with the neighboring atom. When the alkoxy radical reacts with O_2, an aldehyde and a hydroperoxy radical, $HO_2\cdot$, are formed.

The relative importance of the two mechanistic pathways—decomposition and reaction with O_2—for the MTBE alkoxy radical can be determined by examining the carbon product yields of the oxidation of MTBE. The alkoxy radical generated from the attack at site 1 reacts with O_2 to form *t*-butyl formate, or breaks the C–O bond to form formaldehyde and acetone, as illustrated in Figure 3.2. The alkoxy radical generated from the attack at site 2 reacts with O_2 to form 2-methoxy-2-methyl propionaldehyde (the latter of which was not observed in this study) or breaks the C–C bond to form formaldehyde, acetone and methyl acetate (which was also not observed), as shown in Figure 3.3. The decomposition products, formaldehyde and acetone, are the most abundant oxidation products in the first product study experiment, with carbon yields of 12.4 ± 1.3% and 4.46 ± 0.45%, respectively. The principal decomposition products of the second product study experiment, formaldehyde and acetone, are also the most abundant oxidation products, with carbon yields of 10.0 ± 1.0% and 3.45 ± 0.35%, respectively. *tert*-Butyl formate, formed via the O_2 reaction pathway, has relatively small carbon yields of 2.75 ± 0.10% and 1.55 ± 0.05% in the first and second product study experiments, respectively. Thus, hydrogen abstraction is more likely to occur at the methyl group adjacent to the oxygen at site 1, shown in Figure 3.2. This can be attributed to steric hindrance effects associated with the *tert*-butyl group; thereby severely restricting the ability of a reactive

Reproduced with permission of the copyright owner. Further reproduction prohibited without permission.

species to abstract a hydrogen from site 2, illustrated in Figure 3.3. As for the relative importance of the decomposition and reaction with O_2 pathways, experimental data suggests that decomposition dominates with insignificant amounts of 3-methoxy-2-methyl propionaldehyde and *tert*-butyl formate being formed with respect to acetone and formaldehyde. As mentioned previously, however, thermal decomposition coupled with electron bombardment is clearly the dominant oxidation mechanism, with carbon dioxide accounting for 41.0 ± 2.6% and 47.0 ± 2.9% of the reacted carbon in the first and second product study experiments, respectively. Figures 3.6 and 3.7 show the time evolution of the carbon balance for these experiments.

To further demonstrate the importance of the electron-impact dissociation mechanism, gas phase oxidation of MTBE in a DMPR was also investigated. A 1-L gaseous sample containing 457 ppm MTBE at 1 atm and 22°C, with oxygen as the diluent, was charged to a Tedlar® bag. The sample was recycled through the plasma zone at a rate of approximately 1 L/min during the experiment. It was found that the MTBE concentration was reduced by 68.5%, with 61.7% of the original MTBE oxidized to CO_2 within 10 min. The large percentage of the original pollutant molecule completely oxidized suggests that complete dissociation of MTBE in the plasma due to interactions with high-energy electrons is the dominate mechanism. If the electron-impact mechanism were negligible, oxidation initiated by ozone, which is produced in large quantities by a plasma discharge in an oxygen atmosphere, would dominate resulting in the formation of large quantities of primary oxidation products. A summary of the experimental conditions and the oxidation results are shown in Table 3.4.

Reproduced with permission of the copyright owner. Further reproduction prohibited without permission.

3.4.2 Removal Rate

The oxidation of organics in an aqueous plasma reactor is dependent on many factors and proceeds by a complex set of chemical reactions, as discussed above. The reaction rate for the destruction of an organic molecule in an aqueous, point-to-plane discharge reactor has been observed to be a function of the current, applied voltage, salinity, electrode spacing, composition of the solution, pH and the particular gas bubbled into the system (Goheen et al., 1992). The removal rate of MTBE in the DMPR is also assumed to be dependent on these parameters. However, since the plasma characteristics are a function of the above parameters and the removal rate is dependent on the plasma as well as inter-phase mass transfer, a general rate equation which depends on MTBE and active oxidizing species' concentrations as well as the flux of MTBE from the liquid to the gas phase can be written as

$$-\frac{dC_{MTBE}}{dt} = kC_{MTBE}^{m}C_{A}^{a}C_{B}^{b}\ldots C_{N}^{n} + \frac{V_G}{V_L}\left(\frac{dC_{MTBE}}{dt}\right)_G, \tag{3.4}$$

where k is the reaction rate constant; C denotes species concentration; A,B,...,N are active oxidizing species produced by the plasma discharge; V_L is the liquid volume; V_G is the gas volume; and $(dC_{MTBE}/dt)_G$ is the accumulation of MTBE in the gas phase. However, even though the voltage and current fluctuate during the experiments, the applied power is constant, and as a result the rate of the plasma discharge is approximately constant. Therefore, the concentrations of the active oxidizing species are constant and can be combined with the reaction rate constant to produce an observed reaction rate constant, k_{rxn}. The accumulation of MTBE in the gas phase can be expressed as

Reproduced with permission of the copyright owner. Further reproduction prohibited without permission.

$$\left(\frac{dC_{MTBE}}{dt}\right)_G = \frac{A_I}{V_G} W_{MTBE} = \frac{A_I}{V_G}\left\{-D_{MTBE_{mix}} \frac{\Delta C_{MTBE}}{\delta} + y_{MTBE}\left(W_{MTBE} + W_{H_2O}\right)\right\}, \quad (3.5)$$

where $D_{MTBE_{mix}}$ is the diffusivity of MTBE in the mixture, δ is the film thickness, W is the flux and y_{MTBE} is the mole fraction of MTBE. The first term in Eq. (3.5) represents the flux due to molecular diffusion produced by a concentration gradient and the second term is the flux due to bulk fluid flow. However, when the solute is dilute in the solvent and there is no net flux of solvent, the flux due to bulk fluid motion is negligible when compared to the flux due to molecular diffusion. Thus, after simplifying and substituting for the accumulation term in Eq. (3.4), and including k_{rxn}, the rate equation simplifies to

$$-\frac{dC_{\mathrm{MTBE}}}{dt} = C_{MTBE}\left(k_{rxn} C_{\mathrm{MTBE}}^{m-1} + \frac{A_I D_{MTBE_{mix}}}{V_L \delta}\right) = C_{MTBE}\left(k_{rxn} C_{\mathrm{MTBE}}^{m-1} + k_{mt}\right), \quad (3.6)$$

where k_{mt} is the overall mass transfer coefficient. The above equation assumes that k_{mt} is not a function of the MTBE concentration. This assumption is valid for low interphase mass transfer rates and is analyzed further in Chapter 4. To determine the overall order of the MTBE removal from the DMPR, finite difference methods are used to approximate the derivative of C_{MTBE} with respect to time from experimental data. The log of the negative derivative is plotted versus the log of C_{MTBE}, yielding a slope of 1.004 with an R^2 value of 0.994. Based on the results from the finite difference analysis, m is deduced to be unity and the differential equation is integrated; the result is

$$\log C_{\mathrm{MTBE}} = \log C_{\mathrm{MTBE}_0} - k_{\mathrm{obs}} t, \quad (3.7)$$

where $k_{obs} = k_{rxn} + k_{mt}$. The plot of $-\log(C_{\mathrm{MTBE}})$ versus t for the two product study experiments is linear, as shown in Figure 3.8. The agreement between Eq. (3.7) and the

Reproduced with permission of the copyright owner. Further reproduction prohibited without permission.

Table 3.4: Experimental conditions and results for the gas phase oxidation of MTBE in a DMPR.

Experimental Conditions		Experimental Results	
Voltage	50 ± 10 V	MTBE Reduction	68.5%
Current	1.0 ± 0.1 A	CO_2 Concentration	1410 ppm
Sample Volume	1.0 L		
MTBE Concentration	457 ppm	% MTBE Converted to CO_2	61.7%
Gas Recycle Rate	1.0 lpm		
Electrode Gap	500 μm	Total Recovered Carbon	93.2%
Treatment Time	10 min		

Reproduced with permission of the copyright owner. Further reproduction prohibited without permission.

data indicates that the rate equation is pseudo-first order with respect to the MTBE concentration. Further, the reaction rate constant (k) is directly proportional to k_{obs}. Data for the removal of MTBE in two additional reactor configurations and an additional spin rate are also plotted in Figure 3.8. Since only one variable has been varied in each of these experiments, the effect of reactor configuration and pin array spin rate can be compared. Thus, the relative dependence of the reaction rate constant on salinity, electrode spacing, composition of the solution, pH and gas bubbled into the system could be determined at the same energy conditions with additional experimental data.

While the rate constant for the gas discharge configuration is more than double that of both the coaxial configuration at 500 rpm and the original configuration, none of the original MTBE is converted to carbon dioxide. The coaxial reactor configuration has a rate constant higher than that seen for the original configuration for a pin array spin rate of 1000 rpm. This is due to the additional flux of liquid through the reaction zone. However, due to the relatively small amount of carbon introduced into the reactor, the nebulizer did not have a significant net effect on the removal of MTBE from the solution, as shown in Figure 3.9. A small increase (approximately 2% outside the measurement errors) was seen after the 11-min treatment time. The greatest difference in the percent of aqueous MTBE removed from the fluid was at the initial and intermediate stages of the experiments. However, if an aqueous solution with a significant carbon load was treated with the DMPR, the coaxial configuration would reduce the required treatment time due to the increase in oxidation efficiency seen at the beginning and intermediate stages of the MTBE experiments. The increased efficiency is believed to be a result of an increase

Reproduced with permission of the copyright owner. Further reproduction prohibited without permission.

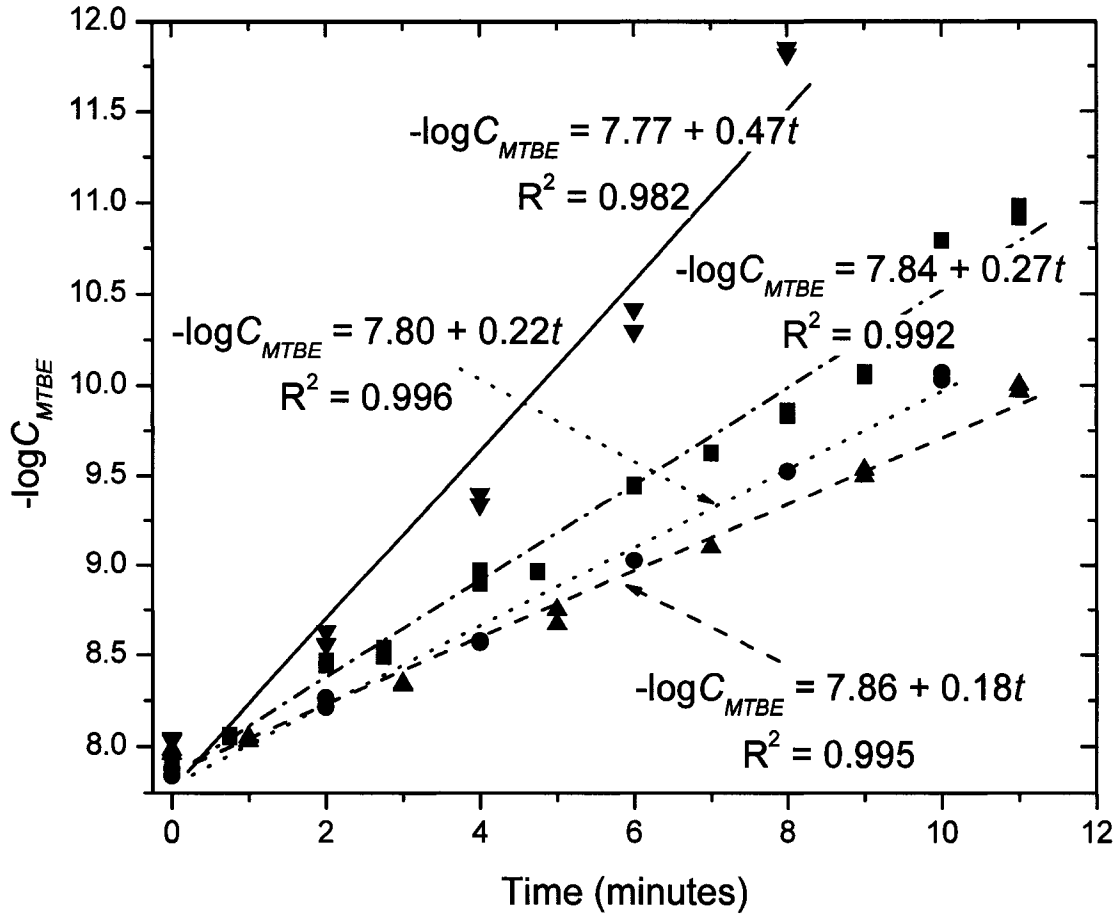

Figure 3.8: A plot of the -log(C_{MTBE}) versus time for the pseudo-first order rate equation of the oxidation of MTBE in the coaxial configuration with a pin array spin rate of 1000 rpm (■) and 500 rpm (●), the original configuration (▲), and the gas discharge configuration (▼).

Reproduced with permission of the copyright owner. Further reproduction prohibited without permission.

in the solvated oxygen concentration in the gap between the pin array and stationary electrode. It is also apparent that the nebulizer, in the coaxially configured DMPR, stabilizes the injection of oxygen; thereby eliminating channeling of the gas. The increased surface area also increases the rate of interphase mass transfer. Thus, a larger amount of MTBE is present in the gas phase before ionization by the electrical discharge, resulting in a reduction in the required treatment time.

Another benefit of the coaxial flow configuration when compared to the original configuration is the reduction of metal deposits on the alumina encapsulating the pin electrodes. When the DMPR is operated in the original configuration, metal sputtered from the pin electrodes deposits on the ceramic surface, shown in Figure 3.10 (a). However, when the DMPR is operated in the coaxial configuration, metal sputtered from the pin electrodes do not deposit on the ceramic surface, shown in Figure 3.10 (b). The scarring of the alumina in the original configuration is observed to decrease with increasing radial position. Thus, a greater amount of metal is deposited toward the center directly above the channel in which oxygen is introduced into the reactor. Therefore, a portion of the metal sputtered from the electrodes remains in the gas phase until contacting the alumina, essentially plating out as a metal film on the ceramic surface. By contrast, in the coaxial configuration, liquid and gas are both introduced into the reactor through the same channel. Thus, the metal sputtered from the electrodes is quenched by liquid before contacting the ceramic surface, resulting in the formation of particles.

Reproduced with permission of the copyright owner. Further reproduction prohibited without permission.

3.4.3 Removal Rate

Given the power input, the volume of solution and the removal of MTBE at a given time, the MTBE removal efficiency of the DMPR can be calculated for the various reactor configurations and spin rates. The removal efficiency (G) denotes the number of molecules removed or degraded with respect to a given amount of energy. The removal efficiency, which includes both chemical and physical attenuation mechanisms, is defined as

$$G_{x_t} = \frac{x_t C_o V_s}{tP}, \tag{3.8}$$

where x_t is the fraction of MTBE removed or degraded at time t, C_o is the initial MTBE concentration, V_s is the volume of the aqueous solution, t is the time and P is the input power. The removal efficiencies as a function of treatment time in the DMPR are shown in Table 3.5 for three reactor configurations and two pin array spin rates.

A common criterion used in the literature to compare the effectiveness of plasma oxidation technologies is the G_{50} factor. It signifies the efficiency of the process to reduce the initial contaminant molecule concentration by 50%. The G_{50} factor can be calculated using one of the following equations: (1) $G_{50} = 0.5 C_o V_s / (t_{50} E_p f)$, when pulsed power is used, and (2) $G_{50} = 0.5 C_o V_s / (t_{50} P)$, when constant power is applied. C_o is the initial concentration of the target molecule, V_s is the solution volume, t_{50} is the time required to reduce the initial target molecule concentration by 50%, E_p is the pulse energy, P is the applied power and f is the frequency. A comparison of the DMPR and other plasma oxidation technologies published in the literature using the G_{50} parameter is presented in Table 3.6. While the DMPR performed better, using the G_{50} comparison, than the other

Reproduced with permission of the copyright owner. Further reproduction prohibited without permission.

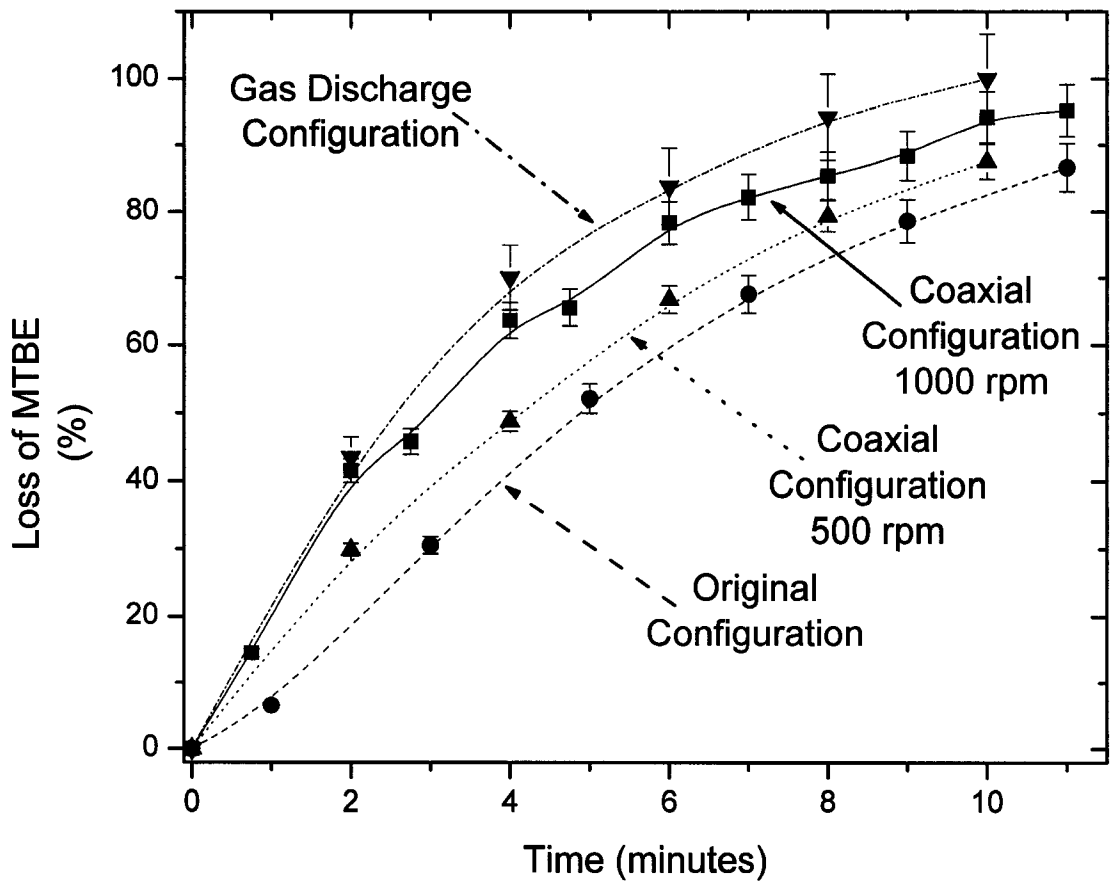

Figure 3.9: A plot of the percent loss of MTBE versus time in the DMPR comparing the performance of the coaxial configuration with a pin array spin rate of 1000 rpm (■) and 500 rpm (▲), the original configuration (●) and the gas discharge configuration (▼).

Reproduced with permission of the copyright owner. Further reproduction prohibited without permission.

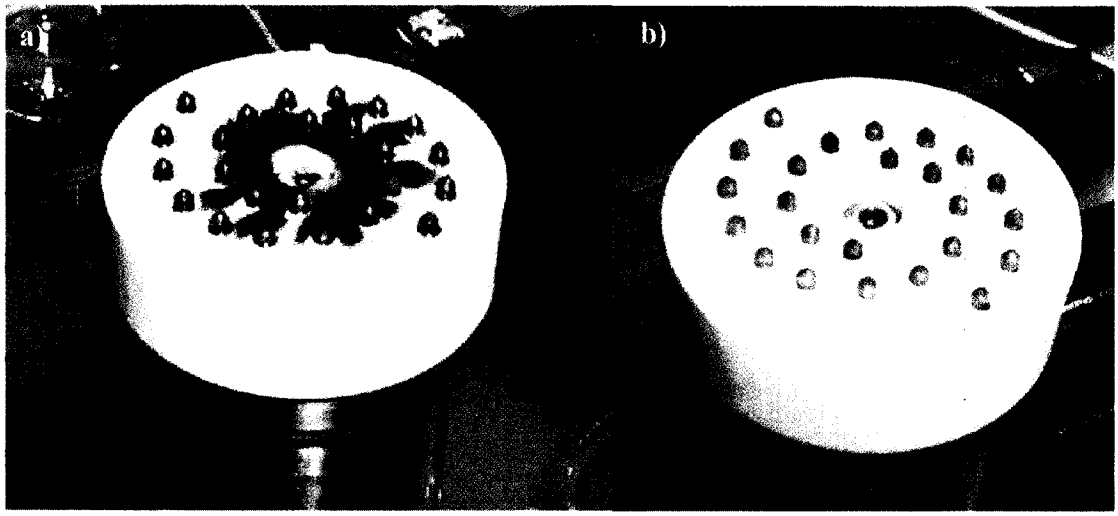

Figure 3.10: The DMPR pin array after aqueous oxidation experiments in the a) original configuration and b) coaxial configuration.

Reproduced with permission of the copyright owner. Further reproduction prohibited without permission.

listed aqueous discharge plasmas, it does not have a better G_{50} factor than the listed gaseous discharge reactors. This is consistent with the results of the gas phase discharge configuration of the DMPR having a G_{50} factor 4 to 5 times higher than the original and coaxial configurations. However, the G_{50} parameter does not take into consideration a decrease in the total organic carbon (TOC) concentration. This parameter is more important than the attenuation of the original target molecule when trying to determine whether a particular technology is a viable wastewater treatment process. Data on the reduction of the TOC concentration for various plasma reactor configurations is tabulated in Table 3.7.

Since TOC concentrations are not traditionally used to compare plasma oxidation technologies, the values are not readily available in the literature; hence the comparison of the DMPR to only one other reactor configuration with varying conditions. However, if comparisons to other gas phase discharge configurations discussed in the literature could be performed, the superior performance of the DMPR is expected to be similar to that seen in Table 3.7. This is based on the fact that when utilizing a gas phase discharge to attenuate a pollutant molecule, large amounts of primary and secondary oxidation products, along with low carbon dioxide yields are seen. This suggests attack of the primary contaminant molecule by reactive species formed by the discharge. This particular degradation process, as discussed previously, leads to the attenuation of the original molecule; however, the original carbon load remains relatively unchanged.

Reproduced with permission of the copyright owner. Further reproduction prohibited without permission.

These experiments have yielded a number of important insights into the mechanistic pathways and kinetics for the oxidation of organic compounds in the DMPR. Most aqueous plasma reactors oxidize organics via attack by reactive oxidizing species produced by the plasma discharge; however, the DMPR has the ability to directly oxidize organic compounds directly to CO_2. The attenuation of MTBE in the DMPR also occurs by reaction with active species, as in most aqueous plasma discharge reactors, as well as interphase mass transfer. Another important feature of the DMPR is that the removal kinetics can be modeled as pseudo-first order with respect to the original pollutant concentration. This is due to the fact that the oxidation of MTBE occurs within the volume of the arc, which remains relatively constant throughout the operating time of the reactor. It is also observed that the removal efficiency of the DMPR increases with an increase in spin rate, and is a function of the reactor configuration, as shown in Figures 3.8 and 3.9. With further design improvements and reactor optimization, the DMPR may become a competitive wastewater treatment technology.

Reproduced with permission of the copyright owner. Further reproduction prohibited without permission.

Table 3.5: The removal efficiency (G) of the DMPR in three reactor configurations for the attenuation of MTBE as a function of time. V_s = 250 mL, P = 200 W (liquid discharges), P = 50 W (gas phase discharges) and $C_o = 4.2\times10^{-4}$ M.

Gas Discharge Configuration			Coaxial Configuration (500 rpm)		
Time (min)	x_t (%)	$G \times 10^9$ (mol/J)	Time (min)	x_t (%)	$G \times 10^9$ (mol/J)
2	43.5	7.60	2	29.9	1.31
4	70.1	6.12	4	48.8	1.07
6	83.8	4.88	6	66.8	0.974
8	94.2	4.12	8	79.3	0.867
10	100	3.50	10	87.5	0.766
Coaxial Configuration (1000 rpm)			Original Configuration		
Time (min)	x_t (%)	$G \times 10^9$ (mol/J)	Time (min)	x_t (%)	$G \times 10^9$ (mol/J)
0.75	14.5	1.69	1	6.57	0.57
2	41.5	1.82	3	30.6	0.89
2.75	45.8	1.46	5	52.1	0.91
4	63.7	1.39	7	67.6	0.85
4.75	65.6	1.21	9	78.6	0.76
6	78.3	1.14	11	86.6	0.69
7	82.2	1.03			
8	85.4	0.934			
9	88.4	0.859			
10	94.2	0.824			
11	95.2	0.757			

Reproduced with permission of the copyright owner. Further reproduction prohibited without permission.

Table 3.6: A comparison of the efficiency of the DMPR, in three reactor configurations, to other plasma discharge technologies found in the literature using the G_{50} parameter. C_o is the initial target compound concentration, V_s is the solution volume, P is the power, E is the energy, f is the frequency and t_{50} is the time required to attenuate 50% of the target compound.

Discharge Description		$C_o \times 10^3$ (M)	V_s (L)	P (W)	E (mJ)	f (Hz)	t_{50} (min)	$G_{50} \times 10^9$ (mol/J)
DMPR[1]	coaxial (10^3 rpm)	0.42	0.25	200	n/a	n/a	3.0	1.46
	coaxial (500 rpm)	0.42	0.25	200	n/a	n/a	4.3	1.02
	original (10^3 rpm)	0.42	0.25	200	n/a	n/a	4.9	0.893
	O_2 gas (10^3 rpm)	0.42	0.25	50	n/a	n/a	2.9	6.04
Corona[2]	O_2 gas (MB)	0.019	0.10	0.20	n/a	n/a	60	1.32
	O_2 gas (MG)	0.016	0.10	0.20	n/a	n/a	60	1.11
Corona[3]	air atmosphere	0.01	0.10	n/a	25	100	6	0.556
Corona[4]	air atmosphere	1.0	0.10	n/a	5.8	100	75	18.0
	Ar atmosphere	1.0	0.10	n/a	10.6	100	90	17.5
Corona[5]	water	0.03	.55	n/a	1750	60	180	0.00728
Corona[6]	water	0.53	1.0	n/a	800	50	260	0.425
Corona[7]	water	0.53	0.25	n/a	880	48	7	3.74
Corona[8]	water	0.02	0.50	n/a	30	50	180	0.309

[1] this work; [2] (Goheen et al., 1992); [3] Hayashi et al., 2000); [4] (Hoeben et al., 1999); [5] (Joshi et al., 1995); [6] (Sunka et al., 1999); [7] (Sun et al., 1999); [8] (van Veldhuizen and Rutgers, 1995)

Reproduced with permission of the copyright owner. Further reproduction prohibited without permission.

Table 3.7: A comparison of the TOC concentration reduction of the DMPR and other non-thermal plasmas.

	Discharge Description	Potential (kV)	O_2 Flow Rate (mL/min)	Time (min)	TOC Removal (%)
Non-thermal[1]	H_2O	20	0	12	16.9
	H_2O	20	5.0	12	37.3
	H_2O	17.5	0	22	83.0
	H_2O	17.5	23	22	86.1
DMPR[2]	Coaxial (1000 rpm)	0.200	400	10	73.5
	Coaxial (1000 rpm)	0.200	400	11	79.6

[1] (Sun et al., 1999); [2] this work;

Reproduced with permission of the copyright owner. Further reproduction prohibited without permission.

3.5 References

Atkinson, R., Aschmann, S.M., Carter, W.P.L., Winer, A.M., Pitts, J.N., 1982. Alkyl Nitrate Formation From The Nox-Air Photooxidations Of C2-C8 N-Alkanes. J. Phys. Chem. 86, 4563-4569.

Burbano, A.A., Dionysiou, D.D., Richardson, T.L., Suidan, M.T., 2002. Degradation of MTBE intermediates using Fenton's reagent. J. Environ. Engin. 128, 799-805.

Burbano, A.A., Dionysiou, D.D., Suidan, M.T., Richardson, T.L., 2005. Oxidation kinetics and effect of pH on the degradation of MTBE with Fenton reagent. Water Res. 39, 107-118.

Buxton, G.V., Greenstock, C.L., Helman, W.P., Ross, A.B., 1988. CRITICAL-REVIEW OF RATE CONSTANTS FOR REACTIONS OF HYDRATED ELECTRONS, HYDROGEN-ATOMS AND HYDROXYL RADICALS (.OH/.O-) IN AQUEOUS-SOLUTION. J. Phys. Chem. Ref. Data 17, 513-886.

Davis, A.P., Huang, C.P., 1990. The Removal of Substituted Phenols by a Photocatalytic Oxidation Process with Cadmium-Sulfide. Water Res. 24, 543-550.

Denes, F.S., Young, R.A., 1996. Apparatus for reactions in dense-medium plasmas. U.S. Patent #5,534,232.

Reproduced with permission of the copyright owner. Further reproduction prohibited without permission.

DeSucre, V.S., Watkinson, A.P., 1981. Anodic-Oxidation of Phenol for Wastewater-Treatment. Can. J. Chem. Eng. 59, 52-59.

Glaze, W. H., Kang, J.W., Chapin, D.H., 1987. The Chemistry of Water-Treatment Processes Involving Ozone, Hydrogen-Peroxide and Ultraviolet-Radiation. Ozone-Sci. Eng. 9, 335-352.

Goheen, S.C., Durhlam, D.E., McCulloh, M., Heat, W.O., 1992. The Degradation of Organic Dyes by Corona Discharge. Proc. Second Int. Symp. Chem. Oxidation. Nashville, TN., 356-367.

Graham J.L., Striebich R., Patterson C.L., Krishnan E.R., Haught R.C., 2004. MTBE oxidation byproducts from the treatment of surface waters by ozonation and UV-ozonation. CHEMOSPHERE 54, 1011-1016.

Gurol, M.D., Vatistas, R., 1987. Oxidation of Phenolic-Compounds by Ozone and Ozone + UV- Radiation - a Comparative-Study. Water Res. 21, 895-900.

Hardison D.R., Cooper W.J., Mezyk S.P., Bartels D.M., 2002. The free radical chemistry of tert-butyl formate: rate constants for hydroxyl radical, hydrated electron and hydrogen atom reaction in aqueous solution. Rad. Phys. Chem. 65, 309-315.

Hayashi, D., Hoeben, W.F.L.M., Dooms, G., van Veldhuizen, E.M., Ruthers, W.R., Kroesen, G.M.W., 2000. LIF diagnostic for pulsed-corona-induced degradation of phenol in aqueous solution. J. Phy. D: Appl. Phy. 33, 1484-1486.

Reproduced with permission of the copyright owner. Further reproduction prohibited without permission.

Hoeben, W.F.L.M., van Veldhuizen, E.M., Rutgers, W.R., and Kroesen, G.M.W., 1999. Gas phase corona discharges for oxidation of phenol in an aqueous solution. J. Phys. D: Appl. Phys. 32, L133-L139.

Hoeben, W.F.L.M., van Veldhuizen, E.M., Rutgers, W.R., Cramers, C.A.M.G., Kroesen, G.M.W., 2000. The degradation of aqueous phenol solutions by pulsed positive corona discharges. Plasma Sources Sci. Technol. 9, 361-369.

Hoigne, J., Bader, H., 1976. Role of Hydroxyl Radical Reactions in Ozonation Processes in Aqueous-Solutions. Water Res. 10, 377-386.

Hoigne, J., Bader, H., 1979. Ozonation of Water - Selectivity and Rate of Oxidation of Solutes. Ozone- Sci. Eng. 1, 73-85.

Joglekar, H.S., Samant, S.D., Joshi, J.B., 1991. Kinetics of Wet Air Oxidation of Phenol and Substituted Phenols. Water Res. 25, 135-145.

Joshi, A.A., Locke, B.R., Arce, P., Finney, W.C., 1995. Formation of Hydroxyl Radicals, Hydrogen-Peroxide and Aqueous Electrons by Pulsed Streamer Corona Discharge in Aqueous-Solution. J. Hazard. Mater. 41, 3-30.

Legrini, O., Oliveros, E., Braun, A.M., 1993. Photochemical Processes for Water-Treatment. Chem. Rev. 93, 671-698.

Lieberman, M.A., Lichtenberg, A.J., 1994. Principles of plasma discharges and materials processing. John Wiley & Sons, New York, NY, USA.

Reproduced with permission of the copyright owner. Further reproduction prohibited without permission.

Manolache, S., Somers, E.B., Wong, A.C.L., Shamamian, V., Denes, F., 2001. Dense medium plasma environments: A new approach for the disinfection of water. Environ. Sci. Technol. 35, 3780-3785.

Mezyk S.P., Jones J., Cooper W.J., Tobien T., Nickelsen M.G., Adams J.W., O'Shea K.E., Bartels D.M., Wishart J.F., Tornatore P.M., Newman K.S., Gregoire K., Weidman D.J., 2004. Radiation chemistry of methyl tert-butyl ether in aqueous solution. Environ. Sci. Technol. 38, 3994-4001.

Nickelsen, M.G., Cooper, W.J., Kurucz, C. N., Waite, T.D., 1992. Removal of Benzene and Selected Alkyl-Substituted Benzenes from Aqueous-Solution Utilizing Continuous High-Energy Electron- Irradiation. Environ. Sci. Technol. 26, 144-152.

Petrier, C., Jiang, Y., Lamy, M.F., 1998. Ultrasound and environment: Sonochemical destruction of chloroaromatic derivatives. Environ. Sci. Technol. 32, 1316-1318.

Riddick, J.A., Bunger, W.B., Sakano, T.K., 1986. Organic solvents, physical properties and methods of purification 4th ed. Wiley, New York, NY, USA, 920-924.

Robinson, J.W., Ham, M., Balaster, A.N., 1973. Ultraviolet-Radiation from Electrical Discharges in Water. J. Appl. Phys. 44, 72-75.

Roth, J.R., 1995. Industrial Plasma Engineering Vol. 1: Principles. Institute of Physics Publishing, Philadelphia, PA, USA.

Reproduced with permission of the copyright owner. Further reproduction prohibited without permission.

Sato, M., Ohgiyama, T., Clements, J.S., 1996. Formation of chemical species and their effects on microorganisms using a pulsed high-voltage discharge in water. IEEE Trans. Ind. Appl. 32, 106-112.

Schuchmann, M.N., Schuchmann, H.P., Vonsonntag, C., 1995. Oxidation of Hydroxy-malonic Acid by OH Radicals in the Presence and in the Absence of Molecular Oxygen - A Pulsed-Radiolysis and Product Study. J. Phys. Chem. 99, 9122-9129.

Solomons, T.W.G., 1996. Organic Chemistry 6th ed. John Wiley & Sons Inc., New York, NY, USA.

Steinfeld, J.I., Francisco, J.S., Hase, W.L., 1999. Chemical Kinetics and Dynamics, 2nd ed. Prentice Hall, Upper Saddle River, NJ, USA.

Sterner, O., 1999. Chemistry, Health and Environment. Wiley-VCH, New York, NY, USA, 21-22.

Stucki, S., Kotz, R., Carcer, B., Suter, W., 1991. Electrochemical Waste-Water Treatment Using High Overvoltage Anodes .2. Anode Performance and Applications. J. Appl. Electrochem. 21, 99-104.

Sun, B., Sato, M., and Clements, J.S., 1997. Optical study of active species produced by a pulsed streamer corona discharge in water. J. Electros. 39, 189-202.

Sun, B., Sato, M., Harano, A., Clements, J.S., 1998. Non-uniform pulse discharge-induced radical production in distilled water. J. Electros. 43, 115-126.

Reproduced with permission of the copyright owner. Further reproduction prohibited without permission.

Sun, B., Sato, M., Clements, J.S., 1999. Use of a pulsed high-voltage discharge for removal of organic compounds in aqueous solution. J. Phy. D: Appl. Phy. 32, 1908-1915.

Sunka, P., Babicky, V., Clupek, M., Lukes, P., Simek, M., Schmidt, J., Cernak, M., 1999. Generation of chemically active species by electrical discharges in water. Plasma Sources Sci. Techno. 8, 258-265.

Thornton, T.D., Savage, P.E., 1990. Phenol Oxidation in Supercritical Water. J. Supercrit. Fluids 3, 240-248.

van Veldhuizen, E.M., Rutgers, W.R., 1995. Pulsed positive corona in water. 12th Int. Symp. Plasma Chem. Minneapolis, MN, 1083-1089.

Vollhardt, K.P.C., Schore, N.E., 1994. Organic Chemistry 2nd ed. W.H. Freeman and Company, New York, NY, USA, 889-890.

Willberg, D.M., Lang, P.S., Hochemer, R.H., Kratel, A., Hoffmann, M.R., 1996. Degradation of 4-chlorophenol, 3,4-dichloroaniline, and 2,4,6-trinitrotoluene in an electrohydraulic discharge reactor. Environ. Sci. Technol. 30, 2526-2534.

Xu X.R., Zhao Z.Y., Li X.Y., Gu J.D., 2004. Chemical oxidative degradation of methyl tert-butyl ether in aqueous solution by Fenton's reagent. CHEMOSPHERE 55, 73-79.

Reproduced with permission of the copyright owner. Further reproduction prohibited without permission.

Chapter Four

4.0 A Computation Fluid Dynamics Investigation of Fluid Flow and Prediction of Reaction Kinetics in a DMPR

Computational fluid dynamics is applied to the study of 3D fluid flow in a dense medium plasma reactor (DMPR) under different operating conditions. Reaction mechanisms and rates for the removal of methyl *t*-butyl ether (MTBE) in a DMPR are developed from experimental data to determine the plasma volume, the rate of interphase mass transfer and the photolysis rate of MTBE via UV emission from the plasma. The simulations show that, in the DMPR, the volume of fluid in contact with the plasma only constitutes a maximum of approximately 10% of the fluid passing through the recirculation channels. This value does vary slightly with operating conditions. The simulations also predict large pressure gradients on the pin electrode tips, resulting in a small discharge area located away from the region in which the radius of curvature is minimized. This result has been confirmed experimentally in the fact that it is observed that the pin electrodes sputter metal from an area of similar size and location to the low-pressure region predicted by the simulations. The chemical kinetics developed in this study are incorporated into the simulation to model the attenuation of MTBE in the DMPR. Fluid volumes are assigned the appropriate reaction mechanism and corresponding reaction rates. The simulation results accurately capture the experimental observations in that the MTBE concentration

Reproduced with permission of the copyright owner. Further reproduction prohibited without permission.

is reduced to approximately 5% of its original value in 11 min. Although only a small fraction of the fluid interacts with the plasma, oxidation due to the plasma is shown to be the major loss mechanism.

4.1 Introduction

An increased awareness of the adverse effects of biological and chemical contamination on human health and the environment has motivated research in pollution prevention and remediation. This has prompted investigations into the disinfection of contaminated water and the removal of organic carbon by thermal and non-thermal plasmas. Plasma treatment is an appealing method due to its ability to disinfect aqueous solutions and oxidize organic compounds simultaneously. The process is characterized by the production of high oxidation potential species and a wide spectral emission. The UV radiation and oxidation species produced by the plasma discharge are effective in deactivating microbial species as well as initiating oxidation reactions. Due to these characteristics, plasma treatment is considered to be a promising alternative to current biological water treatment methods and disinfection processes such as chlorination, ozonation and UV lamps.

4.1.1 Dense Medium Plasma Reactor

The DMPR includes a reaction vessel containing a rotating array of pin electrodes, stationary lower electrode, cooling system, and gas introduction and discharge ports. The reactor was developed to react liquid/vapor phase chemicals in an induced plasma state, using low temperature plasma chemistry in which the liquid temperature remains relatively close to ambient temperatures. A detailed schematic of the reactor developed by Denes and coworkers can be found in Manolache et al. (2001; 2004) and Johnson et al.

Reproduced with permission of the copyright owner. Further reproduction prohibited without permission.

(2003). Descriptions of the original and modified reactor used in the following analysis are also contained in Chapters 2 and 3 with a complete illustration of both the original and coaxial configurations in Figure 3.1.

The DMPR has been investigated as a tool for the disinfection of microbial contaminated water. Experiments conducted by Manolache et al. (2001) focused on quantifying the inactivation of specific bacteria and the mechanisms produced by the DMPR responsible for the disinfection. The oxidation of methyl *tert*-butyl ether (MTBE) and subsequent formation of oxidation products in a DMPR have also been explored (Johnson et al., 2003). The experiments were designed to study MTBE oxidation mechanisms and examine possible operating conditions for promoting the formation of carbon dioxide. The DMPR has also been used to oxidize aqueous benzene, toluene, ethylbenzene, *m*- and *p*-xylene, and *o*-xylene (Manolache et al., 2004). The experiments again demonstrated the ability of the reactor to attenuate contaminant levels below drinking water standards on the order of minutes for small solution volumes.

While the oxidation experiments performed in the DMPR were promising, deviations from the original hypothesis of reaction kinetics dominated by oxidation initiated by reactive species such as hydroxyl radical resulted in additional questions concerning the reaction and plasma discharge mechanisms. The experiments performed by Johnson et al. (2003) demonstrated that if the original contaminant molecule has a vapor pressure such that it can be promoted to the gas phase, and thus enveloped by the plasma, significant quantities of the inputted carbon is completely oxidized to carbon dioxide in the DMPR.

Reproduced with permission of the copyright owner. Further reproduction prohibited without permission.

As a result of the complete oxidation of vapor phase organics to carbon dioxide in the plasma stream, convective and diffusion mechanisms are employed in the DMPR to promote the transport of the contaminate species from the bulk solution to the plasma. To induce convective transport of a pollutant molecule from the bulk fluid to the plasma, the pin array is spun at rates greater than 500 rpm; thereby initiating convective mass transfer and turbulent mixing effects. However, the volume of contaminated liquid that is transformed to a plasma can not be determined experimentally, and thus the efficiency of the reactor regarding the recirculation of the bulk liquid to the plasma is not known. It is also observed experimentally that the plasma discharge is initiated on a specific region of the pin electrode surface that does not correspond to the point for which the radius of curvature is minimized. This result is unexpected due to the fact that a lower radius of curvature in a point-to-plane electrode configuration yields a higher electric field strength, and thus should be the surface position for which the plasma discharge is initiated. However, the discharges occur along the backside of the pin electrode. While the observations invoke additional questions concerning the velocity field, fluid properties and chemical kinetics, the design of the DMPR and the nature of the treatment process make it impossible to further investigate the deviations from the original hypothesis experimentally. Therefore, CFD simulations are employed.

Computational fluid dynamics simulations are uniquely qualified to provide qualitative and quantitative information, which cannot be readily obtained experimentally, regarding the interaction of the liquid in the DMPR with the plasma and the characterization of the fluid in the vicinity of the plasma. The simulations are utilized to answer the questions,

Reproduced with permission of the copyright owner. Further reproduction prohibited without permission.

which are motivated by experimental results, enumerated below:

1.) What is the volumetric flow rate of the liquid through the plasma as a function of pin array spin rate and reactor configuration?

2.) Does spinning the pin array induce a pressure gradient along the surface of the pin electrodes, thus focusing the location of the discharge to a distinct region on the pin electrode surface where the radius of curvature is not minimized?

3.) Is the rate of reaction, while holding all other operating conditions constant, a function of the liquid volumetric flow rate through the plasma?

Before the CFD simulations can be performed, the plasma volume and kinetic rate constants associated with the different attenuation mechanisms must be determined. While both the experiments performed by Johnson et al. (2003) and Manolache et al. (2004) yielded data that can be fitted using a pseudo first-order rate equation, shown in Figure 4.1, the fit is empirical and does not mathematically incorporate the individual loss processes. Thus, a more detailed analysis of the kinetic data and possible removal mechanisms are required to determine the parameters necessary to perform the CFD simulations.

4.2 Kinetic Analysis

Four rate processes must be considered when performing a mass balance on a chemical species in the DMPR—accumulation, convective mass transfer, diffusion, and sources and/or sinks due to physical and chemical mechanisms. The dimensional form of the species conservation equation is

Reproduced with permission of the copyright owner. Further reproduction prohibited without permission.

$$\frac{\partial C_i}{\partial t} + \underline{v} \cdot \nabla C_i = D_{i_{mix}} \nabla^2 C_i + r_i , \tag{4.1}$$

where $\underline{v}$ is the local velocity vector, $D_{i_{mix}}$ is the diffusion coefficient for species i in the mixture and r_i is the net production rate of species i (which in this case is negative) by a series of attenuation mechanisms. The DMPR is operated in a batch configuration, requiring mass not be removed from the system by convective or diffusion mechanisms. There are also virtually no axial, angular or radial concentration gradients because of the turbulent mixing produced by spinning the pin array at such high rates. The species conservation equation thus reduces to the following ideal batch reactor design equation:

$$\frac{\partial C_i}{\partial t} = r_i . \tag{4.2}$$

The sources and sinks of species i in the DMPR can be described as both physical and chemical in origin. The chemical mechanisms can be further broken down into localized and extended effects depending on the region over which the reactions take place (Willberg et al., 1996b). Local effects are defined as the effects that occur in the immediate vicinity of the plasma. These effects include oxidation in the plasma core due to interactions with energetic electrons, as well as reactions with radicals and other highly reactive species in the aureole. The aureole is defined as a region of hot gas which boarders the plasma core where plasma chemistry can occur, but is not in thermal equilibrium with the plasma (Roth, 1995). Radicals and other highly reactive species are formed in the aureoles generated in the DMPR by photolysis and dissociation of water molecules. Photolysis occurs from vacuum ultraviolet (VUV) radiation produced by the plasma discharge and the dissociation reactions are caused by the impact of electrons that are accelerated

Reproduced with permission of the copyright owner. Further reproduction prohibited without permission.

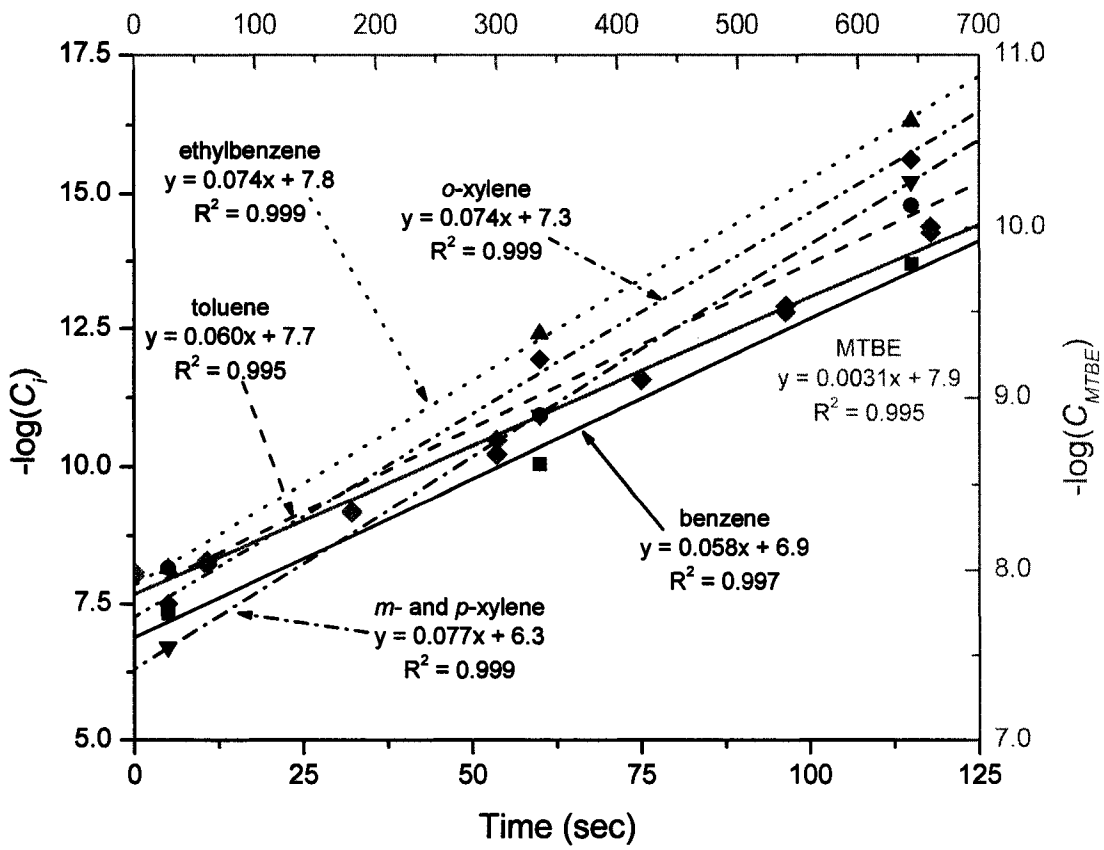

Figure 4.1: Plots of the –log (C_i) versus time for MTBE, benzene, ethylbenzene, toluene, *m*- and *p*-xylene, and *o*-xylene in an originally configured DMPR as well as the first-order fits to the experimental data.

Reproduced with permission of the copyright owner. Further reproduction prohibited without permission.

into the plasma-water interface by the strong electric field produced in the reactor. These processes complement one another to degrade a variety of organic contaminants and are also effective for sterilization.

The extended effects of the plasma discharge in the DMPR are those that occur outside the plasma channel, and are principally due to the UV radiation propagating into the bulk solution (Sun et al., 2000). The UV radiation that propagates through the bulk solution can cause the photo-initiated oxidation of species *i*. As for the physical mechanisms, if species *i* is volatile, interphase mass transfer can be an important removal process and needs to be considered. If only interphase mass transfer is considered, the rate at which species *i* is removed from the DMPR can be expressed as

$$(r_i)_{mt} = -\left(\frac{A_I \mathcal{D}_{i_{mix}}}{V_L \delta}\right) C_i = k_{mt} C_i, \tag{4.3}$$

where A_I is the interfacial area, V_L is the volume of the liquid, $\mathcal{D}_{i_{mix}}$ is the diffusion coefficient for species *i* in the mixture, and δ is the film thickness (Johnson et al., 2003). Eq. (4.3) assumes that the mass transfer rate is low and thus the overall mass transfer rate coefficient (k_{mt}) is not a function of C_i. To validate the assumption, finite difference methods are used to approximate the derivative of C_{MTBE} with respect to time from interphase mass transfer control experiment data. The log of the negative derivative is plotted versus the log of C_{MTBE} to determine the order of the rate of interphase mass transfer. The finite difference analysis yields a slope of 2.05 with an R^2 value of 0.87. Thus, the k_{mt} needs to be corrected for the dependence of the coefficient on the transfer of mass across the interface (Bird et al., 1960). To account for the dependence, both linear and quadratic

Reproduced with permission of the copyright owner. Further reproduction prohibited without permission.

terms are proposed in the mass transfer rate while the higher order terms in the series are truncated. This is consistent with the Burnett equations that result from expressing molecular fluxes in terms of the first and second spatial derivatives of species molar density and the square of the first spatial derivative of species molar density (Hirschfelder et al., 1954). Performing non-linear least squares analysis on the expression containing first and second-order terms yields a linear coefficient that is 5 orders of magnitude smaller than the quadratic coefficient, and results in a R^2 value significantly lower than the R^2 value obtained from the expression that only considers the quadratic term. Based on the above analysis, it is therefore concluded that the overall mass transfer coefficient in Eq. (4.3) is linearly dependent on the molar density of MTBE. To remove the dependence, the interphase mass transfer rate is deduced to be second order, resulting in the following functional form for the rate of interphase mass transfer in the DMPR when employing operating conditions utilized by Johnson et al. (2003).

$$(r_i)_{mt} = -k_{mt} C_i^2 \tag{4.4}$$

Thus, the concentration of species *i* in the DMPR when oxygen is introduced into the system without initiating a plasma discharge at any point in the fluid can be determined by solving Eq. (4.4) and is

$$\frac{C_{i_o}}{C_i} = 1 + C_{i_o} k_{mt}\, t\,. \tag{4.5}$$

Data for the sparging of MTBE in both an originally and coaxially configured DMPR are presented in Figure 4.2. The plot illustrates the second-order loss of MTBE due to interphase mass transfer as a function of time. The rate of mass transfer in the coaxial

Reproduced with permission of the copyright owner. Further reproduction prohibited without permission.

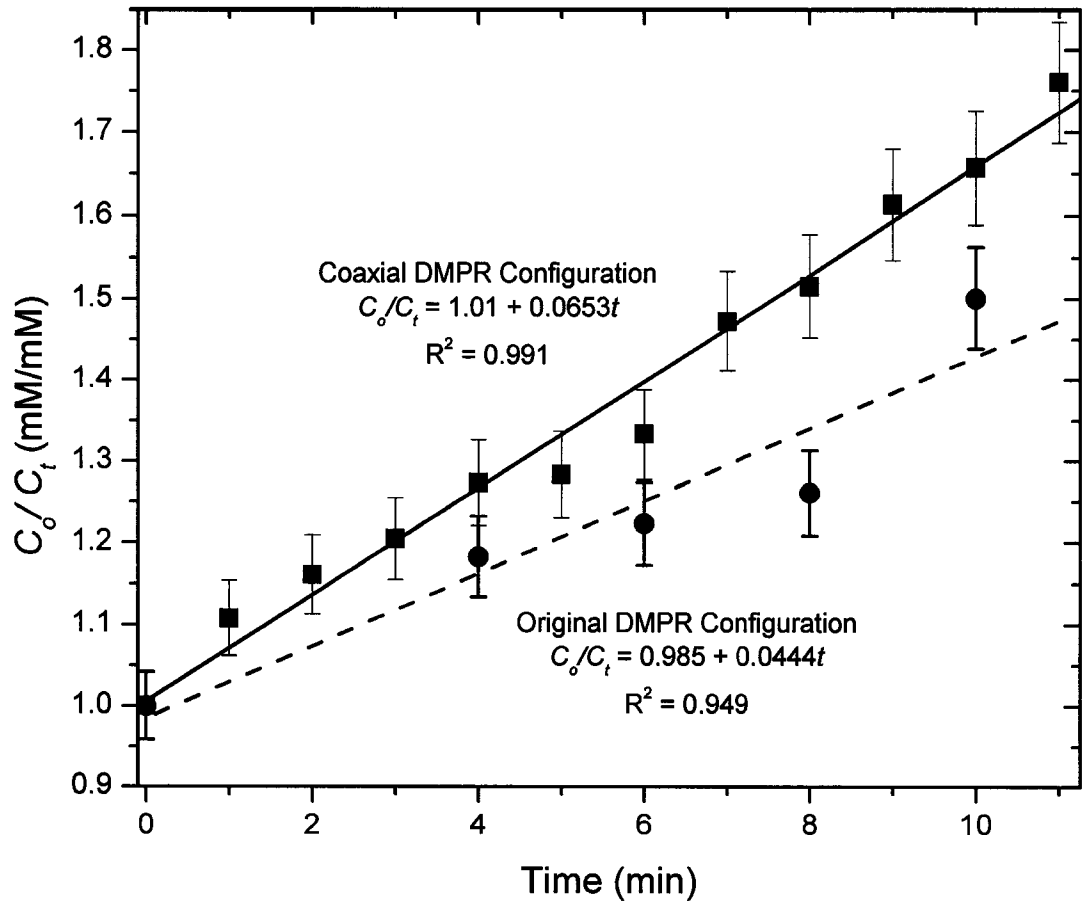

Figure 4.2: A plot of the inverse normalized MTBE concentration as a function of time for an originally and coaxially configured DMPR. The slope of the linear fits can be used to calculate the second-order interphase mass transfer rate coefficient, k_{mt}.

Reproduced with permission of the copyright owner. Further reproduction prohibited without permission.

configuration is approximately 50% greater than the rate associated with the original configuration. This can be attributed to the installation of a nebulizer. While the volume of the gas inputted into the system remains constant, the nebulizer produces bubbles with a smaller diameter, therefore increasing the interfacial area. While the removal of a species by sparging can be an important process in the DMPR, removal mechanisms due to localized and extended effects of the plasma discharge also contribute to the attenuation of the original contaminant molecule.

When evaluating the chemical removal mechanisms due to extended effects, direct photolysis should be considered. The relation of the time dependence on the concentration of species *i* due to oxidation initiated by direct photolysis is

$$(r_i)_{DP} = -\phi(\lambda) I_o(\lambda,t)\{1-\exp(-2.303\varepsilon\, l\, C_i\}, \tag{4.6}$$

where $\phi(\lambda)$ is the photolysis quantum yield, $I_o(\lambda,t)$ is the UV intensity, ε is the extinction coefficient and l is the path length (Willberg et al, 1996a). However, the DMPR produces a continuous plasma discharge which emits a broad radiation spectrum, therefore removing the time and wavelength dependence from the expression. Also, in an aqueous solution, the extinction coefficient is sufficiently large that the exponential term becomes negligible. Thus, the rate of change of the concentration of species *i* in the DMPR due to direct photolysis can be written as

$$(r_i)_{DP} = -\phi\, I_o = -k_{DP}, \tag{4.7}$$

Reproduced with permission of the copyright owner. Further reproduction prohibited without permission.

where k_{DP} is a zero-order rate constant associated with direct photolysis. Lastly, the attenuation of species *i* due to the plasma must be explored to completely describe the removal mechanisms associated with the DMPR.

An organic specie solvated in the fluid that is transferred into the plasma will either undergo electron-impact dissociation reactions or oxidation initiated by hydrogen abstraction reactions with oxidizing species produced by the discharge. If the solution is well mixed, as in the DMPR, the measured concentration of the pollutant molecule for a pulsed discharge reactor after one discharge has been shown to be

$$C_i = \left(\frac{V_T + V_p}{V_T} \right) C_{i_o}, \tag{4.8}$$

where V_T and V_p are the volumes of the solution and plasma, respectively (Willberg et al., 1996a). The expression can be extended to N total discharges, yielding the following result:

$$C_{i_N} = \left(\frac{V_T + V_p}{V_T} \right) C_{i_{N-1}}. \tag{4.9}$$

While the DMPR has an intrinsic time constant (α) associated with the duration of the plasma, the discharge is considered to be continuous due to the fact that the time between discharges is negligible with respect to the lifetime of the plasma. To account for this, an extension of Eq. (4.9) is used to describe the concentration of species *i* as a function of time. Thus at *n* discharges into treatment, the concentration of the original contaminant molecule at any point in the reactor can be expressed as

Reproduced with permission of the copyright owner. Further reproduction prohibited without permission.

$$C_{i_{n\alpha}} = \left(\frac{V_T + V_p}{V_T}\right) C_{i_{(n-1)\alpha}} = \left(\frac{V_T + V_p}{V_T}\right)^n C_o, \tag{4.10}$$

where n is the number of arc events in the DMPR, and α is a time constant associated with the reactor and is equal to 1 ms. Realizing that the total treatment time is equal to the number of arc events multiplied by the time constant ($t = n\alpha$), and taking the derivative of the species concentration with respect to time yields the time dependence of the species concentration as a result of losses associated with the plasma (Eq. (4.11)).

$$(r_i)_{plasma} = C_{i_o} \frac{\ln(1 - V_p/V_T)}{\alpha} \exp\left(\frac{\ln(1 - V_p/V_T)}{\alpha} t\right) \tag{4.11}$$

Combining Eqs. (4.4, 4.7, and 4.11) yields the following species conservation equation applicable to the DMPR:

$$\frac{dC_i}{dt} = -k_{mt} C_i^2 + C_{i_o} \frac{\ln(1 - V_p/V_T)}{\alpha} \exp\left(\frac{\ln(1 - V_p/V_T)}{\alpha} t\right) - k_{DP}. \tag{4.12}$$

Nonlinear least squares analysis and experimental data from Johnson et al. (2003) are utilized in conjunction with MATLAB® optimization routines to determine V_p and k_{DP} in order to conduct the CFD simulations.

4.3 Species Balance Optimization

Non-linear least squares analysis is performed to obtain initial guesses for the plasma volume and zero-order rate constant associated with degradation due to photochemical processes. The accumulation and second-order loss terms in Eq. (4.12) are calculated from experimental data and then grouped together to facilitate the convergence of the

Reproduced with permission of the copyright owner. Further reproduction prohibited without permission.

analysis routine yielding

$$y = \frac{dC_i}{dt} + k_{mt} C_i^2 = C_{i_o} \frac{\ln a}{\alpha} \exp\left(\frac{\ln a}{\alpha} t\right) - k_{DP}, \tag{4.13}$$

where $a = (1 - V_p / V_T)$. An error function (Eq. (4.14)) is then generated which must be minimized while the partial derivatives of the error function with respect to k_{DP} (Eq. (4.15)) and a (Eq. (4.16)) are forced to zero.

$$E_{\min} = \sum_{i=1}^{N} \left(\frac{\ln a}{\alpha} \exp\left(\frac{\ln a}{\alpha} t_i\right) C_o - k_{DP} - y_i \right)^2 \tag{4.14}$$

$$\frac{\partial E}{\partial k_{DP}} = \sum_{i=1}^{N} \left(\frac{\ln a}{\alpha} \exp\left(\frac{\ln a}{\alpha} t_i\right) C_o - k_{DP} - y_i \right) = 0 \tag{4.15}$$

$$\frac{\partial E}{\partial a} = \sum_{i=1}^{N} \left\{ \left(\frac{\ln a}{\alpha} \exp\left(\frac{\ln a}{\alpha} t_i\right) C_o - k_{DP} - y_i \right) \times \left(\frac{C_o}{a\alpha} \exp\left(\frac{\ln a}{\alpha} t_i\right) \right) \times \left(1 + \left(\frac{\ln a}{\alpha} t_i \right) \right) \right\} = 0 \tag{4.16}$$

The values estimated for a and k_{DP} are then incorporated into MATLAB® optimization routines.

Eq. (4.12) and the experimental data collected by Johnson et al. (2003) are analyzed further utilizing MATLAB® to incorporate additional constraints and information related to the behavior of the loss processes in the DMPR. First, the solution is required to asymptote to zero at long treatment times. Second, k_{mt}, which is calculated from experimental data (see Figure 4.2), is allowed to decrease in the optimization routine; thereby giving the model the flexibility to account for the fact that interphase mass transfer is driven by the magnitude of the concentration gradient across the gas-liquid interface. Data col-

Reproduced with permission of the copyright owner. Further reproduction prohibited without permission.

lected from the interphase mass transfer control experiments only account for losses in the liquid phase due to the volatility of MTBE. However, when depletion of the contaminant molecule in the liquid phase is also occurring due to due to photochemical and plasma loss mechanisms, the attenuation of the molecule is occurring at a much fast rate resulting in a significant decrease in the driving force. Thus, the interphase mass transfer control experiments represent the maximum rate at which the volatile species can be removed by this mechanism, and is therefore used as an initial guess and upper boundary for the additional optimization analysis.

The combination of non-linear least squares analysis and MATLAB® optimization techniques yield the zero-order rate constant associated with direct photolysis, the second-order interphase mass transfer rate coefficient and the plasma volume. Predicted concentration profiles for the loss of each species due to interphase mass transfer and the plasma as well as the non-linear least squares fit to experimental data from Johnson et al. (2003) for the combination of the two processes are plotted in Figure 4.3. As shown in Figure 4.3, attenuation of MTBE due to the plasma is the major loss process although only approximately 10 μL of the 250 mL of aqueous liquid is predicted to be promoted to the plasma state. Due to the decrease in the driving force for interphase mass transfer, sparging is predicted to play a minimal role in the removal process with a rate constant of 0.01 $mM^{-1}min^{-1}$, which is approximately an order of magnitude lower than calculated from the control experiments. With respect to direct photolysis, the rate of change of the MTBE concentration is not affected by this loss mechanism. This result is not surprising due to the fact that photochemical processes are negligible in solutions with a low

Reproduced with permission of the copyright owner. Further reproduction prohibited without permission.

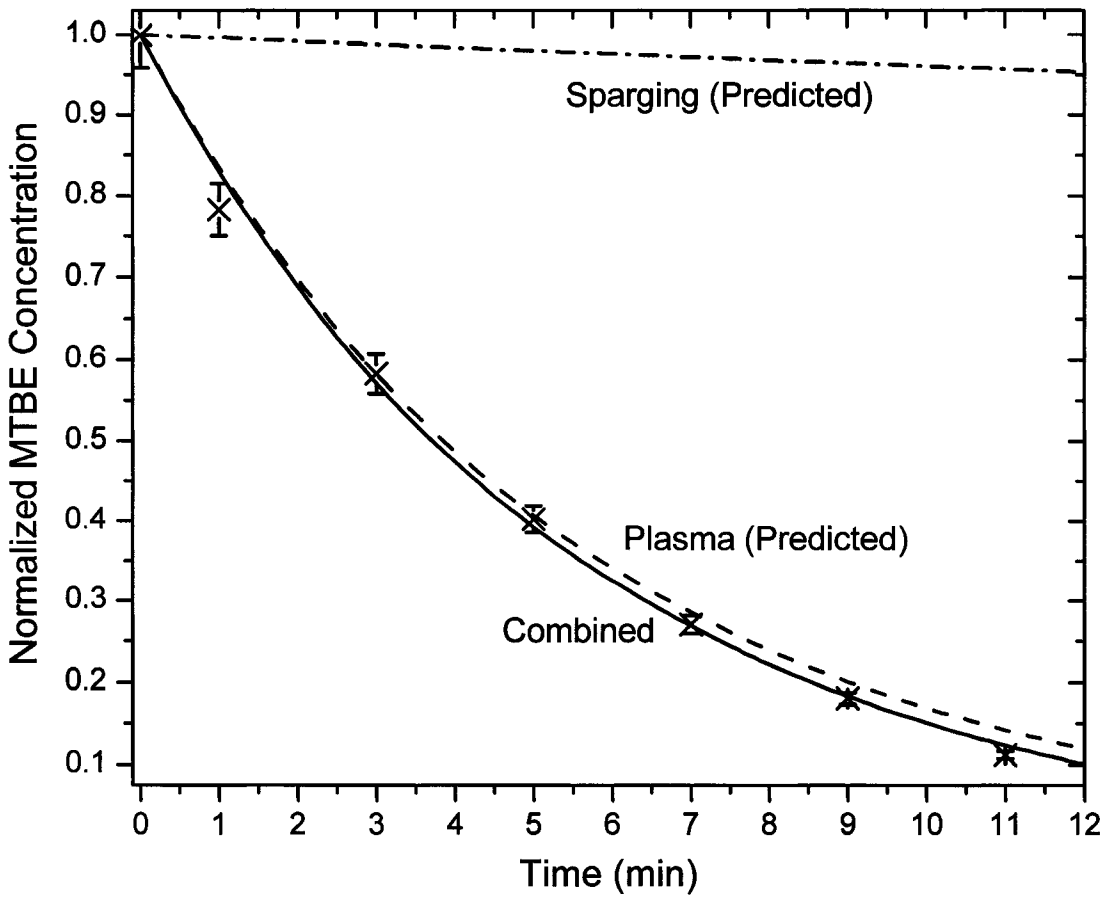

Figure 4.3: Plots of the normalized MTBE concentration as a function of time due to losses associated with interphase mass transfer, the plasma and a combination of the loss processes as well as experimental data collected from Johnson et al. (2003).

Reproduced with permission of the copyright owner. Further reproduction prohibited without permission.

conductivity. The experiments performed utilizing the DMPR solvated MTBE in Millipore water that was generated by a Milli-Q ultrapure water system, resulting in solvent conductivities on the order of 10 μS/cm. Also, the discharge in the DMPR is generated in a location where a significant portion, approximately 85%, of the bulk solution is shielded from the radiation emitted from the discharge. The information gathered from the above analysis is incorporated into the CFD simulations in an effort to provide qualitative and quantitative results regarding the fluid flow and reaction kinetics in the DMPR.

4.4 3D CFD Simulations

FLUENT®, a commercially available CFD software package, is used to model flow characteristics, fluid properties and reaction kinetics for both the original and coaxially configured DMPR. The motivation behind modeling the two configurations, shown in Figure 3.1, is to provide insight into the dependence of the reaction kinetics on the volumetric flow rate of bulk liquid through the plasma under simulated experimental conditions reported by Johnson et al. (2003). The original configuration model simulates fluid flow in the DMPR due to the rotation of the pin array. The central channel in the stationary electrode is not utilized in this model and thus the bulk fluid is only cycled through the electrode gap due to centrifugal forces created by the rotation of the array. The coaxial configuration model simulates fluid flow in the DMPR due to the rotation of the pin array and bulk liquid pumped through the central cylinder into the region between the pin array and stationary electrode. The primary objectives of these models are to quantify the mass fluxes and the volumetric flow rates through important regions of the reactor and predict flow characteristics and fluid properties in the vicinity of the plasma as a function of the

Reproduced with permission of the copyright owner. Further reproduction prohibited without permission.

pin array spin rate and reactor configuration.

Flow characteristics, fluid properties and reaction kinetics are predicted by constructing CFD grids of the DMPR and solving the governing equations at each node. The simulations modeled an incompressible fluid with a constant viscosity for both laminar and turbulent flow conditions utilizing the continuity and Navier-Stokes equations,

$$\nabla \vec{v} = 0 \tag{4.17}$$

$$\rho\left(\frac{\partial \vec{v}}{\partial t} + \nabla(\vec{v}\vec{v})\right) = -\nabla p + \mu \nabla^2 \vec{v} + \rho \vec{g}, \tag{4.18}$$

where ρ is the fluid density, $\vec{v}$ is the velocity vector, t is time, p is the pressure, μ is the dynamic viscosity of the fluid and $\vec{g}$ is gravity. The meshes generated for the CFD simulations, shown in Figure 4.4, are structured and contain approximately 1.1×10^6 nodes encompassed in 318 and 319 grid zones for the original and coaxial configurations, respectively. The large number of zones is necessary in order to generate a structured mesh, which reduces the impact associated with round off errors, thereby facilitating the convergence of the simulations. Structured meshes also have the added benefit of reducing the time necessary to reach a solution. The node density is such that the converged solutions are independent of the grid. A node density gradient is applied to the meshes, requiring a higher density near the walls to ensure the flow behavior is accurately described. The convergence criteria for the steady state simulations are such that the residuals in the continuity, momentum and energy equations must fall below a value of 10^{-4}. Water is used as the fluid, with an initial temperature of 300 K. The reactor pressure is constant at 101.3 kPa. Adiabatic, no-slip boundary conditions are applied at all solid surfaces. For pin array spin rates of 500 rpm or less, the laminar viscous solver is employed.

Reproduced with permission of the copyright owner. Further reproduction prohibited without permission.

Reproduced with permission of the copyright owner. Further reproduction prohibited without permission.

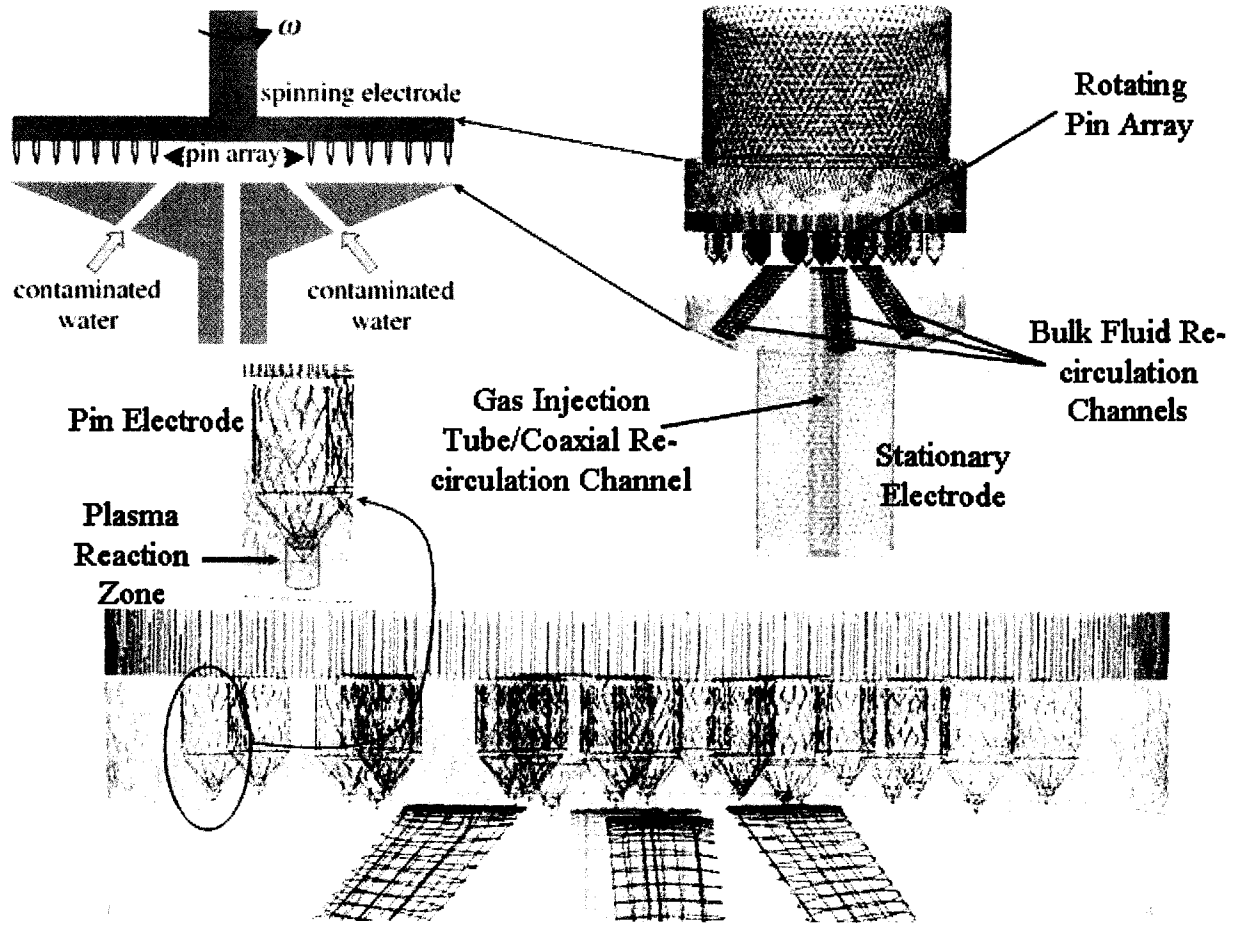

Figure 4.4: A 3D CFD grid of the DMPR along with a 2D representation of the pin and stationary electrodes. The grid zones assigned to simulate the plasma were generated by evenly distributing the total plasma volume, as calculated by the non-linear least squares and optimization analyses, among each of the 25 pin electrodes.

However, to obtain an accurate velocity vector field for spin rates of 750 rpm or above, a more complicated model is needed to accurately simulate the turbulent flow conditions in the DMPR which inherently has a large variation of characteristic lengths ranging from the electrode gap (0.5 mm) to the diameter of the reactor chamber (approximately 200 mm). For these conditions, it has been reported that the RNG based k-ε turbulence model provides the best prediction of the flow field (Choudhury, 1993).

Unsteady state simulations are also performed in order to predict concentration profiles for the attenuation of MTBE in the DMPR. The CFD grids and conditions described above are also applied to the unsteady state simulations. Additional information, however, is required concerning the liquid, which in this case is a mixture. The initial mass fraction of MTBE in the aqueous solution is 3.75×10^{-5}, corresponding to the initial concentrations used in the experiments performed by Johnson et al. (2003). The simulations are designed to model the attenuation of MTBE, not the formation of oxidation products. Thus, the mixture is assumed to have a constant heat capacity, thermal conductivity and viscosity corresponding to that of 300 K water. This is a reasonable assumption considering the concentration of MTBE in the aqueous solution is miniscule. The additional residuals associated with the species equation are, as in the steady state simulations, required to be reduced below 10^{-4}.

With respect to the fluid flow across the plasma-liquid interface, FLUENT®, to the author's knowledge, does not have a standard algorithm to calculate this information due to the cylindrical geometry of the plasma zones. Thus, the following procedure, along with

Reproduced with permission of the copyright owner. Further reproduction prohibited without permission.

Figure 4.5, is used to calculate the volumetric flow rate across interface: (1) the x-, y-, and z- velocity components at the center of each grid cell, as well as the surface area of the cell, are exported from FLUENT®; (2) the magnitude of the velocity vector perpendicular to the surface of the interface is calculated from the exported data; (3) the perpendicular velocity is multiplied by the surface area of the cell, yielding the volumetric flow rate through that cell; and (4) the flow rates through each cell composing the interface are summed and then divided by two; thereby requiring the fluid to be incompressible.

4.5 Simulation Results & Discussion

CFD simulations were performed on both the original and coaxially configured DMPR to yield qualitative and quantitative information concerning fluid flow and fluid properties as a function of pin array spin rate. To aid in the determination of the fluid flow rate through the individual plasma zones and the fluid pressure on the surface of each pin electrode, the recirculation channels and pin electrodes are labeled. Figure 4.6 contains the surface of the stationary electrode with the outlet of the recirculation channels labeled 1-3. Additionally, the pin electrodes are projected onto the stationary electrode surface and subsequently labeled 1-25. The positions of the plasma zones with respect to the location of the recirculation channel outlets are consistent throughout each steady state simulation. The data gathered from the simulations, along with Figure 4.6, are first analyzed to determine the volumetric flow rate of fluid through the plasma.

4.5.1 Velocity Field Analysis

Figure 4.7 contains bar graphs of the volumetric flow rate of the bulk liquid through the plasma in an original DMPR for spin rates of 30, 120, 250 and 500 rpm. Figure 4.8 also

Reproduced with permission of the copyright owner. Further reproduction prohibited without permission.

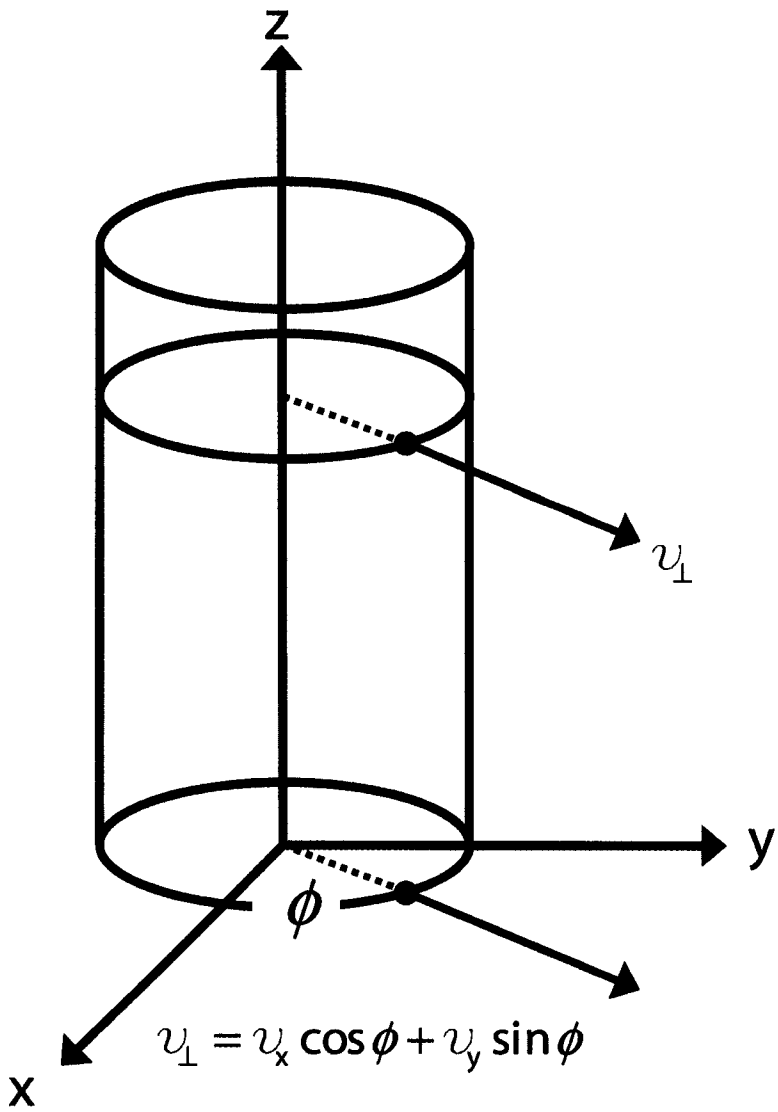

Figure 4.5: Geometrical representation of the plasma zones and the equation used to calculate the velocity perpendicular to the plasma surface in order to determine the total flux of fluid through the plasma-liquid interface.

Reproduced with permission of the copyright owner. Further reproduction prohibited without permission.

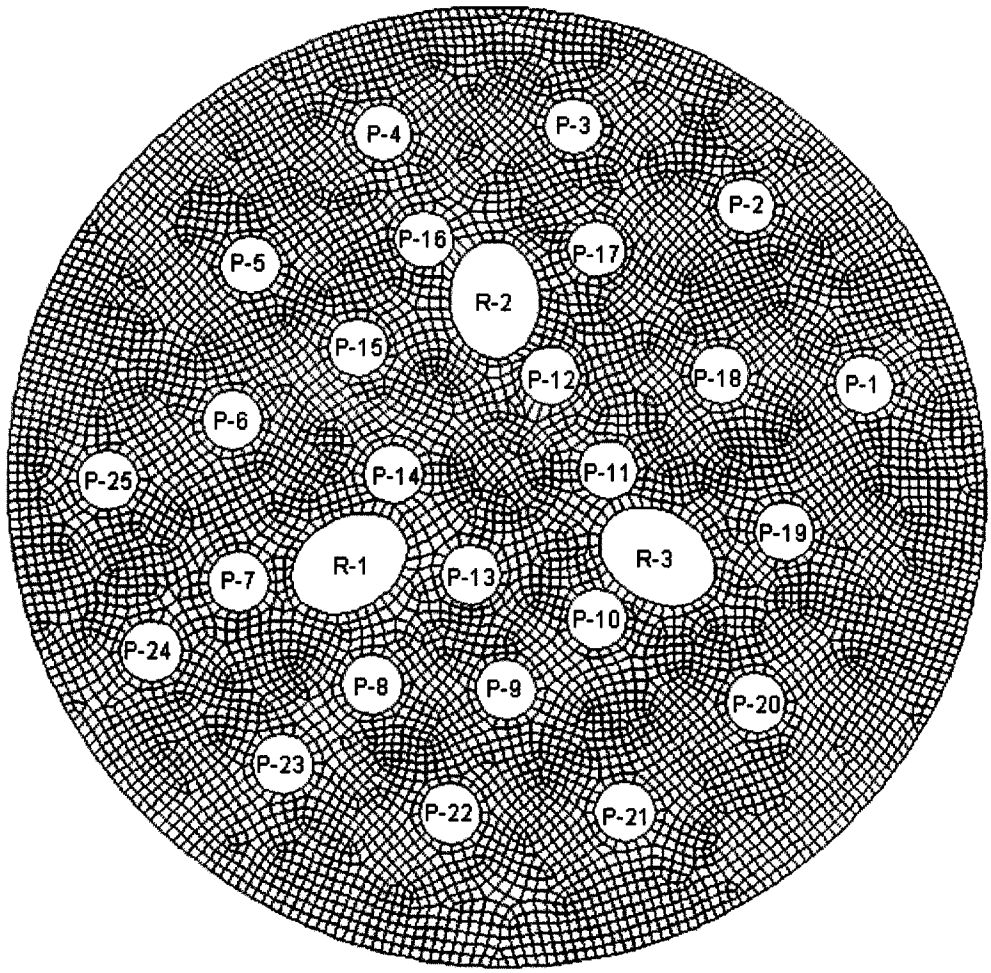

Figure 4.6: Location of the 25 pin electrodes and 3 recirculation channel outlets for the steady state CFD simulations. The pin electrodes and recirculation channels have been labeled in order to compare fluid properties and the velocity field as a function of position in the DMPR.

Reproduced with permission of the copyright owner. Further reproduction prohibited without permission.

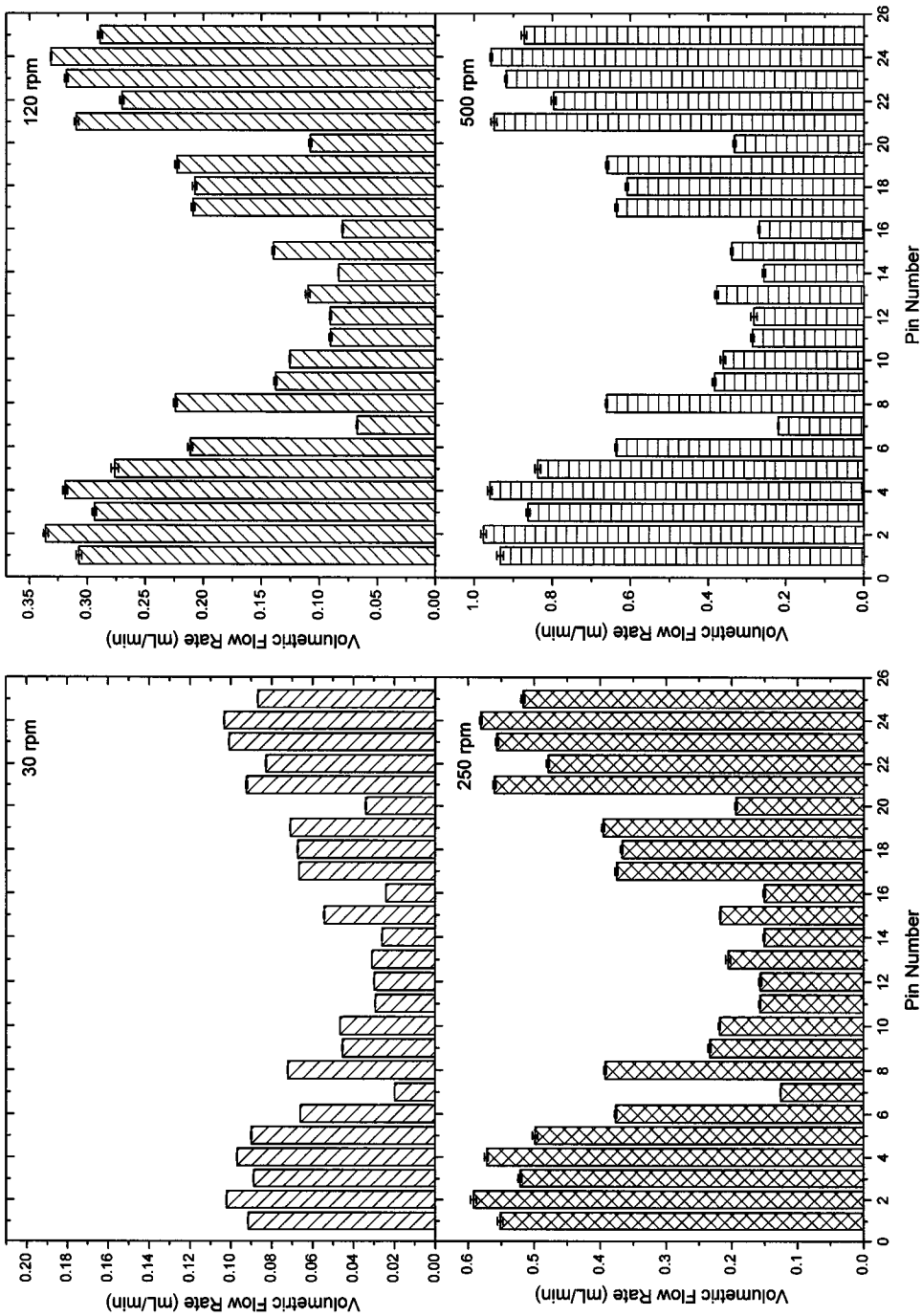

Figure 4.7: Bar graphs of the liquid volumetric flow rate through the plasma zones as a function of location for spin rates of 30, 120, 250 and 500 rpm in an originally configured DMPR. The spin rates presented in the above graphs induce laminar flow conditions.

Reproduced with permission of the copyright owner. Further reproduction prohibited without permission.

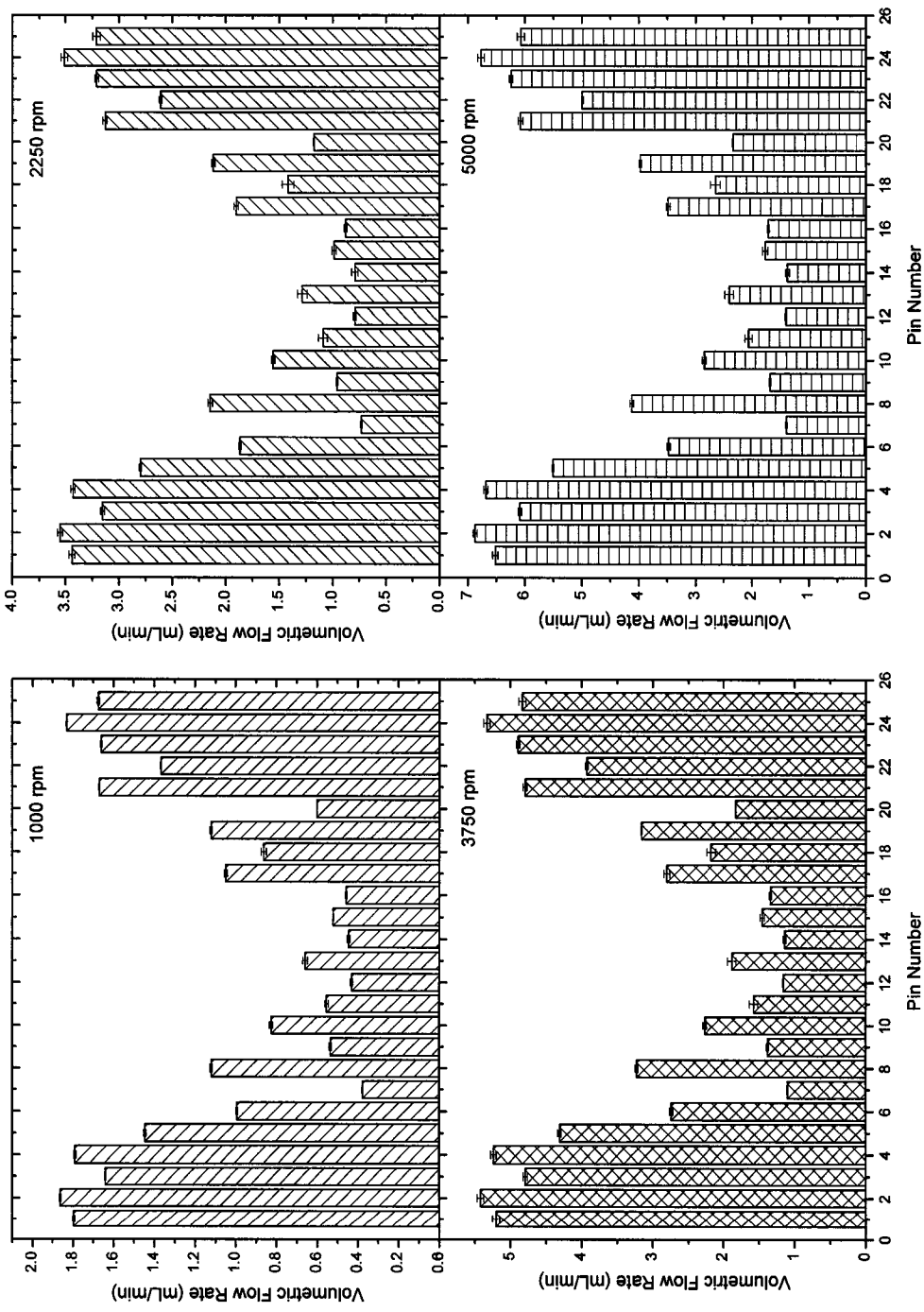

Figure 4.8: Bar graphs of the liquid volumetric flow rate through the plasma zones as a function of location for spin rates of 1000, 2250, 3750 and 5000 rpm in an originally configured DMPR. The spin rates presented in the above graphs induce turbulent flow conditions.

Reproduced with permission of the copyright owner. Further reproduction prohibited without permission.

contains bar graphs of the volumetric flow rate through the plasma in an originally configured DMPR for spin rates of 1000, 2250, 3750 and 5000 rpm. The data plotted in Figure 4.7 are generated by laminar flow conditions while the data in Figure 4.8 are a result of turbulent flow. As shown in both figures, the plasma zones generated from pins with a larger radial distance from the center have higher volumetric flow rates than plasma zones positioned toward the center of the array. (As a reference, pins 11 through 14 correspond to the inner most plasma zones.) This can be explained by the fact that the angular velocity of the pins further away from the center is larger and therefore sweeps over a larger volume than a pin placed towards the center of the array, thereby yielding the parabolic and symmetric profile of the bar graphs. A departure from this behavior is observed, for example, for pin 8, which has a higher flow rate through the plasma than some zones with a larger radial distance. The increased flow seen for some of the inner plasma zones is due to their proximity to the recirculation channel outlets.

At 1000 rpm, the spin rate at which the original configuration experiments were performed, the total flow rate through the plasma and recirculation channels is predicted to be 27 and 673 mL/min, respectively. While the recirculation of the bulk fluid through the recirculation channels is sufficient, corresponding to cycling a fluid volume equal to that of the bulk through the gap between the pin array and stationary electrode approximately 2.7 times per minute, only 4% of the recirculated fluid comes into contact with the plasma. Thus, it would require approximately 9.3 minutes to cycle the same fluid volume through the plasma. Figure 4.9 contains plots of the flow rates through the recirculation channels and the plasma as well as the percent of the total flow rate through the

Reproduced with permission of the copyright owner. Further reproduction prohibited without permission.

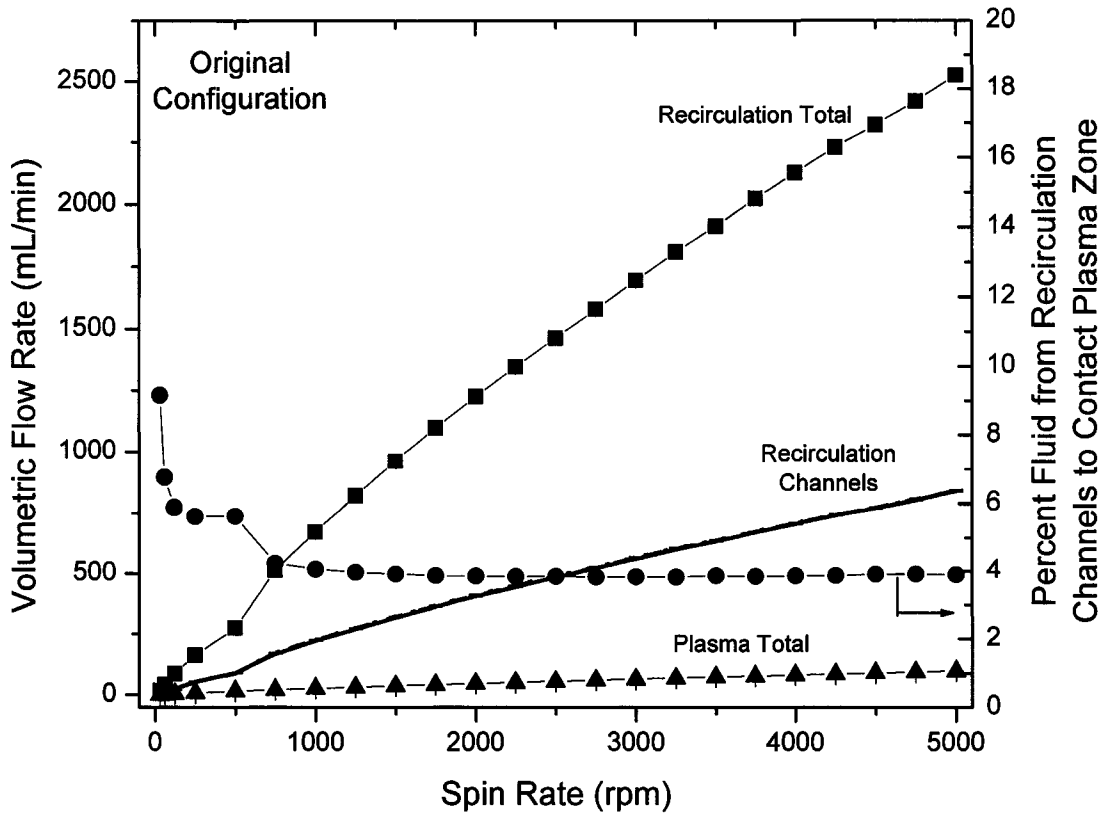

Figure 4.9: Plot of the individual recirculation channel flow rates, total recirculation channel flow rate and total flow rate through the plasma (left axis) as well as the percent of the total flow rate through the recirculation channels to contact the plasma (right axis) as a function of spin rate for the original configuration. Note: the individual recirculation channel flow rates are indistinguishable on this scale.

Reproduced with permission of the copyright owner. Further reproduction prohibited without permission.

recirculation channels to contact the plasma as a function of spin rate for the original configuration. As shown in Figure 4.9, the percent of the fluid traveling through the recirculation channels that contacts the plasma decreases with an increase in flow rate for laminar flow conditions. However, for turbulent flow conditions, the percentage remains relatively constant at 4% and thus is not a function of spin rate. The steady drop off from approximately 9%, predicted at 30 rpm, to approximately 4%, predicted for spin rates inducing turbulent flow conditions, can be explained using the velocity vector plots contained in Figure 4.10.

Velocity vectors for a plane bisecting recirculation channel 2 are plotted in Figure 4.10 for spin rates of 30, 1000 and 5000 rpm. The CFD grids for the pin electrodes and stationary electrode are overlaid on top of the plane containing the velocity vectors to orient the reader. At 30 rpm, the exit velocity of the fluid is such that inertia associated with the exiting fluid does not overwhelm the centrifugal forces produced by spinning the pin array. However, as the spin rate is increased, the fluid velocity exiting the recirculation channels also increases resulting in inertial forces that cause the exiting fluid to continue to travel vertically until contacting the top of the pin array before centrifugal forces result in a radial velocity and force the liquid out of the gap. Thus, at 30 rpm, a larger fraction of the exiting fluid passes through the plasma zones as it is expelled out of the gap between the pin array and stationary electrode when compared to higher spin rates. With respect to the percent fluid to contact the plasma being constant for turbulent flow conditions, the simulations predict a relatively monotonic increase of both the rate at which the fluid flows through the recirculation channels and the plasma, resulting in a contact

Reproduced with permission of the copyright owner. Further reproduction prohibited without permission.

Reproduced with permission of the copyright owner. Further reproduction prohibited without permission.

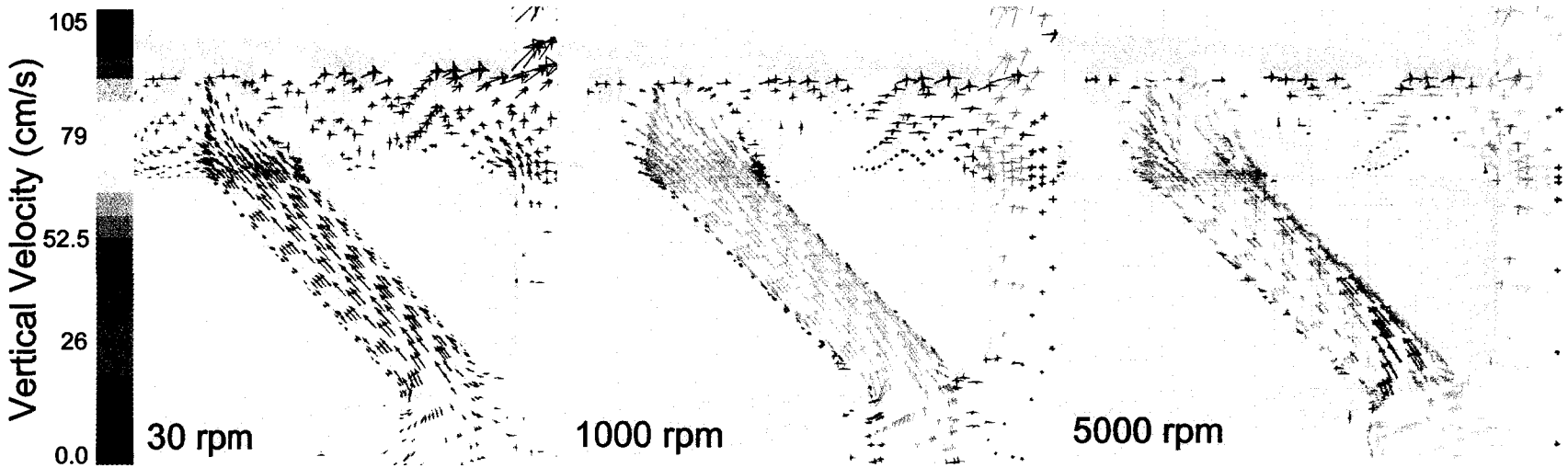

Figure 4.10: Plots of velocity vectors induced by pin array spin rates of 30, 1000 and 5000 rpm traveling in a vertical plane that bisects recirculation channel 2.

percent that is not a function of the spin rate. Trends similar to that predicted for the original configuration are also seen for the coaxial configuration.

In order to compare the simulation results from the original configuration to that of the coaxial configuration, a similar analysis is performed on the CFD data from the coaxial model. Figure 4.11 contains bar graphs of the volumetric flow rate through the plasma in a coaxial DMPR for spin rates of 30, 120, 250 and 500 rpm, corresponding to laminar flow conditions. Figure 4.12 also contains bar graphs of the flow rate through the plasma in a coaxially configured DMPR for spin rates of 1000, 2250, 3750 and 5000 rpm, which generate turbulent flow conditions. As in the simulations conducted on the original configurations, a parabolic and symmetric profile in the bar graphs is seen due to the larger angular velocity of the pins further away from the center. Cycling bulk fluid through the center of the stationary electrode does not qualitatively alter this aspect of the velocity field when compared to the original configuration. Departures from this behavior are again predicted for some of the plasma zones due to their close proximity to the recirculation channel outlets.

At 500 and 1000 rpm, the spin rate at which the coaxial configuration experiments were performed, the total flow rate through the plasma is predicted to be approximately 15 and 26 mL/min while the combined total flow rate through the recirculation and coaxial channels is approximately 378 and 776 mL/min, respectively. While the recirculation of the bulk fluid through the gap between the pin array and stationary electrode, approximately 1.5 (500 rpm) and 3.1 (1000 rpm) times per minute, is again sufficient in the coaxial

Reproduced with permission of the copyright owner. Further reproduction prohibited without permission.

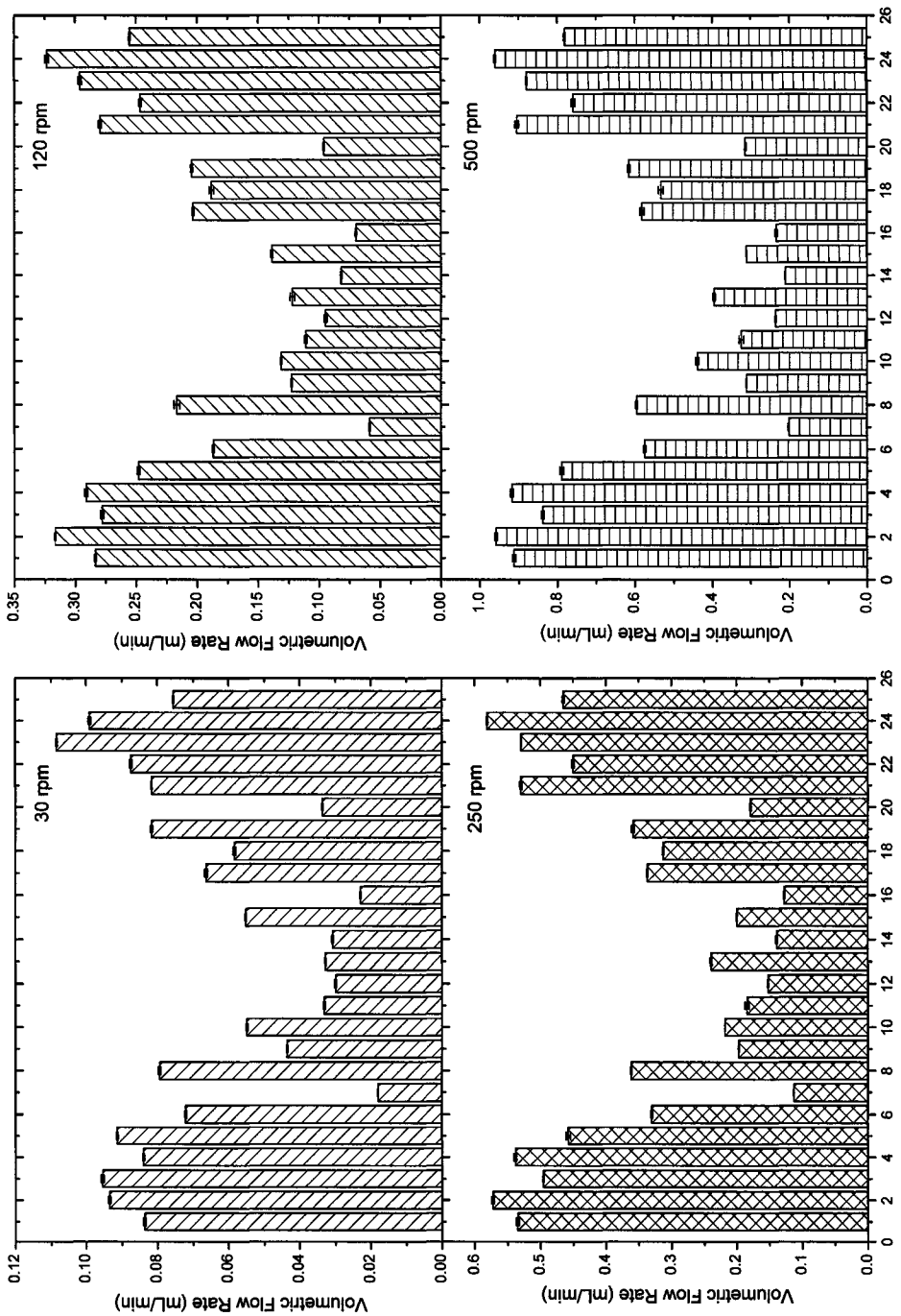

Figure 4.11: Bar graphs of the liquid volumetric flow rate through the plasma zones as a function of location for spin rates of 30, 120, 250 and 500 rpm in a coaxially configured DMPR. The spin rates presented in the above graphs induce laminar flow conditions.

Reproduced with permission of the copyright owner. Further reproduction prohibited without permission.

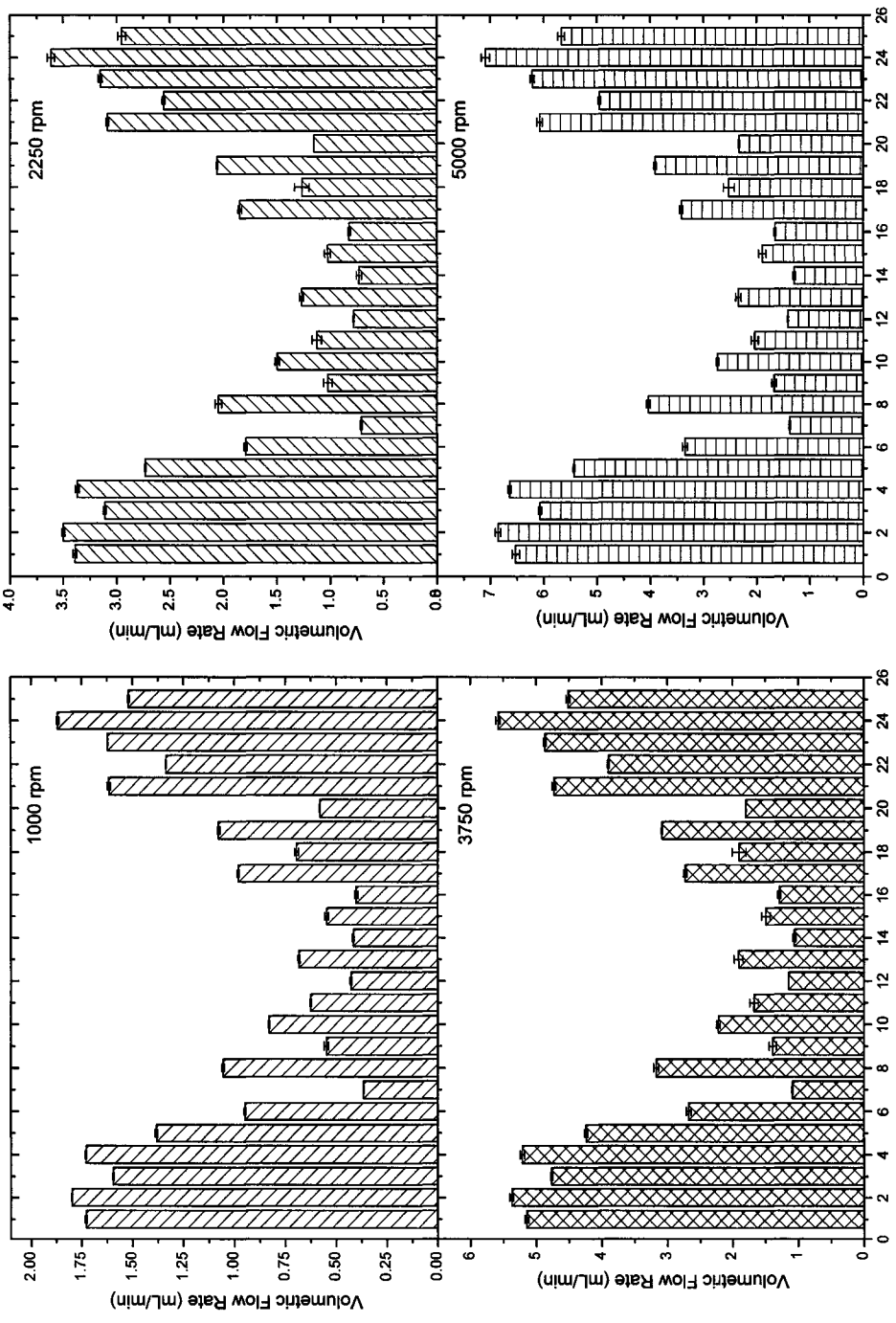

Figure 4.12: Bar graphs of the liquid volumetric flow rate through the plasma zones as a function of location for spin rates of 1000, 2250, 3750 and 5000 rpm in a coaxially configured DMPR. The spin rates presented in the above graphs induce turbulent flow conditions.

Reproduced with permission of the copyright owner. Further reproduction prohibited without permission.

configuration, only 3.5% (500 rpm) and 4% (1000 rpm) of the cycled fluid comes into contact with the plasma. Thus, it would require approximately 17 and 9.6 minutes to cycle the same fluid volume through the plasma for spin rates of 500 and 1000 rpm, respectively. Figure 4.13 contains plots of the flow rates through the coaxial channel, recirculation channels and the plasma as well as the percent of the total flow rate through the gap between the pin array and stationary electrode to contact the plasma as a function of spin rate for the coaxial configuration. As shown in Figure 4.13, the percent of the fluid traveling through the channels that contact the plasma increases with an increase in spin rate for laminar flow conditions. For turbulent flow conditions, however, the percentage remains relatively constant at 3.75%, again leading to the conclusion that the contact percent, if not independent, is a weak function of spin rate. The increase from 1.15% at 30 rpm to 3.75% for spin rates inducing turbulent flow conditions can be explained utilizing the velocity vector plots for varying spin rates contained in Figure 4.14.

Velocity vectors for a plane bisecting recirculation channel 2 and the coaxial channel are plotted in Figure 4.14 for spin rates of 30, 1000, 2500 and 5000 rpm. As in the original configuration analysis, the CFD grids for the pin electrodes and stationary electrode are overlaid on top of the plane containing the velocity vectors to orient the reader. As depicted in Figure 4.14, a volumetric flow rate of 5 mL/min from each of the recirculation channels at 30 rpm is miniscule when compared to the pump driven flow rate of 125 mL/min through the coaxial channel. Due to the large vertical velocity of the fluid exiting the coaxial channel when compared to the radial velocity induced by spinning the pin array, the fluid travels vertically to the top surface of the pin array, away from the plasma

Reproduced with permission of the copyright owner. Further reproduction prohibited without permission.

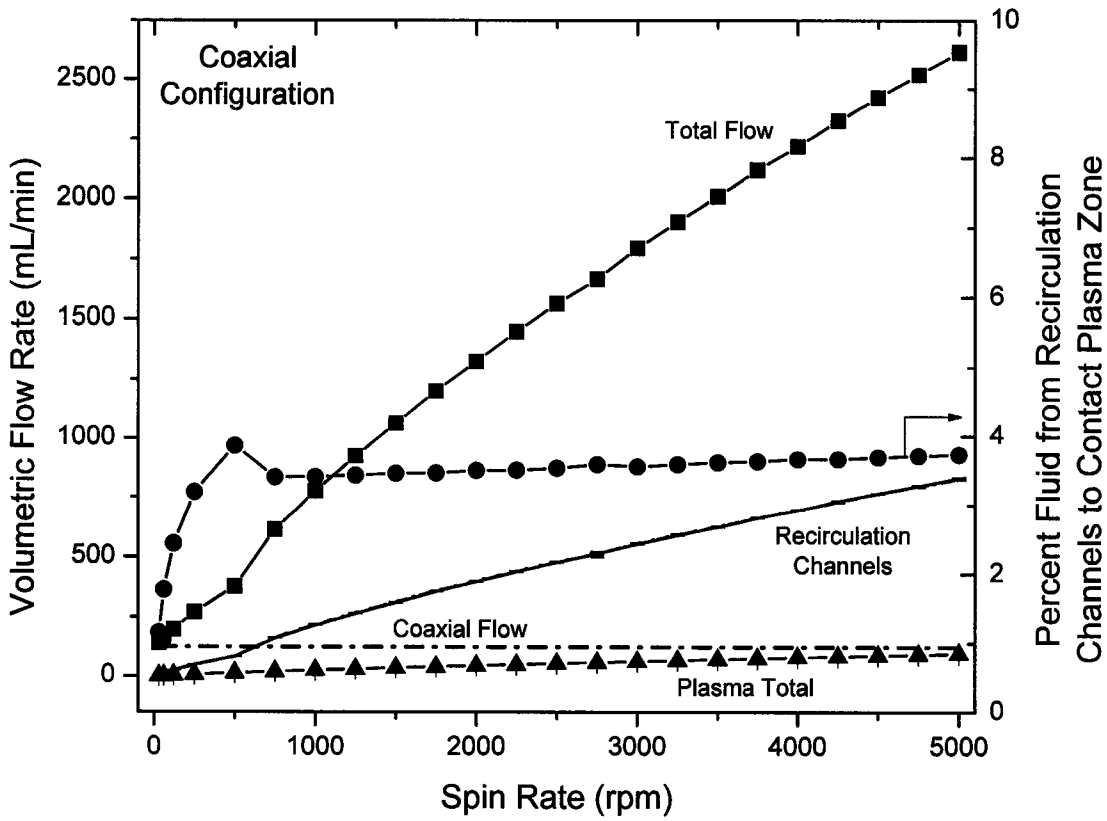

Figure 4.13: Plot of the individual recirculation channel flow rates, coaxial channel flow rate, total flow rate through the gap between the pin array and stationary electrode, and total flow rate through the plasma (left axis) as well as the percent of the total flow rate through the recirculation channels to contact the plasma (right axis) as a function of spin rate for the coaxial configuration. Note: the individual recirculation channel flow rates are indistinguishable on this scale.

Reproduced with permission of the copyright owner. Further reproduction prohibited without permission.

Reproduced with permission of the copyright owner. Further reproduction prohibited without permission.

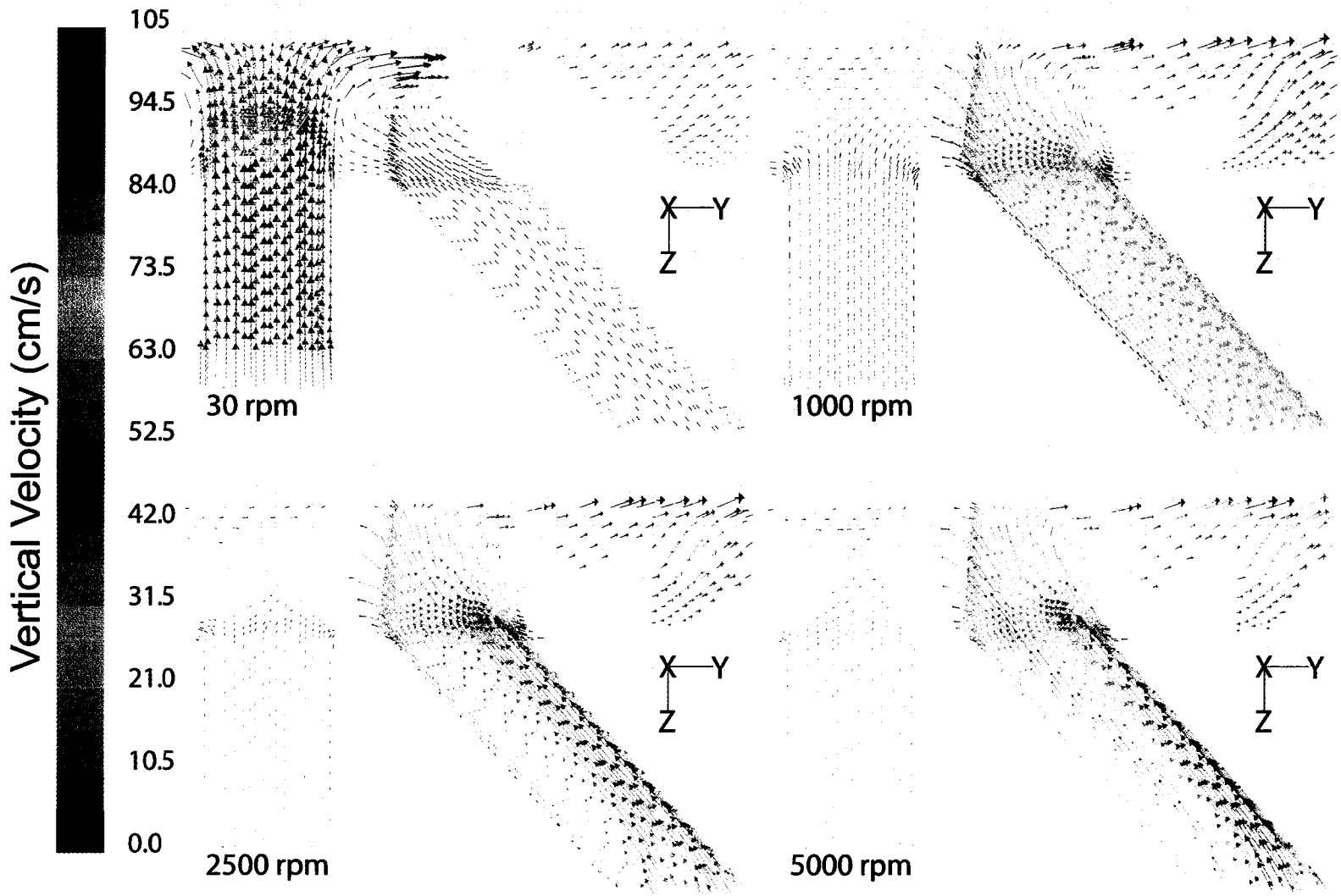

Figure 4.14: Plots of velocity vectors induced by pin array spin rates of 30, 1000, 2500 and 5000 rpm traveling in a vertical plane that bisects recirculation channel 2 and the coaxial channel.

zones. This results in a low percentage of the overall fluid passing through the gap between the pin array and stationary electrode to travel through the plasma. Thus, the spin rate is too low to generate centrifugal forces with the ability to counteract the inertial forces generated by the pump and force more of the fluid through the plasma. Therefore, the flow in the coaxial configuration at 30 rpm is dominated by the external pump whereas at higher spin rates, the flow contribution of the external pump to the overall velocity field becomes negligible when compared to the contribution of the spinning pin array. As the pin array spin rate is increased, the centrifugal forces begin to play a more dominate role in the velocity field resulting in an increase in the plasma contact percent, as shown in Figure 4.13. The departure from the trend at spins rates in the vicinity of 500 rpm is due to the transition from laminar to turbulent flow. As the flow becomes turbulent, the plasma contact percent becomes less dependent on the spin rate until the flow exiting the recirculation channels renders any contribution made by the external pump to the velocity field irrelevant. At that point, the plasma contact percent, as previously seen in the original configuration, is no longer a function spin rate. As in the original configuration, this can be attributed to the monotonic increase of both the rate at which the fluid flows through the recirculation channels and the plasma.

4.5.2 Fluid Pressure Analysis

The maximum electric field, and thus the minimum applied potential, required to initiate an arc discharge in a point-to-plane electrode configuration is produced by minimizing the radius of curvature of the pin electrode. In the DMPR, which employs a point-to-plane electrode configuration, the pin electrodes are mechanically sharpened at an angle of 30° to capitalize on the lower power requirements as a result of sharper pin tips. It is

Reproduced with permission of the copyright owner. Further reproduction prohibited without permission.

observed experimentally, however, that the plasma discharge originates from an area of the pin electrode surface that does not correspond to the minimum radius of curvature. Thus, the CFD simulation data for both the original and coaxial configurations are analyzed to determine if the fluid pressure adjacent to the pin electrode surfaces fluctuates, thereby focusing the location of the discharge to a distinct region of the pin electrode surface for which the electric field strength is not maximized.

Static pressure contour plots of the pin electrodes surface in the original DMPR configuration are contained in Figure 4.15 for pin array spin rates of 30, 1000, 2500 and 5000 rpm. As illustrated in Figure 4.15, pressure gradients develop for spin rates as low as 30 rpm and become more pronounced as the spin rate is increased. The maximum pressure difference predicted by the simulations for 30, 1000, 2500 and 5000 rpm are approximately 10, 450, 2000 and 6400 Pa, respectively. The contours generated by the simulations also demonstrate that the minimum pressure occurs on the back face of the pin electrodes. This behavior can be explained utilizing Figure 4.16 which contains a contour plot of the total pressure in the original DMPR from a horizontal plane 1 mm above the stationary electrode surface for a pin array spin rate of 2000 rpm. As the pin electrodes travel through the fluid in a clockwise direction, flow separation around the pin electrodes is predicted resulting in a region of higher pressure on the front face and a stagnation region of lower pressure along the back face. The stagnation regions predicted by the simulations correspond to the regions for which the plasma discharge is experimentally observed to originate, but is not, however, the region on the pin electrode surface for which the electric field strength is maximized. The origination of the plasma arcs

Reproduced with permission of the copyright owner. Further reproduction prohibited without permission.

Reproduced with permission of the copyright owner. Further reproduction prohibited without permission.

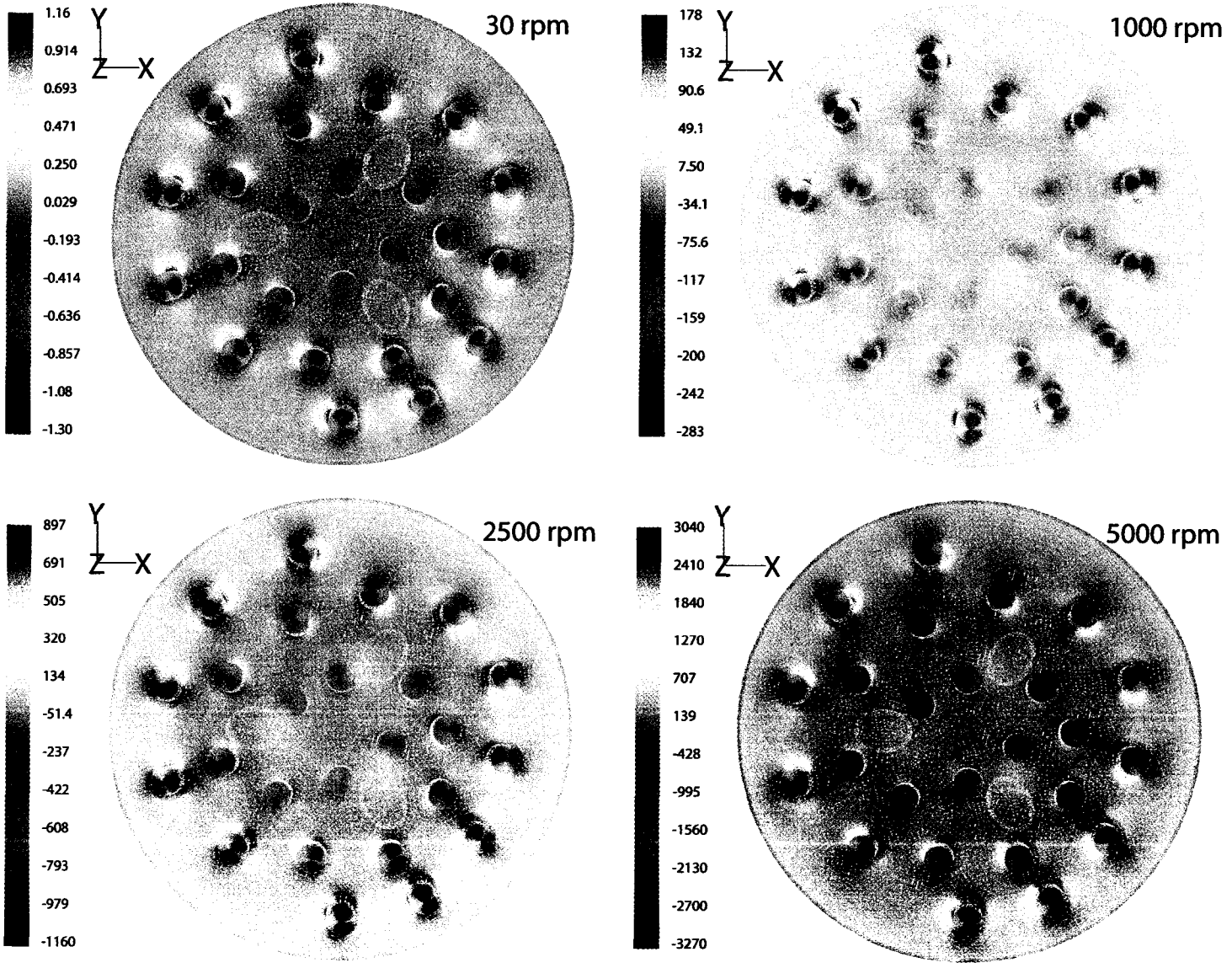

Figure 4.15: Contour plots of static pressure (Pa) on the surface of the pin electrodes and ceramic pin holder in the original DMBR for spin rates of 30, 1000, 2500 and 5000 rpm

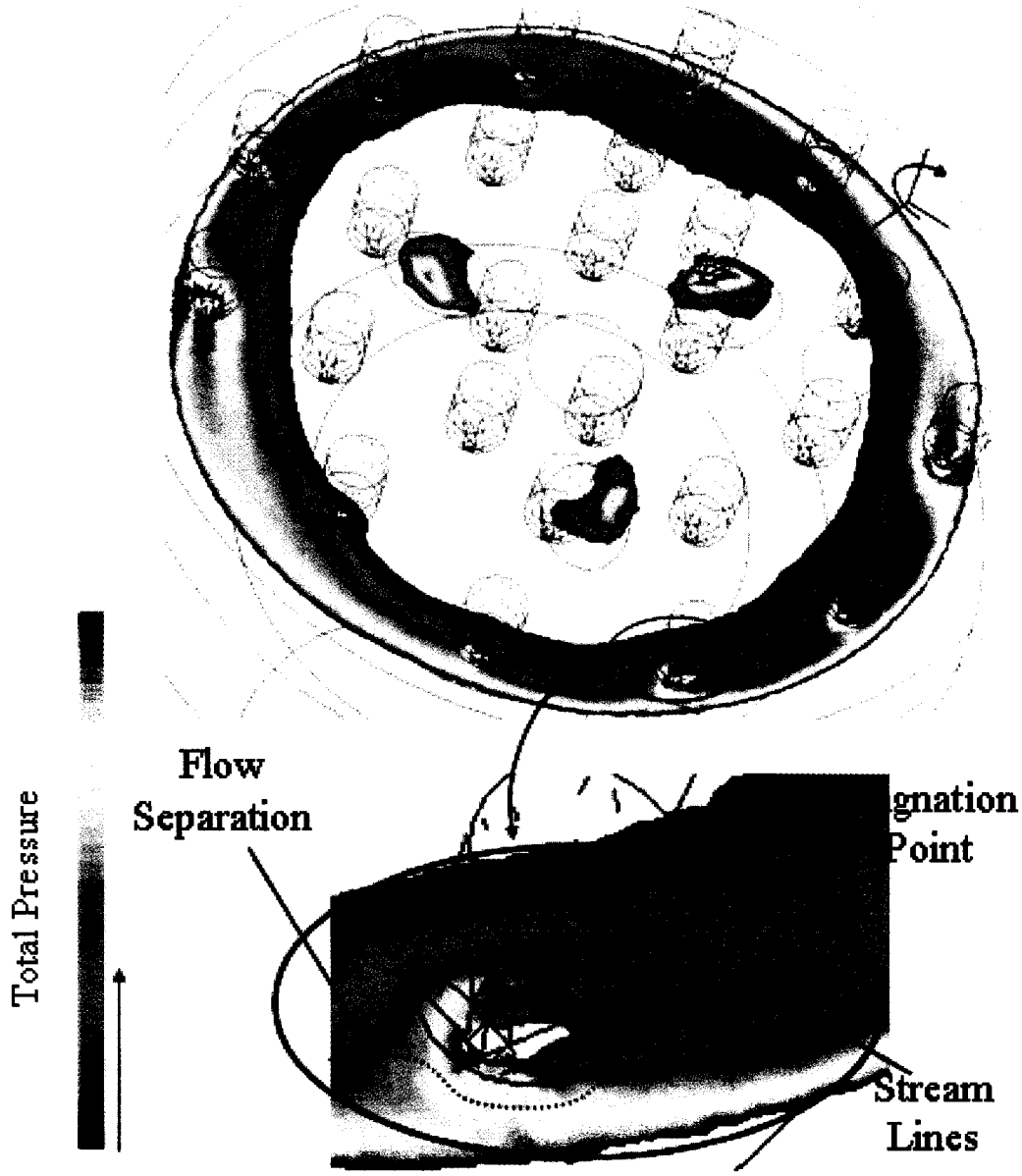

Figure 4.16: Pressure contours generated by a pin array spin rate of 2000 rpm in the original configuration from a horizontal plane 1 mm above the stationary electrode surface.

Reproduced with permission of the copyright owner. Further reproduction prohibited without permission.

from a region of lower pressure can be explained using the Paschen curve contained in Figure 4.17.

The Paschen curve relates the breakdown voltage to the product of the pressure and electrode gap for a given electrode geometry and discharge conditions. The segment of the curve with a negative slope describes the breakdown behavior of gases at pressures considerably below atmospheric. As the pressure between the electrodes is reduced towards complete vacuum, the breakdown of the gas becomes more difficult to initiate, that is a higher applied potential is needed, due to the fact that the gap is devoid of molecules to which the electrons emitted from the electrodes can collide and thus generate a plasma. However, as the pressure is increased for a specified electrode gap, the curve goes through a minimum and the slope becomes positive. This is the region of the curve applied to plasmas initiated at approximately atmospheric pressure, and is thus applicable to the plasma generated in the DMPR. The curve therefore predicts that as the fluid pressure decreases the potential drop across the electrodes required to initiate an arc discharge in the DMPR also decreases. Thus, for the experimental conditions employed by Johnson et al. (2003), the reduction in the fluid pressure adjacent to the pin electrode surface due to spinning the pin array outweighs the larger electric field strength at the pin tip when initiating an arc discharge. To ascertain the possible increase in the electrode gap, which also is a variable in determining the breakdown voltage, the distance above the stationary electrode surface for which the pin electrode surface pressure is a minimum for a given pin location and spin rate is tabulated in Table 4.1.

Reproduced with permission of the copyright owner. Further reproduction prohibited without permission.

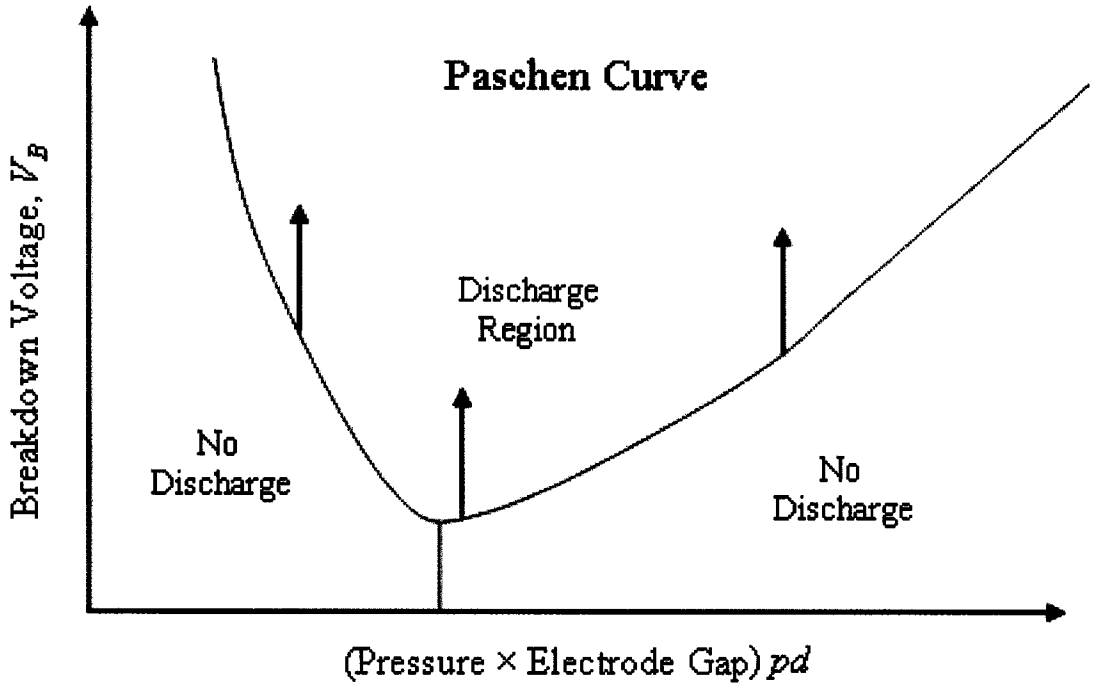

Figure 4.17: Plot of a qualitative Paschen Curve which relates the breakdown voltage to the product of the pressure and electrode gap.

Reproduced with permission of the copyright owner. Further reproduction prohibited without permission.

Reproduced with permission of the copyright owner. Further reproduction prohibited without permission.

Table 4.1: Height (μm) above the stationary electrode surface for which the pressure is a minimum as a function of pin location and spin rate in an originally configured DMPR.

Spin Rate (rpm)	Pin Number																							
	1	2	3	4	5	6	7	8	9	10	11	12	13	14	15	16	17	18	19	20	21	22	23	24	25
30	583	583	583	583	583	701	853	583	583	867	672	583	583	690	583	583	583	583	583	583	583	583	583	583	583
60	583	583	583	583	583	701	853	583	583	867	583	583	583	583	583	583	583	583	583	583	583	583	583	583	701
120	583	583	583	583	583	701	853	583	583	867	681	583	634	681	583	583	583	583	681	583	583	583	583	583	701
250	583	583	583	583	583	813	853	583	583	867	700	583	889	700	583	583	583	583	700	583	583	583	583	583	701
500	583	583	583	583	583	813	853	583	583	872	700	583	889	700	583	583	583	583	583	583	583	583	583	583	701
750	583	583	583	583	583	813	946	583	583	895	700	583	889	700	583	583	583	583	583	583	583	583	583	583	701
1000	583	583	583	583	583	813	946	583	583	895	700	583	889	700	583	583	583	583	583	583	583	583	583	583	701
1250	583	583	583	583	583	813	946	583	583	895	700	583	889	700	583	583	583	583	583	583	583	583	583	583	701
1500	583	583	583	583	583	813	946	583	583	895	700	583	889	700	583	583	583	583	583	583	583	583	583	583	583
1750	583	583	583	583	583	813	946	583	583	895	700	583	889	700	583	583	583	583	583	583	583	583	583	583	583
2000	583	583	583	583	583	813	946	583	583	895	700	583	889	700	583	583	583	583	583	583	583	583	583	583	583
2250	583	583	583	583	583	813	946	583	583	895	700	583	889	700	583	583	583	583	583	583	583	583	583	583	583
2500	583	583	583	583	583	813	946	583	583	895	700	583	889	681	583	583	583	583	583	583	583	583	583	583	583
2750	583	583	583	583	583	813	946	583	583	895	700	583	889	583	583	583	583	583	583	583	583	583	583	583	583
3000	583	583	583	583	583	813	946	583	583	895	700	583	889	583	583	583	583	583	583	583	583	583	583	583	583
3250	583	583	583	583	583	813	946	583	583	895	700	583	889	583	583	583	583	583	583	583	583	583	583	583	583
3500	583	583	583	583	583	813	946	583	583	895	602	583	889	583	583	583	583	583	583	583	583	583	583	583	583
3750	583	583	583	583	583	813	946	583	583	895	583	583	889	583	583	583	583	583	583	583	583	583	583	583	583
4000	583	583	583	583	583	813	946	583	583	895	583	583	889	583	583	583	583	583	583	583	583	583	583	583	583
4250	583	583	583	583	583	813	946	583	583	895	583	583	889	583	583	583	583	583	583	583	583	583	583	583	583
4500	583	583	583	583	583	813	946	583	583	895	583	583	889	583	583	583	583	583	583	583	583	583	583	583	583
4750	583	583	583	583	583	813	946	583	583	895	583	583	889	583	583	583	583	583	583	583	583	583	583	583	583
5000	583	583	583	583	583	813	946	583	583	895	583	583	889	583	583	583	583	583	583	583	583	583	583	583	583

As illustrated by the Paschen curve contained in Figure 4.17, an increase in the electrode gap dictates an increase in the voltage required to initiate an arc. However, the CFD simulations predict that a discharge originating from the point of minimum pressure results in an increase in the electrode gap of only 83 μm for a majority of the pin electrodes. In some cases, as for pin 7, an increase in the distance from the stationary electrode to the point on the pin electrode surface corresponding to the minimum pressure of approximately 450 μm is predicted. Such a substantial increase in the distance from the stationary electrode for which the surface pressure is minimized at pins 6, 7, 10, 11, 13 and 14 can be attributed to their location with respect to the recirculation channel outlets. As shown in Figure 4.6, the close proximately of the pins to the outlets could result in varying fluid conditions due to the contribution of the bulk fluid exiting the recirculation channels. However, pins 8, 9 and 12 do not demonstrate this behavior suggesting that the increased distances from the stationary electrode surface is time dependent and thus a function of ϕ as well as radial distance from the center when using the coordinate system employed in Figure 4.5. While it has been shown that an increase in the pin array spin rate results in a large pressure gradient along the pin electrode surface, thereby altering the plasma discharge characteristics, the simulations also predict a substantial increase in the magnitude of the pressure gradient with an increase in the radial distance from the center of the pin array.

The increase in the pressure gradient along the pin electrode surface, and thus the decrease in the stagnation region minimum pressure, is due to the fact that as the distance from the center increases, the magnitude of the angular velocity also increases. To de-

Reproduced with permission of the copyright owner. Further reproduction prohibited without permission.

termine the effect of pin position on the minimum pressure, a surface plot of the minimum static pressure as a function of radial position and spin rate is contained in Figure 4.18. The radial distance for each spiral strand of pin electrodes, illustrated in Figure 4.6, increases from the middle of the surface plot, pins 12 and 13, to the edges, pins 1 and 25. As illustrated by the plot, the minimum pressure does not appear to be a strong function of radial position at lower spin rates. As the spin rate increases, however, the change in the minimum pin electrode surface pressure as a function of radial position becomes appreciable. In fact, the decrease in pressure due to an increase in radial position is comparable to the decrease resulting from an increase in spin rate. The parabolic nature in the y-z plane of the surface plot is due to the fact that the pins in the center of the surface plot also correspond to the pin positions that are closest to the center of the pin array. The deviations from the parabolic trend seen in Figure 4.18 are due to the bulk liquid exiting the recirculation channels and the close vicinity of the pin electrodes to the recirculation channel outlets. The existence of three recirculation channels also contributes to the anomalies present in the surface plot. To perform a more quantitative analysis on the changes in pressure as a function of radial position and spin rate, the radial position and minimum pressure predicted by the simulations as a function of pin number and spin rate are contained in Tables 4.2 and 4.3.

Table 4.2 contains the minimum static pressure as a function of pin number and spin rate for the original DMPR. The maximum change in surface pressure predicted by the CFD simulations for spin rates of 30, 1000, 2500 and 5000 rpm are 2.0, 447, 1914 and 5382 Pa, respectively. The distinguishable differences in minimum surface pressure from the

Reproduced with permission of the copyright owner. Further reproduction prohibited without permission.

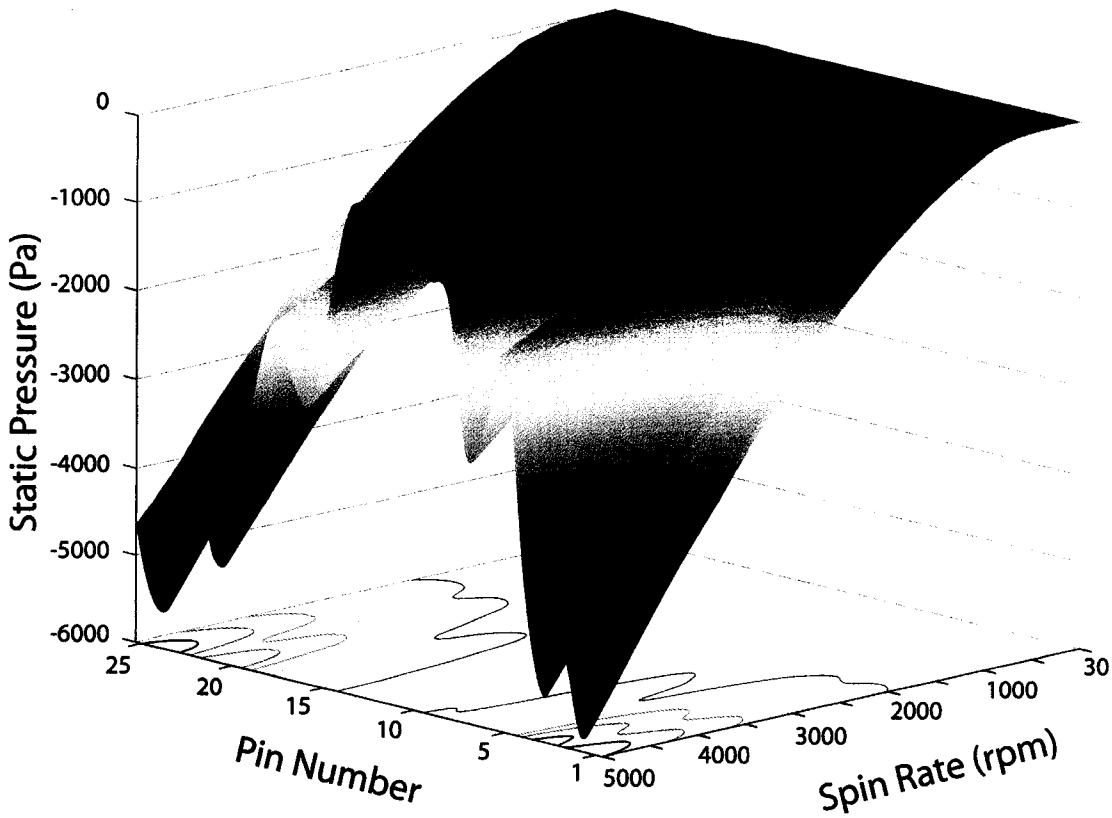

Figure 4.18: Surface plot of the minimum static pressure predicted by the CFD simulations on the pin electrode surface in the original configuration as a function of pin number and spin rate.

Reproduced with permission of the copyright owner. Further reproduction prohibited without permission.

inner pins to the outer pins is consistent with experimental observations relating an increased sputtering rate to pins with larger radial distance when compared to pin electrodes close to the center of the array. As seen at higher spin rates, the change in pressure as a function of pin location is comparable to changes resulting from an increase in spin rate. For example, an increase from 30 to 5000 rpm results in a pressure change of 5846 Pa for pin 2, whereas the maximum pressure change due to an increase in radial position at 5000 rpm is 5382 Pa. Thus, the comparable changes in pressure as a result of pin location and spin rate requires that angular velocity be considered when evaluating the discharge conditions. The pressure difference caused by pin location is more pronounced when considering increases in spin rate of only 250 rpm. Spin rate increases from 750 to 1000 rpm, 2250 to 2500 rpm and 4750 to 5000 rpm result in changes of pressures of 184, 312 and 402 Pa, respectively; all of which are lower than the changes predicted as a result of an increase in the radial position. Table 4.3 contains the radial position at which the minimum surface pressure occurs as a function of pin number and spin rate. As expected, the radial position increases with an increase in the distance of the pin electrode from the center of the array. However, the simulations also predict in some cases, as for pin 9, fluctuations in the radial distance as a function of spin rate. This is again attributed to their location with respect to the recirculation channel outlets suggesting that the variations in radial distance as a function of spin rate for a given pin electrode is time dependent and thus a function of ϕ. A similar analysis is performed on the data gathered from the coaxial configuration simulations in order to determine if the trends predicted for the original configuration also apply to the coaxial configuration.

Reproduced with permission of the copyright owner. Further reproduction prohibited without permission.

Reproduced with permission of the copyright owner. Further reproduction prohibited without permission.

Table 4.2: Minimum static pressure (Pa) predicted on the pin electrode surface in the original configuration as a function of pin location and spin rate. Negative values represent pressures below operating conditions.

Spin Rate (rpm)	Pin Number																								
	1	2	3	4	5	6	7	8	9	10	11	12	13	14	15	16	17	18	19	20	21	22	23	24	25
30	-1.8	-2.1	-2.0	-2.1	-1.7	-0.7	-0.7	-1.4	-0.9	-0.3	-0.3	-0.5	-0.2	-0.3	-0.8	-1.3	-1.3	-1.2	-1.1	-1.7	-2.0	-1.8	-2.0	-2.2	-1.6
60	-4.7	-5.4	-5.3	-5.6	-4.1	-2.1	-2.3	-3.3	-2.3	-0.9	-0.7	-1.0	-0.6	-0.6	-1.9	-3.2	-3.2	-2.9	-2.9	-4.2	-5.2	-4.5	-5.0	-5.7	-4.4
120	-12	-13	-13	-14	-10	-5	-7	-8	-5	-2	-2	-2	-1	-1	-4	-8	-8	-7	-7	-10	-13	-11	-12	-14	-12
250	-40	-46	-44	-48	-34	-20	-25	-25	-16	-8	-5	-6	-5	-5	-12	-26	-25	-21	-24	-35	-44	-37	-43	-46	-40
500	-116	-135	-124	-137	-101	-61	-74	-74	-44	-26	-17	-16	-16	-14	-34	-76	-73	-59	-69	-106	-129	-106	-127	-131	-112
750	-263	-307	-270	-291	-220	-113	-142	-152	-79	-60	-35	-33	-31	-28	-72	-149	-146	-113	-152	-238	-266	-219	-279	-292	-254
1000	-425	-491	-427	-463	-352	-175	-221	-241	-119	-97	-55	-52	-52	-44	-115	-237	-230	-176	-241	-382	-419	-344	-446	-466	-399
1250	-612	-704	-607	-660	-505	-245	-314	-345	-166	-138	-80	-75	-75	-62	-167	-335	-327	-247	-345	-548	-594	-487	-639	-667	-562
1500	-824	-942	-805	-880	-678	-322	-417	-461	-218	-183	-105	-101	-102	-81	-226	-447	-435	-328	-461	-735	-788	-644	-855	-894	-749
1750	-1043	-1195	-1014	-1114	-867	-404	-528	-588	-275	-231	-132	-129	-129	-101	-290	-569	-552	-416	-589	-938	-997	-813	-1089	-1133	-944
2000	-1290	-1477	-1250	-1375	-1072	-490	-649	-730	-331	-285	-168	-162	-159	-120	-360	-701	-679	-501	-726	-1157	-1216	-996	-1344	-1399	-1169
2250	-1541	-1765	-1488	-1640	-1289	-578	-777	-877	-396	-337	-193	-194	-187	-142	-436	-839	-811	-605	-873	-1389	-1455	-1186	-1610	-1672	-1395
2500	-1817	-2077	-1744	-1928	-1519	-671	-908	-1034	-459	-394	-227	-231	-223	-163	-512	-991	-953	-709	-1027	-1636	-1701	-1388	-1894	-1964	-1642
2750	-2089	-2390	-2000	-2217	-1757	-765	-1047	-1194	-533	-450	-250	-265	-251	-191	-597	-1141	-1097	-833	-1190	-1893	-1972	-1595	-2186	-2258	-1887
3000	-2382	-2725	-2282	-2534	-2006	-869	-1193	-1369	-601	-511	-291	-306	-279	-216	-686	-1293	-1244	-940	-1358	-2159	-2243	-1812	-2493	-2581	-2159
3250	-2685	-3072	-2567	-2855	-2264	-965	-1343	-1544	-672	-574	-318	-344	-314	-246	-776	-1459	-1399	-1072	-1534	-2439	-2540	-2039	-2811	-2902	-2430
3500	-3030	-3456	-2897	-3223	-2538	-1071	-1499	-1734	-747	-641	-367	-389	-358	-270	-868	-1632	-1562	-1188	-1713	-2730	-2837	-2284	-3155	-3278	-2771
3750	-3353	-3822	-3199	-3558	-2811	-1168	-1653	-1918	-827	-706	-393	-429	-391	-305	-966	-1807	-1723	-1334	-1900	-3029	-3162	-2526	-3489	-3612	-3047
4000	-3673	-4208	-3536	-3935	-3091	-1291	-1814	-2127	-903	-776	-457	-478	-426	-330	-1061	-1996	-1890	-1431	-2084	-3329	-3455	-2779	-3842	-3983	-3353
4250	-4030	-4610	-3875	-4313	-3389	-1392	-1979	-2322	-980	-847	-491	-523	-478	-365	-1158	-2195	-2070	-1583	-2281	-3646	-3792	-3041	-4204	-4347	-3672
4500	-4398	-5020	-4230	-4702	-3693	-1502	-2169	-2529	-1067	-917	-535	-568	-506	-398	-1270	-2361	-2234	-1736	-2487	-3971	-4150	-3314	-4584	-4762	-4032
4750	-4761	-5446	-4594	-5103	-3996	-1626	-2338	-2747	-1148	-989	-588	-619	-556	-429	-1369	-2580	-2421	-1861	-2686	-4300	-4474	-3588	-4961	-5146	-4349
5000	-5092	-5848	-4932	-5478	-4306	-1744	-2520	-2959	-1230	-1065	-637	-669	-593	-466	-1477	-2779	-2601	-2007	-2891	-4630	-4818	-3861	-5337	-5515	-4638

Reproduced with permission of the copyright owner. Further reproduction prohibited without permission.

Table 4.3: Radial position (μm) at which the minimum pin electrode surface pressure is predicted with respect to the axial center of the original DMPR as a function of pin number and spin rate.

Spin Rate (rpm)	Pin Number																								
	1	2	3	4	5	6	7	8	9	10	11	12	13	14	15	16	17	18	19	20	21	22	23	24	25
30	19779	19593	19357	19373	17072	14293	14987	12949	11313	9307	5586	5795	5635	5592	9910	13074	13111	12693	15111	17740	18683	17971	18912	20274	20301
60	19779	19593	19357	19373	17072	14293	14987	12949	11351	9307	5558	5795	5635	5558	9910	13074	13111	12693	15111	17740	18683	17971	18912	20274	20447
120	19779	19593	19357	19373	17072	14293	14987	12949	11342	9307	5681	5795	5675	5681	9910	13074	13111	12693	15067	17740	18683	17971	18912	20274	20447
250	19779	19593	19357	19373	17072	14387	14987	12949	11304	9307	5705	5795	5874	5705	9910	13074	13111	12693	15194	17740	18683	17971	18912	20274	20447
500	19779	19593	19357	19373	17072	14387	14987	12949	11304	9319	5705	5795	5874	5705	9910	13074	13111	12693	15111	17740	18683	17971	18912	20274	20447
750	19779	19593	19357	19373	17072	14387	15049	12949	11360	9377	5705	5795	5874	5705	9910	13074	13111	12693	15111	17740	18683	17971	18912	20274	20447
1000	19779	19593	19357	19373	17072	14387	15049	12949	11360	9377	5705	5795	5874	5705	9910	13074	13111	12693	15111	17740	18683	17971	18912	20274	20447
1250	19779	19593	19357	19373	17072	14387	15049	12949	11360	9377	5705	5795	5874	5705	9910	13074	13111	12693	15111	17740	18683	17971	18912	20274	20447
1500	19779	19593	19357	19373	17072	14387	15049	12949	11360	9377	5705	5795	5874	5705	9910	13074	13111	12693	15111	17740	18683	17971	18912	20274	20360
1750	19779	19593	19357	19373	17072	14387	15049	12949	11360	9377	5705	5795	5874	5705	9910	13074	13111	12693	15111	17740	18683	17971	18912	20274	20360
2000	19779	19593	19357	19373	17072	14387	15049	12949	11332	9377	5705	5795	5874	5705	9910	13074	13111	12693	15111	17740	18683	17971	18912	20274	20360
2250	19779	19593	19357	19373	17072	14387	15049	12949	11342	9377	5705	5795	5874	5705	9910	13074	13111	12693	15111	17740	18683	17971	18912	20274	20360
2500	19779	19593	19357	19373	17072	14387	15049	12949	11342	9377	5705	5795	5874	5690	9910	13074	13111	12693	15111	17740	18683	17971	18912	20274	20360
2750	19779	19593	19357	19373	17072	14387	15049	12949	11351	9377	5705	5795	5874	5616	9910	13074	13111	12693	15111	17740	18683	17971	18912	20274	20360
3000	19779	19593	19357	19373	17072	14387	15049	12949	11323	9377	5705	5795	5874	5616	9910	13074	13111	12693	15111	17740	18683	17971	18912	20274	20360
3250	19779	19593	19357	19373	17072	14387	15049	12949	11342	9377	5705	5795	5874	5616	9910	13074	13111	12693	15111	17740	18683	17971	18912	20274	20360
3500	19779	19593	19357	19373	17072	14387	15049	12949	11323	9377	5631	5795	5874	5616	9910	13074	13111	12693	15111	17740	18683	17971	18912	20274	20360
3750	19779	19593	19357	19373	17072	14387	15049	12949	11342	9377	5616	5795	5874	5616	9910	13074	13111	12693	15111	17740	18683	17971	18912	20274	20360
4000	19779	19593	19357	19373	17072	14387	15049	12949	11323	9377	5616	5795	5874	5616	9910	13074	13111	12693	15111	17740	18683	17971	18912	20274	20360
4250	19779	19593	19357	19373	17072	14387	15049	12949	11332	9377	5616	5795	5874	5616	9910	13074	13111	12693	15111	17740	18683	17971	18912	20274	20360
4500	19779	19593	19357	19373	17072	14387	15049	12949	11351	9377	5616	5795	5874	5616	9910	13074	13111	12693	15111	17740	18683	17971	18912	20274	20360
4750	19779	19593	19357	19373	17072	14387	15049	12949	11332	9377	5616	5795	5874	5616	9910	13074	13111	12693	15111	17740	18683	17971	18912	20274	20360
5000	19779	19593	19357	19373	17072	14387	15049	12949	11332	9377	5616	5795	5874	5616	9910	13074	13111	12693	15111	17740	18683	17971	18912	20274	20360

Static pressure contour plots of the pin electrode surface in the coaxial DMPR configuration are contained in Figure 4.19 for pin array spin rates of 30, 1000, 2500 and 5000 rpm. In contrast to what is predicted for the original DMPR, pressure gradients do not develop on the surface of the pin electrodes at spin rates close to 30 rpm. As illustrated in Figure 4.19, the flow at 30 rpm is dominated by a pressure drop across the x-y plane due to the external pump driving fluid into the reactor through the middle of the stationary electrode. As the spin rate increases, however, the flow generated by the external pump becomes miniscule when compared to the flow generated by the spinning pin array, resulting in pressure gradients on the pin electrodes surface, which, as in the original configuration, become more pronounced as the spin rate increases. The maximum pressure difference predicted by the simulations for 30, 1000, 2500 and 5000 rpm are approximately 2.4, 460, 2100 and 6300 Pa, respectively. The pressure values are similar to what is predicted for the original configuration at 1000, 2500 and 5000 rpm. This result is consistent with the fact that as the spin rate increases, the contribution from the external pump to the velocity field decreases. As in the original configuration, the simulations predict the minimum pressure to occur on the back face of the pin electrodes. This behavior is attributed to the same mechanisms discussed previously for the original configuration. The distance above the stationary electrode surface for which the pressure is minimized is also investigated to determine a possible increase in the electrode gap.

Data from the coaxial CFD simulations contained in Table 4.4 predict that a discharge originating from the point of minimum pressure results in an increase of 82 μm in the electrode gap for a majority of the pin electrodes. As seen in the original configura

Reproduced with permission of the copyright owner. Further reproduction prohibited without permission.

Reproduced with permission of the copyright owner. Further reproduction prohibited without permission.

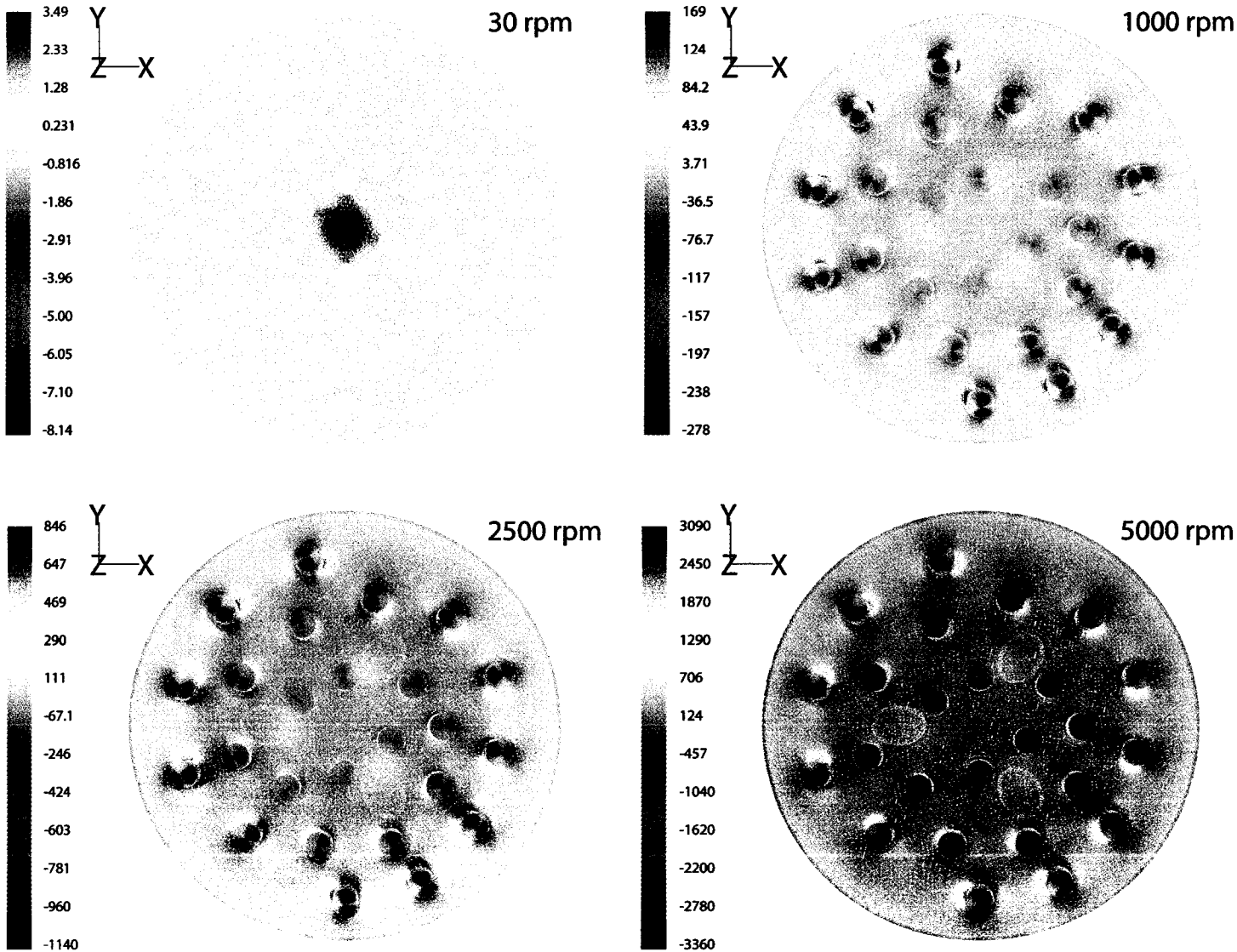

Figure 4.19: Contour plots of static pressure (Pa) on the surface of the pin electrodes and ceramic pin holder in the coaxial DMPR for spin rates of 30, 1000, 2500 and 5000 rpm.

Reproduced with permission of the copyright owner. Further reproduction prohibited without permission.

Table 4.4: Height (μm) above the stationary electrode surface for which the pressure is a minimum as a function of pin location and spin rate in a coaxially configured DMPR.

Spin Rate (rpm)	Pin Number																							
	1	2	3	4	5	6	7	8	9	10	11	12	13	14	15	16	17	18	19	20	21	22	23	24	25
30	582	582	582	582	582	700	852	582	582	582	582	582	582	582	582	582	582	582	582	582	582	582	582	582	582
60	582	582	582	582	582	700	852	582	582	866	582	582	582	582	582	582	582	582	582	582	582	582	582	582	700
120	582	582	582	582	582	812	852	582	582	866	582	582	791	699	582	582	582	582	699	582	582	582	582	582	700
250	582	582	582	582	582	812	852	582	582	866	699	582	888	699	582	582	582	582	699	582	582	582	582	582	700
500	582	582	582	582	582	812	852	582	582	894	699	582	888	699	582	582	582	582	582	582	582	582	582	582	700
750	582	582	582	582	582	812	945	582	582	894	699	582	888	699	582	582	582	582	582	582	582	582	582	582	700
1000	582	582	582	582	582	812	945	582	582	894	699	582	888	699	582	582	582	582	582	582	582	582	582	582	700
1250	582	582	582	582	582	812	945	582	582	894	699	582	888	699	582	582	582	582	582	582	582	582	582	582	700
1500	582	582	582	582	582	812	945	582	582	894	699	582	888	699	582	582	582	582	582	582	582	582	582	582	660
1750	582	582	582	582	582	812	945	582	582	894	699	582	888	699	582	582	582	582	582	582	582	582	582	582	582
2000	582	582	582	582	582	812	945	582	582	894	699	582	888	699	582	582	582	582	582	582	582	582	582	582	582
2250	582	582	582	582	582	812	945	582	582	894	699	582	888	699	582	582	582	582	582	582	582	582	582	582	582
2500	582	582	582	582	582	812	945	582	582	894	699	582	888	641	582	582	582	582	582	582	582	582	582	582	582
2750	582	582	582	582	582	812	945	582	582	894	699	582	888	582	582	582	582	582	582	582	582	582	582	582	582
3000	582	582	582	582	582	812	945	582	582	894	699	582	888	582	582	582	582	582	582	582	582	582	582	582	582
3250	582	582	582	582	582	812	945	582	582	894	680	582	888	582	582	582	582	582	582	582	582	582	582	582	582
3500	582	582	582	582	582	812	945	582	582	894	582	582	888	582	582	582	582	582	582	582	582	582	582	582	582
3750	582	582	582	582	582	812	945	582	582	894	582	582	888	582	582	582	582	582	582	582	582	582	582	582	582
4000	582	582	582	582	582	812	945	582	582	894	582	582	888	582	582	582	582	582	582	582	582	582	582	582	582
4250	582	582	582	582	582	812	945	582	582	894	582	582	888	582	582	582	582	582	582	582	582	582	582	582	582
4500	582	582	582	582	582	812	945	582	582	894	582	582	888	582	582	582	582	582	582	582	582	582	582	582	582
4750	582	582	582	582	582	812	945	582	582	894	582	582	888	582	582	582	582	582	582	582	582	582	582	582	582
5000	582	582	582	582	582	812	945	582	582	894	582	582	888	582	582	582	582	582	582	582	582	582	582	582	582

tion for pin electrodes in close proximity to the recirculation channel outlets, substantial increases in the distance from the stationary electrode surface to the point on the pin electrode surface corresponding to the minimum pressure is predicted for pins 6, 7 10, 11, 13 and 14, but not for other pins with similar radial distances. This result again suggests that the increased distances from the stationary electrode surface is time dependent and thus a function of ϕ as well as radial distance when using the coordinate system employed in Figure 4.5. To determine the effect of pin position on the minimum pressure, a surface plot of the minimum static pressure as a function of radial position and spin rate is contained in Figure 4.20. As predicted for the original configuration, the minimum pressure does not appear to be a strong function of radial position at lower spin rates. The effect of the coaxial channel is not apparent in Figure 4.20 because the pressure gradients on the pin electrode surfaces develop at spin rates for which the contribution of the external pump to the velocity field becomes negligible. The same behavior and trends present in the original configuration surface plot —such as the parabolic nature of the surface, deviations from the parabolic trend and changes in the minimum pin electrode surface pressure as a function of radial position—is apparent for the coaxial configuration as well. A more quantitative analysis on the changes in pressure as a function of radial position and spin rate is performed utilizing the data contained in Tables 4.5 and 4.6.

Table 4.5 contains the minimum static pressure as a function of pin number and spin rate for the coaxial DMPR. The maximum change in surface pressure predicted by the CFD simulations for spin rates of 30, 1000, 2500 and 5000 rpm are 1.9, 439, 1902 and 5408 Pa, respectively. The changes in pressure are almost identical to those predicted for the

Reproduced with permission of the copyright owner. Further reproduction prohibited without permission.

original configuration, even at 30 rpm where it has been previously shown that the velocity field is dominated by the external pump. This can be explained by the fact that the velocity of the fluid exiting the coaxial channel is such that it bypasses the plasma zones, and thus the pin electrodes tips, in a manner similar to that seen for the bulk fluid exiting the recirculation channels at high pin array spin rates. As shown in Figure 4.20, the change in pressure due to pin location is comparable to changes resulting from an increase in spin rate. For example, an increase from 30 to 5000 rpm results in a pressure change of 5889 Pa for pin 2, whereas the maximum pressure change due to an increase of radial position at 5000 rpm is 5408 Pa; thereby making the increase in angular velocity as a function of radial position an important variable when considering the discharge conditions. The pressure difference caused by pin location is again more pronounced when considering increases in spin rate of only 250 rpm. Spin rate increases from 750 to 1000 rpm, 2250 to 2500 rpm and 4750 to 5000 rpm result in changes of pressures of 182, 312 and 423 Pa, respectively, while the changes invoked due to an increase in the angular velocity are more pronounced. Table 4.3 contains the radial position at which the minimum surface pressure occurs as a function of pin number and spin rate. As in the original configuration, the simulations predict fluctuations in the radial distance as a function of spin rate, but the fluctuations are less severe than in the original configuration. This is again attributed to their location with respect to the recirculation channel outlets suggesting that the variations in radial distance as a function of spin rate for a given pin electrode is time dependent.

4.5.3 Kinetic Analysis

The attenuation of MTBE in an original DMPR is simulated utilizing the equations and

Reproduced with permission of the copyright owner. Further reproduction prohibited without permission.

kinetic parameters developed in sections 4.2 and 4.3 which specify the removal rates associated with interphase mass transfer, the plasma and the combination of the loss processes. Figure 4.21 contains data points of the simulated normalized MTBE concentration for the different loss processes versus time as well as the curves generated by the combination of non-linear least squares and optimization analyses. As shown in Figure 4.21, the equations incorporated into the CFD model match the curves well. However, when the equation developed for the plasma loss is substituted for a physical interpretation of the process, that is complete attenuation of MTBE in the plasma zones, the simulated attenuation of MTBE does not follow the curve predicted by the analyses contained in sections 4.2 and 4.3. Figure 4.22 contains contour plots of the normalized MTBE concentration at times of 1 ms and 1 s. As illustrated by the plots, MTBE is completely attenuated in the fluid zones corresponding to the plasma volumes. When the data from the physical interpretation of the plasma process is plotted and compared to the predicted plasma loss, as in Figure 4.23, the simulation results compare poorly to what is observed experimentally. Thus, modeling the removal of MTBE from the DMPR due to complete attenuation in the plasma zone in conjunction with the kinetics for interphase mass transfer, yield unrealistic results and thus changes in the reaction rate as a result of changes in the volumetric flow through the plasma zones cannot be simulated using this model.

4.6 Conclusions

The CFD simulations modeling both the original and coaxial configurations yielded qualitative and quantitative results relating the fluid flow and fluid properties to reactor parameters such as pin array spin rate and pin location. The simulations predict a region

Reproduced with permission of the copyright owner. Further reproduction prohibited without permission.

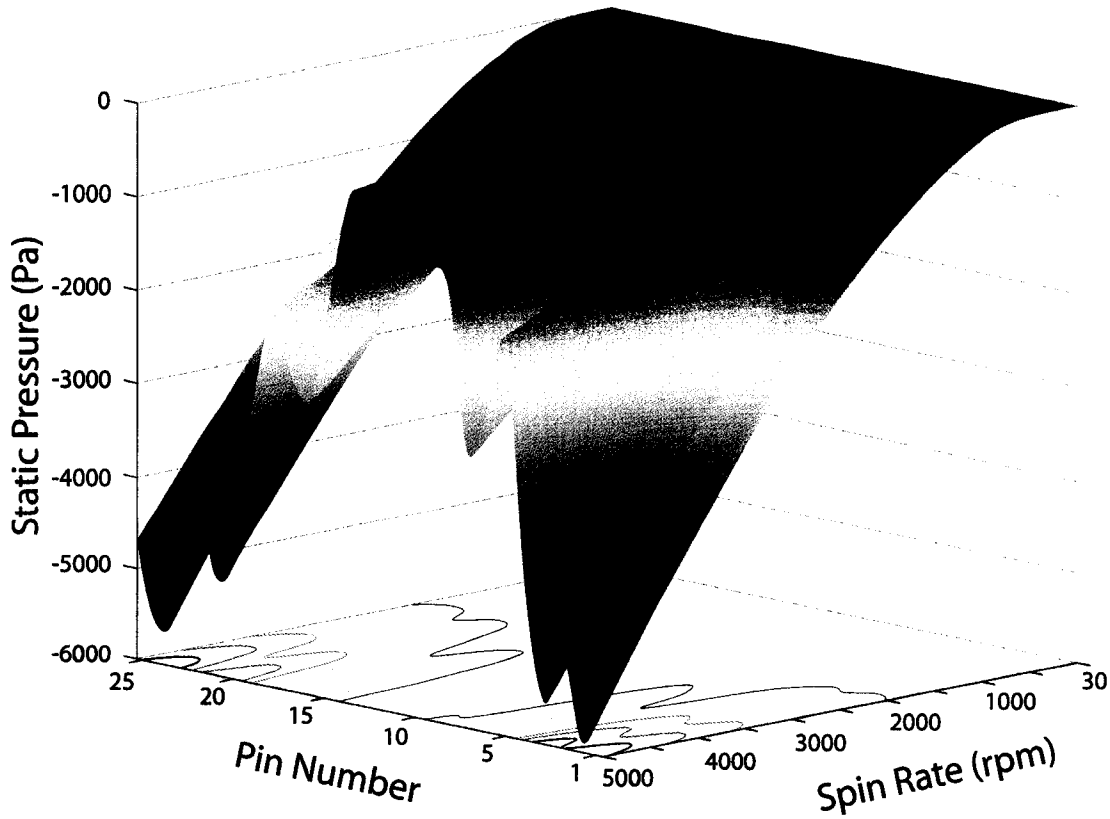

Figure 4.20: Surface plot of the minimum static pressure predicted by the CFD simulations on the pin electrode surface in the coaxial configuration as a function of pin number and spin rate.

Reproduced with permission of the copyright owner. Further reproduction prohibited without permission.

Reproduced with permission of the copyright owner. Further reproduction prohibited without permission.

Table 4.5: Minimum static pressure (Pa) predicted on the pin electrode surface in the coaxial configuration as a function of pin location and spin rate. Negative values represent pressures below operating conditions.

Spin Rate (rpm)	Pin Number																								
	1	2	3	4	5	6	7	8	9	10	11	12	13	14	15	16	17	18	19	20	21	22	23	24	25
30	-1.9	-2.1	-2.3	-2.0	-1.9	-0.9	-0.8	-1.6	-1.0	-0.5	-0.6	-0.6	-0.4	-0.5	-1.0	-1.4	-1.5	-1.2	-1.5	-1.8	-1.9	-2.0	-2.3	-2.2	-1.7
60	-4.6	-5.4	-5.4	-5.3	-4.2	-2.2	-2.4	-3.7	-2.2	-1.1	-1.1	-1.1	-0.7	-0.9	-2.2	-3.1	-3.5	-2.9	-3.3	-4.2	-4.9	-4.7	-5.1	-5.5	-4.5
120	-13	-15	-15	-15	-11	-6	-7	-9	-5	-3	-2	-3	-2	-2	-5	-8	-8	-7	-8	-11	-14	-12	-14	-15	-13
250	-40	-47	-44	-46	-34	-19	-24	-25	-14	-9	-7	-6	-6	-5	-12	-24	-24	-20	-24	-35	-43	-37	-43	-46	-41
500	-118	-138	-125	-135	-101	-59	-72	-71	-38	-29	-18	-16	-18	-14	-35	-71	-71	-56	-68	-106	-127	-104	-128	-131	-112
750	-258	-303	-268	-288	-218	-112	-140	-148	-84	-63	-41	-35	-37	-31	-76	-142	-145	-107	-151	-237	-264	-219	-278	-288	-252
1000	-416	-485	-426	-458	-348	-175	-220	-237	-129	-102	-65	-56	-58	-46	-123	-225	-229	-163	-239	-379	-415	-344	-444	-461	-393
1250	-603	-696	-604	-654	-500	-243	-312	-337	-190	-140	-89	-79	-85	-65	-175	-324	-326	-237	-342	-546	-591	-487	-637	-660	-558
1500	-814	-932	-806	-874	-672	-321	-416	-455	-240	-184	-116	-106	-109	-83	-239	-425	-434	-313	-459	-731	-788	-644	-853	-890	-747
1750	-1036	-1189	-1017	-1109	-860	-401	-526	-579	-316	-231	-145	-136	-142	-104	-302	-553	-552	-401	-585	-935	-998	-815	-1088	-1127	-943
2000	-1285	-1471	-1254	-1372	-1065	-487	-648	-720	-376	-283	-178	-169	-172	-123	-374	-680	-679	-486	-722	-1154	-1223	-999	-1343	-1396	-1173
2250	-1532	-1757	-1491	-1636	-1282	-577	-773	-867	-439	-336	-208	-204	-202	-145	-451	-818	-813	-587	-867	-1384	-1458	-1187	-1608	-1663	-1387
2500	-1806	-2069	-1746	-1923	-1511	-666	-906	-1021	-521	-391	-239	-241	-238	-167	-529	-969	-955	-696	-1021	-1631	-1711	-1392	-1894	-1957	-1636
2750	-2083	-2384	-2013	-2223	-1748	-767	-1045	-1186	-566	-449	-277	-279	-265	-192	-617	-1109	-1098	-798	-1179	-1880	-1969	-1596	-2184	-2262	-1895
3000	-2377	-2724	-2289	-2534	-1999	-865	-1187	-1358	-650	-510	-308	-320	-303	-221	-705	-1276	-1252	-923	-1350	-2154	-2254	-1819	-2496	-2575	-2149
3250	-2693	-3079	-2593	-2874	-2260	-969	-1343	-1542	-700	-573	-349	-362	-333	-249	-800	-1429	-1406	-1037	-1524	-2433	-2549	-2050	-2823	-2926	-2458
3500	-3012	-3444	-2912	-3230	-2529	-1080	-1502	-1734	-741	-638	-395	-406	-360	-279	-900	-1587	-1566	-1154	-1703	-2719	-2853	-2288	-3159	-3288	-2769
3750	-3352	-3834	-3233	-3590	-2807	-1176	-1647	-1919	-857	-707	-436	-452	-417	-312	-989	-1790	-1738	-1287	-1888	-3020	-3163	-2537	-3503	-3630	-3062
4000	-3696	-4229	-3574	-3968	-3093	-1288	-1811	-2121	-933	-774	-485	-499	-452	-341	-1090	-1969	-1907	-1412	-2078	-3328	-3490	-2796	-3863	-4013	-3391
4250	-4024	-4616	-3903	-4332	-3384	-1398	-1979	-2323	-995	-845	-526	-545	-485	-378	-1197	-2149	-2077	-1552	-2272	-3638	-3826	-3053	-4220	-4373	-3681
4500	-4393	-5038	-4262	-4733	-3685	-1504	-2147	-2532	-1088	-918	-578	-596	-538	-412	-1294	-2357	-2263	-1687	-2471	-3963	-4157	-3326	-4598	-4759	-4011
4750	-4751	-5468	-4636	-5152	-3997	-1634	-2314	-2752	-1171	-990	-642	-651	-592	-442	-1391	-2587	-2459	-1801	-2668	-4286	-4472	-3598	-4980	-5152	-4345
5000	-5143	-5891	-4983	-5526	-4308	-1731	-2517	-2964	-1248	-1061	-660	-693	-617	-483	-1516	-2747	-2622	-1990	-2886	-4637	-4888	-3895	-5381	-5571	-4684

Reproduced with permission of the copyright owner. Further reproduction prohibited without permission.

Table 4.6: Radial position (μm) at which the minimum pin electrode surface pressure is predicted with respect to the axial center of the co-axial DMPR as a function of pin number and spin rate.

Spin Rate (rpm)	Pin Number																								
	1	2	3	4	5	6	7	8	9	10	11	12	13	14	15	16	17	18	19	20	21	22	23	24	25
30	19754	19569	19333	19349	17051	14276	14968	12933	11290	9088	5551	5788	5628	5551	9898	13058	13095	12678	15092	17718	18660	17948	18888	20249	20276
60	19754	19569	19333	19349	17051	14276	14968	12933	11327	9296	5551	5788	5628	5551	9898	13058	13095	12678	15092	17718	18660	17948	18888	20249	20421
120	19754	19569	19333	19349	17051	14369	14968	12933	11346	9296	5551	5788	5436	5659	9898	13058	13095	12678	15175	17718	18660	17948	18888	20249	20421
250	19754	19569	19333	19349	17051	14369	14968	12933	11346	9296	5698	5788	5867	5698	9898	13058	13095	12678	15175	17718	18660	17948	18888	20249	20421
500	19754	19569	19333	19349	17051	14369	14968	12933	11346	9365	5698	5788	5867	5698	9898	13058	13095	12678	15092	17718	18660	17948	18888	20249	20421
750	19754	19569	19333	19349	17051	14369	15031	12933	11346	9365	5698	5788	5867	5698	9898	13058	13095	12678	15092	17718	18660	17948	18888	20249	20421
1000	19754	19569	19333	19349	17051	14369	15031	12933	11346	9365	5698	5788	5867	5698	9898	13058	13095	12678	15092	17718	18660	17948	18888	20249	20421
1250	19754	19569	19333	19349	17051	14369	15031	12933	11346	9365	5698	5788	5867	5698	9898	13058	13095	12678	15092	17718	18660	17948	18888	20249	20421
1500	19754	19569	19333	19349	17051	14369	15031	12933	11346	9365	5698	5788	5867	5698	9898	13058	13095	12678	15092	17718	18660	17948	18888	20249	20392
1750	19754	19569	19333	19349	17051	14369	15031	12933	11346	9365	5698	5788	5867	5698	9898	13058	13095	12678	15092	17718	18660	17948	18888	20249	20334
2000	19754	19569	19333	19349	17051	14369	15031	12933	11346	9365	5698	5788	5867	5698	9898	13058	13095	12678	15092	17718	18660	17948	18888	20249	20334
2250	19754	19569	19333	19349	17051	14369	15031	12933	11346	9365	5698	5788	5867	5698	9898	13058	13095	12678	15092	17718	18660	17948	18888	20249	20334
2500	19754	19569	19333	19349	17051	14369	15031	12933	11346	9365	5698	5788	5867	5654	9898	13058	13095	12678	15092	17718	18660	17948	18888	20249	20334
2750	19754	19569	19333	19349	17051	14369	15031	12933	11346	9365	5698	5788	5867	5609	9898	13058	13095	12678	15092	17718	18660	17948	18888	20249	20334
3000	19754	19569	19333	19349	17051	14369	15031	12933	11346	9365	5698	5788	5867	5609	9898	13058	13095	12678	15092	17718	18660	17948	18888	20249	20334
3250	19754	19569	19333	19349	17051	14369	15031	12933	11346	9365	5683	5788	5867	5609	9898	13058	13095	12678	15092	17718	18660	17948	18888	20249	20324
3500	19754	19569	19333	19349	17051	14369	15031	12933	11327	9365	5609	5788	5867	5609	9898	13058	13095	12678	15092	17718	18660	17948	18888	20249	20334
3750	19754	19569	19333	19349	17051	14369	15031	12933	11346	9365	5609	5788	5867	5609	9898	13058	13095	12678	15092	17718	18660	17948	18888	20249	20324
4000	19754	19569	19333	19349	17051	14369	15031	12933	11318	9365	5609	5788	5867	5609	9898	13058	13095	12678	15092	17718	18660	17948	18888	20249	20315
4250	19754	19569	19333	19349	17051	14369	15031	12933	11327	9365	5609	5788	5867	5609	9898	13058	13095	12678	15092	17718	18660	17948	18888	20249	20315
4500	19754	19569	19333	19349	17051	14369	15031	12933	11337	9365	5609	5788	5867	5609	9898	13058	13095	12678	15092	17718	18660	17948	18888	20249	20315
4750	19754	19569	19333	19349	17051	14369	15031	12933	11327	9365	5609	5788	5867	5609	9898	13058	13095	12678	15092	17718	18660	17948	18888	20249	20305
5000	19754	19569	19333	19349	17051	14369	15031	12933	11337	9365	5609	5788	5867	5609	9898	13058	13095	12678	15092	17718	18660	17948	18888	20249	20324

of low pressure on the back face of the pin electrodes which increase in magnitude with an increase in spin rate. The reduced pressure on the pin electrode surface due to an increase in spin rate allows an increase in the electrode gap while maintaining a constant voltage drop. Thus, increasing the spin rate above that utilized by Johnson et al. (2003) would allow an increase in the electrode gap while still employing an applied potential of approximately 200V. The increase in the electrode gap will reduce the residence time required to treat of given amount of fluid in the DMPR by increasing the plasma volume. The fact that the plasma arc originates from a region of the pin electrode surface corresponding to the lowest pressure and not the highest electric field strength demonstrates that reducing the radius of curvature by mechanical and/or electrochemical processes is unnecessary if an appreciable reduction in the pin electrode surface pressure can be achieved. Thus, innovative approaches to further reduce the surface pressure in addition to increasing the spin rate should be sought to further reduce the power requirements of the DMPR. The change in the minimum pressure as a function of pin location also has implications to the scalability of the DMPR.

The minimum pin electrode surface pressure dependence on radial position dictates that the diameter of the pin array, and thus the number of pin electrodes that can be incorporated into the DMPR, is finite. This is due to the fact that as the minimum pressure decreases, the resistance of the fluid between the electrodes also decreases. Thus, at a given distance from the center of the array, the fluid resistance will be such that the energy required to breakdown the fluid at the center of the pin array will not be sufficient. The inner most pins will stop producing a plasma and the current flow will therefore bypass

Reproduced with permission of the copyright owner. Further reproduction prohibited without permission.

the inner pins and flow through the plasma channels generated by the outermost pin electrodes. To counteract this limitation in order to increase the volume of fluid the DMPR can treat, it is important to develop an electrode configuration that generates a consistent angular velocity regardless of radial location. Another option is to design a conical pin array in which the electrode gap increases with an increase in radial position to compensate for the decrease in pressure.

Reproduced with permission of the copyright owner. Further reproduction prohibited without permission.

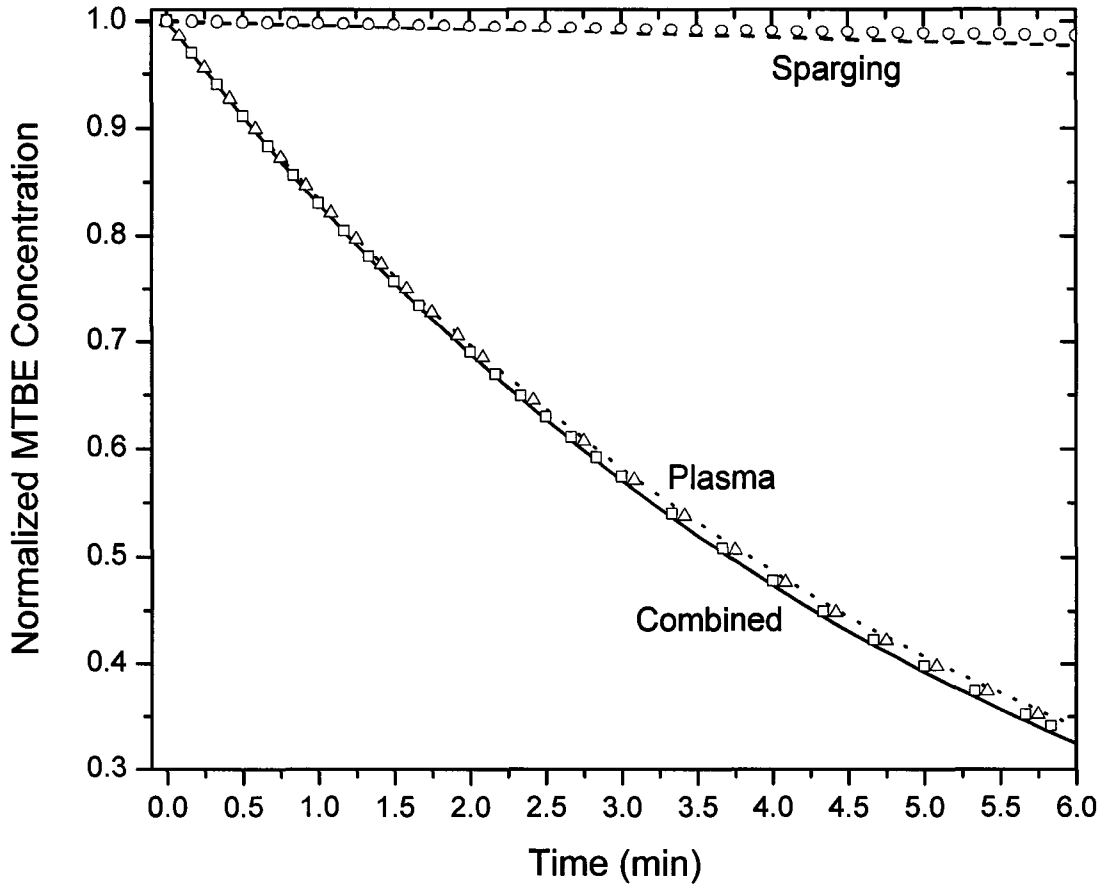

Figure 4.21: Plot of the simulated normalized MTBE concentration versus time as well as the curves generated by a combination of the non-linear least squares and optimization analysis discussed in section 4.3 describing losses due to sparging (_ _ _), the plasma (.....) and the combined effects of the discharge (___).

Reproduced with permission of the copyright owner. Further reproduction prohibited without permission.

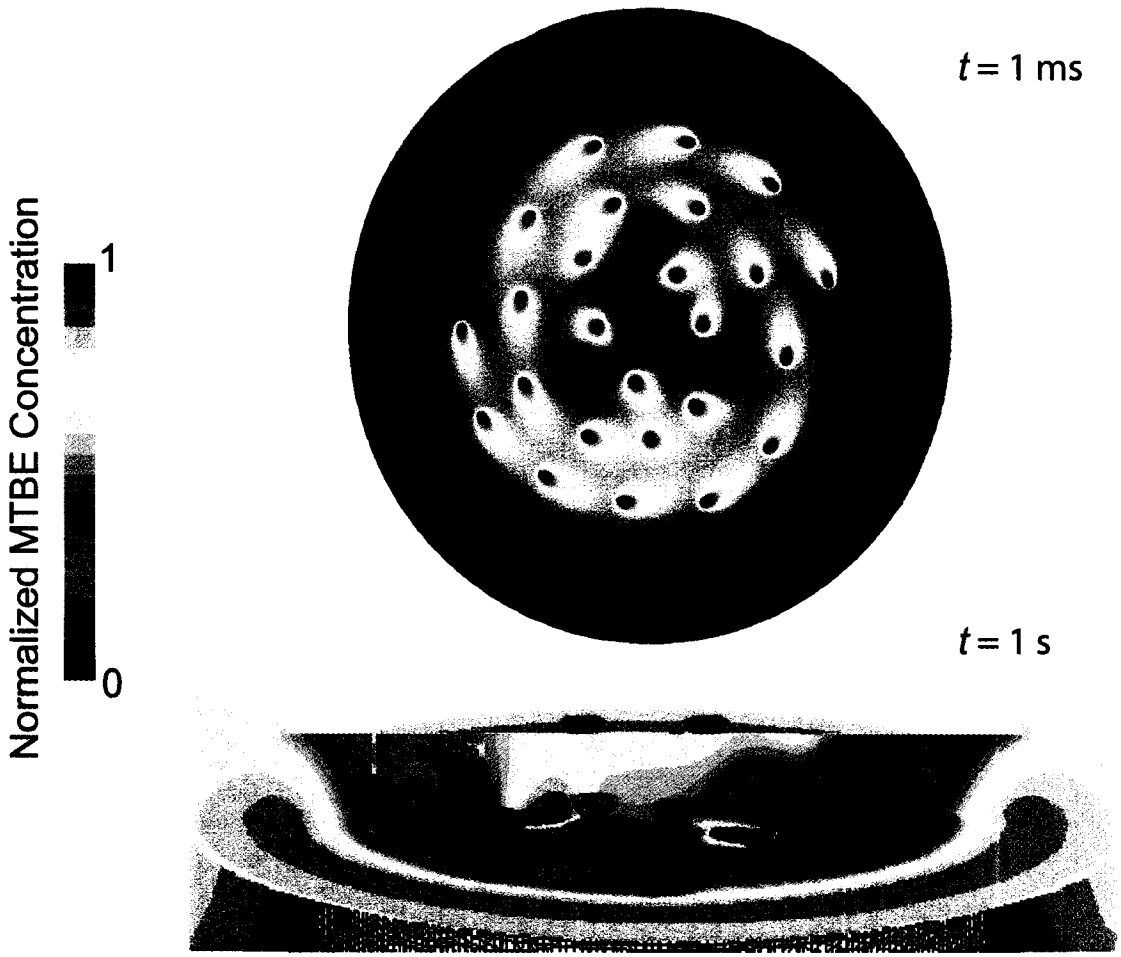

Figure 4.22: Contour plots of the normalized MTBE concentration at 1 ms and 1 s when complete attenuation of MTBE is achieved in the plasma zones.

Reproduced with permission of the copyright owner. Further reproduction prohibited without permission.

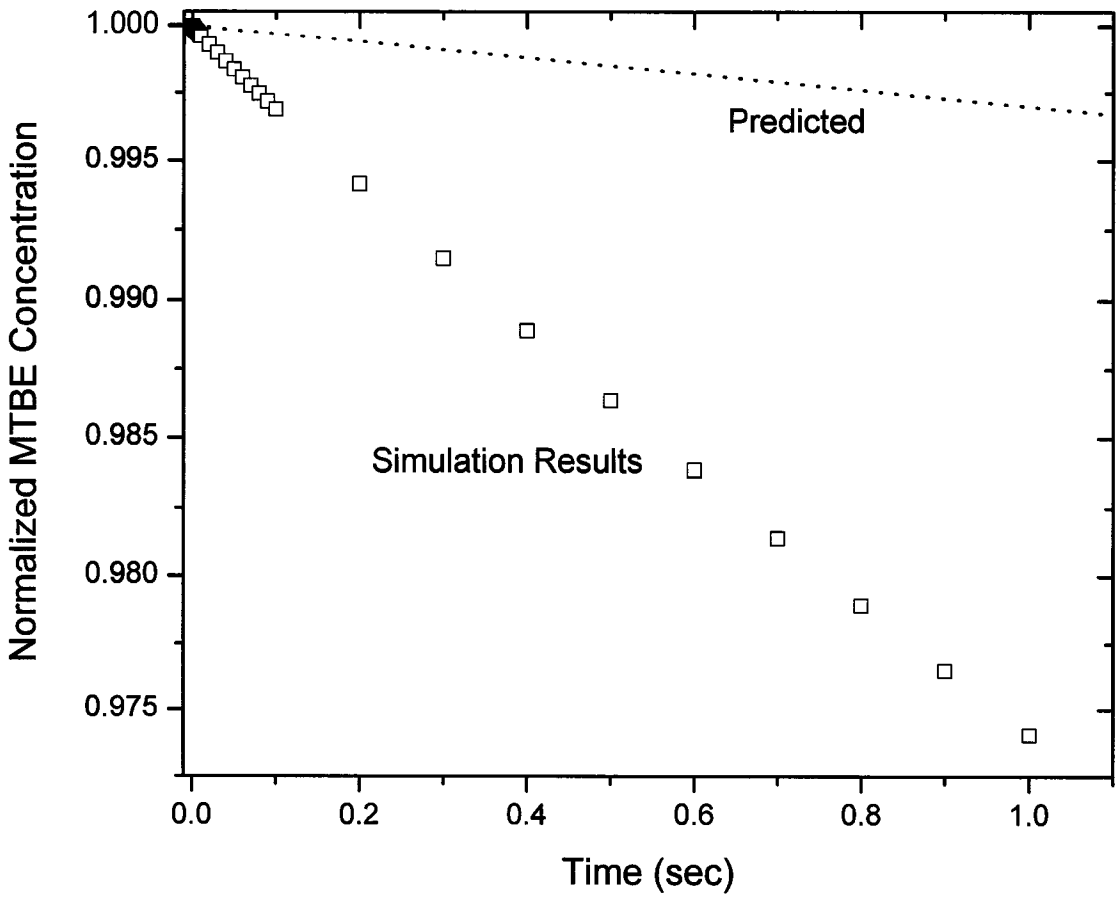

Figure 4.23: Plot of the simulated reduction in the normalized MTBE concentration due to complete attenuation in the plasma zones versus time as well as the curve generated by a combination of the non-linear least squares and optimization analysis describing the loss due to the plasma (.....).

Reproduced with permission of the copyright owner. Further reproduction prohibited without permission.

4.7 References

Bird, R.B., Stewart, W.E., Lightfoot, E.N., 1960. Transport Phenomena. John Wiley & Sons, New York, NY, USA.

Choudhury, D., 1993. Introduction to the Renormalization Group Method and Turbulence Modeling. Fluent Inc. Technical Memorandum TM-107.

Hirschfelder, J.O., Curtiss, C.F., Bird, R.B., 1954. Molecular Theory of Gases and Liquids. John Wiley & Sons, New York, NY, USA.

Johnson, D.C., Shamamian, V.A., Callahan, J.H., Denes, F.S., Manolache, S.O., Dandy, D.S., 2003. Treatment of methyl tert-butyl ether contaminated water using a dense medium plasma reactor: A mechanistic and kinetic investigation. Environ. Sci. Technol. 37, 4804-4810.

Manolache, S., Somers, E.B., Wong, A.C.L., Shamamian, V., Denes, F., 2001. Dense medium plasma environments: A new approach for the disinfection of water. Environ. Sci. Technol. 35, 3780-3785.

Manolache, S.O., Shamamian, V.A., Denes, F., 2004. Dense medium plasma-plasma-enhanced decontamination of water of aromatic compounds. J. Environ. Engin. 130, 17-25.

Reproduced with permission of the copyright owner. Further reproduction prohibited without permission.

Roth, J.R., 1995. Industrial Plasma Engineering Vol. 1: Principles. Institute of Physics Publishing, Philadelphia, PA, USA.

Sun, B., Sato, M., Clements, J.S., 2000. Oxidative processes occurring when pulsed high voltage discharges degrade phenol in aqueous solution. Environ. Sci. Technol. 34, 509-513.

Willberg, D.M., Lang, P.S., Hochemer, R.H., Kratel, A., Hoffmann, M.R., 1996a. Degradation of 4-chlorophenol, 3,4-dichloroaniline, and 2,4,6-trinitrotoluene in an electrohydraulic discharge reactor. Environ. Sci. Technol. 30, 2526-2534.

Willberg, D.M., Lang, P.S., Hochemer, R.H., Kratel, A.W., Hoffmann, M.R., 1996b. Electrohydraulic destruction of hazardous wastes. CHEMTECH 26, 52-57.

Reproduced with permission of the copyright owner. Further reproduction prohibited without permission.

The text of Chapter 5 consists of an article that appears in Water Research 40 (2), 311-322 (2006).

Reproduced with permission of the copyright owner. Further reproduction prohibited without permission.

Chapter Five

5.0 Development of a Tubular High-Density Plasma Reactor for Water Treatment

Experiments have yielded a number of important insights into the energy distribution, sparging and oxidation of methyl *tert*-butyl ether (MTBE), benzene, ethylbenzene, toluene, *m*- and *p*-xylene, and *o*-xylene (BTEX) in a dense medium plasma reactor (DMPR). It has been found that the DMPR transferred a relatively small amount of electrical energy, approximately 4% in the form of sensible heat, to the surrounding bulk liquid. Rate constants associated with plasma initiated oxidation, interphase mass transfer and photolysis were determined using a combination of nonlinear least squares analysis and MATLAB® optimization routines for each species. The rate constants developed for the DMPR, in conjunction with a species mass balance on a prototype tubular high-density plasma reactor, have been applied to determine the removal rates of MTBE and BTEX when operating in batch and continuous flow configurations. The dependence of contaminant concentration on parameters such as treatment time, the number of pin electrodes, electrode gap and volumetric flow rate has been determined. It was found that, under various design specifications and operating conditions, the tubular high-density plasma reactor may be an effective tool for the removal of volatile organic compounds from aqueous solutions.

Reproduced with permission of the copyright owner. Further reproduction prohibited without permission.

5.1 Introduction

The dense medium plasma reactor (DMPR), developed by Denes and coworkers (Denes and Young, 1996) and shown in Figure 3.1, was designed to react liquid/vapor phase species in an induced plasma state using low temperature plasma chemistry. The DMPR has been investigated as a tool for the disinfection of microbial contaminated water. Experiments conducted by Manolache et al. (2001) focused on quantifying the inactivation of specific bacteria and the mechanisms within the DMPR responsible for the disinfection. Water was artificially contaminated with sixteen gram positive and gram negative bacterial species. To reduce the voltage required to initiate a plasma discharge, oxygen or argon was bubbled through the plasma zone. With 20 s of argon plasma treatment, 91% of the colony forming units (cfu) per mL of solution were either inactivated or destroyed. This increased to greater than 98% when the solution was treated for 60 s. The results were slightly better with an oxygen plasma treatment. After 20 s, 98.8% of the cfu/mL were disinfected, with only a slight increase of 0.13% and 0.53% for an additional 40 and 100 s of treatment, respectively. The additional disinfection capability of the oxygen plasma can be attributed to the formation of ozone, a powerful disinfectant.

The oxidation of methyl *tert*-butyl ether (MTBE) and formation of oxidation products in a DMPR have also been explored (Johnson et al., 2003). It was found that carbon dioxide was formed due to electron-impact dissociation reactions in the oxygen plasma, while acetone, *tert*-butyl formate and formaldehyde were formed as a result of oxidation initiated by species formed due to the plasma discharge. To determine the effect of increased

Reproduced with permission of the copyright owner. Further reproduction prohibited without permission.

volumetric flow rate of the bulk solution through the plasma on the reaction rate, a modification was made to the original reactor. As illustrated in Figure 3.1, the center shaft in the stationary electrode was modified to create an annulus in which oxygen passed through the center and the aqueous solution flowed through the outer annular ring. To compare the rate constants for MTBE removal between the original DMPR and the modified reactor, a pseudo first-order rate equation was developed. It was found that the rate constant associated with the modified reactor was approximately 33% higher than that of the original reactor.

The DMPR has also been used to oxidize aqueous aromatic organic pollutants (Manolache et al., 2004). Distilled water was contaminated with benzene, toluene, ethylbenzene, *m*- and *p*-xylene, and *o*-xylene (BTEX), with initial concentrations ranging from 194 to 860 ppm. Five experiments were performed to quantify the effects of varying the oxygen flow rate and current on the removal of the organic species from solution. Of the compounds examined, benzene was found to be the most difficult species to remove. It was observed that the attenuation of all compounds depended strongly on the current intensity and oxygen flow rate (Manolache et al., 2004). However, this dependence was not monotonic across the range of current values and gas flow rates tested. As a result, Manolache et al. (2004) proposed that an optimal condition exists for the oxidation of the aromatic compounds that did not necessarily correspond to the highest current and oxygen flow rate.

While the oxidation and disinfection experiments performed in the DMPR have shown

Reproduced with permission of the copyright owner. Further reproduction prohibited without permission.

promising results, the solution volume that can be treated in the reactor is quite small. This is due to the small plasma volume generated from each pin electrode and the fact that the oxidation chemistry is performed in the plasma and/or in the vicinity of the plasma/liquid interface. This technology would be more applicable to large-scale treatment processes if the plasma volume and the plasma-liquid surface area could be dramatically increased. The DMPR, in addition to being a batch treatment process, is not inherently scalable. It also does not utilize the advantage associated with plasma treatment at atmospheric pressure; the ability to continuously treat liquid. In the present work, a kinetic analysis of the data from the oxidation experiments discussed previously (Johnson et al., 2003; Manolache et al., 2004), together with energy distribution data, are used to develop a tubular high-density plasma reactor capable of continuously treating contaminated liquid feeds at high rates.

5.2 Experimental Methods

Interphase mass transfer and energy consumption experiments were carried out independently using the DMPR. A schematic of the reactor, showing the two configurations used in the experiments conducted by Johnson et al. (2003), is shown in Figure 3.1. The major components of the DMPR include a reaction vessel containing a rotating upper pin electrode array, a stationary lower electrode, cooling system, and gas introduction and discharge ports. The reactor is equipped with a cooling jacket that allows for control of the system temperature when a plasma discharge is initiated. A more detailed description of the reactor can be found in Manolache et al. (2001; 2004).

Reproduced with permission of the copyright owner. Further reproduction prohibited without permission.

For the interphase mass transfer experiments, 250 mL solutions containing either 50 ppm MTBE or 20 ppm benzene were charged to the DMPR. Oxygen was bubbled through the middle of the stationary electrode at 400 mL/min and was not recirculated. The electrode gap between the pin tips and the lower, stationary electrode was 500 μm, and the upper pin array was spun at 1000 rpm. MTBE (≥99.8% purity) and benzene (99.6% purity) were obtained from Aldrich Chemical Co. Millipore water was generated by a Milli-Q ultra pure water system and was used as the solvent phase. The analytical techniques and procedures used to quantify MTBE and benzene are described in Johnson et al. (2003).

For experiments focused on energy distribution, the DMPR was charged with 250 mL of millipore water. Again, the electrode gap was 500 μm and the upper pin electrode array was spun at 1000 rpm. Tap water, at a temperature of approximately 295 K, was flushed through the jacket at 1.17 ± 0.04 L/min. The temperature of the bulk liquid was recorded by an Orion 550A temperature and conductivity meter, as shown in Figure 3.1, at 30 s intervals and transmitted to LabWorks® via a RS-232 serial connection. The energy transferred to the body of the reactor, recirculation loops and pumps had a negligible impact on the bulk liquid temperature for the time scale of the experiments. Data for the oxidation experiments were taken from Johnson et al. (2003) and Manolache et al. (2004).

5.3 Results & Discussion

Initial experiments conducted with the DMPR provided data associated with the energy distribution and the interphase mass transfer of benzene and MTBE from the liquid to the

Reproduced with permission of the copyright owner. Further reproduction prohibited without permission.

gas phase within the reactor. An energy balance on the DMPR was carried out to quantify the energy transferred into the bulk liquid from the plasma discharge in the form of sensible heat. The rate of change of the bulk liquid temperature is equal to the heat generation rate of the plasma discharge and the rate of heat loss to the cooling jacket. This energy balance statement can be written as

$$\left(\frac{dT}{dt}\right)_{\text{Reactor}} = \left[\frac{\dot{g}_{\text{exp}}}{\rho C_p} - \left(\frac{dT}{dt}\right)_{\text{Cooling Jacket}}\right], \tag{5.1}$$

where $\dot{g}_{\text{exp}}$ is the plasma power density, ρ is the liquid density and C_p is the liquid heat capacity. The density and heat capacity of the liquid were assumed to be constant and that of 30 °C water, with values of 996 kg/cm^3 and 4178 J/(kg·K) (Cengel, 1998), respectively.

Three experiments were performed to determine the rate of change of the bulk liquid temperature and the rate of heat transfer to the cooling jacket. The results are shown in Figure 5.1. Calculated values for the rate of change of the bulk liquid temperature at times t = 10 and 11 min were determined using the experimental data and are listed in Table 5.1. Once the plasma was extinguished, the rate of energy loss to the cooling jacket decayed exponentially. Semi-log plots of temperature verses time, along with linear fits, are shown in Figure 5.2. The corresponding changes in log (T) with time, which were used to calculate the rate of energy dissipation to the cooling jacket, are also listed in Table 5.1. The plasma power density, displayed in Table 5.1 for each experiment, is subsequently determined utilizing the calculated energy transfer rates to both the reactor and the cooling jacket in conjunction with Eq. (5.1). It was found from experimental data

Reproduced with permission of the copyright owner. Further reproduction prohibited without permission.

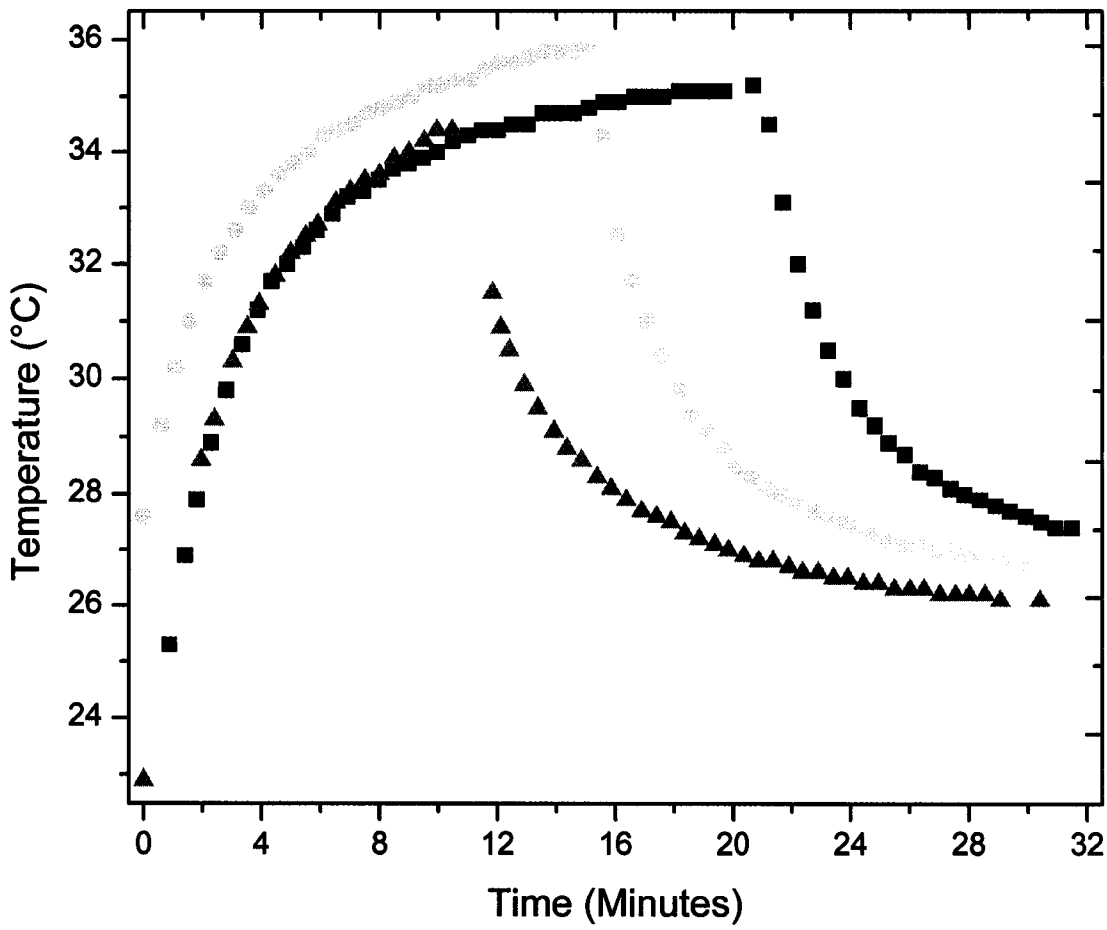

Figure 5.1: Plots of the bulk liquid temperature in the DMPR as a function of time during energy distribution experiments and the dissipation of energy to the cooling jacket when the plasma was deactivated.

Reproduced with permission of the copyright owner. Further reproduction prohibited without permission.

Table 5.1: Computed values for the rate of change of the bulk liquid temperature and the plasma power density, $\dot{g}_{exp}$, at times t = 10 and 11 min.

Bulk Liquid Increase in Temperature	10 min (K/min)	11 min (K/min)	Rate of Energy Loss to Cooling Jacket		$\dot{g}_{exp}$ (kW/cm^3) 10 min	$\dot{g}_{exp}$ (kW/cm^3) 11 min
$\left(\frac{\Delta T}{\Delta t}\right)_1$	1.16	1.08	$\left(\frac{d(\log T)}{dt}\right)_1$	-0.283	30.8	29.0
$\left(\frac{\Delta T}{\Delta t}\right)_2$	0.754	0.703	$\left(\frac{d(\log T)}{dt}\right)_2$	-0.238	5.8	5.6
$\left(\frac{\Delta T}{\Delta t}\right)_3$	1.14	1.06	$\left(\frac{d(\log T)}{dt}\right)_3$	-0.213	36.1	33.5
$\left(\frac{\Delta T}{\Delta t}\right)_{avg}$	1.02	0.945	$\left(\frac{d(\log T)}{dt}\right)_{avg}$	-0.239	24.2	22.7

Reproduced with permission of the copyright owner. Further reproduction prohibited without permission.

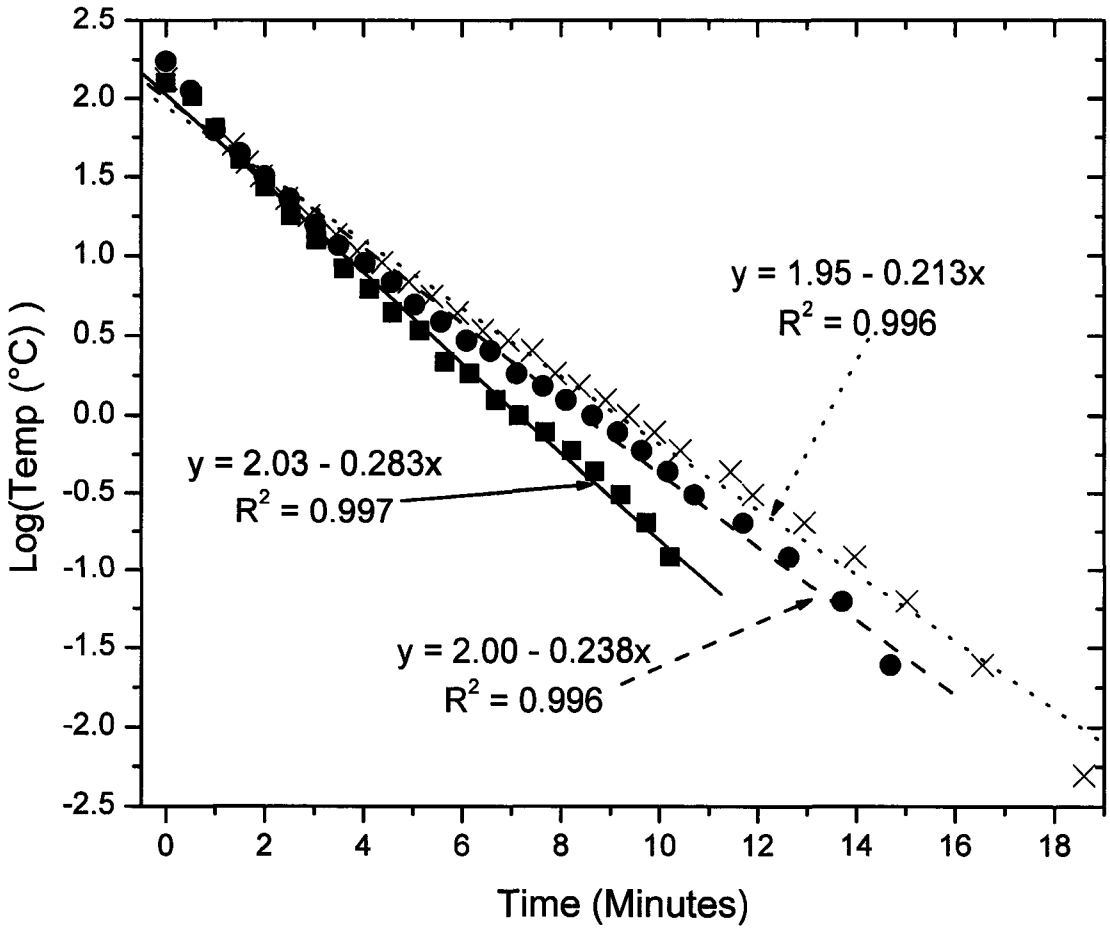

Figure 5.2: Semi-log plots of the reactor fluid temperature versus time for three aqueous DMPR experiments due to heat loss to the cooling jacket as well as the linear fit used to determine the rate of energy loss.

Reproduced with permission of the copyright owner. Further reproduction prohibited without permission.

that the *average* plasma power density was 23.5 kW/cm^3. To calculate an estimate of the *applied* plasma power density, $\dot{g}_{calc}$, it is assumed that the input power is constant. Then, for an applied power $\dot{G} = 200$ W, $\dot{g}_{calc} = \dot{G} / V_{plasma} \approx 645$ kW/cm^3 when the plasma volume generated at each pin electrode is 3.1×10^{-4} cm^3. This predicted value is significantly greater than the 23.5 kW/cm^3 obtained from the experiments. As a result, it is estimated that approximately 4% was transferred into the bulk liquid as sensible heat.

Interphase mass transfer data obtained from these experiments and Manolache et al. (2004) are combined with modified Raoult's law to calculate the equilibrium ratios for each organic molecule—MTBE and the BTEXs—solvated in water. Modified Raoult's law may be written as $K_i = \gamma_i P_i^s / P$ and is applicable to non-ideal liquid solutions at near-ambient pressures. The equilibrium ratio, $K_i = y_i / x_i$, is the ratio of the vapor and liquid phase mole fractions of a species. The activity coefficients (γ_i) are calculated by first estimating the infinite dilution activity coefficients (γ_i^∞), calculating the van Laar coefficients (A_{i,H_2O} and $A_{H_2O,i}$) and then using the van Laar equations with the appropriate experimental data to calculate the activity coefficients, $\gamma_i(x_i)$ and $\gamma_{H_2O}(x_i)$ (Seader and Henley, 1998; Walas, 1985; Turner et al., 1996).

The infinite dilution activity coefficients were estimated to be the reciprocal of their solubility in mole fractions (Walas, 1985). This approximation is valid for solvent activity coefficients near unity and relatively low solubilities (Turner et al., 1996), making this approach applicable. The van Laar coefficients were then calculated using the infinite

Reproduced with permission of the copyright owner. Further reproduction prohibited without permission.

dilution activity coefficients and the following equations (Seader and Henley, 1998):

$$A_{i,H_2O} = \ln \gamma_i^{\infty} \tag{5.2}$$

$$A_{H_2O,i} = \ln \gamma_{H_2O}^{\infty} \tag{5.3}$$

The van Laar coefficients in conjunction with the van Laar equations, Eqs. (5.4) and (5.5), were utilized to determine the activity coefficients (Seader and Henley, 1998).

$$A_{i,H_2O} = \ln \gamma_i \left(1 + \frac{x_{H_2O} \ln \gamma_{H_2O}}{x_i \ln \gamma_i} \right)^2 \tag{5.4}$$

$$A_{H_2O,i} = \ln \gamma_{H_2O} \left(1 + \frac{x_i \ln \gamma_i}{x_{H_2O} \ln \gamma_{H_2O}} \right)^2 \tag{5.5}$$

x_i and x_{H_2O} are the mole fractions of species *i* and water, respectively.

The *K*-values for MTBE and the BTEXs are calculated using modified Raoult's law with activity coefficients calculated from the van Laar equations. The vapor pressures (P_i^s) and activity coefficients, along with calculated *K*-values for MTBE and the BTEXs are listed in Table 5.2. The *K*-values for the aromatic compounds are approximately 50 times that of MTBE, indicating that the aromatic compounds are transferred from the liquid to the gas phase much more readily than MTBE for the experimental conditions used in the DMPR. The result is consistent with the experimental data comparing benzene and MTBE, plotted in Figure 5.3, in which benzene is transferred to the gas from the liquid phase at a higher rate. This is not surprising since the vapor pressures of the BTEXs are higher than that of MTBE. This result is advantageous because, as shown below during

Reproduced with permission of the copyright owner. Further reproduction prohibited without permission.

Table 5.2: Selected physical properties as well as calculated values needed to determine the binary system equilibrium ratio of MTBE, benzene, ethylbenzene, toluene, *m*- and *p*-xylene, and *o*-xylene solvated in water (Turner et al., 1996; Burdick and Jackson, 2002).

Properties	MTBE	Benzene	Ethyl-benzene	Toluene	*m*- and *p*-Xylene	*o*-Xylene
Solubility in water (mole %)	4.8	0.041	0.0029	0.010	0.0030	0.0030
Solubility of water (mole %)	1.5	0.302	0.256	0.257	0.267	0.261
P_i^s (atm)	0.316	0.124	0.0125	0.0371	8.69×10^{-3}	8.69×10^{-3}
Calculated Values	MTBE	Benzene	Ethyl-benzene	Toluene	*m*- and *p*-Xylene	*o*-Xylene
γ_i^∞	20.83	2466	34898	9604	33134	33134
$\gamma_{H_2O}^\infty$	66.67	331	391	389	375	383
A_{i,H_2O}	3.036	7.81	10.5	9.17	10.4	10.4
$A_{H_2O,i}$	4.200	5.80	5.97	5.96	5.93	5.95
γ_i	20.82	2455	34550	9550	32100	32675
K-value	6.57	305	433	354	279	384

Reproduced with permission of the copyright owner. Further reproduction prohibited without permission.

the development of the tubular high-density plasma reactor, the rate of plasma-initiated oxidation is enhanced by higher interphase mass transfer coefficients.

5.4 Tubular High-Density Plasma Reactor (THDPR)

As discussed above, the DMPR was used to treat water artificially contaminated with MTBE and BTEX. Although the DMPR has been shown to be a promising tool for the treatment of organically contaminated aqueous solutions, the original design is not robust, presents scale-up difficulties and has a high capital cost. Data from previous experiments performed by Johnson et al. (2003) and Manolache et al. (2004), along with a species balance, have been used to identify the dimensions and operating conditions for a prototype tubular high-density plasma reactor.

The tubular high-density plasma reactor, shown in Figure 5.4, contains an inner stationary shaft (through which a gas is introduced into the system), a middle rotating cylinder (to which the pin electrodes are attached) and an outer stationary cylinder. Contaminated water is continuously fed into the top of the reactor through ports on the outer stationary cylinder and travels axially through the gap between the outer cylinder and the middle rotating cylinder either by a pressure drop or gravimetric forces. Pin electrodes, represented by black dots, protrude outward from the middle cylinder and are arranged in a helical pattern. For the following analysis, it is important to note that the electrode gap, or distance between the pin tips and the outer stationary cylinder, is virtually identical to the distance between the middle rotating cylinder and the outer cylinder. Once the gas is introduced into the bulk solution, through small holes in the center of each pin electrode,

Reproduced with permission of the copyright owner. Further reproduction prohibited without permission.

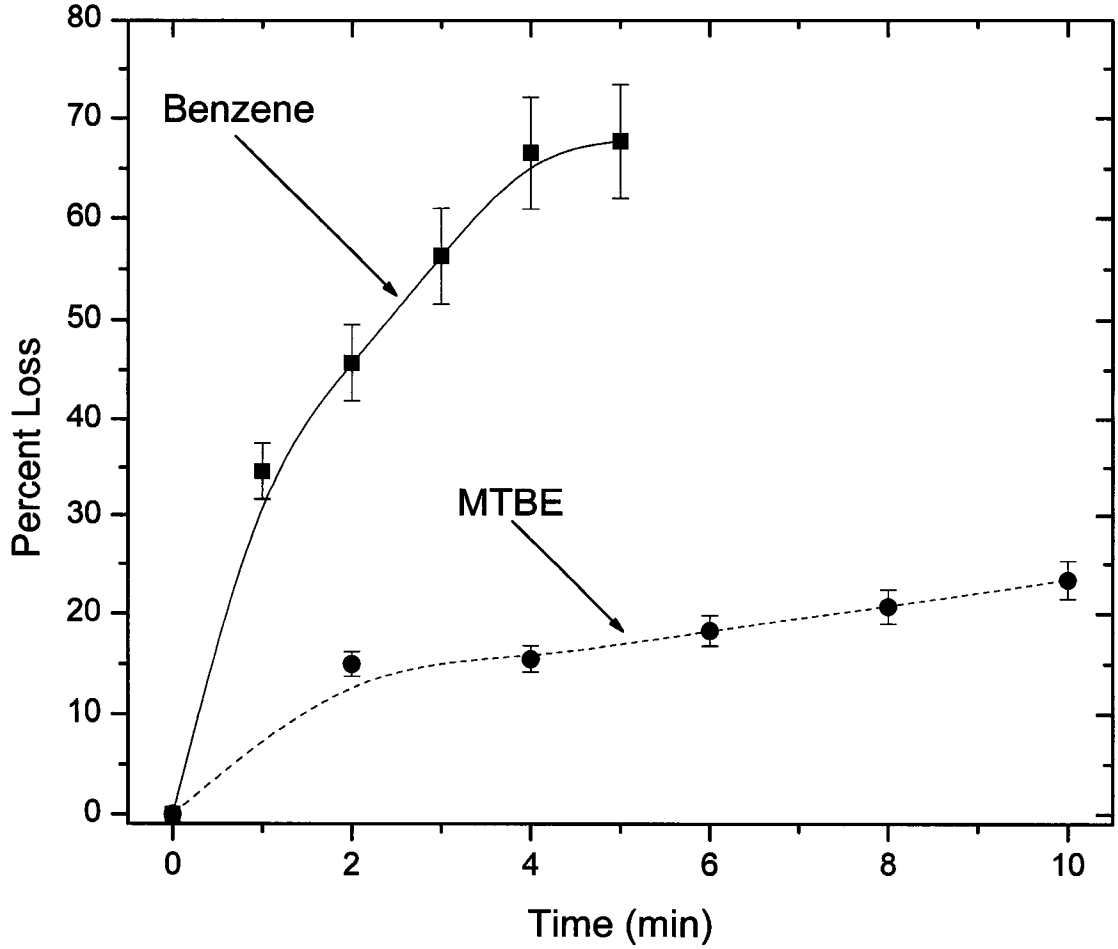

Figure 5.3: Plots of the percent loss of benzene and MTBE due to interphase mass transfer as a function of time in a DMPR without plasma treatment.

Reproduced with permission of the copyright owner. Further reproduction prohibited without permission.

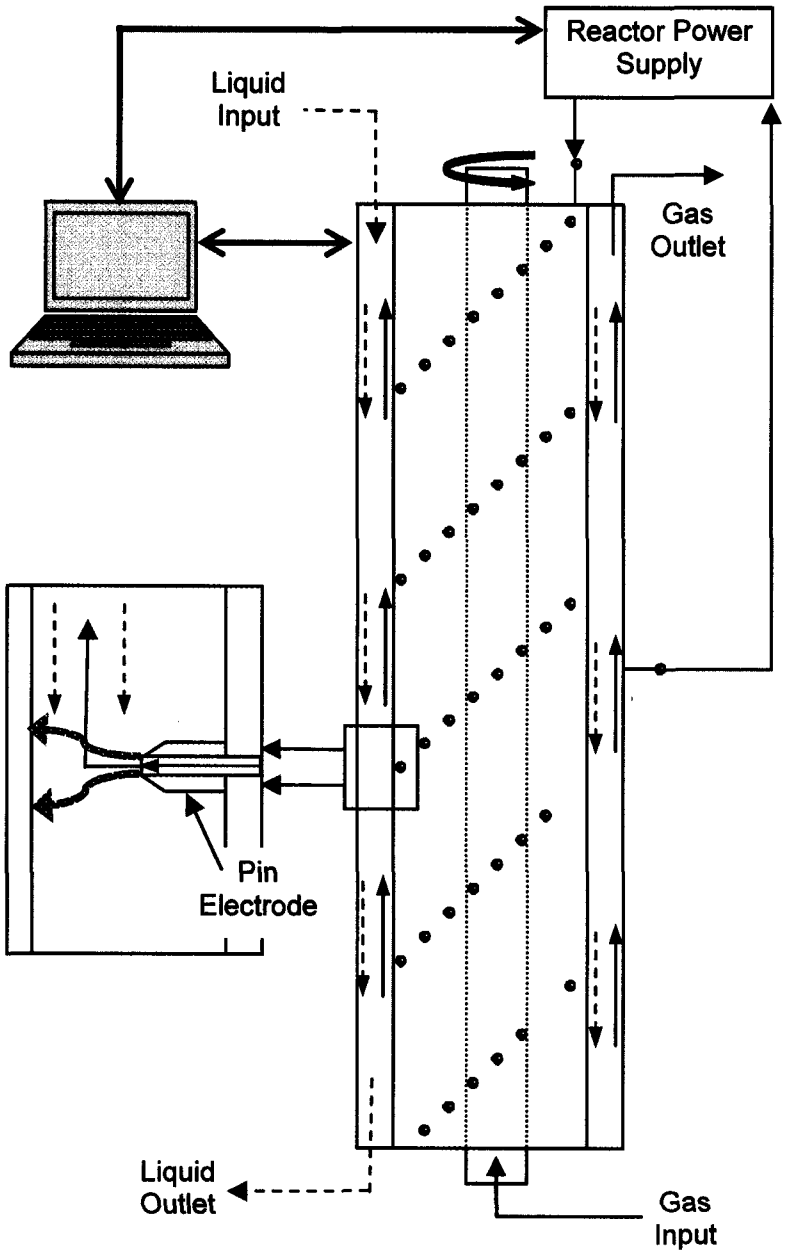

Figure 5.4: A schematic of a prototype tubular high-density plasma reactor. Gas (——►) and liquid (- - - - -►) flow patterns are shown as well as the possible plasma discharge path from the pin electrodes to the cylindrical electrode through the passing fluid, which is a combination of the gas introduced through the middle of the pin electrodes and the liquid flowing through the annulus. Note: lengths are not to scale.

Reproduced with permission of the copyright owner. Further reproduction prohibited without permission.

it travels countercurrently with respect to the aqueous solution and is released through a valve at the top of the reactor. When a potential is applied to the middle cylinder, a discharge is initiated at the tips of the pin electrodes that propagates radially to the outer cylinder.

5.4.1 Advantages Over State-of-the-Art

Numerous research teams have conducted experiments utilizing nonthermal, point-to-plane aqueous plasma discharge reactors for organic oxidation and microbial inactivation. Two reactor configurations dominate the literature: (1) pin electrodes discharging in the gas phase above the solution (Goheen et al., 1992; Hoeben, et al., 1999; Hayashi et al., 2000; Hoeben et al., 2000) and (2) a point-to-plane electrode configuration submersed in a liquid solution (Sun et al., 1997; Willberg et al., 1996a; Sun et al., 1999; Sun et al., 1998; Sunka, et al., 1999; Joshi et al., 1995; Lang et al., 1998; Lisitsyn et al., 1999; Malik et al., 2001; Mikula et al., 1997; Sharma et al., 1993; Shin et al., 2000; Sun et al., 2000; Wen and Jiang, 2000; Willberg et al., 1996b). The first configuration is characterized by the large production rate of gas phase oxidants such as ·OH, O_3, ·O, $\cdot HO_2$, and O_2^-, especially when the discharge atmosphere is manipulated to contain a high water vapor and O_2 partial pressure. In this reactor configuration, however, reaction and disinfection rates are not dominated by kinetics, but by mass transfer. The oxidation of organic contaminants and inactivation of microbes in the aqueous solution is hindered by the rates of diffusion of the oxidizing species through the gas/liquid interface. Another disadvantage of this reactor configuration is that the oxidation and disinfection proceeds solely by reaction with oxidizing species produced by the discharge. This is due to the fact that neither the organic molecules nor the microorganisms come into contact with the plasma; thus,

Reproduced with permission of the copyright owner. Further reproduction prohibited without permission.

interactions with high-energy electrons do not occur in this configuration. The consequence of losing this reaction pathway, with respect to organic oxidation, is that although the original organic may be attenuated faster than in the second reactor configuration, the carbon is still in solution in the form of oxidation products. Thus, the total organic carbon (TOC) concentration of the solution takes longer to reduce. In the case of microbial inactivation, plasma treatment is more effective when the microbes come into direct contact with the plasma. Another problem inherent with this design is that it presents scale up difficulties and is normally a batch process.

In the second reactor configuration, high potential oxidizing species such as ·OH, H_2O_2, ·O, $\cdot HO_2$, O_2^-, and O_3 (if O_2 is bubbled into the system) are also produced. However, the reaction and disinfection rates are still controlled by mass transfer and large plasma volumes can be difficult to sustain. As a result, the fluid volume in which oxidation reactions and microbial inactivation occur consists of a thin film around the plasma discharge. Thus, while the reaction rate is not hampered by diffusion across a gas/liquid interface, it is diminished due to the need of the organic species and microbes to be transported, normally by diffusion, from the bulk solution to the plasma/liquid interface. This configuration does possess an advantage over the previous reactor configuration since electron-impact dissociation reactions and microbial interactions with high-energy electrons are viable pathways. Thus, although the attenuation of the original organic contaminate is normally slower in this configuration, the TOC concentration is reduced at a higher rate. However, this design also presents scale up difficulties.

Reproduced with permission of the copyright owner. Further reproduction prohibited without permission.

The first attempt to rectify the problems inherent in the two above mentioned configurations was the development of the DMPR by Denes and coworkers (Denes and Young, 1996). They attempted to create a large volume, aqueous plasma discharge where the transport of the contaminants and the microbes are controlled by convective mass transfer. Utilizing this reactor, work conducted by Johnson et al. (2003) demonstrated that by promoting a volatile organic species to the plasma state, electron-impact dissociation reactions would completely oxidize the carbon in the molecule to CO_2 without the formation of intermediate byproducts. Essentially, the interaction with the high-energy electrons atomizes any organic species present in the plasma consequently forming the most thermodynamically favored species upon exiting the plasma. While the DMPR has been shown to be a promising tool for organic oxidation and microbial disinfection and is superior to other comparable plasma processing technologies published in the literature, it is also plagued by some of the problems associated with the reactor configurations mentioned previously. First, it is not robust, presents scale up difficulties and has a high capital cost. Second, although turbulent flow is induced within the reactor, the configuration only cycles approximately 5% of the bulk fluid through the plasma, thus limiting electron-impact dissociation reactions. However, these shortcomings are rectified in the design and fabrication of the tubular high-density plasma reactor.

5.4.2 Species Mass Balance

Four rate processes must be considered when performing a mass balance on a chemical species in the tubular high-density plasma reactor—accumulation, convective mass transfer, diffusion, and sources and/or sinks due to physical and chemical mechanisms. The dimensional form of the species conservation equation is

Reproduced with permission of the copyright owner. Further reproduction prohibited without permission.

$$\frac{\partial C_i}{\partial t} + \underline{v} \cdot \nabla C_i = D_{i_{mix}} \nabla^2 C_i + r_i, \tag{5.6}$$

where $\underline{v}$ is the local velocity vector, $D_{i_{mix}}$ is the diffusion coefficient for species i in the mixture and r_i is the net production rate of species i (which in this case is negative) by a series of homogeneous reactions. Concentration profiles for MTBE and the BTEXs are developed for the tubular reactor when operating under batch and steady flow conditions.

5.4.3 *Batch Operation*

To compare the ability of the tubular high-density plasma reactor to treat organically contaminated aqueous solutions with that of the DMPR, concentration profiles for batch operation have been developed. When operated in a batch configuration, the tubular reactor has virtually no axial, angular or radial concentration gradients because the plasma discharge is, in effect, uniform throughout the reactor. The species conservation equation thus reduces to the following ideal batch reactor design equation:

$$\frac{\partial C_i}{\partial t} = r_i. \tag{5.7}$$

To evaluate the production rate of species i, three loss processes are considered when removing a volatile organic compound from an aqueous solution in the reactor: oxidation due to the plasma, interphase mass transfer and photolysis. These loss processes can be expressed as

$$r_i = \frac{\ln a}{\alpha} C_{i_o} \exp\left(\frac{\ln a}{\alpha} t\right) + k_{mt} C_i^2 + \phi(\lambda) I_o(\lambda, t)[1 - \exp(-2.303 \varepsilon L C_i)]. \tag{5.8}$$

Reproduced with permission of the copyright owner. Further reproduction prohibited without permission.

The first term describes the loss of species i due to the plasma, where a is the volume fraction of fluid not in the plasma state, α is a time constant associated with the discharge characteristics of the reactor and has a value of 1 ms, t is time, and C_{i_o} is the initial concentration of species i (Willberg et al., 1996a). The second term describes the loss of species i through interphase mass transfer (Johnson et al., 2003), and the third due to photolysis (Sun et al., 2000). However, Eq. (4) can be rearranged, and further simplified, yielding

$$\frac{dC_i}{dt} = -k_{rxn}C_i - k_{mt}C_i^2 - k_p, \tag{5.9}$$

where k_{rxn} is a first-order rate constant associated with degradation due to the plasma, k_{mt} is a second-order interphase mass transfer rate constant and k_p is a zero-order photolysis rate constant. A combination of non-linear least squares analysis and MATLAB® optimization techniques were used to determine the rate constants, which are listed in Table 5.3 for each species. Predicted concentration profiles for the loss of each species due to interphase mass transfer and the plasma as well as the non-linear least squares fit to experimental data from Johnson et al. (2003) and Manolache et al. (2004) for the combination of the two processes are plotted in Figure 5.5.

The concentration at any point in the fluid can be determined by solving Eq. (5.9) and is

$$C_i = \frac{\phi\exp(\varepsilon t + \omega) + k_{rxn} + \varepsilon}{2k_{mt}(\exp(\varepsilon t + \omega) - 1)}, \tag{5.10}$$

where $\varepsilon = \sqrt{(-k_{rxn})^2 - 4k_{mt}k_p}$, $\omega = \log[(-2k_{mt}C_{i_o} - k_{rxn} - \varepsilon)/(-2k_{mt}C_{i_o} - k_{rxn} + \varepsilon)]$ and

Reproduced with permission of the copyright owner. Further reproduction prohibited without permission.

$\phi = \varepsilon - k_{rxn}$. The first-order rate constant, k_{rxn}, is a function of the plasma volume, which is estimated to be a linear function of the electrode gap and number of pin electrodes (Roth, 1995). Concentration profiles developed using the rate constants in Table 5.3, and accounting for changes in the electrode gap and number of pin electrodes, demonstrate that the tubular high-density plasma reactor has the ability to efficiently remove volatile organic compounds from aqueous solutions. Figure 5.6 contains predicted values of normalized species concentrations as a function of treatment time for varying electrode gaps and number of pin electrodes.

When the tubular reactor with 500 pin electrodes is configured with an electrode gap of 500 μm, a treatment time of approximately 2.2 min is required to reduce the MTBE—the most difficult to remove of the species considered—concentration below the recommended drinking water standard of approximately 20 ppb (U.S. EPA, 2002). The remaining BTEX concentrations are more readily removed from solution, and thus meet drinking water standards at lower treatment times. The predicted time needed to reduce each species concentration below the drinking water standard for different reactor configurations are listed in Table 5.4. A reasonable dimension for a reactor housing 500 pin electrodes is 150 cm (5 ft) in length and 7.6 cm (3 inch) in diameter. Using these dimensions and an electrode gap of 500 μm, it is estimated that the treatment volume is 180 mL. One route to larger treatment volumes is to increase the electrode gap, provided the plasma discharge can be sustained. For example, the same reactor configured with an electrode gap of 2 cm would reduce the time to degrade MTBE to 3.3 s while also treating approximately 5.4 L of contaminated liquid. Figure 5.7 contains two contour plots

Reproduced with permission of the copyright owner. Further reproduction prohibited without permission.

Table 5.3: Rate constants for the removal of MTBE, benzene, ethylbenzene, toluene, *m*- and *p* xylene, and *o*-xylene in a DMPR along with diffusion coefficients used to calculate specie pro files in conjunction with the mass balance.

	MTBE	Benzene	Ethyl-benzene	Toluene	*m*- and *p*-Xylene	*o*-Xylene
k_{rxm} (s^{-1})	0.003	0.172	0.172	0.172	0.172	0.172
k_{mt} (1/ppm/s)	1.40×10^{-6}	3.70×10^{-5}	5.13×10^{-5}	5.47×10^{-5}	1.26×10^{-5}	2.70×10^{-5}
k_p (ppm/s)	0	0	0	0	0	0
D_{i,H_2O} (cm^2/s)	1.04×10^{-5}	1.14×10^{-5}	9.31×10^{-4}	1.02×10^{-5}	9.31×10^{-4}	9.31×10^{-4}

Reproduced with permission of the copyright owner. Further reproduction prohibited without permission.

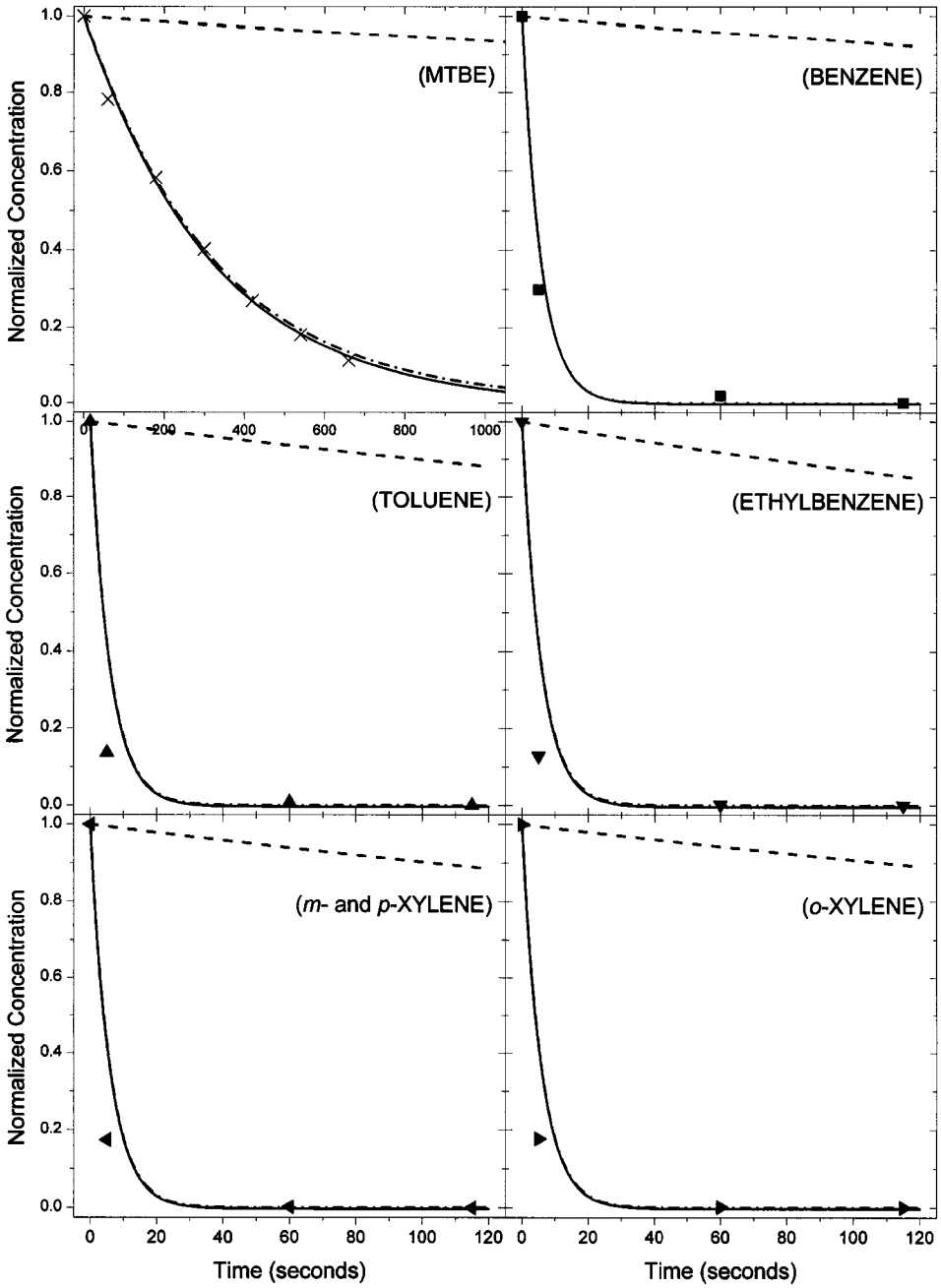

Figure 5.5: Plots of the normalized species concentration versus time for the removal of MTBE (×), benzene (■), toluene (▲), ethylbenzene (▼), *m*- and *p*-xylene (◀) and *o*-xylene (▶) in a DMPR (Johnson et al., 2003; Manolache et al., 2004), as well as the curves describing losses due to sparging (_ _ _), the plasma (_ . _) and the combined effects of the discharge (___). Notice that for the BTEXs, the plasma curve and combined effects curve are almost indistinguishable.

Reproduced with permission of the copyright owner. Further reproduction prohibited without permission.

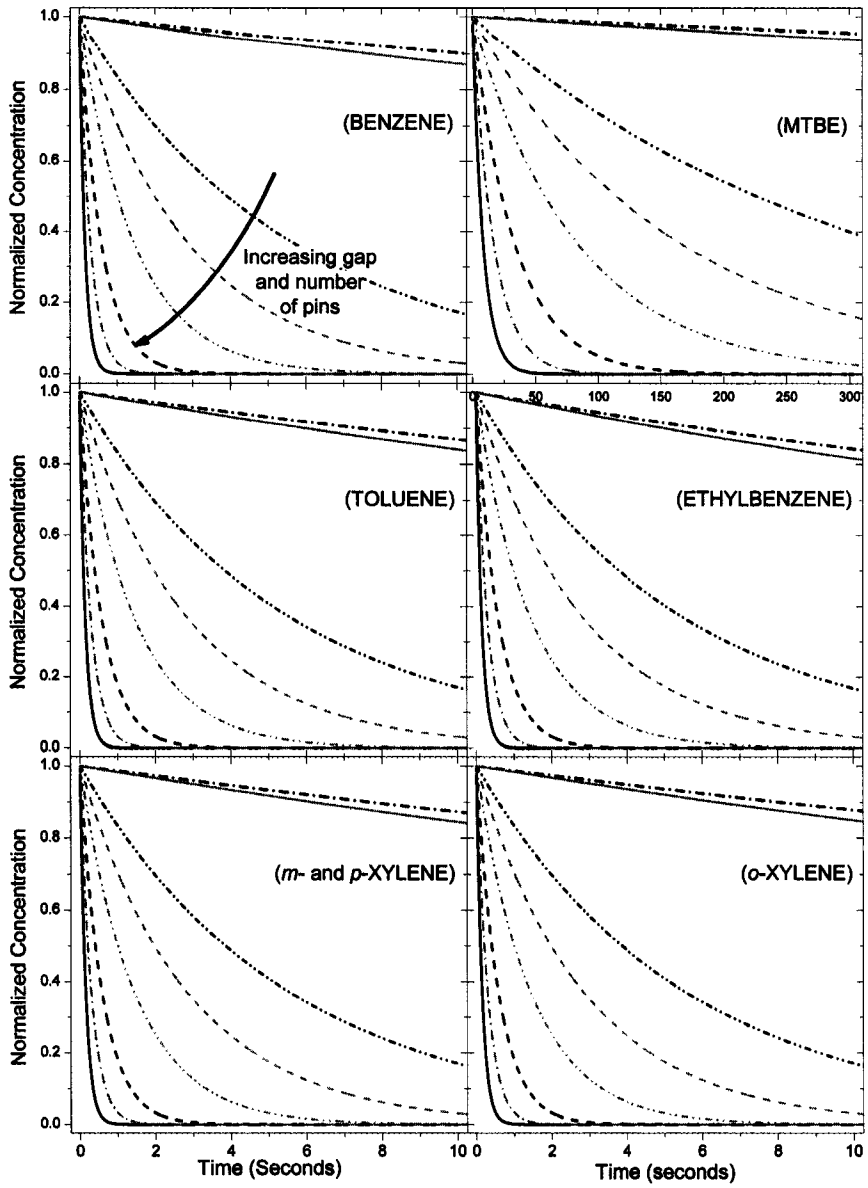

Figure 5.6: Plots of the predicted normalized concentration profiles for the removal of benzene, MTBE, toluene, ethylbenzene, *m*- and *p*-xylene, and *o*-xylene from an aqueous solution versus treatment time in a tubular high-density plasma reactor operated under batch conditions for varying electrode gaps and number of pin electrodes. Black curves correspond to 25 pin electrodes and electrode gaps of 0.001 cm (— . —), 0.05 cm (— . . —), 0.5 cm (– –) and 2 cm (——). Gray curves correspond to an electrode gap of 0.05 cm and 1 pin electrode (——), 50 pin electrodes (– –), 100 pin electrodes (— . . —) and 500 pin electrodes (— . —).

Reproduced with permission of the copyright owner. Further reproduction prohibited without permission.

for the removal of MTBE and ethylbenzene as a function of the number of pin electrodes and electrode gap for 3.3 s of treatment. It is clearly shown that increasing the number of pins and the electrode gap will reduce the time required for treatment. It is also apparent when comparing the MTBE contour plot with that of ethylbenzene, a species with a higher *K*-value will be removed from solution at a faster rate. The higher volatility of the aromatic compounds more readily promotes them to the plasma state where electron dissociation reactions occur, thus increasing the removal rate. Although operating the tubular high-density plasma reactor in a batch configuration may be a viable treatment option for organically contaminated aqueous solutions, the system is more effective operating under continuous flow conditions when targeting scale-up and throughput issues.

5.4.4 *Continuous Operation*

To determine the effectiveness of the tubular reactor in its intended operational configuration, concentration profiles for MTBE and the BTEXs are developed for continuous flow. Under steady state conditions, the first term in Eq. (5.6) vanishes and further simplifications may be possible, depending on the relative magnitudes of the convection and diffusion terms. To investigate this, the species equation is written in dimensionless form. Rewriting each term with a dimensionless concentration, $\varphi_i = C_i / C_{i_o}$, and its corresponding dimensional scaling factor, the dimensionless form of the equation is

$$Pe_i\left(\frac{d\varphi_i}{d\zeta}\right) = \frac{d^2\varphi_i}{d\zeta^2} + \sum_{ij} Da_{ij} r_{ij}^{*}, \tag{5.11}$$

where $Pe_i = Lv_{avg} / D_{i_{mix}}$, $Da_{ij} = k_{ij} L^2 C_{i_o}^{n-1} / D_{i_{mix}}$, L is the length of the reactor, $\zeta = z / L$ is the dimensionless reactor length and $r_{ij}^{*} = r_{ij} / (k_{ij} C_{i_o}^{n})$. The tubular high-density plasma

Reproduced with permission of the copyright owner. Further reproduction prohibited without permission.

Table 5.4: Treatment time and corresponding concentration for the removal of MTBE, benzei ethylbenzene, toluene, *m*- and *p*- xylene, and *o*-xylene in a batch tubular high-density plasma rea tor as well as volumetric flow rate and exit concentration for a tubular reactor with a continuc feed for varying electrode gaps and number of pin electrodes.

	MTBE	Benzene	Toluene	Ethylbenzene	*m*- and *p*-Xylene	*o*-Xylen
# of pins electrode gap	Time (s) Conc. (ppb)	Time (s) Conc. (ppb)	Time (s) Conc. (ppb)	Time (s) Conc. (ppb)	Time (s) Conc. (ppb)	Time (s Conc. (p
Batch Configuration						
25 pins	1.2×10^{5}	2.7×10^{3}	1.2×10^{3}	1.3×10^{3}	8.9×10^{2}	6.8×1
0.001 cm	20	5.0	10	7.0	10	10
25 pins	2.6×10^{3}	61	31	34	26	21
0.05 cm	20	5.0	10	6.9	9.9	10
25 pins	2.6×10^{2}	6.2	3.1	3.5	2.6	2.1
0.5 cm	19	4.5	10	7.0	10	10
25 pins	6.6×10^{1}	1.5	0.78	0.87	0.65	0.53
2 cm	19	5.0	10	7.0	9.9	9.9
1 pin	6.1×10^{4}	1.4×10^{3}	6.4×10^{2}	7.0×10^{2}	5.1×10^{2}	4.0×1
0.05 cm	20	5.0	10	7.0	10	10
50 pins	1.3×10^{3}	31	16	17	13	11
0.05 cm	20	4.9	10	7.0	9.9	9.9
100 pins	6.5×10^{2}	15	7.9	8.7	6.5	5.3
0.05 cm	20	4.8	9.4	6.7	9.7	9.7
500 pins	1.3×10^{2}	3.1	1.6	1.7	1.3	1.1
0.05 cm	18	5.0	10	7.0	10	10
500 pins	3.3	7.7×10^{-2}	4.0×10^{-2}	4.4×10^{-2}	3.3×10^{-2}	2.7×1
2 cm	18	4.9	9.0	6.4	9.2	9.2
# of pins electrode gap	Q (L/min) Conc. (ppb)	Q (L/min) Conc. (ppb)	Q (L/min) Conc. (ppb)	Q (L/min) Conc. (ppb)	Q (L/min) Conc. (ppb)	Q (L/mi Conc. (p
Continuous Flow Configuration						
25 pins	7.3×10^{-9}	1.5×10^{-5}	3.6×10^{-5}	2.9×10^{-5}	4.4×10^{-5}	5.8×1
0.001 cm	20	2.1	840	300	6800	7700
25 pins	8.4×10^{-4}	3.6×10^{-2}	7.0×10^{-2}	6.4×10^{-2}	8.5×10^{-2}	1.0×1
0.05 cm	20	5.0	980	690	9800	9900
25 pins	8.1×10^{-2}	3.5	6.7	6.0	8.1	9.8
0.5 cm	20	5.0	960	620	9600	9400
25 pins	1.1	49	96	87	120	140
2 cm	20	4.9	960	680	9700	9800
50 pins	2.5×10^{-3}	1.1×10^{-1}	2.1×10^{-1}	1.9×10^{-1}	2.5×10^{-1}	3.1×1
0.05 cm	20	4.9	1000	700	10000	10000
100 pins	6.7×10^{-3}	2.8×10^{-1}	5.5×10^{-1}	5.1×10^{-1}	6.5×10^{-1}	8.0×1
0.05 cm	20	5.0	880	700	8600	8700
500 pins	1.7×10^{-1}	7.1	14	12	17	20
0.05 cm	20	4.9	990	690	9900	9400
500pins	228	9900	19000	18000	23000	29000
2 cm	17	4.9	1000	700	9900	9900

Reproduced with permission of the copyright owner. Further reproduction prohibited without permission.

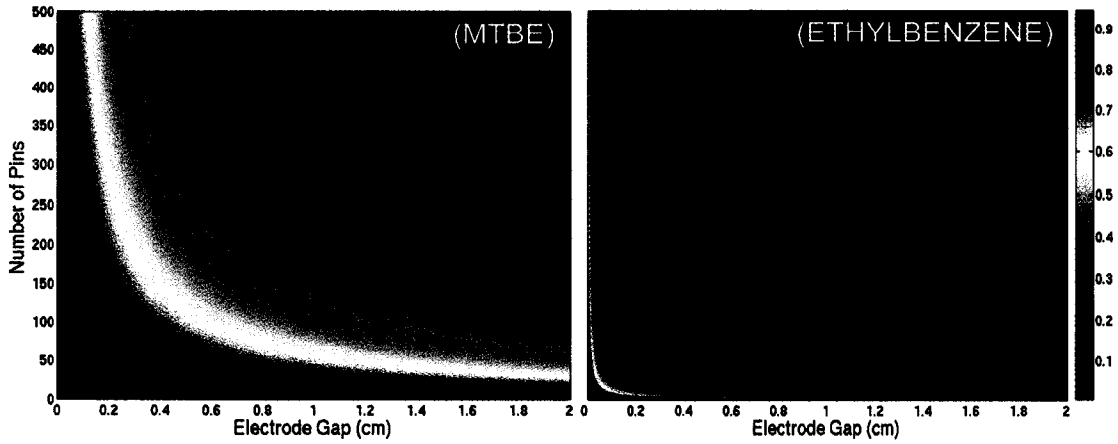

Figure 5.7: Contour plots of the predicted normalized concentrations of MTBE and ethylbenzene in the tubular high-density plasma reactor operating in a batch configuration as a function of the electrode gap and number of pin electrodes at a residence time of 3.3 s.

Reproduced with permission of the copyright owner. Further reproduction prohibited without permission.

reactor has a continuous input and an impermeable outer wall. Thus, the local velocity vector is replaced with a scalar cross-sectional average velocity and is contained in the mass transfer Peclet number, *Pe*. The mass transfer Peclet number relates the rate of convective mass transfer to the rate of diffusion. When $Pe >> 1$, as is typical in a liquid, the diffusion term in Eq. (5.11) may be neglected if the Damköhler number, *Da*, is also large, resulting in the classic plug flow equation. Therefore, it is important to consider whether the system is mass transfer limited by evaluating *Da*. The Damköhler number relates the rate of reaction of species *i* to the rate of transport of species *i* through the reaction zone. Using the empirical Wilke-Chang equation (Wilke and Chang, 1955) to calculate $D_{i_{mix}}$, which are listed in Table 5.3, it was found that $Da >> 1$ for all species and operating conditions; thus, the rate of diffusion is negligible relative to the reaction rate.

When neglecting diffusion and using the expression for r_i developed previously, the dimensionless species balance can be further reduced and expressed as

$$\frac{d\varphi_i}{d\zeta} = -\frac{L}{v_{avg}}\left(k_{rxn}\varphi_i + k_{mt}C_{i_o}\varphi_i^2 + \frac{k_p}{C_{i_o}}\right). \tag{5.12}$$

Thus, the normalized concentration of species *i* as a function of axial position is

$$\varphi_i = \frac{\phi\exp(\omega - \varepsilon\tau\zeta) - k_{rxn} + \varepsilon}{2k_{mt}C_{i_o}\left(1-\exp(\omega-\varepsilon\tau\zeta)\right)}, \tag{5.13}$$

where $\varepsilon = \sqrt{k_{rxn}^2 - 4k_{mt}k_p}$, $\omega = \log[(2k_{mt}C_{i_o} + k_{rxn} - \varepsilon)/(2k_{mt}C_{i_o} + k_{rxn} + \varepsilon)]$, $\phi = k_{rxn} + \varepsilon$ and $\tau = L/v_{avg}$ is the average residence time. As before, the first-order rate constant, k_{rxn}, is a function of the plasma volume, making this quantity directly proportional to the

Reproduced with permission of the copyright owner. Further reproduction prohibited without permission.

electrode gap and number of pin electrodes. Concentration profiles are again computed using the rate constants in Table 5.3 while accounting for changes in the electrode gap and number of pin electrodes. Trends in the predicted normalized concentration for all six species as a function of the electrode gap and number of pin electrodes are similar to that found for the batch configuration. The exit concentration, corresponding to a dimensionless length of unity, decreases with an increase in the electrode gap and number of pin electrodes when the inlet fluid velocity and species concentration are fixed.

To compare the different modes of operation, batch and continuous flow, the same design specifications as in the previous section are used in the following calculations. Instead of residence time in the tubular reactor, however, the results are presented as a function of volumetric flow rate. Figure 5.8 contains calculated normalized concentration profiles for MTBE and the BTEXs versus volumetric flow rate for varying operating conditions. A reactor housing 500 pin electrodes configured with electrode gaps of 0.05 and 2 cm will reduce the MTBE concentration below the recommended drinking water standard at volumetric flow rates of 1.7×10^{-1} and 228 L/min, respectively. The remaining BTEX concentrations are reduced below drinking water standards at higher flow rates. The volumetric flow rates predicted for each species for various reactor configurations are listed in Table 5.4.

5.5 Summary

A tubular high-density plasma reactor may be an effective tool in the removal of volatile organic compounds from aqueous solutions. The new design is easier to scale for

Reproduced with permission of the copyright owner. Further reproduction prohibited without permission.

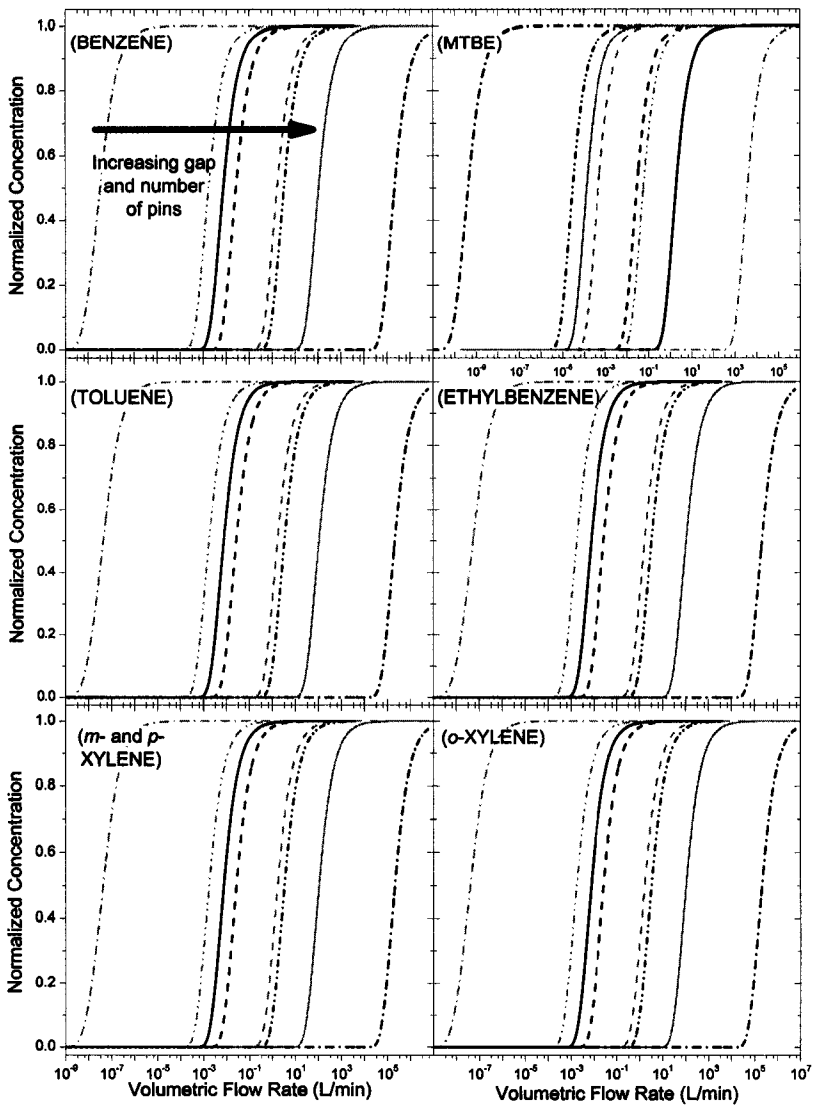

Figure 5.8: Plots of the calculated normalized concentration profiles for the removal of benzene, MTBE, toluene, ethylbenzene, *m*- and *p*-xylene and *o*-xylene from an aqueous solution versus volumetric flow rate in a tubular high-density plasma reactor operated under continuous feed conditions for varying electrode gaps and number of pin electrodes. Gray curves correspond to 25 pin electrodes and electrode gaps of 0.001 cm (— — —), 0.05 cm (— — —), 0.5 cm (— —) and 2 cm (——). Black curves correspond to an electrode gap of 0.05 cm and 50 pin electrodes (——), 100 pin electrodes (— —), 500 pin electrodes (— · · —), and an electrode gap of 2 cm with 500 pin electrodes (— · —).

Reproduced with permission of the copyright owner. Further reproduction prohibited without permission.

industrial use, especially when operated under continuous flow conditions. The prototype reactor also reduces the sputtering rate, i.e. the wear, of the electrodes when compared to other point-to-plane reactors. This is accomplished by incorporating a large number of pins in parallel, thereby reducing the current density at the pin tip, which controls the sputtering rate, while still applying the same voltage drop across the electrode gap. Although rate constants for the removal of volatile organics have been determined for only six compounds, the removal rate constant for a given species, voltage, current, electrode gap, gas composition and gas flow rate should be higher than that of MTBE if its *K*-value is also higher. If MTBE is used as a surrogate molecule for contaminated water, a configuration of 12 reactors, each 5 ft in length configured with an electrode gap of 2 cm and 500 pin electrodes, has the potential to treat 1 MGD of contaminated liquid. However, MTBE has a vapor pressure higher than most contaminants in wastewater streams. Thus, to ascertain the volumetric flow rate needed to treat waste streams more representative of what is produced industrially, it is important to determine the rate constants associated with the treatment of water contaminated with species having a *K*-value of approximately zero.

The tubular plasma reactor is also designed to maximize the time in which a fluid element moving axially through the reactor is in contact with the plasma. This is accomplished by minimizing the distance that the pin electrodes protrude from the rotating cylinder. Because of this design implementation, the fraction of fluid in the annular gap contacting the plasma is maximized, a significant improvement over the initial DMPR design, whereby a significant fraction of the fluid (approximately 95%) bypasses the

Reproduced with permission of the copyright owner. Further reproduction prohibited without permission.

plasma as it moves through the reaction zone. As a result, the first-order rate constant associated with the plasma will be higher in the tubular reactor, so that the results displayed in Table 5.4 may be viewed as upper limits. Also, the zero-order rate constant associated with photolysis may not be negligible in the tubular reactor, particularly when 500 pin electrodes are employed, 20 times more than in the DMPR configuration. Thus, the rate constants used in this study to predict the effectiveness of the prototype reactor are conservative, and experiments conducted on the tubular reactor should yield lower treatment times and higher volumetric flow rates.

Reproduced with permission of the copyright owner. Further reproduction prohibited without permission.

5.6 References

Burdick & Jackson, (Nov. 12, 2002). Solvent Physical Properties.http://www.bandj.com/-BJSolvents/ Solvents/MethyltbutylEther/MtBEther.htm.

Cengel, Y.A., 1998. Heat Transfer: A Practical Approach. WCB, McGraw-Hill, Boston, MA, USA.

Denes, F.S., Young, R.A., 1996. Apparatus for reactions in dense-medium plasmas. U.S. Patent #5,534,232.

Goheen, S.C., Durhlam, D.E., McCulloh, M., Heat, W.O., 1992. The Degradation of Organic Dyes by Corona Discharge. Proc. Second Int. Symp. Chem. Oxidation. Nashville, TN., 356-367.

Hayashi, D., Hoeben, W.F.L.M., Dooms, G., van Veldhuizen, E.M., Rutgers, W.R., Kroesen, G.M.W., 2000. LIF diagnostic for pulsed-corona-induced degradation of phenol in aqueous solution. J. Phys. D: Appl. Phys. 33, 2769-2774.

Hoeben, W.F.L.M., van Veldhuizen, E.M., Rutgers, W.R., and Kroesen, G.M.W., 1999. Gas phase corona discharges for oxidation of phenol in an aqueous solution. J. Phys. D: Appl. Phys. 32, L133-L139.

Reproduced with permission of the copyright owner. Further reproduction prohibited without permission.

Hoeben, W.F.L.M., van Veldhuizen, E.M., Rutgers, W.R., Cramers, C.A.M.G., Kroesen, G.M.W., 2000. The degradation of aqueous phenol solutions by pulsed positive corona discharges. Plasma Sources Sci. Technol. 9, 361-369.

Johnson, D.C., Shamamian, V.A., Callahan, J.H., Denes, F.S., Manolache, S.O., Dandy, D.S., 2003. Treatment of methyl *tert*-butyl ether contaminated water using a dense medium plasma reactor: A mechanistic and kinetic investigation. Environ. Sci. Technol. 37, 4804-4810.

Joshi, A.A., Locke, B.R., Arce, P., Finney, W.C., 1995. Formation of Hydroxyl Radicals, Hydrogen-Peroxide and Aqueous Electrons by Pulsed Streamer Corona Discharge in Aqueous-Solution. J. Hazard. Mater. 41, 3-30.

Lang, P.S., Ching, W.K., Willberg, D.M., Hoffmann, M.R., 1998. Oxidative degradation of 2,4.6-trinitrotoluene by ozone in an electrohydraulic discharge reactor. Environ. Sci. Technol. 32, 3142-3148.

Lisitsyn, I.V., Nomiyama, H., Katsuki, S., Akiyama, H., 1999. Streamer discharge reactor for water treatment by pulsed power. Rev. Sci. Instrum. 70, 3457-3462.

Malik, M.A., Ghaffar, A., Malik, S.A., 2001. Water purification by electrical discharges. Plasma Sources Sci. Technol. 10, 82-91.

Manolache, S., Somers, E.B., Wong, A.C.L., Shamamian, V., Denes, F., 2001. Dense medium plasma environments: A new approach for the disinfection of water. Environ. Sci. Technol. 35, 3780-3785.

Reproduced with permission of the copyright owner. Further reproduction prohibited without permission.

Manolache, S.O., Shamamian, V.A., Denes, F., 2004. Dense medium plasma-plasma-enhanced decontamination of water of aromatic compounds. J. Environ. Engin. 130, 17-25.

Mikula, M., Panak, J., Dvonka, V., 1997. The destruction effect of a pulse discharge in water suspensions. Plasma Sources Sci. Technol. 6, 179-184.

Roth, J.R., 1995. Industrial Plasma Engineering Vol. 1: Principles. Institute of Physics Publishing, Philadelphia, PA, USA.

Seader, J. D., Henley, E. J., 1998. Separation Process Principles. John Wiley & Sons, Inc., New York, NY, USA.

Sharma, A.K., Locke, B.R., Arce, P., Finney, W.C., 1993. A Preliminary-Study of Pulsed Streamer Corona Discharge for the Degradation of Phenol in Aqueous-Solutions. Hazard. Waste Hazard. Mater. 10, 209-219.

Shin, W.T., Yiacoumi, S., Tsouris, C., Dai, S., 2000. A pulseless corona-discharge process for the oxidation of organic compounds in water. Ind. Eng. Chem. Res. 39, 4408-4414.

Sun, B., Sato, M., and Clements, J.S., 1997. Optical study of active species produced by a pulsed streamer corona discharge in water. J. Electros. 39, 189-202.

Sun, B., Sato, M., Harano, A., Clements, J.S., 1998. Non-uniform pulse discharge-induced radical production in distilled water. J. Electros. 43, 115-126.

Reproduced with permission of the copyright owner. Further reproduction prohibited without permission.

Sun, B., Sato, M., Clements, J.S., 1999. Use of a pulsed high-voltage discharge for removal of organic compounds in aqueous solution. J. Phy. D: Appl. Phy. 32, 1908-1915.

Sun, B., Sato, M., Clements, J.S., 2000. Oxidative processes occurring when pulsed high voltage discharges degrade phenol in aqueous solution. Environ. Sci. Technol. 34, 509-513.

Sunka, P., Babicky, V., Clupek, M., Lukes, P., Simek, M., Schmidt, J., Cernak, M., 1999. Generation of chemically active species by electrical discharges in water. Plasma Sources Sci. Techno. 8, 258-265.

Turner, L.H., Chiew, Y.C., Ahlert, R.C., Kosson, D.S., 1996. Measuring vapor-liquid equilibrium for aqueous-organic systems: Review and a new technique. AIChE J. 42, 1772-1788.

U.S. EPA, (Nov. 26, 2002). MTBE in Drinking Water. http://www.epa.gov/safewater-/mtbe.html.

Walas, S.M., 1985. Phase equilibria in chemical engineering. Butterworth, Boston, MA, USA.

Wen, Y., Jiang, X., 2000. Degradation of acetophenone in water by pulsed corona discharges. Plasma Chem. Plasma Process. 20, 343-351.

Wilke, C.R., Chang, P., 1955. Correlation of diffusion coefficients in dilute solutions. AIChE J. 1, 264-270.

Reproduced with permission of the copyright owner. Further reproduction prohibited without permission.

Willberg, D.M., Lang, P.S., Hochemer, R.H., Kratel, A.W., Hoffmann, M.R., 1996a. Electrohydraulic destruction of hazardous wastes. CHEMTECH. 26, 52-57.

Willberg, D.M., Lang, P.S., Hochemer, R.H., Kratel, A., Hoffmann, M.R., 1996b. Degradation of 4-chlorophenol, 3,4-dichloroaniline, and 2,4,6-trinitrotoluene in an electrohydraulic discharge reactor. Environ. Sci. Technol. 30, 2526-2534.

Reproduced with permission of the copyright owner. Further reproduction prohibited without permission.